University of Catania

Department of Biological, Geological and Environmental Sciences

Ph.D. in Earth Science XXVIII cycle (2013-2015)

Complex Pore Geometries in Natural Building Stones:

an experimental and theoretical approach for the modeling of porosity changes in natural, degraded and treated calcarenites

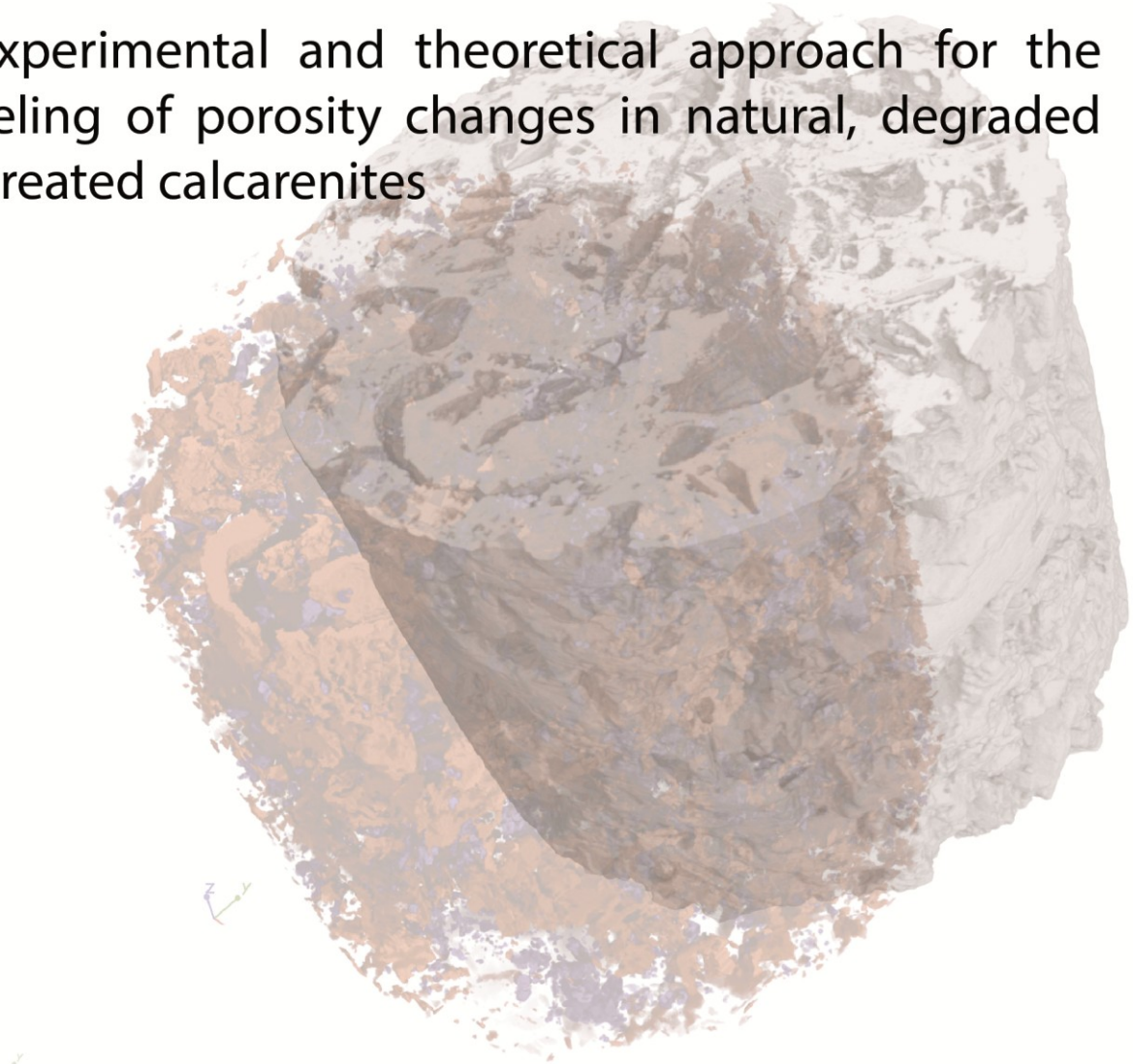

Simona Raneri

The past is always present, as the context from which the present has emerged;
thus, there is theoretical continuity between material changes in the past, present, and future.

Mostafavi and Leatherbarrow (1993)

University of Catania

Department of Biological, Geological and Environmental Sciences

Ph.D. in Earth Science XXVIII cycle (2013-2015)

Complex Pore Geometries in Natural Building Stones: an experimental and theoretical approach for the modeling of porosity changes in natural, degraded and treated calcarenites

by

Simona Raneri

Under the supervision of

Prof. Germana Barone

Prof. Paolo Mazzoleni

ABSTRACT

Calcarenites are the most widely used natural stones in Sicily as building materials. The comprehension of the degradation style of these natural building stone is of great interest in order to preserve the ancient masonry, especially in the case of relevant Cultural Heritages. A large number of Sicilian monuments are included in UNESCO Heritage List as their special cultural or physical significance. Considering the cultural importance of these ones, smart solutions are required in the perspective of their conservation.

In the framework of restoration actions, the complete knowledge of the internal structure of building stones is fundamental in order to estimate durability and prevent degradation processes. Salt growth is a significant cause of damage for natural stones. The effects of the salt weathering are, in addition to the properties of the salt itself and the climatic conditions, strongly related to the structural and textural features of materials. For this reason, an integrate study on petrographic, physical, mechanical and porosimetric proprieties changes due to salts crystallization could be useful to highlight correlation among textural, structural and engineering parameters. Moreover, one of the main problems in conservation field is the use of suitable consolidant and protective treatments able to preserve the masonry, being compatible with the stone substrate and not affecting its aesthetical proprieties. There are numerous tests able to verify the efficiency of consolidant or protective products, mainly devoted to verify their ability to not modify the appearance of stone and its physical proprieties, especially against water; however, particularly in the case of consolidant, one of the most important feature is related to its penetration depth, often difficult to evaluate by using the standard test routines.

For aforementioned, this research work is devoted to apply a multi-methodological approach for characterizing and modeling pore structure modifications due to weathering processes in a coarse grained Sicilian calcarenite used as building and replace stones in Sicilian Cultural Heritages (Sabucina Stone), also through fractal models and innovative and non invasive methods. The obtained data on Sabucina stone have been employed for planning conservative treatments devoted to coarse grained calcarenite substrates. Therefore, innovative nanostructured and hybrid consolidant and protective products have been experimented and the results of efficiency tests along with the determination of surface and sub-surface changes due to the treatments are proposed.

In conclusion, the applied theoretical and empirical approach has allowed to: highlight the potential of classical and innovative complementary methods in quantifying the structural changes in porous materials due to degradation processes and conservative treatments, explain how they help to facilitate the understanding of stone weathering and validate the use of geometrical models in describing complex pore systems.

RIASSUNTO

Nel panorama dei materiali lapidei naturali utilizzati come pietre da costruzione nell'edilizia storica siciliana, le calcareniti rappresentano uno dei litotipi maggiormente impiegati; testimonianza di ciò è la particolare diffusione di tali materiali nella maggior parte dei Beni di interesse storico e culturale, tra i quali numerosi sono quelli inclusi nella Lista del patrimonio UNESCO. In ragione di ciò, è di prioritaria importanza l'adozione di soluzioni idonee e specifiche per la loro protezione e conservazione.

Al fine di programmare e pianificare adeguati interventi di conservazione e restauro è di fondamentale importanza una corretta caratterizzazione delle proprietà fisiche e strutturali dei materiali, avendo queste un'influenza diretta sulla durabilità degli stessi e sull'evoluzione dei processi di alterazione e degrado. La cristallizzazione dei sali rappresenta uno degli agenti maggiormente dannosi nei confronti dei materiali lapidei naturali; nel caso del degrado da sali solubili, l'entità del danno causato è influenzata non solo dalle proprietà chimico-mineralogiche dei sali, ma anche dalle condizioni climatico-ambientali, nonché dalle modificazioni indotte nella struttura e tessitura dei materiali interessati dal processo.

Da quanto detto appare chiaro che la valutazione dello stato di conservazione e delle modificazioni indotte dal degrado da sali solubili nei materiali lapidei naturali non può che prevedere l'applicazione di un approccio integrato e multidisciplinare, capace di indagare tutte le proprietà soggette all'azione della cristallizzazione salina, sia quelle prettamente materiche (petrografiche, mineralogiche, chimiche e fisiche), che quelle tecniche (ingegneristiche, meccaniche e micro-strutturali).

Altro aspetto di interesse nella conservazione dei materiali lapidei naturali riguarda l'intervento diretto di restauro; deprecabile è l'utilizzo di consolidanti e protettivi senza verificarne la loro compatibilità materica ed estetica con il substrato. A tal proposito, diverse metodologie permettono di valutare l'efficienza e la capacità di questi di non interferire con le proprietà chimico-fisiche del materiale; tuttavia, per i consolidanti, aspetti quali la loro profondità di penetrazione, sono spesso di difficile valutazione attraverso l'esecuzione di test standard.

Alla luce di quanto detto, il presente lavoro di tesi espone lo sviluppo di un approccio multi-metodologico basato sull'applicazione integrata di metodi classici e innovativi, finalizzato a indagare le modificazioni della struttura porosa indotte dalla cristallizzazione salina nella Pietra di Sabucina, calcarenite grossolana utilizzata come materiale da restauro e da costruzione in Sicilia centro-orientale. Ciò ha consentito l'elaborazione di un modello interpretativo del processo di degrado, descrittivo dell'evoluzione micro-strutturale e tessiturale della roccia e dell'influenza dello stesso sulle sue caratteristiche fisico-meccaniche, nonché funzionale alla scelta delle più idonee modalità di intervento conservativo. La particolare diffusione, nel panorama attuale, di prodotti nanostrutturati, ha indirizzato alla scelta di sistemi ibridi,

innovativi, ecocompatibili e ad alta efficienza; in riferimento a ciò, sono state verificate le caratteristiche di compatibilità chimico-fisica ed estetica con il litotipo oggetto di studio e le eventuali modificazioni micro-strutturali e micro-tessiturali indotte nello stesso.

L'insieme dei risultati ottenuti ha consentito quindi di verificare le potenzialità dell'applicazione di metodologie complementari, tradizionali e innovative, atte a quantificare e visualizzare le modificazioni strutturali e tessiturali superficiali e sub-superficiali indotte dal degrado e dai trattamenti conservativi nei materiali lapidei naturali, indicando quindi un *modus operandi* capace di descrivere geometrie complesse attraverso modelli teorici ed empirici.

RESUMÈ

Les calcarénites sont les pierres les plus utilisés en Sicile comme matériaux dans constructions. La compréhension des mécanismes de dégradation de ce matériel naturel a un grand intérêt pour la préservation de l'ancienne maçonnerie, surtout lorsqu'il s'agit de patrimoine culturels reconnu. Un grand nombre des monuments siciliens sont inclus dans la Liste du Patrimoine de l'Unesco grâce à leur portée culturelle et diversification des matériaux composants. Pour cette raison il faut identifier des solutions appropriées afin de les conserver.

Dans le cadre des activités de restauration, la connaissance complète de la structure interne des pierres de construction est essentielle pour estimer la durabilité et prévenir la dégradation du matériau. La croissance des sels est l'une des premières causes des altérations des pierres naturelles. En addition à les propriétés du sel lui-même et des conditions climatiques, les effets d'altération de la pierre sont fortement associés aux caractéristiques structurelles et à la texture des matériaux. Pour cette raison il est nécessaire un étude intégré sur le changement des propriétés pétrographiques, physiques, mécaniques et des pores lié à la présence des sels pour mettre en évidence les corrélations entre les paramètres de la texture, de la structure et de la mécanique. En outre, la science de la conservation a le devoir de considérer le problème des traitements, de la consolidation et de la protection qui doivent être compatibles avec les caractéristiques de la pierre et ne pas altérer l'esthétique du monument. Différents test sont disponibles pour vérifier l'efficacité d'un produit de consolidation ou de protection, la plus part ont l'objectif de prouver la capacité des produits de ne pas altéré l'apparence des pierres et ses propriétés physiques, en particulier vers l'eau; cependant, pour les consolidants, en outre un de plus grand problème est lié à la profondeur de la pénétration de ces produits, souvent difficile à déterminer par le test de routine.

En conséquence, ce travail de recherche a l'objectif d'appliquer une approche multi-méthodologique avec des techniques innovatrices et très avant-gardistes pour le regroupement d'informations qui nous permettrons de créer un modèle d'interprétation du processus d'altération de la structure de pore sur une calcarénite sicilienne à grain grossier (Sabucina Stone). Cette pierre est très utilisée pour la construction et la restauration de monuments siciliens. Les données obtenues ont été utilisés pour la planification des traitements conservateurs spécifiques aux calcarenites. Pour cette raison des consolidants et protecteurs, hybrides, innovants et nanostructurés, ont été testés sur le matériau; cette expérience fais surgir l'efficience des produits employés et leur interaction avec la superficie et l'intérieure de la pierre en question.

L'ensemble des résultats met en évidence la potentialité de l'utilisation des méthodes complémentaires, traditionnelles et innovantes, pour quantifier le changement structurel des matériaux poreux causé par la détérioration et par l'utilisation des traitements conservateurs.

L'approche utilisée explique clairement comme interpréter les mécanismes de dégradation des pierres en utilisant des modèles empiriques and théoriques pour décrire des géométries complexes des pores.

Acknowledgments

This Thesis work is the result of several scientific collaborations, internship activities and international projects. Therefore, I would like to thank all supervisors and collaborators who support my researches.

Firstly, my supervisors Germana Barone and Paolo Mazzoleni; they introduced me in the field of conservation studies, especially in geomaterial researches concerning degradation processes in building and decorative stones. In addition, during my Ph.D. studies, they involved me in several projects about archeaometry and applied petrography and mineralogy, allowing me to acquire expertise and skills in several research fields; they also encouraged me to participate to numerous International Schools, Conferences and Congresses, during which I had not only the opportunity to share our researches to the International Scientific Community, but also enrich my personal and professional profile. They revised with great care this thesis work, significantly improving the research. Thanks for all these opportunities, for the scientific criticism, for the educational support, for the advises and the suggestions, and, last but not least, thanks for all the signs of respect and affection for me.

I'd like to thank Giovanni Predieri, Pier Paolo Lottici, Danilo Bersani and their research teams for letting me work in their group at the Departments of Chemistry and Physic at the Parma University (Italy) during several internship activities in 2013 and 2014. Thank to Giovanni Predieri for introducing me in the field of nano-technologies and nanostructured materials for the conservation and protection of building stones, as well as for training in Chemistry laboratories and for supplying the innovative products tested in the framework of this research. Thank to Pier Paolo Lottici and Danilo Bersani for their charming guest at the Physic laboratories and for endorsing my knowledge about spectroscopic methods and applications.

I would like to greatly thank Veerle Cnudde for hosting me during an internship activity in 2014 at the University of Ghent (Belgium) and supervising my researches at UGCT Facility. Thanks for the warming welcome and the absolutely indispensible educational training in high-resolution X-ray techniques, without which an important section of this research cannot be realized. Thank also to all her great research team for supporting me in my researches; thanks to Tim De Kock, Hannelore Derluyn, Jeroen Van Stappen, Tom Bultreys, Wesley De Boever and Marijn Boone.

I'm also grateful to Donatella Capitani, Noemi Proietti and Valeria di Tullio who let me visit their NMR laboratory at CNR in Rome (Italy) during an internship activity in 2015. Thank for the training in the field of nuclear magnetic resonance methods and applications and for having

supervised me in the acquisition and processing of portable-NMR data about my research, allowing the development of a relevant part of this work.

I want also thank Josè Teixiera and Eva Rabot for supporting me in the acquisition and processing of neutron imaging data during an experimental session performed in 2015 at IMAGE beamline in LLB, Saclay (France). Thank for all contributes in the correct interpretation of data and also for "working remotely" together.

I would like to greatly thank Marco Giamello and Jacopo Crezzini for their contribute in the surface metrology studies included in this work. Thank for the measurements performed at the University of Siena (Italy) and for the fruitfully discussions about data acquisition and processing.

I want also thank all the researchers of the Department of Biological, Geological and Environmental Sciences of the University of Catania who collaborated with me in the development of this research. Thank to Professors, technicians and colleagues for all their support.

Furthermore, I want thank all the colleagues and researches met during these years in the framework of Schools and Conferences for the really productive scientific discussions in *multifarious research topics*. Special thanks to the students of GDSISN 2014; I'd like to wish to all of them a brilliant academic career. Thank also to all the students met during seminars and thesis works which I had co-supervised; thank for the incentives, scientific questions and didactic issues inspected together.

Moreover, thank to Silvia and Chiara for the linguistic support in the developing of the "resumé" of this thesis work.

Finally, I would greatly thank my parents Rosario e Pina, my sister Cinzia, all my family (especially who be no more here and should be really proud of me) and my lovely partner Federico, for having support me during this demanding and laborious Ph.D. studies. Thanks for their patient, enthusiasm, advises, suggestions and anxiety during my numerous abroad trips. A special thank for having encouraged me to persevere, in spite of difficulties, in the field of the research and academic career. Thank for their unconditional love, fondness and consideration.

November 2015
Simona Raneri

List of Figures and Tables

SUMMARY

Introduction

Research highlights

The durability of natural building stones when they are subjected to weathering processes is a current issue in geological, engineering and conservation fields in the perspective of preserving Cultural Heritage. The esteem of this parameter is strongly related to several features of rocks, namely mineralogical, petrographic, chemical, textural and physical-mechanical proprieties, including pore structure[1].

Among the previous ones, the description of the pore structure is one of the more difficult to obtain, because of the variability of the size distribution of voids, ranging from nanometers to millimeters, which is generally not accessible by a single methodology. For this reason, a multi-technique approach is often required for obtaining a complete model of internal structure of building stones that usually exhibits complex pore geometries[2].

Moreover, as the great influence of porosity on durability, the quantification of the eventually changes in pore structure due to degradation processes represents a key element in the correct interpretation of stone behavior as well as in the correct use of conservative treatments in the framework of restoration works[3]. Finally, as degradation processes greatly affect not only the inner structure of building stones but also their surface, the analysis of surface texture changes due to weathering represents an additional tool in understanding these processes.

In the recent literature, durability of natural stones is usually esteemed by using parameters based on physical, mechanical and porosimetric data[4]; additionally, useful information can be obtained by accelerated aging tests such as frost resistance (EN 12371), resistance to ageing by SO_2 action in the presence of humidity (EN 13919), resistance to ageing by thermal shock (EN 14066), resistance to ageing by salt mist (EN 14147) and by sodium sulphate solutions (UNI EN 12370). However, during accelerated aging tests, the evaluation of behavior of stones is mainly based on visual inspection and only some quantitative analysis on inner micro-structural modification are available in a non-destructive way, for example by using sound propagation tests[5]. Furthermore, although the origin of the extensive damage caused by some weathering agents is widely inspected (for example in the case of salt crystallization[6]), the comprehension of how the complex porous network of a stone is modified from these processes is actually incomplete. Usually, in order to characterize pore structure of stone materials, classical approach by using intrusion methods (*e.g.*, mercury intrusion porosimetric) are used; these methods allow to investigate a great number of features such as pore size distribution, total pore volume or porosity, skeletal and apparent density, specific surface of samples[7-8]. However, intrusion methods exhibits numerous limits due to assumption made in the process.

In recent years, the use of innovative, non-invasive and non-destructive technique able to characterize both sub-surface and surface features of porous materials has largely increased,

especially in stone conservation studies. Among them, neutron and X-Ray imaging methods have been proved to be really valuable procedure for the characterization of archaeological, geological and industrial materials[9-11]. The results of the imaging analyses are, in fact, not limited to a simple 2D or 3D representation of the studied objects, as a large amount of quantitative information can be also obtained; in the field of geomaterial, for example, by analyzing and processing radiographies and tomographies aspects as porosity, water movement in porous structure, degradation effects, amount and distribution of degradation products, penetration depth of protective and consolidant products can be extensively inspected. In the framework of non-destructive and non-invasive techniques able to characterize the pore structure of stones, NMR (*i.e.* Nuclear Magnetic Resonance) applications are widely used to study the petrophysical features of rock materials, especially porosity and permeability[12-13].Beside the investigation of sub-surface modifications, the understanding of the weathering on exposed surfaces is a key element in building stone conservation studies, as surface represents the direct interface with atmosphere and, therefore, with the weathering agents. In this context, the recent development of non-destructive digital image techniques provides a new tool for measuring changes in stone surfaces in response to weathering, assuring a high resolution and the possibility to monitor the measured parameters over the time[14-15].

On the basis of the aforementioned, the main goal of this project consists in applying a multi-methodological approach for the modeling of porosity and surface changes in natural, degraded and treated building stones, for a complete understanding of degradation process due to salt crystallization and the effectiveness of nanostructured and innovative hybrids organic-inorganic products for their preservation and conservation. The research aims also to validate the use of different methods and models in studying porous materials, especially in the framework of innovative, non-invasive and non-destructive techniques.

In detail, this empirical approach has been applied on a Sicilian coarse grained calcarenite known as *Pietra di Sabucina*, widely used as building and replacement stone[16] and particularly suitable for this study, as characterized by a wide range of pores and a complex porous structure.

Outlines

This dissertation consists in seven parts in which are proposed four main research topics, *i.e.* a) characterization of porous structure and surface features of natural building stones; b) 2d and 3d models and methods for complex porosity and pore geometry; c) innovative consolidant and protective treatment for calcarenite substrate; d) quantification of pore structure, surface texture, physical-mechanical proprieties changes due to degradation processes and conservative treatments, by using a multi-methodological approach.

First of all, an introduction section devoted to coarse grained calcarenite used as natural building stones and a focus on Sabucina Stone is proposed (Chapter 1); in particular, the main features that affect the behavior of the stones when they are used in masonry are investigated in order to understand the influence of microtextural, microstructural, physical-mechanical and especially porosimetric proprieties in degradation processes. Finally, a complete characterization of studied stone is supplied. Classical destructive (*i.e. mercury intrusion porosimetry*) and innovative non invasive methods (*i.e. X-ray tomography, neutron radiography and tomography, nuclear magnetic resonance, digital surface analysis*) for the 2D and 3D characterization of complex porosity and pore geometry are summarized in Chapter 2. In Chapter 3 the results obtained by comparative standard tests, mercury intrusion porosimetry (MIP), X-Ray and neutron imaging, nuclear magnetic resonance (NMR) and 3D digital microscope analyses carried out on fresh and artificially weathered samples are discussed, with the aim to quantify changes in physical and mechanical proprieties as well as surface and sub-surface modification of the studied stone due to salt crystallization action. On the basis of experimental numerical data, geometrical models (*i.e.* fractal models) are applied in order to investigate the potential of fractal dimension in studying and describing complex pore networks (Chapter 4). Finally, the obtained results on Sabucina stone are employed for planning conservative treatments devoted to coarse grained calcarenite substrate. For aforementioned, a complete overview on innovative protective and consolidant products based on sol-gel process is proposed in Chapter 5. In detail, the efficiency of self-cleaning photocatalytic nanoparticles TiO_2-based surface coatings and hybrids organic-inorganic products are evaluated by standard test on treated samples of Sabucina Stone. Moreover, pore structure and surface modifications of studied stone due to treatments are investigated in Chapter 6 by using porosimetric, X-ray and neutron imaging and 3D digital microscope analysis techniques. All data acquired are discussed in Chapter 7, highlighting the complementary of the applied methodologies and models in studying complex pore geometries in natural building stones.

Bibliography

[1] Anania L, Badalà A, Barone G, Belfiore C, Calabrò C, Mazzoleni P, Pezzino A. The stones in monumental masonry buildings of the "Val di Noto" area: New data on the relationships between petrographic characters and physical-mechanical properties. Construction and Building Materials, 2012. 33:122-132.

[2] Barone G, Crupi V, Longo F, Majolino D, Mazzoleni P, Raneri S, Teixeira J, Venuti V. A multi-technique approach for the determination of the porous structure of building stone. European Journal of Mineralogy, 2014. 26:189-198.

[3] Bergamonti L, Alfieri I, Lorenzi L, Montenero A, Predieri G, Barone G, Mazzoleni P, Pasquale S, Lottici PP. Nanocrystalline TiO_2 by sol-gel: characterization and photocatalytic activity on Modica and Comiso stones. Appl. Surf. Sci., 2013. 282: 165-173.

[4] Yu S, Oguchi CT. Role of pore size distribution in salt uptake, damage, and predicting salt susceptibility of eight types of Japanese building stones. Engineering Geology, 2010. 115:236-226.

[5] Barbera G, Barone G, Mazzoleni P, Scandurra A. Laboratory measurement of ultrasound velocity during accelerated aging tests: Implication for the determination of limestone durability. Construction and Building Materials, 2012. 36:977–983

[6]Scherer GW. Stress from crystallization of salt. Cement and Concrete Research, 2004. 34:1613–1624.

[7]Giesche H. Mercury Porosimetry: A General (Practical) Overview. Part. Part. Syst. Charact. 2006. 23:9–19

[8] Leòn y Leòn CA. New perspectives in mercury porosimetry. Advances in Colloid and Interface Science, 1998. 76-77: 341-372

[9] Cnudde V, Boone M. High-resolution X-ray computed tomography in geosciences: a review of the current technology and applications Earth-Science Reviews, 2013. 123:1-17.

[10] Derluyn H, Griffa M, Mannes D, Jerjen I, Dewanckel J, Vontobel P, Sheppard A, Derome D, Cnudde V, Lehmann E, Carmeliet J. Characterizing saline uptake and salt distributions in porous limestone with neutron radiography and X-ray micro-tomography. Journal of Building Physics, 2013. 36:353-374.

[11] Perfect E, Cheng CL, Kanga M, Bilheux MZ, Lamanna JM, Gragg MJ, Wright DM. Neutron imaging of hydrogen-rich fluids in geomaterials and engineered porous media: A review. Earth-Science Reviews, 2014. 129:120:135.

[12] Capitani D, Di Tullio V, Proietti N. Nuclear magnetic resonance to characterize and monitor cultural heritage. Progress in nuclear magnetic resonance spectroscopy, 2012. 64: 29-69

[13] Proietti N, Capitani D, Di Tullio V. Applications of Nuclear Magnetic Resonance Sensors to Cultural Heritage. Sensors, 2014. 14:6977-6997

[14] Turkington AV, Paradise TR. Sandstone weathering: a century of research and innovation. Geomorphology, 2005. 67: 229–253.

[15] Moses C, Robinson D, Barlow J. Methods for measuring rock surface weathering and erosion: A critical review. Earth-Science Reviews, 2014. 135: 141–161.

[16] Bellanca A, Curcuruto E, Lo Bue S, Neri R. Petrografia, geochimica e riferimenti all'impiego storico delle calcareniti plioceniche di Sabucina, Sicilia Centrale. Mineralogica et petrographica acta, 1999. 42:210-193.

Chapter 1. Characterization of porous structure and surface features of natural building stones: the case of Sabucina Stone (Sicily, Italy)

1.1 Natural Building Stones

Much of the history of the world's civilizations is recorded in stones. Stones can be considered the primary building materials taken from the crust of the Earth; in fact, they have been employed since the earliest times of human history for convenience, endurance, and visualimpact[1]. Among them, worthy of note are *decorative stones*, referring with this term to a group of polishable rocks, widely used in modern buildings and in archeological and monumental artifacts. This definition includes metamorphic, magmatic and sedimentary rocks with particular esthetic qualities, generally indicated in the trade contexts as *marbles*. Of course, the use of decorative stone in building has to be adapted to the mineralogical, physical and mechanical properties of them, as well as to the different architectural and sculptural issues.

1.1.1 Limestone and sandstone as building stones: the case of Noto Valley (Sicily)

Among sedimentary rocks, calcarenites are the most used building stone in Sicily, especially in the South-East area of the island, in view of their suitable proprieties, as availability, color, easy extractability and good workability. In particular, various typologies of Oligocene-Miocene limestone cropping out in different segments of the Hyblean Plateau and Pliocene sandstones outcropping in Central Sicily have been used over the time in the local masonry, especially in the historical town centers. A large use of these local stones, mainly characterized by white-cream and ochre colors, has be attested during the reconstruction of the *Noto Valley* cities after the well-known earthquake occurred in 1693. In this framework, the *Baroque* architectural style flourished and the majority of the new built monuments exhibited standards of beauty devoted to emphasize volumes and voids. The requirements of the new established architectural rules found a good agreement with the easy workability and bright color of these limestones and sandstones, so that all the nowadays appearance of the South-East Sicilian historical town center is characterized by Baroque civil and religious monuments, bestowing the characteristic frame of the Noto Valley. Considering the special cultural and physical significance of Baroque buildings, several monuments are nowadays included to the UNESCO Heritage List. Therefore, in view of preserving these Cultural Heritages, the complete knowledge of the features and the behavior of the building stones employed in local masonry is fundamental for planning appropriate conservation actions.

1.1.2 Complex porous structure in building stones

Porosity and pore structure represent relevant features for the conservation of stones materials, as they influence the permeability of liquids transport through them; water and moisture are, in fact, the most relevant agents in buildings and monuments deterioration processes.

Porosity of a rock is defined as the volume of void respect to the total volume. In rocks, porosity generally exhibits a "dual" behavior, as it is possible discriminate a open (or effective) porosity, *i.e. accessible to fluid flow*, and a closed porosity, *i.e. in which fluids or gases are present but in which fluid flow cannot effectively take place*. In general, porosity (both accessible and inaccessible) strong affects physical and mechanical behavior of stones; however, for weathering processes, only the open/accessible porosity is of relevant interest as it is able to vehicle the water moisture responsible of frost and salt weathering[2].

The effective porosity is usually investigated by means of microscopic observations combined with image analysis and porosimetric techniques based on gas adsorption and mercury intrusion. Nevertheless, these methods appear inadequate for the complete modeling of the microstructure of the rock, since they are destructive, measure only the open porosity and explore a limited dimensional range. Moreover, most of these techniques are based on assumptions about pores shape and dimension, representing an ideal geometric model of them. On the contrary, natural pores exhibit a complex geometrical form. Therefore, the determination of pore size by using these methods often gives back arbitrary results.

For aforementioned, a unique quantitative description of rock micro-architecture is generally very difficult, considering the variability in the dimensional distribution of the voids (ranging over length scales ranging four to five orders of magnitude, i.e. from nanometers to centimeters) and their real complex geometry.

In this framework, the application of mathematical models able to describe complex chaotic systems with an high degree of heterogeneity by using a single numerical value can be considered a useful tool for studying porosity in building stones. Among them, *fractal geometry* represents one of the most powerful methods.

1.1.3 Fractal geometry in natural building stones

Fractals are real and mathematics objects characterized by non-integer value of dimension. For fractal surfaces, fractal dimension can assume any value between 2 and 3; more it approach to 3, more complex is the surface. In this sense, the fractal dimension (D) describes *"how"* objects occupy the space.

Assuming a non-planar surface, we want measure the area of this surface determining how many squares of ϵedge are needed. The number of squares N (ϵ) needed to cover the surface are described by the following equation:

$$N(\epsilon) = k \left(\frac{1}{\epsilon}\right)^2 \qquad (1)$$

With k = 1, ½, π/4, …, depending on the shape of the non-planar surface.
The exponent 2 represents the dimension of the surface, as following:

$$N(\epsilon) = k\left(\frac{1}{\epsilon}\right)^2 \rightarrow \ln N(\epsilon) = \ln k + 2\ln\frac{1}{\epsilon} \rightarrow 2 = \frac{lnN(\epsilon)}{\ln\frac{1}{\epsilon}} - \frac{\ln k}{\ln\frac{1}{\epsilon}} \quad (2)$$

if $\epsilon \rightarrow 0$, so that the edge of the planar squares tend to zero, $\frac{\ln k}{\ln\frac{1}{\epsilon}} \rightarrow 0$

the equation is:

$$2 = \frac{lnN(\epsilon)}{\ln\frac{1}{\epsilon}} \quad (3)$$

In general, the previous can be written as:

$$D = \frac{lnN(\epsilon)}{\ln\frac{1}{\epsilon}} \quad (4)$$

with *D* representing the fractal dimension of the surface.
For aforementioned, a fractal surface is characterized by a non integer fractal dimension *D* that is invariant at any scale used to examine it (*i.e.*, self-similarity).
In conclusion, a fractal object is characterized by non-integer dimension and self-similarity proprieties at any scale of observation.
Stones contain pores with a large radius interval, so they can be associate to a fractal model represented by the *Menger sponge*[3](Figure 1.1), even if a real system exhibits pores only in a specific dimensional range and fractal behavior is defined in a specific interval between r_{max} and r_{min} pore value.

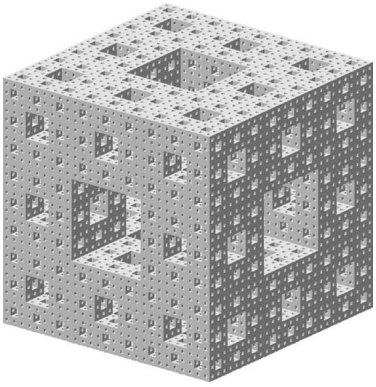

Figure 1.1 - The iterative structure of Menger sponge

However, fractal geometry has been successfully applied to a great variety of porous solid materials[4-7]. Among the application of fractal geometry on complex pore systems, several researches demonstrate the fractal behavior of pores in stones[8-10], also for the prediction of physical proprieties as permeability[11]. Additionally, recently application of fractal geometry on weathered building stones demonstrates the powerfully of this method in describing the modification of pore system related to degradation processes[12,13].

1.1.4 Weathering process: the role of salts crystallization in masonry decay

Even if rocks are considered really durable materials, they suffer of degradation processes that affect their physical, mechanical and aesthetical proprieties. Among them, weathering is a common process that interests natural stones and consists in structural and compositional modification of the material due to external factors, implying a worsening of its characteristics from a conservation point of view. The comprehension of weathering processes, in term of external agents, interaction between them, response of the rocks, scale and rate of action, represents therefore an element of great interest not only in conservation studies but also in geomorphology and rocks stability fields. Rock weathering is considered, in fact, one of the most relevant agents able to modify natural and artificial landscapes. For aforementioned, throughout the last centuries, several researchers have been focused on weathering studies, getting to numerous theories and models (*e.g.* traditional structural theory, climatic theory, single process model, reductionism, etc.[14]).

Generally speaking, weathering is considered the results of several external agents that can operate independently or simultaneously, determining modifications in morphology, structure, chemical and mineralogical composition and physic features under specific environmental conditions. In this sense, weathering can be expressed by the following general formula that takes in account all the previously in a certain time lap[15]:

$$F = f(E, M, P)dt \qquad (5)$$

with: F, morphological elements; P, processes operating; E, environmental conditions controlling the processes; M, materials upon which the processes operate over periods of time t.

It is quite clear that each of these elements has to be in-depth analyzed and therefore correlated with the other ones in order to have a complete overview on weathering process.

Referring to processes (P), they can occur by different mechanisms and can be distinguished mainly in mechanical and chemical processes. Mechanical damage results when stones are subjected to a stress major than their mechanical resistance; sources of mechanical decay are ascribable to growth of vegetation, thermal stress, hydric swelling and salts growth. Chemical damage processes refer to the dissolution or alteration of the mineral constituents of a stone material by chemical reactions and they mainly consist in mineral dissolution reactions, surface recession, and action of salts. These processes produce in rocks different weathering patterns often due to the interaction of several external agents; therefore, in order to assess the relative importance of different processes and their rates, a detailed understanding of the underlying mechanisms and the interaction between processes is indispensable. In this framework, the interactions among processes can act in three different ways: in synergy, in mutually exclusive way and independently. The comprehension of how these factors affect the weathering process can therefore supply additional information, also considering the different scale at which processes take place (*i.e.* granular and outcrop/building scale).

On the basis of the aforementioned, weathering process can be considered as the results of external disturbances that determine changes in rocks after a given relaxation time useful tore-establish an equilibrium. In addition, as the complexity of the interaction between processes and the tendency of rocks to balance these disequilibria, weathering has to be considered a non-linear process that produce chaotic patterns[16-23].This is evidenced by the high degree of spatial and temporal variability of weathering and decay on buildings, monuments and outcrops. However, despite of this variability, a continuity in weathering process over the time can be asses; in fact, given the irreversible nature of weathering and decay process outcomes, stone decay is affected by previously processes. As suggested by Mostafavi and Leatherbarrow[24], *the past is always present, as the context from which the present has emerged; thus, there is theoretical continuity between material changes in the past, present, and future*.

Another key factor in weathering studies is represented by scale; in fact, due to the complexity of the process, a multiscale observation is mandatory in order to delineate the ability of the different agents to modify all the elements of materials, *i.e. from nano-micro-scale to outcrop one*, simultaneously or in a definite range of scale. In this sense, laboratory simulation at small scale can be extended to landforms and, on the other hand, outcrop information can be useful to predict small scale behavior. However, in view of the non-linearity of weathering process, the extrapolation of data from small to large scale events and/or the downscaling of the processes from outcrop evidences to laboratory samples are complicated by the scarcity of information on weathering rate.

The latter one represents a really difficult element to evaluate; in fact, even if laboratory simulations could be useful also in this context, the variability in term of space and time of the environmental conditions that can act in different way and time laps makes the determination of rate a complicate issue. Additionally, the selective influence of the processes at different scales can affect the velocity of the stone response, accelerating or delaying the reestablishment of the equilibrium. As suggested by Viles[25] the main problem related to the up-scaling of small scale weathering contribution to landform and landscape is the understanding of the possible assessment of characteristic spatial-temporal scales of landforms and processes, the eventually correspondence between observation scales and scale processes, the methods by which up-scaling or/and down-scaling the processes and the interaction between processes in producing small and large scale effects.

Another interesting issue related to weathering is represented by the quantification of its effects in term of damage. The first attempts focused on this topic have been published in the nineteenth century and are represented by empirical measurements performed on samples by using laboratory simulations. For example, the first accelerated aging test has been proposed by Brard in 1828[26]; he suggested, in fact, a method able to evaluate salt and frost damage in stones

by performing wet-dry cycles (consisting in immersion in boiled sodium sulfate solution and drying at ambient condition), getting the basis for the nowadays standard recommendations.

Beside the efficiency of the simulation experiments in defining stone behavior and predict decay, on the basis of the aforementioned complicated relations between scale, rate and external agents interaction, only a multiscale analysis of the process could allow to extend the results obtained in laboratory to outcrops one, even if opportune limitations have to be considered as the impossibility to perfectly replicate the exposure conditions[27].

The application of multidisciplinary and multiscale approaches on weathering process investigation has become a current issue in the last centuries, especially in building stone researches. In fact, as the multiple implications (cultural and financial) involved in conservation strategies, the in-depth comprehension of these processes can offer a significant contribution in planning efficient activity and invest substantial resources. At the same time, the ancient masonry represents for geomorphologist a good analogue for rock behavior in specific environments, offering a suite of decay processes extendible also to outcrops conditions.

In the framework of masonry decay, one of the weathering processes that greatly affect building stones is represented by salt crystallization. Among all salts able to damage porous stones, sodium sulphate is one of the worst. The main mechanism proposed to explain the extensive damage determined by sodium sulphate is related to volume increasing associated with hydration reactions of therardite (*i.e.*, thenardite, the anhydrous phase of sodium sulphate, converts to mirabilite, decahydrate phase, determining a volume expansion of about 314%; see Figure 1.2). However, recent researches[28-32] highlight that the destructive effects of sodium suplhate can be related to the growth of mirabilite from highly saturated solution generated by the dissolution of anhydrous therardite. In this sense, when porous materials containing thenardite are exposed to water or high humidity at ambient conditions, the thermodynamic equilibrium of sodium sulphate determines the dissolution of thenardite and the precipitation of mirabilite.

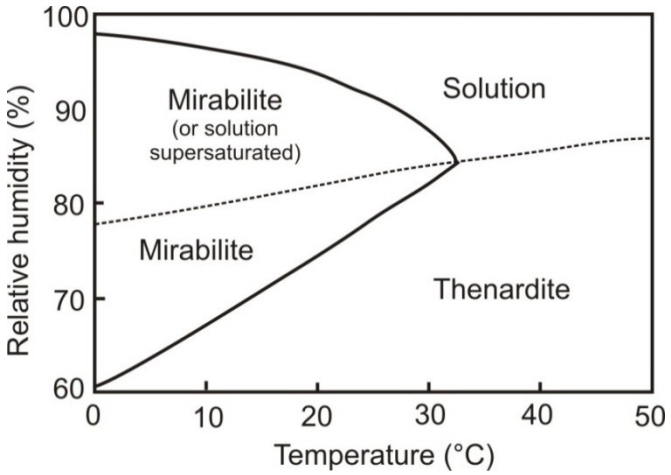

Figure 1.2 - From Kracek FC, International Critical Tables 3, 1928, Na_2SO_4: p. 371

This situation is particularly stressed during the laboratory accelerated aging tests, characterized by several cycles of wetting and drying[34].

According to this interpretation, the precipitation of mirabilite is alone responsible of decay in porous building material. The maximum crystallization pressure developed by mirabilite at the interface salt-material is higher than the tensile strength of most stones and concrete; moreover, it is also higher than the crystallization pressure determined by other salts. It's note worthy that the previously is only a schematic view of the weathering process, as damage due to salt crystallization is quite dynamic and several factor should be considered in the thermodynamic study of dissolution-crystallization equilibria (*i.e.*, all the parameters that control the degree of supersaturation, crystal size, pore size, time, etc.[35-37]).

Therefore, considering the importance of the understanding how this process affects the behavior of porous rock materials when they are subjected to salt weathering, the investigation of the potential of methods and models in visualizing and quantifying changes due to salt weathering in building stones would seem appropriate. In fact, only by understanding how processes act could be possible to clarify the effects determined by all the factors involved in weathering; in this way more detailed information on the weathering behavior of stone has become available.

1.2 Sabucina Stone

1.2.1 Geological framework, quarries and use of Sabucina Stone as building material

In this work, an empirical and experimental approach for the modeling of porosity and surface changes in natural, degraded and treated building stonechats been applied on a Sicilian coarse grained calcarenite known as Pietra di Sabucina, widely used as building and replacement stone and particularly suitable for this study, as characterized by a wide range of pores and a complex porous structure.

The studied stone is quarried in an area located 4 kilometers away from the urban center of Caltanissetta, in central Sicily; this sector of the island holds several syntectonic sedimentary basins, formed since Upper Tortonian.

In detail, Sabucina Stone is a Pliocene yellow bioclastic calcarenite belonging to the Piacenzian-Enna Formation (Capodarso Calcarenites)[38] which is formed by marls and marly clays in the lower part and sands-calcarenites in the upper part. This Formation lies unconformably on the lower Pliocene deposits and it is covered by the marly clays of the Geracello Formation.

The stone is quarried on the homonym mountain 720 m high (37° 29' 37" N – 14° 7' 49" E), on the west side of the Salso River and it is a widely used building material in Sicily, especially in the area of Caltanissetta in central Sicily[39].On the Sabucina Mountain mainly outcrops an alternation of calcarenites, sandstones and clayey sands belonging to Enna Fm. (Medium

Pliocene)[40]. Even if several quarries are visible on the plateau, only one of them is actually active. In the latter one, the Sabucina Stone is quarried by surface mining technique; in detail, an open-pit mining methods is applied by cutting large slabs and removing them from the quarry (Figure 1.3).

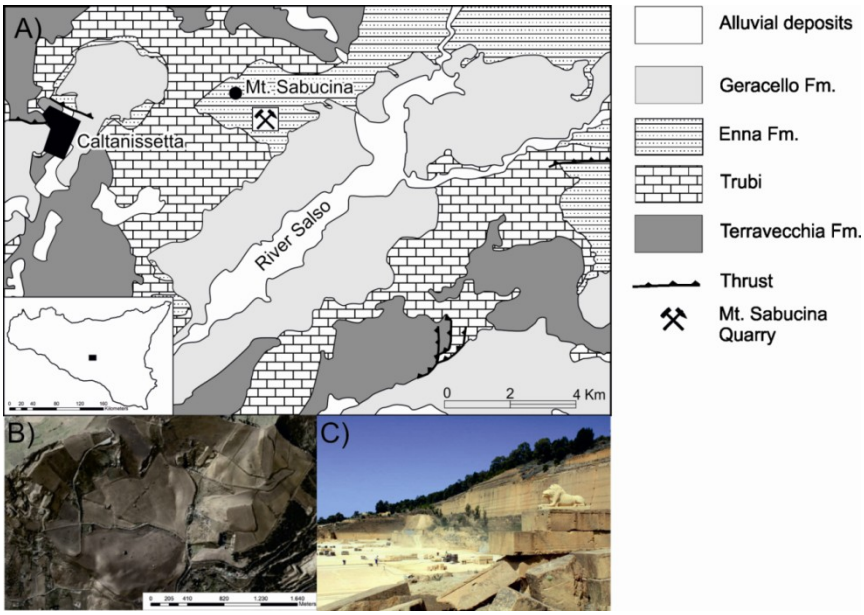

Figure 1.3 - (a) Geological sketch map and localization of the quarried area of Sabucina Stone; (b) Aerial view of the Sabucina quarry (digital elevation model and orthophotos); (c) Photograph of the quarry.

Historical and modern quarries have been used during the centuries to supply material incorporated into locally relevant architectural structures and sculptures.

The use of the stone in buildings and sculptures is attested from the Bronze Age, as documented by several archaeological remains of huts and artefacts (as grindstones, loads, etc.) dated back to Late Bronze Age and recovered near the extraction sites. During the next centuries, the stone was constantly quarried and used especially as building stone; in particular, during the VI century B.C. the material was used for the construction of fortification as well as religious and civil structures in the local Greek urban centers. The use of the stone is also attested over the time for the construction of several monuments in the area, especially in the city of Caltanissetta. In particular, among the monuments of the city, the more ancient structure built by using this stone is represented by the S. Spirito Abbey, dated back to 1151 and restored in 1568.

The aesthetical features and the bright ochre color of the stone have been used in order to create dichromatic architecture arrangements, as in the case of S. Maria degli Angeli Church, in which the stone is associated with white limestone.

During 16^{th} – 17^{th} centuries several monuments have been built by using Sabucina Stone in the city of Caltanissetta (S. Sebastiano Church (1550), S. Maria Nova Church (1539-1570), Abbadia Church (1539), Capuchin Monastery (1580), Jesuit Monastery (1588), S. Agata al

Collegio Church (1605), Benedictine Monastery (1592, now S. Flavia Church), Palazzo del Magistrato (1570), Capodarso Bridge (1556)).

Recently, due to its excellent properties and aesthetic features, it is widely used as a replacement stone, especially in Baroque monuments of the Noto Valley (belonging to the UNESCO Heritage List). An example of this application is represented by the restoration works carried out on the S. Nicolò Cathedral in Noto (Sicily), in which the Sabucina Stone has been used in several architectural elements of the monument, especially in dome and other covering parts[41].

Figure 1.4 - The use of Sabucina Stone in some representative monuments of southern Italy. (a) S. Spirito Church; Caltanissetta (1151); (b) Capodarso bridge (1556); (c) Noto Cathedral (1703-2007); (d) Caltanissetta Cathedral.

1.2.2 Petrographic, mineralogical and chemical proprieties

1.2.2.1 Optical microscopy

From a petrographic point of view, the yellowish and coarse-grained Sabucina calcarenite exhibits a texture that varies between grainstone and packestone[42], due to the irregular distribution of sparite and micrite, the latter being enriched in iron oxides and thus responsible for the stone color (Figure 1.5). Allochems are mainly formed by small fragments of foraminifera, bryozoa, lamellibranchia, crinoid, echinidae, algae and gastropoda ranging from 200 µm to 1.5 mm in dimension. The siliciclastic component is composed mainly by sub-rounded grains of quartz (2-3 vol %) with an average diameter of 100 µm. According to Choquette and Pray (1970)[43], porosity (20-30 vol %) can be classified as inter-particle, moldic and vuggy. Petrographically, the stone is a biosparite[44]. It is mainly isotropic, and no orientation of the bedding is visible at outcrops or by macroscopic and microscopic inspection.

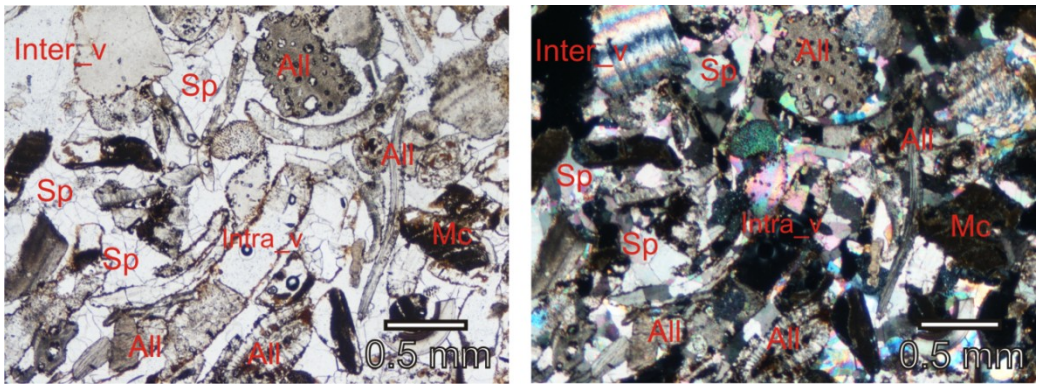

Figure 1.5 - Microphotographs of Sabucina Stone. All, allochems; Sp, sparite; Mc, micrite; Inter_v, inter-particle voids; Intra_v: intra particle voids. Intra_v, intraparticle voids

1.2.2.2 X-Ray diffraction on insoluble residue

In order to obtain information on mineralogical composition of the stone, X-ray diffraction analysis has been performed by using a Siemens D-5000 diffractometer on randomly oriented powders and on insoluble residue of bulk rock. The insoluble residue of Sabucina Stone has been obtained starting from 6.7 g of bulk rock after acid attack with a solution of chloride acid at 0.1 N[45]. After the complete dissolution of carbonate fraction, 0.12 g of insoluble residue has been obtained (1.74%).

Spectra have been acquired using the range 2°-65°2θ, step-size of 0.02°θ and step-time of 2 s/step. The presence of swelling clay minerals in the fine fraction of insoluble residue has been determined on oriented slides by treating samples with ethylene glycol at 60 °C for 12 h.

X-ray diffraction patterns (Figure 1.6) of studied stone highlight the presence of (in order of abundance) calcite, dolomite and quartz as main mineralogical phases. The semi-quantitative mineralogical composition of insoluble residue obtained from acid attack of bulk rock (1.74%) reveals the presence of quartz, clay minerals, hematite and goethite (Table 1). Referring to clay minerals in the fine grain size fraction, the XRD patterns highlight the presence of predominant low-crystalline smectite and subordinate illite.

Table 1.1 - Semi-quantitative mineralogical composition of the bulk rock and insoluble residue. Cc = calcite; Dol= dolomite; Qz = quartz; Hm = hematite; Goeth = goethite; C. M. = clay minerals. xxx = abundant; xx = present; x = scarce; tr = traces; – = absent.

	Cc	***Dol***	***Qz***	***Hm***	***Goeth***	***C. M.***
Bulk rocks	xxx	xx	x	tr	tr	x
Insoluble residue	-	-	xxx	xx	x	xx

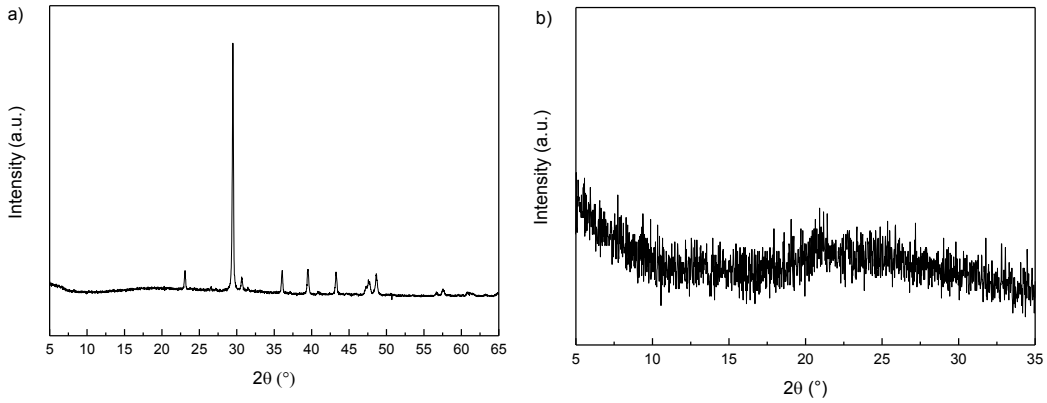

Figure 1.6 - X-ray diffraction patterns acquired on (a) randomly oriented powders and (b) on insoluble residue of bulk rock oriented slides

1.2.2.3 Single phases chemical composition

Chemical analysis have been performed by using Tescan Vega LMU scanning electron microscope (SEM), equipped with an EDAX Neptune XM4-60 micro-analyzer, characterized by an ultra-thin Be window. Data have been collected by using micro-map and spot mode analyses on polished thin section with 20 kV accelerating voltage and 0.2 mA beam current.

The obtained results (Figure 1.7) allow to determine the average composition of spatic calcite (CaO~97%), micrite (mainly composed by SiO_2~50%, CaO~15% and small amount of Al_2O_3, K_2O and FeO_{tot}) and oxides (ilmenite and pyrite, due to the presence of SO_3, FeO_{tot}, TiO_2) present in the sample (Table 1.2). Moreover, dolomite crystals dispersed in the micrite fraction have been identified (MgO~30%, CaO~70%; see Figure 1.6(b)), suggesting an initial dolomitization of the stone.

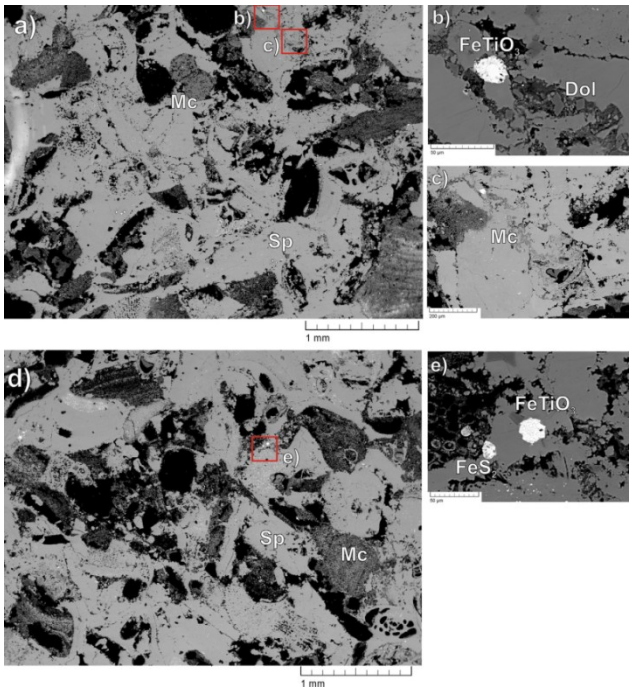

Figure 1.7 - SEM images of Sabucina Stone. Textural features analyzed are shown. Mc = micrite; Sp = sparite; Dol = dolomite; $FeTiO_3$ = iron titanium oxide; FeS_2 = iron sulfide oxide.

Table 1.2 - Average values and standard deviations of the chemical composition of the principal textural and petrographic component of the studied stone are reported. Values are assessed on almost three point analyses.

Average Values	***MgO***	***Al_2O_3***	***SiO_2***	***K_2O***	***SO_3***	***CaO***	***TiO_2***	***FeO_{tot}***
Spatic Calcite	2.38 (±0.841)	-	-	-	0.57 (±0.01)	96.69 (±1)	-	-
micrite	4.68 (±0.85)	18.52 (±1.09)	55.73 (±9.25)	3.17 (±0.64)	-	11.47 (±2.43)		5.03 (±1.35)
Fe-S oxides	1.25 (±0.48)	-	5.99 (±0.56)	-	21.18 (±1.03)	1.90 (±0.26)	-	69.62 (±0.76)
Fe-Ti oxides	-	-	0.76	-	-	1.99	52.7	43.01
dolomite	32.52	-	-	-	-	67.48	-	-

1.2.2.4 Non-destructive chemical analyses by using portable X-Ray fluorescence

Portable X-ray measurements have performed on Sabucina stone with the aim at improving the database about chemical composition of decorative stones[46] and Sicilian limestones[47]widely used in ancient and modern building and artistic industry.

In detail, chemical composition has been obtained by means of the portable-XRF spectrometer 'Alpha 4000' (Innov-X system), equipped with an X-ray tube (Ta anode) and a Si-PiN diode detector (resolution 236 eV). The spot size for this analyzer is approximately 170 mm^2. Control of the instrument and data storage was performed through a Hewlett Packard iPAQ Pocket PC. In this configuration, it was possible to detect the elements from P (Z = 15) to Pb (Z = 82), from levels of parts per million (ppm), by means of two sequential tests. In particular, the beam current voltages were 40 kV for the first measurement and 15 kV for the second one, respectively. This latter measurement was performed by means of the Light Element Analysis Program suite, which works by changing the X-ray tube beam conditions to settings that are optimized for the detection of elements lighter than iron. The measurement time was 60 s for each test. The calibration was performed by Soil Light Element Analysis Program II and it was verified using alloy certified reference materials produced by Analytical Reference Materials International. Considering the chromatic heterogeneity of the Sabucina stone, almost six measurements have been performed on the darker and lighter portions. In Table 1.3the average chemical composition obtained by portable X-ray spectrometer on darker (SAB2, SAB3, SAB6) and lighter (SAB1, SAB4, SAB5) areas of the stone are reported.

Table 1.3 - Chemical composition of Sabucina Stone inspected by using X-ray portable equipment (data are expressed as cps)

Analysis spots	***K***	***Ca***	***Mn***	***Fe***	***Zn***	***As***	***Sr***	***Zr***
SAB 1	b.d.l.	881255±19634	54±14	12871±296	24±5	53±6	2974±45	b.d.l.
SAB 2	4312±657	802737±18299	82±18	30914±710	25±5	67±7	2758±42	b.d.l.
SAB 3	b.d.l.	909293±21563	93±17	19689±475	26±5	108±8	2809±42	19±6
SAB 4	b.d.l.	928673±21968	83±15	11601±285	22±5	52±6	2934±44	b.d.l.
SAB 5	b.d.l.	889068±21046	118±17	18412±445	19±5	110±8	2790±42	b.d.l.

SAB6	2694±650	863815±19669	54±14	11541±273	34±5	78±7	2838±43	b.d.l.
Average	**3503±1530**	**879140±20363**	**81±16**	**17505±414**	**25±5**	**78±7**	**2851±43**	**19±16**

Since aesthetic features of Sabucina Stone are similar to those of another local stone (Giuggiulena Stone, Siracusa, Sicily) that cannot be quarried nowadays, it has been recently employed as good alternative for replacing damaged stones during restoration actions. Therefore, the chemical composition of the studied material has been compared with reference data on Giuggiulena Stone[47] in order to discriminate, on chemical bases, these coarse-grained calcarenites. Data reported in Table 1.4 highlight higher levels of all detected elements in Giuggiulena Stone than in Sabucina one, except for Fe and Zn levels; moreover, the presence of S and Ti in the former stone, absent in the latter one, can be considered a discriminating criteria for distinguishing the two calcarenites.

Table 1.4 - Comparison on chemical bases between Sabucina and Giuggiulena Stones. Average data collected by using X-ray portable equipment (data are expressed as cps) are reported

Samples	*S*	*K*	*Ca*	*Ti*	*Mn*	*Fe*	*Ni*	*Zn*
Giuggiulena Stone	**21400**	**2810**	**894000**	**630**	**277**	**11000**	**78**	**19**
Sabucina Stone	**0**	**1168**	**879140**	**0**	**81**	**17506**	**11**	**25**

1.2.3 Physical proprieties

1.2.3.1 Water absorption by capillarity

The determination of the water absorption by capillarity has been carried out following the standard recommendation NORMAL 11/88[48].

Cubic samples 4 cm and 7 cm in edges have been tested with the aim at verify the eventually dimensional effects on the behavior of the stone against water[49].

Samples have been placed in a vessel on a blotting paper stratum saturated with deionized water. The water level was maintained constant throughout the test. The amount of absorbed water Q_i at time t_i has been calculated by:

$$Q_i = \frac{M_i - M_0}{A} \qquad (6)$$

where M_0 is the mass of the dry specimen, M_i the mass at time t_i and A is the area in contact with the wet paper. Measurements were made at regular steps (1 min, 3 min, 5 min, 10 min, 15 min, 20 min, 30 min, 60 min) and then at subsequent 24h intervals until $t=t_f$, when the difference between two consecutive weighing was less than 1% of the initial mass of the specimen. The calculated values of Q_i are reported (in g/cm^2) as a function of the square root of time ($t^{1/2}$). The absorption coefficient AC (g/cm^2) is evaluated as the slope of the curve Q_i at low times (<30 minutes), where the amount of the absorbed water vs. $t^{1/2}$ should be approximately linear

according to the model for the capillarity absorption. The slope was calculated by a linear fitting of the data requiring that $Q_i=0$ for $t_i=0$.

Referring to cubic samples 4 cm in edge, in Figure 1.8 (a, b) the curves of the capillarity absorption (Q_i) are plotted as a function of the square root of time (in seconds). The average of measurements on three samples is reported. The absorption coefficient AC, evaluated as the slope of the fitted line to the Q_i curve vs. $t^{1/2}$ in the first 30 minutes (b), is 0.02 g/cm^2.

Also in the case of cubic samples 7 cm in edge (see Fig. 1.8 (c, d)) the capillarity coefficient obtained is 0.02 g/cm^2.

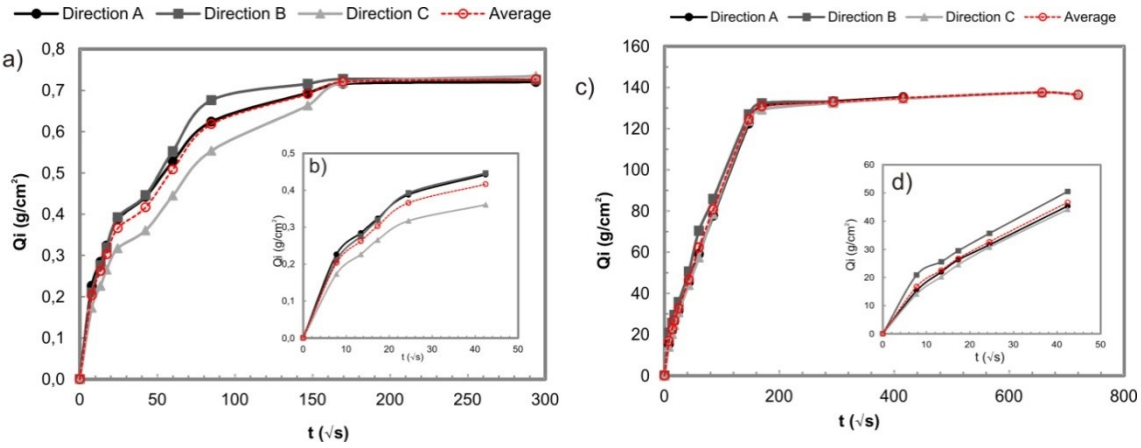

Figure 1.8 - Water absorption by capillarity: (a) curves related to the three investigated directions and average curve in 4 cm cubic samples and (b) absorption in the first 30 minutes. (c) Curves related to the three investigated directions and average curve in 7 cm cubic samples and (d) absorption in the first 30 minutes.

Noteworthy is that no significant variations of the water absorption coefficient by capillarity along three investigated directions are detected, according to the isotropic texture of the stone.

1.2.3.2 Water absorption by total immersion

The determination of the water absorption by total immersion has been carried out following the recommendation NORMAL 7/81[50].The test allows to calculate the weight % (with respect to the dry mass of the sample) of the water absorbed by a sample completely immersed in water. The shape of samples should be regular and the minimum size needs to be compatible with the homogeneity of the material. Samples should be carefully washed to remove dust from the surface. Samples have to be dried in oven at (60 ± 5) °C until constant weight before the test.

Dried samples are located in a container, minimizing the surface of contact of the base. De-ionized water is poured in until samples are completely covered (2 cm). At regular intervals of time (to be defined by a preliminary trial on the basis of the material) samples are extracted rapidly weighed. After each measurement, the samples are again immersed in water. The measure continues at intervals of 24 hours until the quantity of water absorbed in two successive measurements is less that 0.1%.

The quantity of absorbed water *(ΔM/M) %* in the time t_i is given by:

$$\frac{\Delta M}{M}\% = \frac{M_i - M_0}{M_0}100 \quad (7)$$

where: M_i= mass (g) of the sample with absorbed water at the time t_i; M_0 = mass (g) of the dry sample; M_i-M_0 = mass (g) of water absorbed at time t_i. The average value of quantity of absorbed water is reported in function of time (in hours). Finally, the imbibitions coefficient CI is calculated by the following:

$$CI = \frac{M_{max} - M_{0f}}{M_{0f}}100 \quad (8)$$

where: M_{max} = mass (g) of the sample at the end of the test; M_{0f} = mass (g) of the dry sample at the end of the test.

In this work, cubic samples 4 cm in edge and 7 cm in edge have been tested with the aim at verify the eventually dimensional effects on the behavior of the stone against water[49].

In Figure 1.9 the curves of the water absorbed are plotted as a function of time (in hours) for (a) 4 cm and (b) 7 cm samples. The average of measurements on three samples is reported. The imbibitions coefficient CI is11.62% and 11.07% for 4 and 7 cm samples, respectively.

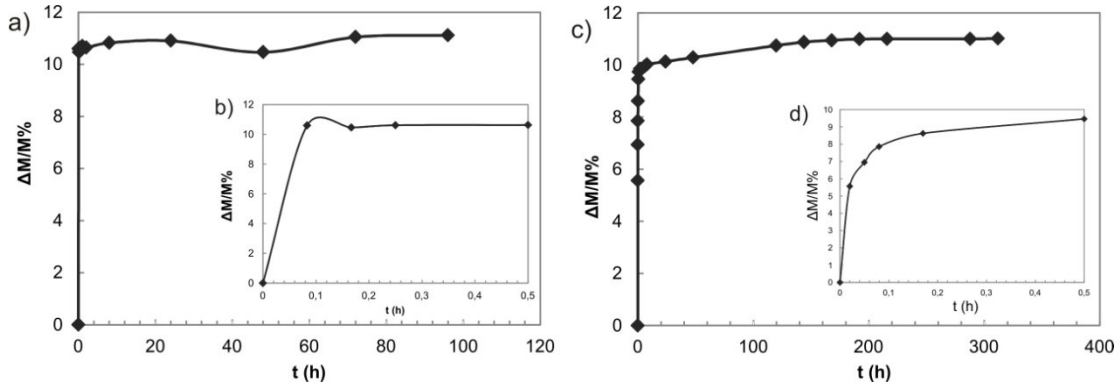

Figure 1.9 - Water absorption by total immersion: averages curve referred to the whole duration of the test and water absorption in the first 30 minutes for cubic samples of 4 cm (a, b) and 7 cm (c, d).

1.2.3.3 Drying index

The determination of the drying index has been carried out following the NORMAL 29/88 standard recommendation[51].The test allows to calculate the water loss by a saturated sample over the time. For the test, saturated samples from the NORMAL 7/81 test have to be used; therefore, the mass M_0at the start of the test corresponds to the M_{max} of the previous one. Samples are placed in a dessiccator equipped with silica gel containers in order to maintain constant humidity conditions at room temperature of 20±1 °C. At regular intervals of time (the same used for the water absorption by total immersion) samples are extracted from the

dessiccator and weighed. After each measurement, samples are again placed in the dessiccator. The measures continue at intervals of 24 hours, until the following condition is reached:

$$1 \leq \frac{m_0 - m_{i-1}}{m_0 - m_i} \leq 0.9 \quad (9)$$

with m_0= mass (g) of the sample at t_0 (h); m_{i-1} = mass (g) of the sample at t_{i-1} (h); m_i = mass (g) of the sample at t_i (h).

At the end of the test, samples are dried in oven at 60 ± 5 °C, until constant mass.

For each time interval, the percentage of water loss at t_i can be determined as:

$$Q_i = \frac{m_i - m_f}{m_f} \cdot 100 \quad (10)$$

with m_i = mass (g) of the sample at t_i (h); m_f = mass (g) of the sample at t_f (h). The drying curve is therefore obtained by plotting the Q_i values in function of time (in hours).

Finally, the drying index IA is calculated by the following:

$$IA = \frac{\int_{t0}^{tf} f(Q_i)dt}{Q_{max} \cdot t_f} \quad (11)$$

with Q_i = percentage of water loss at t_i; Q_{max}= percentage of water at t_0; t_f=time (in hour) at the end of the test; t_0= 0.

For the determination of the integral of the curve, the Simpson method can be used:

$$\frac{t_f - t_0}{3} \cdot \left[Q_{max} - Q_f + 2(Q_2 + Q_4 + \ldots + Q_{n+2}) + 4(Q_1 + Q_3 + \ldots + Q_{n-1})\right] \quad (12)$$

with Q_{max}= percentage of water at t_0; Q_f = percentage of water after the drying in oven; t_0= time (in hour) at the start of the test; n = number of time intervals; t_f = time (in hour) at the end of the test.

In this work, saturated cubic samples 4 cm in edge have been tested in order to determine the drying index of Sabucina stone. In detail, in Figure 1.10 the curve of the amount of water loss Qi plotted as a function of time (in hours) is reported. For the test, the integral of the curve has been calculated following the Simpson method. The dry index coefficient calculated for the stone is IA = 0.4.

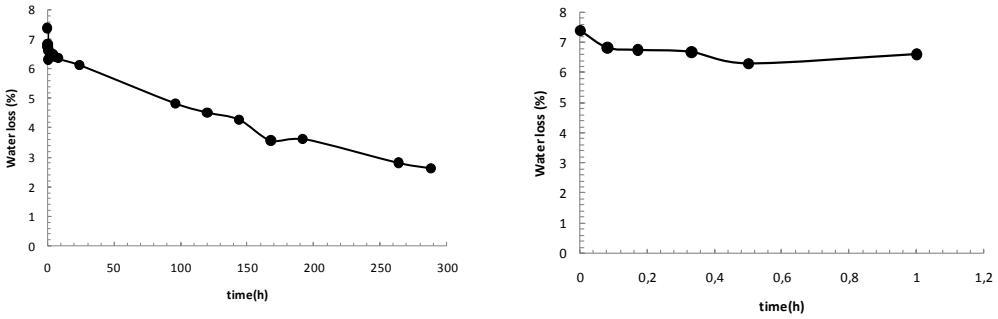

Figure 1.10 - Curves of the amount of water loss Qi plotted as a function of time (in hours)

1.2.3.4 Resistance to salts crystallization

Artificially weathered samples have been obtained according to the UNI EN 12370 standard[34] on the resistance of natural stones to crystallization damage. For the test, cubic samples with an edge of 4 cm and 7 cm have been used. The test consists of 15 cycles. Each cycle started with immersing the samples for 2h at room temperature of 20±5 °C in sodium sulphate solution (14% volume concentration), followed by 16h of drying at 105 ± 5 °C and by 2.0 ± 0.5 h of cooling at room temperature before the next immersion cycle. At the end of each cycle the loss of mass was measured. In samples of 7 cm of edge, resistance to salts crystallization have been determined for eight cycles; the weight loss percentages calculated during the weathering cycles allow to draft a curve that describe the degradation style of the studied stone. During the first six cycles, a mass increasing due to crystallization of salts within the pore structure is described by positive values of ΔM%; on the contrary, from the seventh weathering cycle negative ΔM%s have been recorded. Overall, samples show an average weight loss of-4.16% at the end of 8thcycle. The average mass loss after the cleaning of samples in deionised water in order to remove salts is -6.15%. The main degradation forms are represented by granular disintegration and powdering, in association with slight chromatic changes (see Fig. 1.11 (a, b)).

Referring to 4 cm edge samples (Fig. 1.11 (c, d)), the weight loss at the end of the 15th cycle show an average value of -11.09%. The curves relative to the average weight-loss percentages show a first stage, with a slight mass increase (due to the crystallization of salt within the pore structure) until the fourth and fifth cycles, and a second stage, which shows an incremental weight loss. Samples begin to degrade during the sixth cycle of crystallization mainly from the edges and exhibit white patinas. All samples at the end of the 15thcycle of crystallization show alteration and degradation forms mainly consisting of chromatic change, granular disintegration and powdering.

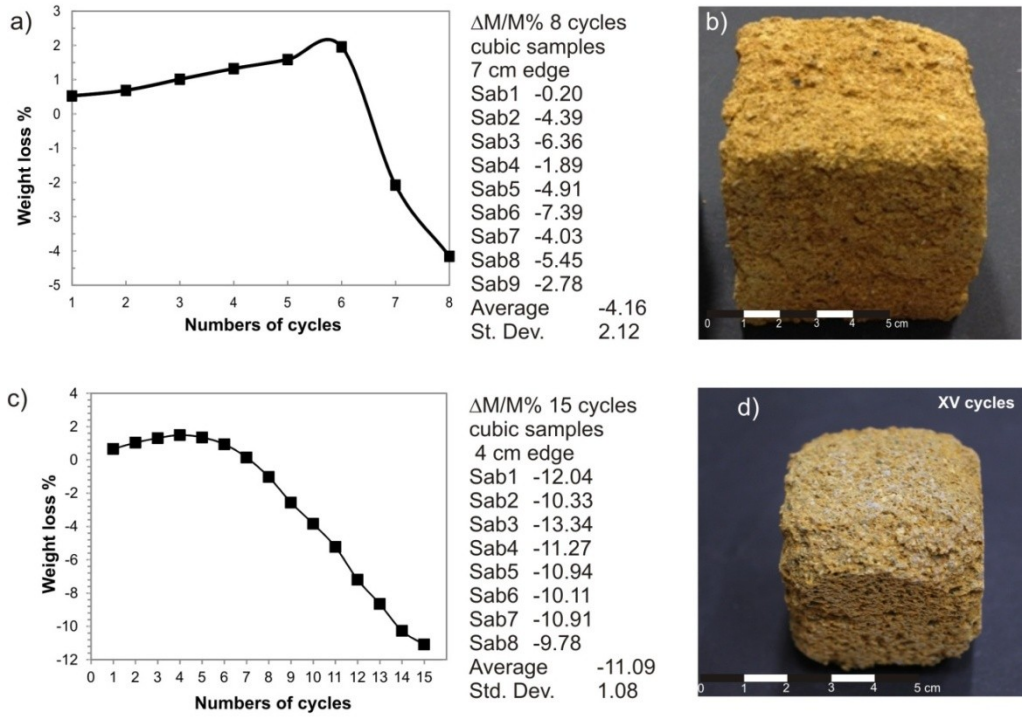

Figure 1.11 - Average curve of weight loss percentage during crystallization cycles and picture of sample at the end of the test in 7 cm (a, b) and 4 cm (c, d) cubic samples, respectively.

1.2.4 Ultrasonic test, mechanical proprieties and density

1.2.4.1 Ultrasonic test

The propagation speed of longitudinal ultrasonic waves has been measured for each specimen according to the European recommendation NORMAL 22/86[52] along the three directions (x, y and z) for each specimen arbitrarily chosen since neither preferential orientation in the quarry, nor sedimentary planes in the stone were observed. The test has been performed by a pulser/receiver device (M.A.E. A5000U) and a couple of transducers operating at 200kHz, allowing the input of the sound energy in the specimen and the measurement of its travel time. In addition, both dry and wet fresh specimens have been analyzed. Measurements allowed the calculation of the related seismic anisotropy, by using the formula:

$$A\% = 100 \cdot \frac{V_{max} - V_{min}}{V_{mean}} \quad 53 \qquad (13)$$

The average V_p values have been measured both in dry and wet conditions with the aim to evaluate the structural anisotropy of the studied stone. The mean velocity measured in the dry specimen is 2040 m/s (±46.16) with a mean anisotropy value of 7.09%, while for wet specimens a mean velocity of 3042 m/s (±77.2) with 9.09% of anisotropy have been obtained, suggesting a quite isotropic arrangement of structural and textural elements.

1.2.4.2 Compressive strength

Uniaxial Compressive Strength (UCS) has been estimated through laboratory tests according to UNIEN 1926[54]. UCS, which is considered one of the basic geomechanical parameters for the characterization of a rock, has been measured on 12 cubical specimens, both in wet and dry conditions. The UCS values in dry condition ranges from a minimum of 5.21 to a maximum of 7.03 MPa, while in wet condition ranges between 4.26 and 8.09 MPa, with average values quite similar each other (6.12±0.8 MPa and 5.80±1.25 MPa, respectively). This evidence suggest that the mechanical behavior of the stone is not strongly affected by the presence of water, even if a slight decrease of compressive resistance can be observed in saturated samples. The failure mode is characterized by fractures with orientation from parallel to 30° of inclination with respect to the axis of load and by a quasi-brittle behavior; in fact, the load-time curves show a linear trend until the failure of the specimen, which is followed by a rapid unloading phase.

1.2.4.3 Flexural strength

The Flexural Strength have been estimated through laboratory tests according to UNIEN 12372 recommendation[55]. The Flexural Strength has been determined on 10 specimens with size 15x7.5x2.5 cm.

The evaluation of resistance to flexural mechanical stress in dry conditions give back values ranging between 4.12 and 8.83 MPa, with average flexural strength of 6.53±1.4 MP, slightly higher than compressive strength.

1.2.4.4 Apparent and real density and porosity

Information on real and apparent density and porosity have been obtained following UNI EN 1936:2001[56] standard test. Referring to parameters definitions, real density is defined as the ratio of the dry specimen mass to the volume of its solid part; apparent density is the ratio between the mass of the specimen and the apparent volume, made up of solid part plus the volume of cavities; open porosity is defined as the ratio between the volume of open pores and apparent volume of the specimen; finally, total porosity is defined as the ratio of the entire pore space in a rock to its bulk volume.

Apparent density and open porosity have been determined by using a method based on the principle of Archimedes (a body immersed in a fluid is buoyed up by a force equal to the weight of the fluid displaced by the object). Cubes are dried at t=70 ± 5°c until the mass is constant (the difference in mass between two weighs at an interval of 24 ± 2h must be <0.1%). The specimens are left in a drier until they reach room temperature and then they are weighed (m_d). Specimens are placed in an evacuation vessel where pressure is lowered to 2kPa and kept for two hours. The vessel is then filled with deionised water so that specimens are completely

immersed in no less than 15 minutes. When all the specimens are immersed the vessel is brought again to atmospheric pressure and specimens are left at atmospheric pressure for 24 hours. Afterwards, each saturated specimen is weighed in water by means of an instrument capable of weighing specimens in water (m_s) and in air (m_h) after having wiped them quickly with a dampened cloth.

The apparent density (Kg/m^3) is expressed by:

$$\rho_b = \left(\frac{m_d}{m_s - m_h}\right) \cdot \rho_{rh} \qquad (14)$$

with ρ_{rh} = density of the water at 20°C (998 Kg/m^3).

While the open porosity is calculated using the following equation:

$$\varphi_A = \left[\frac{m_s - m_d}{m_s - m_h}\right] \cdot 100 \qquad (15)$$

The determination of real density has been carried out by pycnometer method. After the determination of apparent density and open porosity, each specimen is separately grounded to powder size and dried. About 20 g of the powder are weighed (me) and introduced into a pycnometer half full of water. Then the pycnometer is filled with deionised water and weighed (m_1). Finally the pycnometer is emptied and washed, filled with deionised water only and weighed (m_2). The real density is expressed as the ratio of the mass of the ground dry specimen me to the volume of liquid displaced by this mass, by the following equation:

$$\rho_r = \left(\frac{m_e}{m_2} + m_e - m_1\right) \cdot \rho_{rh} \qquad (16)$$

with ρ_{rh} = density of the water at 20°C (998 Kg/m^3).

While the total porosity is calculated using the following equation:

$$\varphi_{TOT} = \left[1 - \left(\frac{\rho_B}{\rho_R}\right)\right] \cdot 100 \qquad (17)$$

Twelve cubic samples 7 cm in edge have been used for the determination of apparent density and open porosity, while real density and total porosity have been determined by pycnometer method using about 25 g of powered sample (≥0,063 mm grain size).

The average real density, refereed to the volume of the specimen with no voids and determined through the pycnometer method, is 2.67 g/cm^3, while the average apparent density measured, considering the presence of pores, is 1.87 g/cm^3. Referring to porosity, average total and effective porosity are 30% and 29%, respectively; a comparison between this two latter data and the imbibitions coefficient obtained (ranging from 13% to 16%) suggest a really high permeability of the rock.

In Table 1.5 physical and mechanical proprieties determined through laboratory tests on fresh samples of Sabucina Stone with indication of samples ID, average values and standard deviation (St. Dev).

Table 1.5 - Physical and mechanical proprieties determined through laboratory tests on fresh samples of Sabucina Stone with indication of samples ID, average values and standard deviation (St. Dev).

Sample ID	Weight (g)		Imbibitions coefficient	Apparent density	Porosity (%)		Ultrasonic velocity (m/s)		Anisotropy (%)		UCS (MPa)	
	Dry	Wet	(%)	(g/cm³)	Total	Efficient	Dry	Wet	Dry	Wet	Dry	Wet
7	629.2	725	15.23	1.87	29.85	28.86	2063.22	3088.78	2.91	14.58	5.55	
11	631	724.7	14.85	1.89	29.24	28.39	2053	3173.44	5.78	5.99	7.03	
16	626	720	15.02	1.87	29.96	28.42	1998	3175.56	3.15	9.45	5.44	
44	644	732.4	13.73	1.92	28.10	26.67	2110	3245	10.97	12.17	6.81	
49	617.4	713.3	15.53	1.84	30.92	29.00	1961	2955	7.73	14.31	5.21	
58	618.6	717.3	15.96	1.84	31.08	29.71	1953.33	2959.56	3.75	4.35	6.65	
38	629.7	724.6	15.07	1.88	29.70	28.63	2030.78	3045.56	4.87	15.21		5.73
40	625.9	721	15.19	1.87	30.12	28.69	2028.8	2875.8	12.86	15.71		8.09
42	631.8	723.9	14.58	1.89	29.36	27.83	2100	3154	3.11	1.57		5.48
45	622.8	718.6	15.38	1.86	30.32	28.97	2008	3031.44	17.15	4.37		5.49
46	619.4	716.6	15.69	1.85	30.90	29.31	2010	2787.33	8.97	6.69		4.26
48	618.5	716.4	15.83	1.84	31.00	29.52	2020	3019	3.88	4.65		5.76
Min	**617.40**	**713.30**	**13.73**	**1.84**	**28.10**	**26.67**	**1953.33**	**2787.33**	**2.91**	**1.57**	**5.21**	**4.26**
Max	**644.00**	**732.40**	**15.96**	**1.92**	**31.08**	**29.71**	**2110.00**	**3245.00**	**17.15**	**15.71**	**7.03**	**8.09**
Average	**626.19**	**721.15**	**15.17**	**1.87**	**30.05**	**28.67**	**2028.01**	**3042.54**	**7.09**	**9.09**	**6.12**	**5.80**
St. Dev.	**7.66**	**5.23**	**0.61**	**0.02**	**0.89**	**0.81**	**48.18**	**134.35**	**4.58**	**5.09**	**0.80**	**1.25**

1.2.5 Mercury intrusion porosimetry (MIP) test

Mercury porosimetry is an extremely useful technique able to characterize porous material. For detail on the method (*see Chapter 2, paragraph 2*).

In general, the methodology provides a wide range of information, *e.g.* the pore size distribution, the total pore volume or porosity, the skeletal and apparent density, and the specific surface area of a sample.

For aforementioned, mercury intrusion porosimetry tests carried out on Sabucina fresh samples in order to investigate porosity and pore size distribution of studied stone. Porosimetric analysis was carried out with a Thermoquest Pascal 240 macropore unit in order to explore a porosity range ~0.0074 μm < r <~15 μm (r being the radius of the pores), and by a Thermoquest Pascal 140 porosimeter instrument in order to investigate a porosity range from ~ 3.8 μm< r <~ 116 μm. In detail, the distribution of pore size has been determined on small samples similar in dimension and shape. For each sample measurements have been performed on almost three specimens sampled from the same cubic one in order to verify the reproducibility of test. Data have been processed by using Thermo Scientific SOL.I.D (Solver of Intrusion Data) Software. Measurements have been performed on almost three samples in order to verify the

reproducibility of the test. With the aim to de-noise the original data to produce high-resolution distribution curve two models have been applied: the *moving average method*, able to rebuilds the experimental data curve considering the average value calculated on a chosen number of points (N can be chosen between 1 and 100 points; in this case 19 value has been used) and the *exponential smoothing*, a mathematical operation that reduces the discrepancy between one point and the next one; the Smooth Factor (DF) can be chosen between 0 and 0.99, and in this case DF = 0.8 has been applied.

Porosity and pore size distribution of studied stone (fresh_#) have been investigated by mercury intrusion porosimetry tests (MIP). Cumulative pore volumes vs. pore radius and pore size distribution curves are shown in Figure 1.12. The obtained results (Table 1.6) highlight a total accessible porosity of 26.86% and a total pore volume of 0.1356 g/cm^3. Referring to pore size distribution, average pore radius of 0.1442 μm and mode peak at 8.5567 μm have been obtained.

Table 1.6 - Porosimetric data of analyzed fresh samples.

	Total intruded volume (cm^3/g)	***Bulk density (g/cm^3)***	***Apparent density (g/cm^3)***	***Porosity %***	***Total surface area (m^2/g)***	***Average pore radius (μm)***	***Modal pore radius (μm)***	***Median pore radius (μm)***
Fresh_1	0.1283	2.05	2.77	26.24	1.68	0.1527	5.1102	2.1119
Fresh_2	0.1429	1.96	2.71	27.94	2.07	0.1379	9.4878	2.3103
Fresh_3	0.1356	1.95	2.65	26.41	1.91	0.1419	11.0720	2.3245
Average	**0.1356**	**1.98**	**2.71**	**26.86**	**1.89**	**0.1442**	**8.5567**	**2.2489**
St. Dev	0.0073	0.05	0.06	0.94	0.20	0.0077	3.0880	0.1189

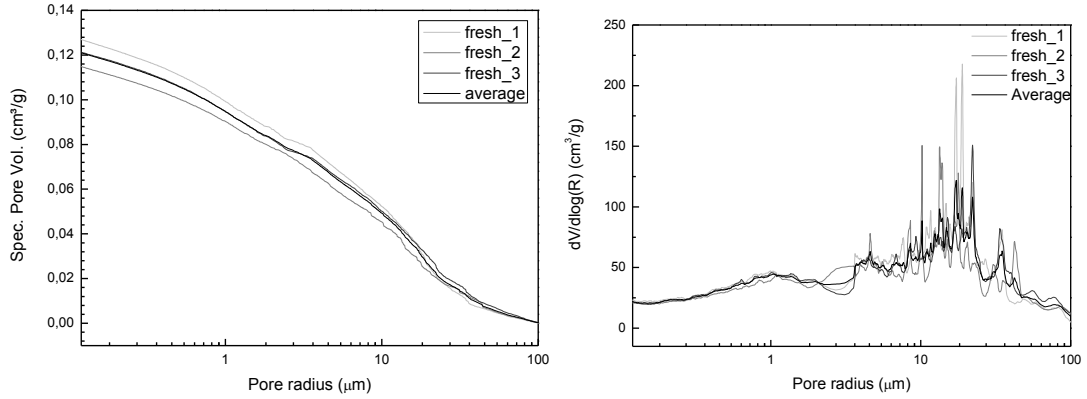

Figure 1.12 - (a) cumulative pore volume (cm^3/g) vs. pore radius (μ) and (b) pore size distribution dV/dlog(R) (cm^3/g) vs. pore radius (μ) curves of fresh samples. Measurements have been performed on three samples (gray scale curves); the average curve is shown in black.

1.3 Discussion and conclusions

A complete characterization of the Sabucina Stone, form the petrographic, mineralogical, geochemical, physical and mechanical point of view has been supplied.

Among the obtained results, noteworthy is that a variability in mechanical parameters have been observed; this features can be explained only considering the micro-textural and micro-

structural heterogeneity observed during the characterization of the stone, in which the ranging of petrographic classification determine a significant range of value, the maximum and the minimum ones equally representative of its behavior. For aforementioned, in the study of this stone should be better considered a range of values in spite of average values in order to take in account its micro-textural and micro-structural heterogeneity.

In conclusion, the obtained results highlight the necessity of a multi-methodological approach in investigating the characteristics of this building stone for allowing the correct interpretation of data, in consideration of its microtextural and microstructural proprieties.

1.4 Bibliography

[1] Siegesmund S, Snethlage R (eds.), Stone in Architecture, Springer-Verlag Berlin Heidelberg, 2011.

[2] Steiger M, Asmussen S. Crystallization of sodium sulfate phases in porous materials: The phase diagram Na_2SO_4–H_2O and the generation of stress. Geochimica et Cosmochimica Acta, 2008. 72:4306-4291.

[3]Friesen WI, Mikula RJ. Fractal Dimensions of Coal Particles. Journal of Colloid and Interface Science, 1987. 120: 263-271

[4] Perfect E & Kay BD. Applications of fractals in soil and tillage research: a review. Soil and Tillage Res., 1995. 36:1–20.

[5] Giménez D, Perfect E, Rawls WJ, Pachepsky Y. Fractal models for predicting soil hydraulic properties: a review Engineering Geology, 1997. 48:161–183.

[6] Radliński AP, Radlińska EZ, Agamalian M, Wignall GD, Lindner P, Randl OG. Fractal Geometry of Rocks. Phys. Rev. Lett., 1999. 82: 3078 -3081

[7] Radlinski AP, Ioannidis MA, Hinde AL, Hainbuchner M, Baron M, Rauch H, Kline SR. Angstrom-to-millimeter characterization of sedimentary rock microstructure. Journal of Colloid and Interface Science, 2004. 274: 607–612.

[8] Katz AJ &Thompson AH. Fractal Sandstone Pores: Implications for Conductivity and Pore Formation. Phys. Rev. Lett. 1985. 54: 1325-1328.

[9] Bernal PJL, Bello MA. Fractal geometry and mercury porosimetry. Comparison and application of proposed models on building stones. Appl. Surf. Sci., 2001. 185:99-107.

[10] Barbera G, Barone G, Mazzoleni P, Scandurra A. Laboratory measurement of ultrasound velocity during accelerated aging tests: Implication for the determination of limestone durability. Construction and Building Materials, 2012. 36:977–983

[11] Schlueter EM, Zimmermana RW, Witherspoon PA, Cook NGW. The fractal dimension of pores in sedimentary rocks and its influence on permeability. Eng. Geol., 1997. 48:199-215.

[12] Bernal PJL, Bello MA. The fractal dimension of stone pore surface as weathering descriptor. Appl. Surf. Sci., 2000. 161:47-53.

[13] Zorlu K. Description of the weathering states of building stones by fractal geometry and fuzzy interference system in the Olba ancient city (Southern Turkey). Engineering Geology, 2008. 101: 124–133.

[14] Turkington AV, Paradise TR. Sandstone weathering: a century of research and innovation. Geomorphology, 2005. 67: 229–253.
[15] Gregory KJ. The Changing Nature of Physical Geography. 2000. Arnold, London, p. 368
[16] Nahon DB. Self-organization in chemical lateritic weathering. Geoderma, 1991. 51: 5 –13.
[17] Mayer L. Some comments on equilibrium concepts and geomorphic systems. Geomorphology, 1992. 5: 277– 295.
[18]Phillips JD. Nonlinear dynamical systems in geomorphology: revolution or evolution. Geomorphology, 1992. 5: 219– 229.
[19] Phillips JD. Earth Surface Systems. 1999. Blackwell Publishers, p. 180.
[20] Phillips JD. Signatures of divergence and self-organization in soils and weathering profiles. J. Geol., 2000. 108: 91– 102.
[21] Phillips JD. Inherited versus acquired complexity in east Texas weathering profiles. Geomorphology, 2001. 40: 1 – 14.
[22] Renwick WH. Equilibrium, disequilibrium and non equilibrium landforms in the landscape. Geomorphology, 1992. 5: 265–276.
[23] Ortoleva PJ. Geochemical Self-Organization. 1994. Oxford University Press, New York, p. 432.
[24] Mostafavi M, Leatherbarrow D. On Weathering. The Life of Buildings in Time. 1993. MIT Press, Cambridge, MA.
[25] Viles HA. Scale issues in weathering studies. Geomorphology, 2001.41, 63– 71.
[26] De Thury H. On the method proposed by Mr. Brard for the immediate detection of stones unable to resist frost action. Ann. Chim. Phys., 1828. 38: 160– 192.
[27] McGreevy JP, Smith BJ. Salt weathering in hot deserts: observations on the design of simulation experiments. Geogr. Ann., 1982. 64A (3–4): 161–17.
[28] Flatt RJ, Scherer GW. Hydration and crystallization pressure of sodium sulfate: a critical review. In: Vandiver PB, Goodway M,Mass JL (Eds.) Materials Issues in Art & Archaeology VI, MRS Symposium Proc., 712, Materials Res. Soc., Warrendale, PA. 2002, pp. 29– 34.
[29] Flatt RJ. Salt damage in porous materials: how high supersaturations are generated, J. Cryst. Growth, 2002. 242: 435–454.
[30] Tsui N, Flatt RJ, Scherer GW. Crystallization damage by sodium sulfate. J. Cult. Herit., 2003. 4: 109– 115.
[31] Steiger M, Asmussen S. Crystallization of sodium sulfate phases in porous materials: The phase diagram Na2SO4–H2O and the generation of stress. Geochimica et Cosmochimica Acta, 2008. 72:4291–4306.
[32] Rodriguez-Navarro C, Doehne E, Sebastian E. How does sodium sulfate crystallize? Implications for the decay and testing of building materials. Cem. Concr. Res., 2000. 30:1527-1534.
[33] Kracek FC. International Critical Tables 3, 1928, p. 371.
[34] UNI EN 12370, Natural stones test methods: Determination of resistance to salt crystallization, UNI ed., Milano, 2001.
[35] Steiger M. Crystal growth in porous materials—I: The crystallization pressure of large crystals. Journal of Crystal Growth, 2005. 282:455–469.

[36] Steiger M. Crystal growth in porous materials—II: Influence of crystal size on the crystallization pressure. Journal of Crystal Growth, 2005. 282: 470–481.
[37] Scherer GW. Crystallization in pores. Cement and Concrete Research, 1999. 29: 1347–1358.
[38] Di Grande A, Giandinoto V. Plio-Pleistocene sedimentary facies and their evolution in centre-south-eastern Sicily: a working hypothesis EGU Stephan Mueller Spec. Publ., 2001. 75: 211–221.
[39] Bellanca A, Curcuruto E, Lo Bue S, Neri R. Petrografia, geochimica e riferimenti all'impiego storico delle calcareniti plioceniche in Sabucina, Sicilia centrale. Mineralogica et petrographica acta, 1999. 42:210-193.
[40] Tortorici L, Grasso M, Catalano S, Monaco C, De Guidi G, Pappalardo G, Curcuruto E, Brescia M, Di Stefano A, Maniscalco R, Barreca G, Sturiale G. Carta Geologica d'Italia. Scala 1:50.000 Foglio 631 Caltanissetta 2010.
[41] De Benedictis R, Tringali S. La ricostruzione della Cattedrale di Noto. L.C.T. Ed., 2000.
[42] Dunham RJ. Classification of carbonate rocks according to their depositional texture. In: Ham E (Eds) Classification of Carbonate Rocks, Tulsa: American Association of Petroleum. Geologists Memoir, 1962. p. 21-108.
[43] Choquette PW, Pray LC. Geological nomenclature and classification of porosity in sedimentary carbonates. American Association of Petroleum Geologists Bulletin, 1970. 54:250-207.
[44] Folk RL. Practical petrographic classification of limestones. Am. Assoc. Pet. Geol. Bull. 1959, 43:38-1.
[45] Ostrom ME. Separation of clay minerals from carbonate rocks by using acid. J. Sed. Pet., 1961. 31:123-129.
[46] Barone G, Crupi V, Longo F, Majolino D, Mazzoleni P, Raneri S, Venuti V. A multi-technique approach for the characterization of decorative stones and non-destructive method for the discrimination of similar rocks. X-Ray Spectrometry, 2013. 43: 83-91.
[47] Barbera G, Barone G, Crupi V, Longo F, Majolino D, Mazzoleni P, Venuti V. Nondestructive analyses of carbonate rocks: applications and potentiality for museum materials. X-Ray Spectrometry, 2013. 42:8-15.
[48] NORMAL 11/88 Natural stones test methods: Determination of water absorption coefficient by capillarity.
[49] Fitzner B. Die Prüfung der Frostbeständigkeit von Naturbausteinen. Dissertation RWTH. Aachen. 1970.
[50] NORMAL 7/81 Natural stones test methods: Determination of water absorption by total immersion.
[51] NORMAL 29/88 Natural stones test methods: Determination of dry index.
[52] NORMAL 22/86 Natural stones test methods: Determination of ultrasonic waves velocity.
[53] Birch F. The velocity of compressional waves in rocks to 10 Kbar: Part 2. J. Geophys. Res. 1961. 66:2199-2224.
[54] UNI EN 1926 Natural stones test methods: Determination of compression strength, UNI ed., Milano, 2000.
[55] UNI EN 12372, Natural stones test methods: Determination of flexural strength resistance under concentrated load, UNI ed., Milano, 2001.

[56] UNI EN 1936 Natural stones test methods: Determination of real density and apparent density and of total and open porosity, UNI ed., Milano, 2001.

Chapter 2. Methods and models for investigating the impact of weathering in the porous system of building stones

2.1 Introduction

This section is focused on methods currently used in the building stones researches in order to characterize the pore network geometry and to monitor and measure the impact of weathering on their surface and sub-surface features.

The main purpose is to demonstrate how methods are complementary in providing information about weathering, durability and stone response, allowing a multiscale modeling of weathering processes; the section provide therefore an overview on advances in methodologies useful to study stone weathering and plan suitable conservation and managements strategies, lighting up also advantages and disadvantages of methods.

The understanding of processes, modes and rates of surface and sub-surface deterioration in stone weathering studies is a quite complex issue, especially considering different environmental contexts and the requirement of a multi-scalar investigation. For this reason, the potential of different techniques to supply complementary data is a key topic in planning a complete and appropriate research activity[1]. This kind of approach can, in fact, facilitate the underlining of climatic, environmental and lithological controls on the evolution of weathering, allowing the development of more detailed models and theories.

As surface of stones is immediately in contact with the environmental conditions, it greatly suffers of weathering processes, exhibiting a multifarious repertoire of degradation patterns. Therefore, the monitoring and measuring of surface changes due to weathering represents a start point in weathering studies. Several methods are used, especially by geomorphologists, in order to estimates the stone surface recession caused by weathering. Relative measurements of stone surface respect to natural reference point or plane of known age represent one of the most used direct methods applied to esteem surface weathering. Despite the advantages of these methodologies, that allow to measure very long term rates (*e.g.* measurements relative to resistant mineral veins[2], lead plugs[3], micro-erosion meters[4], etc.), they suffer of some limits due to the possible modifications of reference points over the time. In the framework of indirect surface measurements, laser scanner is one of the widely used[5], having the great advantage to supply maps of surfaces, allowing to extrapolate a large number of measurements, *e.g.* surface roughness parameters, that can be used as indicators of relative rate of weathering.

Beside the surface, weathering affects greatly also the inner structure of stones, determining significant changes in physical features, especially related to porosity, permeability and mechanical resistance, as well as in chemical ones, due to the precipitation of compounds such as salts or the selective removal of compounds by leaching.

The visualization and quantification of these changes is really difficult to achieve by using a single method and, usually, a multi-methodological approach is required in order to inspect the complete range of scales of porous materials.

Among physical features interested by weathering processes, porosity (percentage of void space in the stone) and permeability (ability of fluids to move through the stone) are of great interest in stone conservation. In fact, changes in these parameters determine modifications in the behavior of the stones as influence the ability of moisture to penetrate into and move within the pore network. The majority of the methods able to measure pore range features in stones are laboratory based and generally destructive or micro-destructive (*i.e.* gravimetric methods, intrusion methods, acoustic monitoring, etc.).As changes in pore network generally determine modifications in mechanical proprieties of the stone, one of the most diffused approaches for assessing the impact of weathering is to measure rock strength. Both destructive (triaxial cells, point load tester) and non destructive (Schmidt Hammer, Portable Ultrasonic Nondestructive Digital Indicating Tester (PUNDIT)) methods are available for measuring rock strength in laboratory and in field set-ups.

In the framework of the aforementioned methodological scenario, mainly based on classical approach characterized by several limits (especially in term of destructivity), recent innovations and technological advancements in the microscope techniques have supplied new opportunities in examining both surface and sub-surface features in a non-destructive and non invasive way, providing high magnification and resolution (*e.g.* confocal laser scanning microscopy (CLSM)[6], Scanning Electron Microscopy (SEM) with X-ray energy dispersive spectroscopy (EDS) or back-scattered electron detection (BSE)[7]; High Resolution TEM Scanning[8]; Force Microscopy (SFM)/Atomic Force Microscopy (AFM); 3D X-ray Microscopy Computed Tomography[9]).

These high number of non-invasive and non-destructive methods able to measure and monitor stone surface and sub-surface weathering can be applied on several interdisciplinary contexts (*i.e.* in material conservation science as well as in geomorphologic, architectural, archaeological, botanical and engineering applications) offering the possibility to obtain multi-scalar data and develop models for the description of complicate patterns, as typical of weathering processes.

For aforementioned, the application of integrate, multidisciplinary and multi-methodological approach in stone weathering researches promises really interesting development in the understanding surface and sub-surface weathering process in term of wide spatial and temporal scales and ranges.

2.2 Mercury Intrusion Porosimetry

Mercury intrusion porosimetry (MIP) is the most wide micro-destructive technique applied for the study of porous materials, being relatively simple, fast and able to give back information

about a wide range of pores, often not investigable by using other intrusion methods[10,11]. The technique is also mentioned in the IUPAC Recommendations as standard method to measure the total pore volume and pore size distribution of porous solids in the macro- and meso- pore ranges[12]. In fact, porosimeters work usually in a range between ~0.005 and ~100 µm, allowing a quite complete description of the pore structure of porous materials. Nerveless, several geometrical and experimental assumptions are inside the method and have to be considered in the data processing of the results.

2.2.1 Theoretical background

The theoretical background of the method is related to the behavior of non-wetting liquids at solid interface under the application of a given external pressure (Figure 2.1). According to Laplace equation[13], the work required expanding a non-spherical fluid surface of principal radii of curvature r_1 and r_2 is equal to the work done to the concave side of the surface and managed to derive the following equilibrium relation:

$$\Delta p = \gamma \left(\frac{1}{r_1} + \frac{1}{r_2}\right) \qquad (18)$$

where γ is the fluid surface tension and Δp is the pressure across the interface. On the basis Eq. 18 and the equations derived from Young[14], Washburn[15] postulate a relation that correlate the aliquot of the pressure at the interface (Δp) and the dimension of a cylindrical pore (r) for a non-wetting liquid with a surface tension γ and a contact angle θ, as following:

$$\Delta p = \frac{-2\gamma \cos\theta}{R} \qquad (19)$$

Therefore, by monitoring the amount of liquid intruded into the pores at a given applied pressure it is possible to obtain a volume distribution of pore size in a porous material.

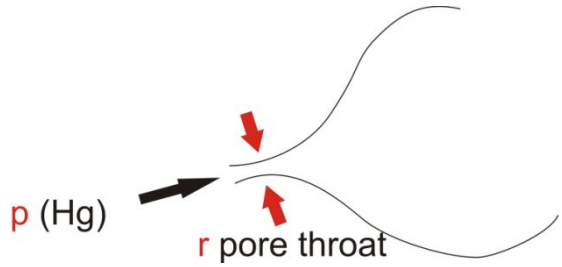

Figure 2.1 - Schematic model of intrusion process for a non-wetting liquid

In order to simplify the data interpretation, cylindrical pore geometry and constant values of surface tension γ (0.485 N/m) and a contact angle θ (140 °) are assumed in a MIP measurement. However, it has to be considered that porous materials often exhibit a more complex pore

network than a cylindrical capillary one, usually characterized by pores connected each other's by smaller throats. Therefore, in the analysis of intrusion curves, an undersized of the real pore distribution could be verified in cases of really emphasized differences between channels and pores. In fact, the presence of a complex system of channels and pores, ranging in dimension, can affect the extrusion behavior of the mercury, usually entrapped in the so called *ink-bottle pores*; the result of this phenomenon is represented by a quite different trend of the mercury extrusion curves, that usually not overlap the intrusion ones (hysteresis)[16].

Several models have been supplied by the literature for the explanation of hysteresis phenomena, *i.e.* the *ink-bottle pore assumption*, the *percolation-connectivity model* and the *contact angle theory*[10]. The first one is suitable to describe systems in which the pores of a give diameter D exhibit throats with size >D. In this case, during the intrusion phase, mercury fills the pores and the throats, while during the extrusion one, mercury is trapped inside the sample due to the arrangement of the pore network. The second model, *i.e.* the percolation-connectivity model, can be considered an extension of the ink-bottle theory and takes in consideration the presence of the connection effects between the pores. In this sense, the filling of the mercury occurs until the entirely volume of large pores surrounded by smaller ones is completely filled; otherwise, during the extrusion, the reverse process occurs and groups of pores trap mercury inside[17]. Finally, the contact angle theory assumes that the contact angle of the non-wetting fluid cannot be considered constant during the measurement, so that a variation between the compressive intrusion contact angle θ_I and the extrusion contact angle θ_E has to be considered. In this condition, a good agreement between the variation of contact angle and the hysteresis gap has been demonstrate[18-20]. Anyway, even if the process of hysteresis affects the results of a MIP experiments, appropriate mathematical relations can be used to esteem the pore/throat ration and better understand the effects of the phenomenon.

2.2.2 MIP measurement

A MIP measurement gives back several information about the investigated solid porous material; among them, porosimetric parameters as *pore volume intruded*, *pore size distribution*, *density*, *surface area*, as well as additional data about *compressibility*, *tortuosity*, *permeability* and *fractal dimension* of pore surface in a give pressure range can be obtained.

1.2.1 Pore volume and pore size distribution

According to the Eq. 19, pressure values measured during a MIP measurements are converted into the correspondent pore size diameter or radius, giving back a penetration plot (pressure vs. volume) that describe intrusion and extrusion processes, as well as the relative pore size distribution by an histogram or a curve that describe the population of pores in a given size range. The statistical treatment of the results allows the determination of parameters as *average*

pore radius/diameter, modal pore radius/diameter and *median pore radius/diameter*, representative of the pore distribution.

1.2.2 Density

In a solid material, density ρ is defined as the ratio between the sample weight and its volume. A MIP measurement allows to determine both *bulk* and *apparent* density, defined as the mass of the material divided by the total volume that it occupies in the environment (including pores) and the mass of the material dived by the total volume without pores, respectively.

Referring to bulk density, the determination of this parameter is allowed to the initial measurement condition; in fact, the sample is first submitted to vacuum in order to degas the material and permit the mercury filling of the dilatometer. When mercury is introduced in the dilatometer under vacuum conditions, it will surround the material without entering pores and inter particles void spaces. Therefore it is possible to compute (by a differential weight) the volume occupied by the material including all the voids volumes. Otherwise, the apparent density from mercury porosimetry is calculated computing the V_{Pore} as the total specific pore volume.

1.2.3 Surface area

For cylindrical pores, the envelope area of each pore class is calculated as:

$$A_i = \frac{2V_i}{r_i} \qquad (20)$$

The cumulative pore surface area is calculated as the sum of the surface areas of all pore classes.

1.2.4 Compressibility

Compressibility β is defined as the fractional change in volume per unit pressure. The linear equivalent is the Young Modulus. Most solids have compressibility values of about10^{-3} to 10^{-4} $(Pa)^{-1}$. Thus, a 1 cm^3 sample will compress by about 0.006 to 0.06 cm^3 at the final pressure of400 MPa. Depending on the pore volume of the sample, this might be a minor effect.

In a MIP measurement compressibility is calculated as following:

$$\beta = V_{pores} - \left[\frac{1}{\rho_{Hg}} - \frac{1}{\rho_{real}}\right] \qquad (21)$$

A difference of 0 means that the sample is not compressible; a positive difference means that the sample is compressed by a volume equal to this difference.

1.2.5 Tortuosity

Considering the diffusion of fluids in porous materials, tortuosity τ represents a factor that describes the deviation of the effective diffusivity from the theoretical one, as following:

$$\tau = \frac{D_{bulk}\ \theta_C}{D_{eff}} \qquad (22)$$

with θ_C the pore volume fraction.

By using appropriate laws that describe the fluid diffusion through cylindrical pores, Carniglia[21] derived the following equation useful to obtain tortuosity from MIP measurements:

$$\tau = 2.23 - 1.13 V_c\ \rho_{Hg} \qquad (23)$$

with V_C the total specific pore volume, approximately equal to the volume of mercury intruded at the maximum pressure and ρ_{Hg} the bulk density of the solid.

The Eq. 23 is valid only for samples in which

$$0.05 \leq V_c\ \rho_{Hg} \leq 0.95 \qquad (24)$$

In all other cases, the determination of tortuosity follow the Carniglia modified equation:

$$\tau = \left(2.23 - 1.13 V_c\ \rho_{Hg}\right)(0.92y)^{1+E} \qquad (25)$$

where

$$y = \frac{4}{s}\Sigma\frac{\Delta V}{d} \qquad (26)$$

and

s = total surface area; ΔV = change in pore volume within a pore size interval; d = average diameter within a pore size interval; E = pore shape exponent (1 for cylindrical geometry).

1.2.6 Permeability

Permeability is defined as the ability of the solid to let fluid travel across it. From a MIP measurement, permeability values can be obtained from tortuosity, by using the following:

$$K = \frac{\phi\ d_p^2}{16\tau} \qquad (27)$$

where φ is the powder bed porosity and d_p is the average diameter of the pores.

1.2.7 Fractal dimension

The fractal dimension *D* of a solid is a parameter that characterizes the degree of roughness of its surface. Real solids expose areas with the fractal dimension of pore surfaces D ranging between 2 for flat surfaces and about 3 for extremely rough surfaces.

Generally, for pore wall surfaces the pore size distribution function $-dV/dr$ could be expressed as:

$$-\frac{dV}{dr} = k_1 r^{(2-D)} \quad (28)$$

where k_1 is proportionality constant, r is the pore radius, and D is the fractal dimension. It follows from the Washburn equation that fractal dimensions can be derived from mercury porosimetry data according to:

$$-\frac{dV}{dP} = k_2 Pr^{(D-4)} \quad (29)$$

where k_2 is another proportionality constant and P is the applied pressure. Taking logarithms on both sides of the expression yields:

$$-\log\frac{dV}{dP} = \log(k_2) + (D-4)\log(P) \quad (30)$$

According to previously, fractal dimension *D* can be derived for the slope of the $\log\frac{dV}{dP}\ vs.\log(P)$ plots. An inspection of porosimetric data for porous solids reveals that a constant slope in given ranges of pressure can be observed, allowing to determine definite D values characteristics of a particular range and type of pores at a given pressure interval.

2.3 Nuclear Magnetic Resonance (NMR)

2.3.1 Theoretical background

Nuclear magnetic resonance is a technique based on the magnetic proprieties of nuclei and their ability to absorb and re-emit energy through interaction with others nuclei under the effect of an external magnetic field. The magnetic signal related to the emission of energy exhibits an exponential decade constant with time, known as *free induction decay* and representing the return of the system to the initial equilibrium condition[22].

In order to better understand the phenomenon, some basic background referred to the behavior of nuclei subjected to magnetic field action is needed.

As it is well known, as nuclei exhibits a spin ≠ 0, they possess a spin angular momentum I defined as:

$$I = \frac{\mu_s}{\gamma} \quad (31)$$

with μ_s = spin magnetic moment and $\gamma = g\frac{q}{2m}$ defined as giromagnetic ratio (g is a dimensionless number, called the g-factor, q is the charge, and m is the mass).

When a nucleus is placed in external magnetic field B_0, the latter one produce a torque of the magnetic moment μ_s dependent to the applied field. On the basis of magnetic proprieties of nuclei, in this condition they start to precess about the external magnetic field and along its direction with a frequency, called *Larmor frequency*, given by:

$$\nu = \frac{\gamma H_0}{2\pi} \quad (32)$$

The possible orientations of the angular moment depend on the magnetic or directional quantum number *m* which can assume only discrete values (*i.e.* m= -I, -I+1, ...-1, 0, 1, ...I-1, I). As a

consequence there are (2I+1) different possible orientations, namely parallel (P) and antiparallel (A) ones, separated by an energetic gap ΔE (Figure 2.2). As an example, if I=1/2 there are two m-values (+1/2 and -1/2), one orientation is parallel and other one is anti-parallel to the magnetic field.

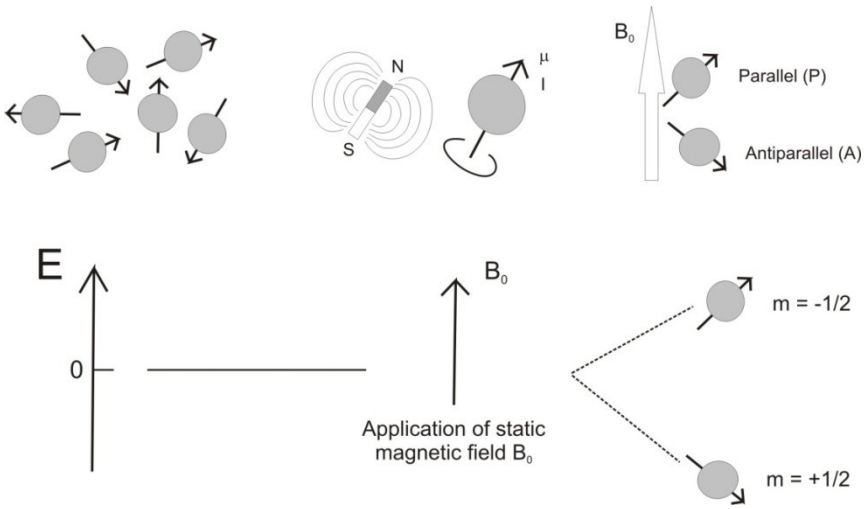

Figure 2.2 - Schematic representation of nuclei in an external magnetic field B_0

According to the Boltzmann statistics

$$\frac{N_P}{N_A} = e^{-\Delta E/KT} \qquad (33)$$

resulting in a total magnetization $M_0 \neq 0$ oriented along the z-axis.

Even if a net magnetization $M_0 \neq 0$ is realized, the energy difference ΔE is very small compared with the average energy KT of the thermal motions, so that the population of parallel energetic state N_P will be most numerous than the antiparallel one N_A. As a consequence, the net magnetization is extremely small and the magnetic signal due to the application of the external field B_0 cannot be observed.

For aforementioned, in order to observe the phenomenon, it is necessary to perturb the system by applying a r.f. magnetic field B_1 in a direction perpendicular to B_0able to allow transitions between the P and A energy states, characterized by a frequency equal to the Larmor frequency of nuclei and energy equal to the energy gap ΔE. Under these conditions, namely *resonance*, the relaxation process related to the magnetic re-equilibrium of the system can be observed as function of time.

In detail, during the application of r.f. B_1perpendicular to B_0, the macroscopic magnetization M_0 (a vector obtained by summing all magnetic moments; see Figure 2.3) is tipped away from the z-axis (the direction of the static field B_0) and tilted in a plane (x-y) by a angle $\theta = \gamma B_1 \tau$(where

θ is the tip angle (degrees), B_1 is the amplitude of an oscillating field and τ is the time over which the oscillating field is applied).

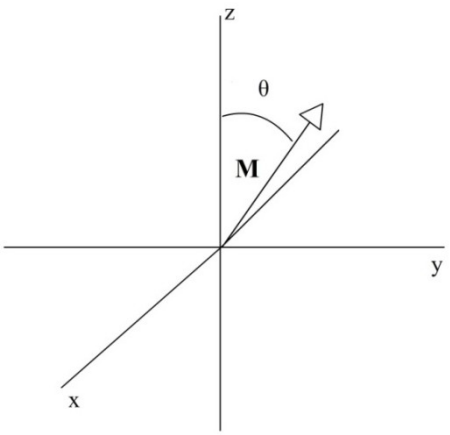

Figure 2.3 - Schematic representation of the magnetization vector M_0

As B_1 is turned off, the magnetization precessing about z-axis, gradually returns to z-axis and its component in the x-y plan tends to zero.

The process is known as *relaxation* and the signal detected is called free induction decay (FID) (Figure 2.4).

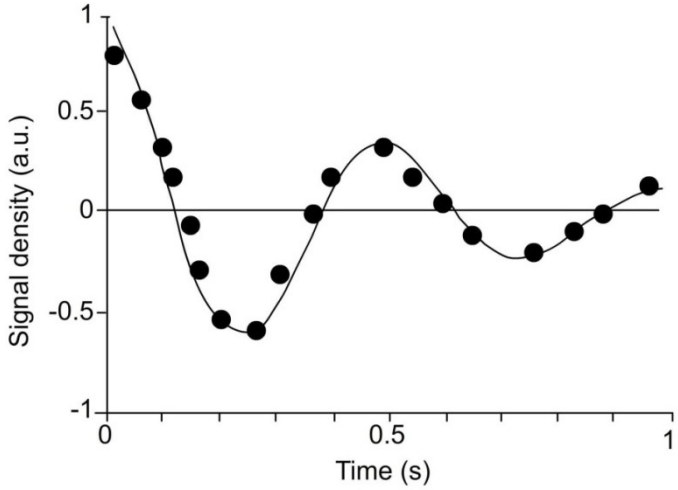

Figure 2.4 - Schematic representation of the free induction decay (FID) signal in function of time

Applying a Fourier transform to FID it is possible to transform data from the time domain into the frequency domain obtaining a NMR spectrum, representing the emission frequencies of atoms or molecules of a given system.

The FID is largely influenced by the magnetic field uniformity and by the presence of paramagnetic nuclei. Because of the complexity of the FID interpretation, multiple and different pulse r.f. frequencies are used in a NMR experiment in order to detect the component about z-axis and x-y plane of the magnetic signal.

Therefore, on the basis of the theoretical background previously exposed, in a NMR experiment the acquisition of the FID is allowed by an experimental set-up as following:

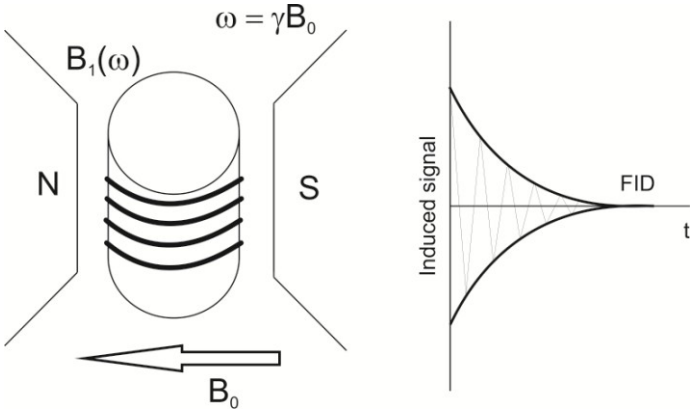

Figure 2.5 - Schematic representation of a NMR set-up

It is composed of a *source*, represented by a magnet generating the static magnetic field B_0, a r.f. coil responsible of the B_1 magnetic field, and a *detector*, able to transform the magnetic signal in electric one (Figure 2.5). In function of the set of the sample, completely immersed in a uniform static magnetic field (high resolution solid state NMR) or partially place in non-uniform magnetic field (unilateral NMR devices), different results can be obtained from NMR measurements.

In general, the induced resonance effect on a specific atom type is used to study the *dynamic arrangement* and the *molecular structure* of a studied system. In detail, the use of specific magnetic field frequencies allows to investigate specific atoms exhibiting a gyromagnetic ratio dependent on the frequency applied to better understand the dynamic processes that occur inside the studied material.

The investigation of the aforementioned aspects, *e.g. dynamic arrangement* and *molecular structure*, can be obtained by the acquisition of the magnetization re-equilibration time, known as *relaxation time*; in a nuclear magnetic resonance experiment, two relaxation time are measured: a *longitudinal relaxation time, T_1*, and a *transversal relaxation time, T_2*, related respectively to the return of magnetization to the equilibrium respect z-axis and x-y plane.

2.3.1.1 Longitudinal relaxation time T_1

As explained above, the application of a B_0 magnetic field determine a magnetization $M_z \neq 0$ in direction parallel to z-axis.

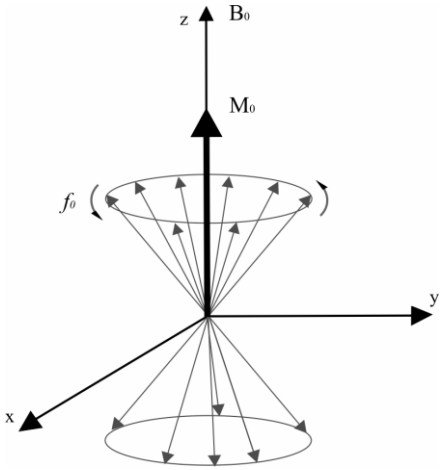

Figure 2.6 - Magnetization of nuclei in external magnetic field B_0

In such condition, the environment of a nucleus with the surrounding molecules can be described as a lattice; in this lattice, the interaction between the magnetic moment of the nuclei and the magnetic and electric fluctuation of the system due to the thermal motions, stimulate transitions between the two possible energy state P and A, with a consequently emission of energy related to the ΔE gap, until the gradually return to the equilibrium M_0, when the external magnetic field B_0 is turned off (Figure 2.6). The process, called spin-lattice relaxation can be described by the following equation:

$$M_z(t) = M_{0z}\left(1 - e^{-\frac{t}{T_1}}\right) \qquad (34)$$

where T_1 is called *spin-lattice relaxation time*, as it describes effectively how the magnetic energy of the spin system is transferred from and to the surrounding. $T_1$is also known as *longitudinal relaxation time* as represents the time that system takes to recover the magnetization along the external magnetic field z-axis from the x-y plane.

The typical pulse sequences used for measuring $T_1$are the *inversion* and the *saturation recovery*, the latter one mainly used for investigating solids.

The inversion recovery consists in a 180° pulse sequence followed by variable recovery time and a *read* 90° pulse. The 180° pulse is able to invert the magnetization vector from the +z-axis to the –z-axis without transverse component. T_1 is than represented by the return of the magnetization vector to the positive z axis; the purpose of the 90° pulse is to direct the FID signal to the receiver (Figure 2.7).

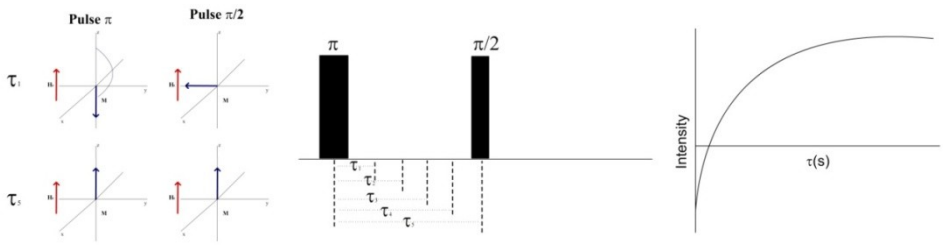

Figure 2.7 - Inversion recovery sequence

For solids, the saturation recovery sequence is preferred; it consists in 90° sequence pulse able to "saturate" the magnetic signal before the next *read* 90° pulse able to direct the FID in the direction of the receiver (Figure 2.8).

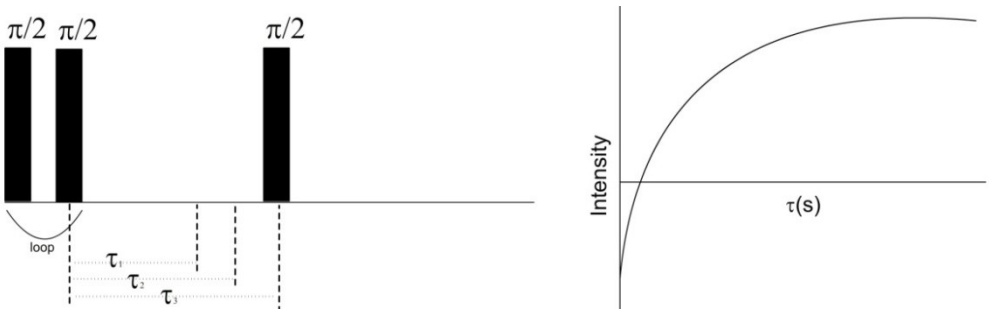

Figure 2.8 - Saturation recovery sequence

2.3.1.2 Transversal relaxation time T_2

The transverse relaxation process describes how the x-y component M_x-M_y of the magnetization M_z return to the equilibrium after the application of the external r.f. magnetic field B_1.The time lap needed for the process is known as *transversal relaxation time* or *spin-spin relaxation time* T_2, as describe the relaxation process that occurs in the x-y plane dependent only by the interaction and the phase coherence of the spins:

$$M_{xy}\ (t) = M_{0xy}\left(1 - e^{-\frac{t}{T_2}}\right) \qquad (35)$$

Also in the case of T_2 measurements, appropriate pulse sequences are needed. One of the most known is the *Hahn's spin echo sequence*[23] (Figure 2.9), consisting in a first 90° pulse able to deflect the magnetization from z-axis to x-y plane, where dephases spins precess along the z axis with slight different Larmor frequencies. After a τ period of time, the application of a new pulse at 180° determines the flipped of dephased spins on the other side of the x-y plane; after a new τ period of time spins become again in phase, due to the reciprocal interaction among the spins, giving back a transverse magnetization signal acquired as an echo.

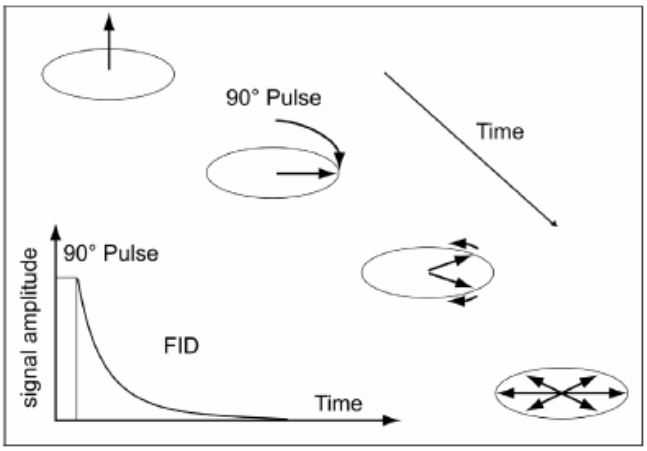

Figure 2.9 - Hahn spin echoes sequence

In order to ameliorate the magnetization signal, more complex pulse sequences have been elaborated over the time. Among them, the *CPMG*[24,25] sequence is one of the most used (Figure 2.10). Its aim is the generation of a train of echoes obtained by repeating 180° pulses separated by appropriate delay times τ (echo time t_E) after an initial pulse of 90°, able to deflect the magnetization on the x-y plane. The 180° pulse, otherwise, has the effect to flip the phase of the spins on the other side of the plane, allowing the re-phase of the spins and the collection the magnetization signal as an echo. The time between two sequences, namely recovery time t_R, must be sufficiently to allow the re-equilibrium of the magnetization.

In an echo-multiple sequence, the height of the successive echoes decreases exponentially with the time with a time constant equal to T_2.

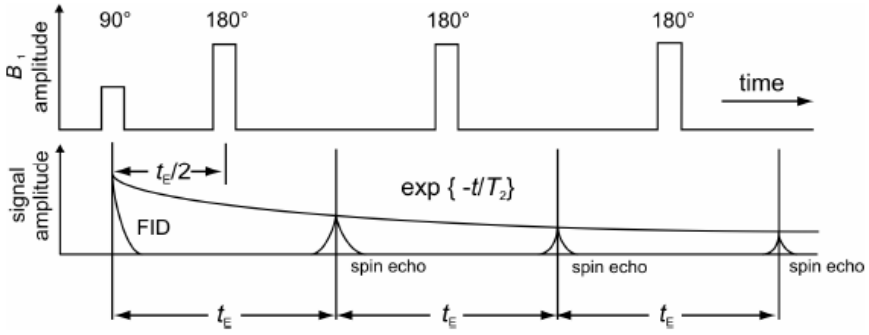

Figure 2.10 - CPMG pulse sequence

The advantage of the CPMG pulse sequence is the much shorter time required to measure at multiple echo times, as the 180° pulses can be applied repeatedly to produce a series of echo trains. With the Hahn sequence, in contrast, only one echo can be measured.

The T_2signal is than transformed by applying an inverse Laplace transformation from FID to T_2 *distribution in function of time* (figure 2.11):

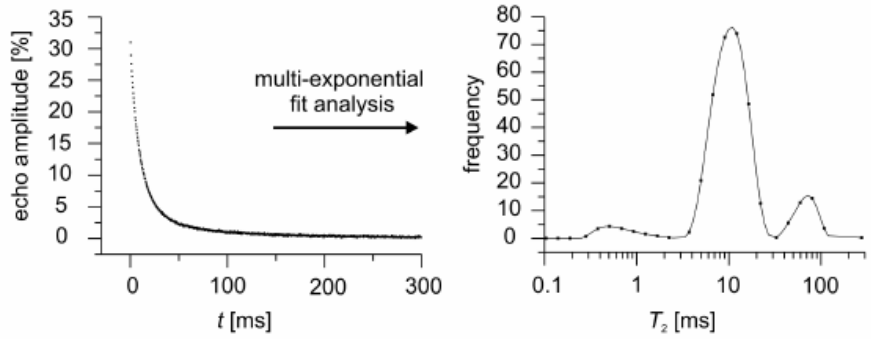

Figure 2.11 - Multi-exponential fit analysis finalized to transform the echo signal in T_2 distribution in function of time

Referring to T_2 measurements, noteworthy is that this parameter is strongly influenced by the *nonuniformity of external magnetic field* and the *diffusive motion of confine liquids*[26]. These two aspects are particularly evident in the case of single-sided NMR sensor, characterized by a high nonuniformity of magnetic field and than by a strong static gradient $G_0 \neq 0$.

In fact, the nuclear spins of liquids can move away from the initial position by diffusive motion due to the presence of a magnetic field gradient. In this condition, in a T_2 measurement carried out as described above, the time decay of the echoes is influenced by the diffusivity and the gradient as following:

$$S(mt_E) = A\, exp\left\{-\left(\frac{1}{T_2}+\frac{1}{12}(\gamma\, G_0 t_E)^2 D\right) mt_E\right\} \qquad (36)$$

with γ = nuclear gyromagnetic ratio, D = self diffusion coefficient of the atom processing the nuclear spin in the fluid, G_0= gradient assumed constant and t_E= echo time.

For aforementioned, it is necessary to use small t_E in order to minimize the effect of diffusive motions. This is the principal purpose of using the CPMG sequence, as allow to apply really small time echo, removing the effect of the gradients in the static magnetic field on the T_2 measurements.

In the framework of the studies of solid materials, the T_2 distributions are able to supply information on porous structure and petrophysical parameters.

2.3.1.3 NMR in porous media

By using appropriate static magnetic field and r.f. magnetic field with appropriate frequencies is possible to investigate H^+ nuclei and therefore to analyze the dynamic of water in porous media. In particular, in saturated rock samples it is possible investigate the relaxation of hydrogen nuclei in the pore space. The values of T_1 and T_2 are affected by the physical and chemical proprieties of the fluid, the uniformity of the magnetic field, the variation in pore size, the difference between the magnetic susceptibility of fluid in pores and rock, the fluid diffusion and the presence of paramagnetic impurity at the interface pore/fluid.

In consideration of the influence of diffusivity in T_2 measurements, the relaxation behavior of hydrogen in pores has to be studied contemplating the diffusion regime of the fluid and the evolution of the polarization of the spins at the fluid/solid interface. Brownstein and Tarr[22] demonstrate that in condition of fast diffusion regime (*i.e.*, the relaxation at the surface is slower than the transport of the hydrogen nuclei to the surface) the relaxation time is related to the characteristic dimension of the porous system:

$$\frac{1}{T_2} \cong \rho a \equiv \rho \frac{S}{V} \qquad (37)$$

being ρ the surface relaxivity, namely a measure of how quickly proton spins lose orientation or phase coherence due to magnetic interactions at the fluid-solid interface and dependent from diffusion, and *S/V* the surface/volume ratio.

Therefore, by using T_2 distribution and applying the appropriate transformations (considering the effect of diffusion) it is possible transform a *time distribution* in a *pore size distribution*. However, the T_2 distribution represents itself a good representation of the water behavior in pore space, as different transverse relaxation times are related to different surface/volume ratio (*i.e.*, as minor is T_2, as smaller are the pore, and *vice versa*; see Figure 2.12). For examples, for sandstones, it is possible to assume three different T_2 ranges correspondent to clay-bound water, capillary- bound water (present in the smallest pores and with lower T_2) and free water (present in the bigger ones and characterized by higher measured T_2).

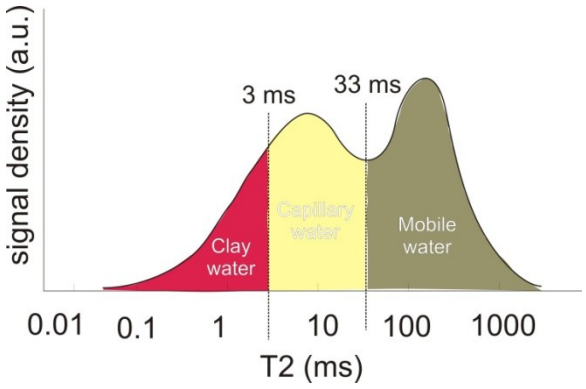

Figure 2.12 - Relation between T2 distribution and pore size in saturated porous media

2.3.1.4 Unilateral portable devices for material science studies

In view of applying NMR method in the field of material science, portable devices have been developed over the time. The most common one is represented by the unilateral NMR-Mouse®[27,28] (Figure 2.13); it consists, in the horseshoe geometry set up, in two permanent magnets separated by a small gap. They are axially magnetized and placed face to face with anti-parallel magnetization in order to maximize the field outside the instrument. The magnetic

field is mostly parallel to the plane surface of the magnets and has a maximum at their surface at about 0.5 T; the frequency of the generated magnetic field is about 13.619 MHz A coil is positioned in the gap between the two permanent magnets and generates an r.f. magnetic field H_1 perpendicular to the surface. By tuning the r.f. frequency, the depth of the distance to the sensor surface where the sensitive volume (about 115 μm; condition of non-uniform magnetic field and constant magnetic gradient) is generated can be shifted; in this way different depths from the surface can be investigated.

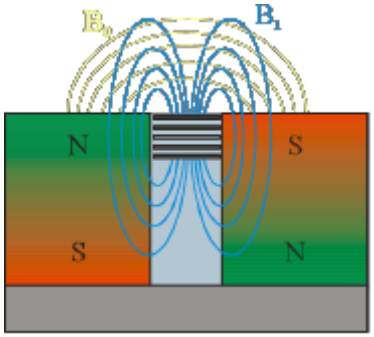

Figure 2.13 - Schematic representation of portable NMR Mouse

The device permits T_1 and T_2 measurements by using the classical pulse sequences (Hahn's echo and CPMG), allowing also to use the non homogeneity of the static magnetic field in order to measure the self-diffusion coefficient of fluids.

2.4 X-ray and neutron imaging

In recent years, many researchers have focused on non-invasive and non-destructive X-ray and neutron imaging techniques as powerful tools to investigate the internal structure of geomaterials[9 and 29]. In particular, in the framework of natural building stones, X-ray micro-tomography (X-ray μCT)[30-42] and neutron radiography and tomography[43-47] have been largely and successfully applied.

The techniques are based on the ability of X-ray and neutron to penetrate materials and give back, if opportunely detected, images of the structural arrangement of the studied matter in function of their attenuation proprieties.

In detail, a monochromatic beam of neutron or X-ray with intensity I_0 that passes through an object will be attenuate according to the following:

$$I = I_0 e^{-\int \mu(s) ds} \qquad (38)$$

where I_0 is the incident beam intensity and μ is the local linear attenuation coefficient along the ray path. On the basis of aforementioned, during an imaging analysis by using X-ray or neutrons, by collecting the intensity of the source beam after the passage through a sample, it is possible to calculate the local value of μfor each point inside the scanned volume. This value

depends on the material density ρ and the mass attenuation coefficient μ/ρ, that are tabulated as energy-dependent values.

The obtained image is therefore a map of the X-ray or neutron attenuation within the sample under investigation.

For a given material, the X-rays and neutrons attenuation coefficient is quite different. In detail, for X-rays the attenuation coefficient is energy-dependent and is approximately proportional to the atomic number[48,49]; otherwise, for neutrons, that interact with the nucleus of the atom rather than with its electron, the interaction forces are not correlated with the atomic number of the element, but depend upon the particular isotope of the element. For example, neutrons are highly sensitive to light isotopes such as ^{1}H, ^{6}Li, ^{10}B, and rather insensitive to heavier isotopes such as ^{82}Pb (Figure 2.14).

For the latter one reason, neutrons are more suitable in the study of soft matter sciences and, in the case of building stones, for performing dynamic studies on the behavior of stones against water as well as in the studies about efficiency of protective and consolidant treatments.

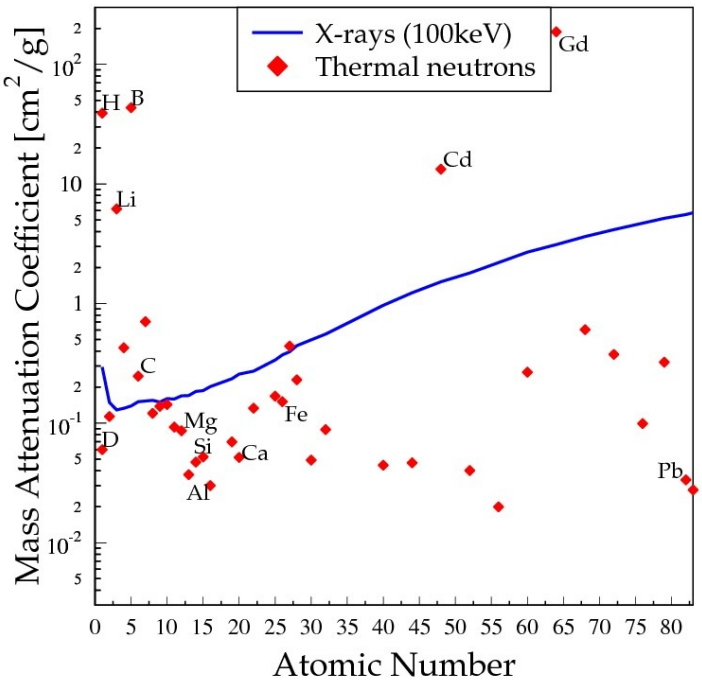

Figure 2.14 - Dependence between mass attenuation coefficient and atomic number for neutrons and X-rays

By using both X-rays and neutrons as source, the typical experimental set-up is composed by a monochromatic source, a collimator, a sample-set and a detector, the latter one usually constituted by a 2D-pixels array like CCD camera (charge-coupled device) able to convert the radiation in digital images (Figure 2.15).

By moving the SSD (source-sample distance) and the SDD (sample-detector distance) is possible to operate on the magnification; in general, closer is the sample to source, higher is the

magnification and the spatial resolution. Noteworthy is that the spatial resolution is not only affected by the magnification but also by factors as the focal spot size of the monochromatic source, the pixel size of the detector and others physical phenomenon due to radiation-matter interaction.

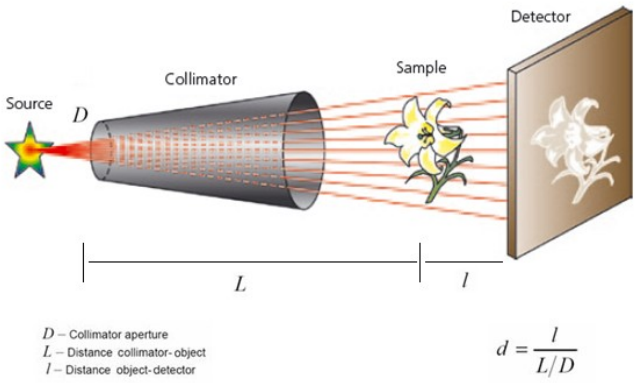

Figure 2.15 - The principle of the radiography system: a surface detector fixed behind the sample records, the radiation emitted by the source, thus revealing the weakening effect within the sample; from [50]

By rotating sample and acquiring a great number of radiographs at different angular steps and using appropriate reconstruction algorithms[51-53], it is possible to obtain a 3D reconstruction of the objects (Figure 2.16).

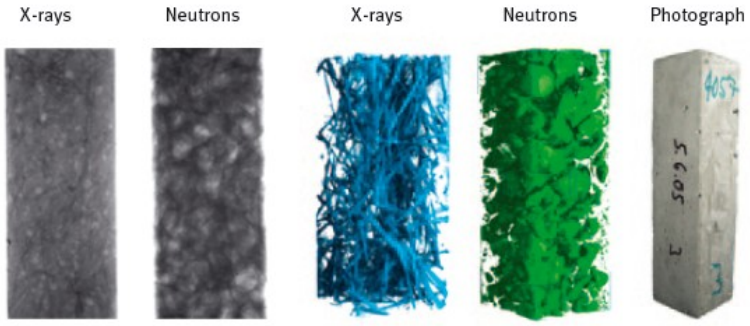

Figure 2.16 - The two images on the left are radiographs of the reinforced concrete sample photographed on the right. The blue and green images are tomograms; from[51]

For both X-ray and neutrons advantages and limitation have to be considered.

Referring to X-ray imaging technique, the main advantage is the ability to perform three-dimensional imaging in anon-destructive way, by using specialized rendering software's that allow the visual inspection of the scanned 3D volume based on the local linear attenuation coefficient. Moreover, by using dedicated software package (Avizo, VGStudio Max, MAVI, Blob3D[54], Pore3D[55], 3DMA-Rock[56], Morpho+[57-58] and Fiji[59]) it is possible to obtain quantitative results on scanned images, as well as texture of a material, component volume fractions, pore and grain size parameters and morphology (shape, sphericity, roundness), surface texture, etc. Another great advantage of the technique is the possibility to monitoring dynamic

processes in the object, as movement of water and so on. The main limitation of the method is related to the voxel size, referring with this term to the minimum volume element reproducible. To avoid severe imaging artefacts, this volume should have similar size as the completesample[60]. Noteworthy is that all features which are smaller than the voxel size cannot be distinguished on the reconstructed dataset.

About artefacts, three main relevant ones have to be considered. The first one is related to the Brehmsstrahlung-spectrum of X-ray source beam; this effect, called *cupping effect*, it is caused by the energy dependence of the linear attenuation coefficient, which implies low-energetic (soft) X-rays to have a higher probability of being absorbed than high-energetic (hard) X-rays. The result is an increase value of attenuation coefficient at the outer regions of the sample. The cupping effect can be diminished by using appropriate beam hardening filters. The second one is due to the conical set up of the experimental session (*cone-beam effect*); in detail, element far away from the centre of the cone can suffer of reconstruction artefacts. This effect is diminished by using iterative reconstruction methods. Finally the third one effect, namely *phase contrast*, is related to the temporal or spatial coherence of the X-ray beam. Several imaging and processing methods are available to benefit from this effect or to correct it.

As far as the limitations of the technique, X-ray image methods are useful to investigate several aspects of materials, especially in geomaterials science. In detail, it is possible to investigate and quantify fundamental parameters as porosity, pore size distribution and pore geometry. In this framework, important features as changes in pore arrangement due to weathering processes or network of fractures can be detected and studied. Another important application is represented by the possibility to monitor dynamic processes, as fluid flow in rocks and, finally, the effectiveness of treatments for conservation and protection of building stone materials.

Beside the advantage of X-ray sources, the use of neutrons is more suitable for imaging of hydrogen-rich fluids in non-hydrogenous porous media; in fact, neutrons are strongly attenuated by hydrogen and therefore they can *see* through the solid matrix in a non-destructive way[29]. For aforementioned, neutrons have been successfully used in porous stone materials studies for monitoring water and other fluids under dynamic conditions (both in conservation material science and reservoir applications) and the penetration depth of protective or consolidant products, mainly consisting in organic matter. Such for X-rays, also in the case of using neutrons some limitations have to be considered and some artefacts have to be corrected in imaging techniques. The main limitation of neutrons is related to the possibility to practically "use" them, as available only in reactor-based facilities, sometimes associated with spallation sources. Referring to artefacts effects, they are mainly due to scattering effects (both primary and secondary). The primary scattering effects are related to the scattering length density of the elements respect to neutrons ($\sigma_i(\lambda) = \mu \frac{M}{m\rho N_A}$, with μ = linear attenuation coefficient, M = molecular weight, m= moles, ρ = density, N_A = Avogadro constant); in detail, samples

exhibiting strong scattering cross section determine the production of numerous scattered neutrons that result in significant deviations from the Eq. 38. Secondary scattering effects are due to the thickness of the sample and the production of multiple scattering processes inside the samples. Usually, to minimize scattering artefacts data are treated with appropriate models of point scattering functions (*i.e.*, Monte Carlo methods). However, the simple way to minimize these effects is the use of appropriate experimental set-up, positioning samples a few to several centimeters away from the detector.

Considering the powerful ability of neutrons in investigating hydrogen-based materials, several application in geomaterials and natural and artificial porous media (*i.e.*, rocks, ceramics, concrete, etc.) are available in literature. In fact, neutron imaging techniques have been used to determine porosity and pore size distribution in crystalline rocks[61] and sandstone[62] in static condition; in addition, dynamic images of water and moisture migration in the porous network of rocks[63-65], ceramics[66,67] and concrete[68] have been collected. In Cultural Heritage and industrial sciences, neutrons have been used to visualize water movements in stones and bricks treated with water repellents[69-71], the uptake of consolidant products[72] and the penetration depth of conservative treatments[73].

2.5 Surface analysis

Beside the investigation of sub-surface features, the understanding of the weathering on exposed surfaces is a key element in building stone conservation studies, as surface represents the direct interface with atmosphere and, therefore, with the weathering agents.

Classical methods finalized to study the surface weathering are usually based on direct observation, thanks to a description of extension and depth of different weathering patterns can be obtained. Among them, the most diffused one in building stone researches is represented by the Fitzner method[74,75]. However, it remains a strictly subjective analysis method, don't allowing an objective quantification of weathering degree. In this framework, the recent development of non-destructive digital image techniques provides a new tool for measuring changes in stone surfaces in response to weathering, assuring a high resolution and the possibility to monitor the measured parameters over the time.

In view of the suitability of the method, it has been largely applied in different research fields, especially in gemomorphology[76-79] and in building stone conservation science[80,81]. Being not destructive, digital imaging can be also used for *in situ* measuring of surface texture in monuments[82-84], as well as in laboratory set-ups in order to monitoring surface change and decay of samples subjected to artificially accelerated weathering tests[85,86].

The acquisition of 2D and/or 3D digital images of exposed surfaces in natural stones allows to highlight their quite complex structure, usually named *surface texture*.

As description, measurement and monitoring of surfaces texture is of great interest in a wide range of material sciences (*i.e.*, from natural stones to manufacture products), the International Standard Organism provides a reference recommendation (ISO 4287: 1997[87]) in which terms, definition and parameters currently used in surface metrology have been defined and standardized. The standard defines the coordinate system in which surface texture parameters are defined, usually represented by rectangular coordinate of a right handed Cartesian set in which the *x axis* provides the direction of trace, the *y axis* lies nominally on the real surface, and the *z axis* is the outward direction from the material to the surrounding.

In this framework, the term *real surface* is referred to the surface limiting the body and separating it from the surrounding medium; the *total surface profile* results from the intersection of the real surface by a specified plane.

On the real surface, profiles and parameters can be extracted and calculated in order to obtain numerical values representative of the surface texture of the studied material.

The basis for digital processing of surfaces consists in the application of profile filters for the subsequent extrapolation of parameters. The first one operation is represented by the extraction of the *primary profile*, defined as the total profile after application of the short wavelength (low pass) filter λs[1].

By a applying a high pass filter that allow to suppress the long-wave component (λc filter[2]) to the primary profile, it is possible to derive the *roughness profile*, from which the most common roughness parameters can be calculated. If larger structures have to be visualized and measured, the surface structures at rather longer wavelengths than the roughness have to be suppressed (λf filter[3]), obtaining therefore the *waviness profile* and the related waviness profile parameters.

The modern standards introduce an important specific concept: the profile geometrical elements consist in peak and valley events. Therefore, by tracing a section of a profile from the point at which it crosses the mean line to the point at which it next crosses the mean line in the same direction (for example, from below to above the mean line), the following can be evaluated (Figure 2.17): *profile peaks*, defined as the part of a profile element that is above the mean line, *i.e.* the profile from where it crosses the mean line in the positive direction until it next crosses the mean line in the negative direction; *profile valleys*, as for peak with the direction reversed; *ordinate value Z(x)*, defined as the height of the assessed profile at any position x (positive or negative depending on the position of the ordinate respect to the x); *profile peak height* Z_p, defined as the distance between the mean line on the x axis and the highest point of the highest profile peak; *profile valley depth* Z_v, representing the distance between the mean line on the x axis and the lowest point of the lowest profile valley; *profile element height* Z_t, defined as the

[1] *This is the filter that defines where the intersection occurs between the roughness and shorter wavelength components present in a surface.*

[2] *This is the filter that defines where the intersection occurs between the roughness and waviness components.*

[3] *This is the filter that defines where the intersection occurs between the waviness and longer wavelength components present in a surface.*

sum of the height of the peak and depth of the valley of the profile element, *i.e.* the sum of Z_p and Z_v.

.

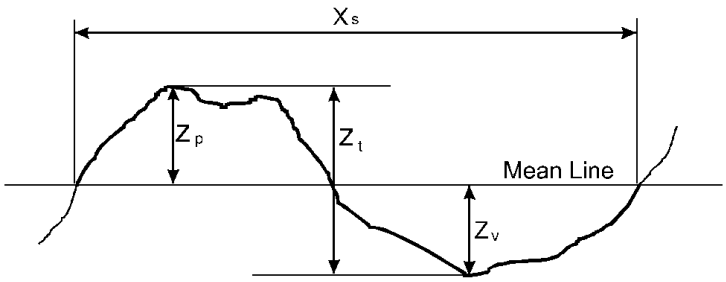

Figure 2.17 - Representation of some profile geometrical elements

Additionally, *amplitude parameters* can be calculated from any profile. The first capital letter in the parameter symbol designates the type of profile under evaluation. For example, R_a is calculated from the roughness profile, W_a from the waviness profile and P_a from the primary profile. They are represented by:

- ✓ *Maximum profile peak height* P_p, R_p, W_p: it is the largest profile peak height Z_p within the sampling length. This measure is the height of the highest point of the profile from the mean line. This parameter is often referred to an extreme-value parameter and can be unrepresentative of the surface as its numerical value may vary so much from sample to sample.
- ✓ *Maximum profile valley depth* P_v, R_v, W_v: it is the largest profile valley depth Z_v within the sampling length. It is the depth of the lowest point on the profile from the mean line and is an extreme value parameter with the same disadvantages as the maximum profile peak height.
- ✓ *Maximum height of profile* P_z, R_z, W_z: it is the sum of the height of the largest profile peak height Z_p and the largest profile valley depth Z_v within a sampling length. R_z does not provide much useful information by itself and is often split into R_p, the height of the highest peak above the mean line, and R_v, the depth of the lowest valley below the mean line.
- ✓ *Total height of profile* P_t, R_t, W_t: it is the sum of the height of the largest profile peak height and the largest profile valley depth within the evaluation length. This parameter is defined over the evaluation length rather than the sampling length.
- ✓ *Arithmetical mean deviation of the assessed profile* P_a, R_a, W_a: it is the arithmetic mean of the absolute ordinate values Z(x) within the sampling length. The R_a of a surface can vary considerably without affecting the performance of the surface. The R_a value does not provide any information as to the shape of the irregularities on the surface. It is possible to obtain similar R_a values for surfaces having very different profiles.

However, for historical reasons, R_a is probably the most common of the all the surface texture parameters.

$$R_a = \frac{1}{n}\sum_{i=1}^{n}|y_i| \qquad (39)$$

- ✓ *Root mean square deviation from the assessed profile P_q, R_q, W_q*: it is the root mean square value of the ordinate values Z(x) within the sampling length.

$$R_q = \sqrt{\frac{1}{n}\sum_{i=1}^{n} y_i^2} \qquad (40)$$

- ✓ *Skewness of the assessed profile P_{sk}, R_{sk}, W_{sk}:* it is the quotient of the mean cube value of the ordinate values Z(x) and the cube of P_q, R_q or W_q, respectively, within the sampling length. The skewness is derived from the amplitude distribution curve; it is the measure of the profile symmetry about the mean line.

$$Z_{sk} = \frac{1}{Rq^3}\left[\frac{1}{n}\sum_{i=1}^{n} Z_i^3\right] \qquad (41)$$

- ✓ *Kurtosis of the assessed profile P_{ku}, R_{ku}, W_{ku}*: it is the quotient of the mean quadratic value of the ordinate values Z(x) and the fourth power of P_q, R_q or W_q, respectively, within the sampling length.

$$Z_{ku} = \frac{1}{Rq^4}\left[\frac{1}{n}\sum_{i=1}^{n} Z_i^4\right] \qquad (4)$$

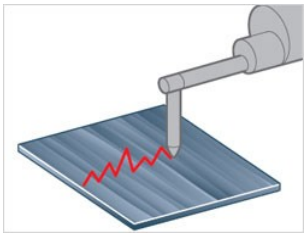

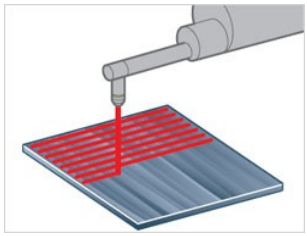

Surface roughness measurement methods include not only linear roughness measurement, which measures a single line on the sample surface, but also areal roughness measurements, from which areal 3D roughness parameters can be extrapolated.

Referring to acquisition mode, there are two ways to measure surface roughness. The instruments for measuring surface roughness can be broadly divided between *contact* and *non-contact types*. In the former, the tip of the stylus directly touches the surface of the sample. As the stylus traces across the sample, it rises and falls together with the roughness on the sample surface. This movement in the stylus is picked up and used to measure surface roughness. The stylus moves closely with the sample surface, so data is highly reliable. In the non-contact type the leading method of this type is light. Light emitted from the instrument is reflected and read, to measure without touching the sample. Various non-

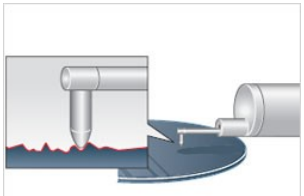

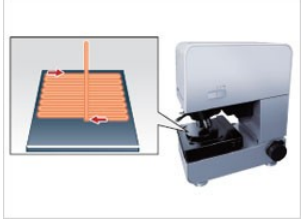

contact systems include the focus detection type, the confocal microscope type, and the interferometer type, and they are, of course, the most suitable ones for building stone conservation studies.

2.6 Bibliography

[1] Moses C, Robinson D, Barlow J. Methods for measuring rock surface weathering and erosion: A critical review. Earth-Science Reviews, 2014. 135: 141–161.

[2] André MF. Rates of Postglacial rock weathering on glacially scoured outcrops (Abisko-Riksgränsen area, 68°N). Geogr. Ann, 2002. 84A: 139–150.

[3] Trudgill ST, Viles H, Inkpen RJ, Cooke RU. Re-measurement of weathering rates, St. Paul's Cathedral, London. Earth Surf. Process. Landf.,1989. 14: 175–196.

[4] Stephenson WJ, Finlayson BL. Measuring erosion with the microerosion meter—contributions to understanding landform evolution. Earth-Sci. Rev., 2009. 95: 53–62.

[5] Williams RGB, Swantesson JOH, Robinson DA. Measuring rates of surface down wearing and mapping micro topography: the use of micro-erosion meters and laser scanners in rock weathering studies. Z. Geomorphol., 2000. 120: 51–66.

[6] Rautureau M, Cooke RU, Boyde A. The application of confocal microscopy to the study of stone weathering. Earth Surface Processes and Landforms, 1993. 18: 769–775.

[7] de los Ríos A, Ascaso C. Contributions of in situ microscopy to the current understanding of stone biodeterioration. Int. Microbiol., 2005. 8: 181–188.

[8] Banfield JF, Eggleton RA. Transmission electron microscope study of biotite weathering. Clays and Clay Minerals, 1988. 36(1): 47–60.

[9] Cnudde V & Boone MN. High-resolution X-ray computed tomography in geosciences: a review of the current technology and applications. Earth-Science Reviews, 2013. 123:1–17.

[10] Giesche H. Mercury Porosimetry: A General (Practical) Overview. Part. Part. Syst. Charact., 2006. 23: 9–19.

[11] Leòn y Leòn AC. New perspectives in mercury porosimetry. Advances in Colloid and Interface Science, 1998. 76-77:341-372.

[12] Rouquerol J, Avnir D, Fairbridge CW, Everett DH, Haynes JH, Pernicone N, Ramsay JDF, Sing KSW, Unger KK. Recommendations for the characterization of porous solids (technical report). Pure Appl. Chem., 1994. 66:1739-1758.

[13] Laplace PS. Mechanique Celeste, Supplement to Book 10, 1806.

[14] Young T. In: Peacock G (Eds), Miscellaneous Works, 1, J. Murray, London, 1855.

[15] Washburn EW. The Dynamics of Capillary Flow. Phys. Rev, 1921. 17:273.

[16] Wardlaw NC, McKellar M. Mercury Porosimetry and the Interpretation of Pore Geometry in Sedimentary Rocks and Artificial Models. Powder Technol., 1981. 29:127–143.

[17] Giesche H. Interpretation of Hysteresis “Fine-Structure” in Mercury-Porosimetry Measurements. In: Komarneni S et al. (Eds) Advances in Porous Materials, Mat. Res. Soc. Symp. Proc., 371, MRS, Pittsburgh, 1995, 505–510.

[18] Lowell S, Shields JE. Powder Surface Area and Porosity, Chapman and Hall, New York,1991.

[19] Lowell S, Shields J.E. Theory of mercury porosimetry hysteresis. Powder Technol., 1984, 38:121-124

[20] Lowell S, Shields J.E. Hysteresis, entrapment, and wetting angle in mercury porosimetry. Colloid Interf. Sci., 1981. 83:273-278.

[21] Carniglia SC. Construction of the tortuosity factor from porosimetry. J. Catal.,1986. 102:401-418.

[22] Dunn KJ, Bergman DJ, LaTorraca GA. Nuclear Magnetic Resonance: Petrophysical and Logging Applications. Helbig K, Treitel S (Eds). Elsevier, PERGAMON, 2002.

[23] Hahn L. Spin echoes. Physical Review, 1950. 80: 580-594.

[24] Carr HY, Purcell EM. Effects of Diffusion on Free Precession in Nuclear Magnetic Resonance Experiments. Physical Review, 1954. 94: 630–638.

[25] Meiboom S, Gill D. Modified spin-echo method for measuring nuclear relaxation times. Review of Scientific Instruments, 1958. 29:668-691.

[26] Rata DG, Casanova F, Perlo J, Demco DE, Blümich B. Self-diffusion measurements by a mobile single-sided NMR sensor with improved magnetic field gradient. Journal of Magnetic Resonance, 2006. 180:229-235.

[27] Casanova F, Perlo J, Blümich B, Sigle-Sided NMR, Springer, 2011.

[28] Perlo J, Casanova F, Blümich B, J. Magn. Resonance, 2005, 176:64-70

[29] Perfect E, Cheng CL, Kanga M, Bilheux MZ, Lamanna JM, Gragg MJ, Wright DM. Neutron imaging of hydrogen-rich fluids in geomaterials and engineered porous media: A review. Earth-Science Reviews, 2014. 129:120:135.

[30] Cnudde V & Jacobs PJS. Monitoring of weathering and conservation of building materials through non-destructive X-ray computed micro tomography. Environmental Geology, 2004. 46: 477-485.

[31] Cnudde V, Cwirzen A, Masschaele B, Jacobs PJS. Porosity and microstructure characterization of building stones and concretes. Engineering Geology, 2009. 103:, 76-83.

[32] Cnudde V, Silversmit G, Boone M, Dewanckele J, De Samber B, Schoonjans T, Van Loo D, De Witte Yonib Y, Elburg M, Vincze L., Van Hoorebeke L, Jacobs P. Multi-disciplinary characterisation of a sandstone surface crust. Science Of The Total Environment, 2009.407: 5417-5427.

[33] Cnudde V, Boone M, Dewanckele J, Dierick M, Van Hoorebeke L, Jacobs P. 3D characterization of sandstone by means of X-ray computed tomography. Geosphere , 2011. 7: 54-61.

[34] Cnudde V, Dewanckele J, Boone M, De Kock T, Brabant L, Dusar M, de Ceukelaire M, de Clercq H, Hayen R, Jacobs P. High-Resolution X-Ray CT for 3D Petrography of Ferruginous Sandstone for an Investigation of Building Stone Decay. Microscopy Research And Technique, 2011. 74: 1006-1017.

[35] De Graef B, Cnudde V, Dick J, De Belie N, Jacobs P, Verstraete W. A sensitivity study for the visualization of bacterial weathering of concrete and stone with computerized X-ray microtomography. Science Of The Total Environment, 2005. 341: 173-183.

[36] De Muynck W, Leuridan S, Van Loo D, Verbeken K, Cnudde V, De Belie N, Verstraete W. Influence of pore structure on the effectiveness of a biogenic carbonate surface treatment for limestone conservation. Applied and Environmental Microbiology, 2011. 77: 6808-6820.

[37] Derluyn H, Griffa M, Mannes D, Jerjen I, Dewanckele J, Vontobel P, Sheppard A, Derome D, Cnudde V, Lehmann E, Carmeliet J. Characterizing saline uptake and salt distributions in porous

limestone with neutron radiography and X-ray micro-tomography. Journal of Building Physics, 2013.36:353-374.

[38] Derluyn H, Dewanckele J, Boone MN, Cnudde V, Derome D, Carmeliet J. Crystallization of hydrated and anhydrous salts in porous limestone resolved by synchrotron X-ray microtomography. Nuclear Instruments and Methods in Physics Research B, 2014. 324:102-112.

[39] Dewanckele J, De Kock T, Boone MA, Cnudde V, Brabant L, Boone MN, Fronteau G, Van Hoorebeke L, Jacobs P. 4D imaging and quantification of pore structure modifications inside natural building stones by means of high resolution X-ray CT. Science of the Total Environment, 2012. 416: 436–448.

[40] Noriel C, Renard F, Doan ML, Gratier JP. Intense fracturing and fracture sealing induced by mineral growth in porous rocks. Chemical Geology, 2010. 269: 197-209.

[41] Ruiz de Argandoña VG, Rodríguez Rey A, Celorio C, Suárez del Río LM, Calleja L, Llavona J. Characterization by computed x-ray tomography of the evolution of the pore structure of a dolomite rock during freeze-thaw cyclic tests. Physics and chemistry of the earth part A – solid earth and geodesy, 1999. 24: 633-637.

[42] Ketcham RA & Carlson WD. Acquisition, optimization and interpretation of X-ray computed tomographic imagery: applications to the geosciences. Computers & Geosciences, 2001. 24: 381-400.

[43] Barone G, Crupi V, Longo F, Majolino D, Mazzoleni P, Raneri S, Teixeira J, Venuti V. Neutron radiography for the characterization of porous structure in degraded building stones. Journal Instrumentation, 2014.9: C05024.

[44] Cnudde V, Dierick M, Vlassenbroeck J. Masschaele B, Lehmann E, Jacobs P, Van Hoorebeke L. Determination of the impregnation depth of siloxanes and ethylsilicates in porous material by neutron radiography, Journal of Cultural Heritage, 2007. 8:331-338

[45] Dierick M, Vlassenbroeck J, Masschaele B, Cnudde V, Van Hoorebeke L, Hillenbach A. High-speed neutron tomography of dynamic processes, Nucl. Instrum. Methods Phys. Res. A, 005. 542: 296–301.

[46] Hameed F, Schillinger B, Rohatsch A, Zawisky M, Rauch H. Investigation of stone consolidation by neutron imaging, Nucl. Instrum. Methods Phys. Res, 2009. A605:150–153.

[47] Masschaele B, Dierick M, Van Hoorebeke L, Cnudde V, Delputte S, Gildemeister A, Gaehler R, Hillenbach A. High speed thermal neutron tomography for the visualization of water repellents, consolidants and water uptake in sand and limestone, Radiat. Phys. Chem., 2004. 71:807–808.

[48] Attix F.H. Introduction to radiological physics and radiation dosimetry. Wiley-VCH, 1986.

[49]Knoll GF. Radiation Detection and Measurement. J. Wiley & Sons. 2000.

[50] Paul Scherrer Institute. Neutron Imaging. How neutrons create pictures. Villigen PSI, 2007, p. 9.

[51]Herman GT. Image reconstruction from projections: The fundamentals of computerized tomography. Computer science and applied mathematics. Academic Press, New York, 1980.

[52]Herman GT, Natterer F. Mathematical aspects of computerized tomography. Springer-Verlag, 1981.

[53] Kak AC, Slaney M. Principles of computerized tomographic imaging. IEEE Press, New York, 1988.

[54] Ketcham RA. Computational methods for quantitative analysis of three-dimensional features in geologic specimens. Geosphere, 2005.1: 32-41.

[55] Brun F, Mancini L, Kasae P, Favretto S, Dreossi D, Tromba G. Pore3D: A softwarelibrary for quantitative analysis of porous media. Nuclear Instruments & Methods in Physics Research, Section A: Accelerators, Spectrometers, Detectors, and Associated Equipment, 2010.615: 326-332.

[56] Lindquist WB. Quantitative analysis of three dimensional X-ray tomographic images. In: U. Bonse (Eds), 3rd Conference on Developments in X-Ray Tomography. Spie-Int Socoptical Engineering, San Diego, CA, 2001. 103-115.

[57] Brabant L, Vlassenbroeck J, De Witte Y, Cnudde V, Boone MN, Dewanckele J, Van Hoorebeke L. Three-dimensional analysis of high-resolution X-ray computed tomography data with Morpho+. Microscopy and Microanalysis, 2011. 17: 252-263.

[58] Vlassenbroeck J, Dierick M, Masschaele B, Cnudde V, Van Hoorebeke L, Jacobs P. Software tools for quantification of X-ray microtomography at the UGCT. Nuclear Instruments & Methods in Physics Research, Section A: Accelerators, Spectrometers, Detectors and Associated Equipment, 2007.580: 442-445.

[59] Schlindelin J, Arganda-Carreras I, Frise E, Kaynig V, Longair M, Petzsch T, Preibisch S, Rueden C, Saalfeld S, Schmid B, Tenevez JY, White DJ, Hartenstein V, Eliceiri K, Tomancak P, Cardona A. Fiji: an open-source platform for biological-image analysis. Nature Methods, 2012. 9(7): 676-682.

[60] Kyrieleis A, Titarenko V, Ibison M, Connolley T, Withers PJ. Region-of-interest tomography using filtered back projection: assessing the practical limits. Journal of Microscopy, 2011.241(1): 69-82.

[61] Pleinert H, Degueldre C. Neutron radiographic measurement of porosity of crystalline rock samples, a feasibility study. J. Contam. Hydrol., 1995. 19: 29–46.

[62] de Beer FC, Middleton MF. Neutron radiography imaging, porosity and permeability in porous rocks. S. Afr. J. Geol., 2006. 109:541–550.

[63] Jasti JK, Fogler HS. Application of neutron radiography to image flow phenomena in porous media. AIChE J, 1992. 38: 481–488.

[64] Hassanein R, Meyer HO, Carminati A, Estermann M, Lehmann E, Vontobel P. Investigation of water imbibition in porous stone by thermal neutron radiography. J. Phys. D, 2006.39: 4284–4291.

[65] Cnudde V, Dierick M, Vlassenbroeck J, Masschaele B, Lehmann E, Jacob P, Van Hoorebeke L. High-speed neutron radiography for monitoring the water absorption by capillarity in porous materials. Nucl. Instrum. Methods Phys. Res. B., 2008.266: 155–163.

[66] Prazak J, Tywoniak J, Peterka F, Slonc T. Description of transport of liquid in porous media —a study based on neutron radiography data. Int. J. Heat Mass Transfer, 1990.33: 1105–1120.

[67] Pleinert H, Sadouki H, Wittmann FH. Determination of moisture distributions in porous building materials by neutron transmission analysis. Mater. Struct., 1998. 31:218–224.

[68] Zeilinger A, Huebner R. Moisture transport in a concrete of the SNR 300 investigated by neutron transmission. Kerntechnik Z. Ing. aller Fachrichtungen, 1976. 18:119–125.

[69] Masschaele B, Dierick M, van Hoorebeke L, Cnudde V, Jacobs P. The use of neutrons and monochromatic X-rays for non-destructive testing in geological materials. Environ. Geol., 2004. 46:486–492

[70] Dierick M, Vlassenbroeck J, Masschaele B, Cnudde V, van Hoorebeke L, Hillenbach A. High-speed neutron tomography of dynamic processes. Nucl. Instrum. Methods Phys. Res. A, 2005. 542:296–301.

[71] Nemec T, Rant J, Apih V, Glumac B. Study of building materials impregnation processes by quasi-real-time neutron radiography. Nucl. Instrum. Methods Phys.Res. A, 1999. 24: 242–247.

[72] Zawisky M, Hameed F, Dyrnjaja E, Springer J, Rohatsch A. Digitized neutron imaging with high spatial resolution at a low power research reactor: applications to steel and rock samples. Nucl. Instrum. Methods Phys. Res. Sect. B, 2010. 268:2446–2450.

[73] Prudencio MI, Pereira MAS, Marques JG, Dias MI, Esteves L, Burdridge CI, Trindade MJ, Albuquerque MB. Neutron tomography for the assessment of consolidant impregnation efficiency in Portuguese glazed tiles (16^{th} and 18^{th} centuries). J. Archaeol. Sci., 2012. 39: 964–969.

[74] Fitzner B, Heinriehs K, Kownatzki R. Weathering forms at natural stone monuments–classification, mapping and evaluation. Int J Restorat Build Monuments, 1997. 3(2):105–24.

[75] Fitzner B, Heinrichs K, La Bouchardiere D. Damage index for stone monuments. In: Protection and conservation of the cultural heritage of the Mediterranean Cities. Swets & Zeitlinger, Lisse: A.A. Balkema Publishers; 2002. p. 315–26.

[76] Robinson DA, Williams RBG. Sandstone Weathering and landforms in Britain and Europe. In: Williams RBG, Robinson DA (Eds.). Rock weathering and Landform Evolution. Wiley, 1994, pp. 371–392.

[77] Robinson DA, Williams RBG. The weathering of Hastings Beds sandstone gravestones in south east England. In: Jones, M.S., Wakefield, R.D. (Eds.), Aspects of Stone Weathering, Decay and Conservation. Imperial College Press, London, 1999, pp. 1–15.

[78] Swantesson JOH. Micro-mapping as a tool for the study of weathered rock surfaces. In: Robinson, D.A.,Williams, R.B.G. (Eds.), Rock weathering and Landform Evolution. Wiley, 1994, pp. 209–222.

[79] McCarroll D, Nesje A. Rock surface roughness as an indicator of degree of rock surface weathering. Earth Surf. Process. Landf., 1996. 21: 963–977.

[80] Robinson DA, Williams RBG. An analysis of the weathering of Wealden sandstone churches. In: Smith, B.J., Warke, P.A. (Eds.), Processes of Urban Stone Decay. Donhead, London, 1996, pp. 133–149.

[81] Cecchi G, Pantani L, Raimondi V, Tomaselli L, Lamenti G, Tiano P, Chiari R. Fluorescence lidar technique for the remote sensing of stone monuments. J. Cult.Herit., 2000. 1: 29–36.

[82] Sharp D, Trudgill ST, Crooke RU, Price CA, Crabtree RW, Pickles AM, Smith D. Weathering of the Balustrade on St Paul's Cathedral, London. Earth Surface Processes and Landforms, 1982. 7: 387-390.

[83] Trudgill ST, Gosling W, Yates T, Collier P, Smith DI, Cooke RU, Viles HA, Inkpen R, Moses C. Twenty-Year Weathering Remeasurements at St Paul's Cathedral, London. Earth Surface Processes and Landforms, 2001. 26: 1129-1142.

[84] Vázquez MA, Galán E, Guerrero MA, Ortiz P. Digital image processing of weathered stone caused by efflorescences: A tool for mapping and evaluation of stone decay. Construction and Building Materials, 2011. 25: 1603–1611.

[85] López-Arce P, Varas-Muriel MJ, Fernández-Revuelta B, Álvarez de Buergo M, Fort R, Pérez-SobaC. Artificial Weathering of Spanish Granites Subjected to Salt Crystallization Tests: Surface Roughness Quantification. Catena, 2010. 83: 170-185.

[86] Birginie JM, Rivas T. Use of a laser camera scanner to highlight the surface degradation of stone samples subjected to artificial weathering. Build. Environ., 2005. 40: 755–764.

[87] ISO 4287 (1997) Geometrical product specifications (GPS) – Surface texture: Profile method – Terms, definitions and surface texture parameters.

Chapter 3. Quantification and visualization of pore structure, surface texture and physical-mechanical futures changes due to salt weathering

3.1 Pore structure modification due to salt weathering

Understanding the behavior of building stones when they are subjected to weathering processes represents an important research field related to the conservation and restoration of Cultural Heritages.

Salt growth is a significant cause of damage for natural stones; in addition to the properties of the salt and the climatic conditions, the effects of salt weathering are strongly related to the structural and textural features of materials. Therefore, detailed knowledge of the internal structure of building stones is fundamental in order to estimate durability and prevent degradation processes.

In this framework, the changes in the porous structure of Sabucina Stone due to salt weathering have been visualized and quantified by using different methodologies (both micro-destructive and non destructive). In detail, mercury intrusion porosimetry measurements have been used in order to obtain information on weathering mechanism occurred in the pore network structure after artificially salts weathering, while the quantification and visualization of pore changes have been obtained by using non-destructive methods as X-ray computed tomography and nuclear magnetic resonance. In addition, the effects on physical proprieties and mechanical resistance of the rocks after salts weathering have been investigated by performing standard tests on samples subjected to different artificial degradation degree with the aim to highlight the influence of microtextural and microstructural modifications related to salt crystallization in the engineering properties of the studied rock. Moreover, the influence of the pore structure changes in fluid flow through porous network of the stone has been studied by using neutron imaging and classical gravimetric standard tests in order to esteem the variation in term of interconnection parameters and visualize the absorption patterns inside the studied stone. Finally, changes in roughness parameters have been esteemed on sample subjected to different degradation degree in order to investigate the surface texture changes related to salts weathering.

The overall of the obtained results have been compared and interpreted according to appropriate empirical models.

3.2 Pore network changes observed by Mercury Intrusion Porosimetry

Mercury intrusion porosimetry tests have been performed on artificially weathered (according to UNI EN 12370) and cleaned samples subjected to 2, 4, 6, 8, 10 and 12 weathering cycles, in order to highlight the difference in pore network arrangement due to salts crystallization over different degradation degree. The distribution of pore size has been determined by using Thermo Electron Porosimeters Pascal 140 and Pascal 240, with maximum pressure of 400 kPa and200 MPa, respectively, on small samples similar in dimension and shape. Data have been processed by using Thermo Scientific SOL.I.D (Solver of Intrusion Data) Software. Measurements have been performed on almost three samples in order to verify the reproducibility of the test; the results have been then interpolated and average pore distribution curves have been obtained for each degradation step.

With the aim to de-noise the original data and produce high-resolution distribution curves, two models have been applied: the *moving average method*, able to rebuilds the experimental data curve considering the average value calculated on a chosen number of points (N can be chosen between 1 and 100 points; in this case 19 value has been used) and the *exponential smoothing*, a mathematical operation that reduces the discrepancy between one point and the next one; for the processing of the data, a Smooth Factor (DF) of 0.8 has been applied.

3.2.1 Weathered samples: degradation mechanism

In Table 3.1 results obtained on weathered samples are summarized, while in Figure 3.1cumulative pore volume vs. pore size and pore size distribution curves (*dV/dlog(R)* vs. pore size) collected for fresh (in red) and weathered samples (gray scale) are shown.

As can be seen in Figure 3.1(a), the total pore volume generally decreases from freshly quarried sample to weathered ones (after 14 cycles), suggesting a decreasing of the global volume accessible to mercury due to the presence of salts crystals; in addition a shift of modal peak of the pore size distribution towards higher pore radius can be observed Figure 3.1 (b), suggesting an enlargement of pores at the end of the weathering process.

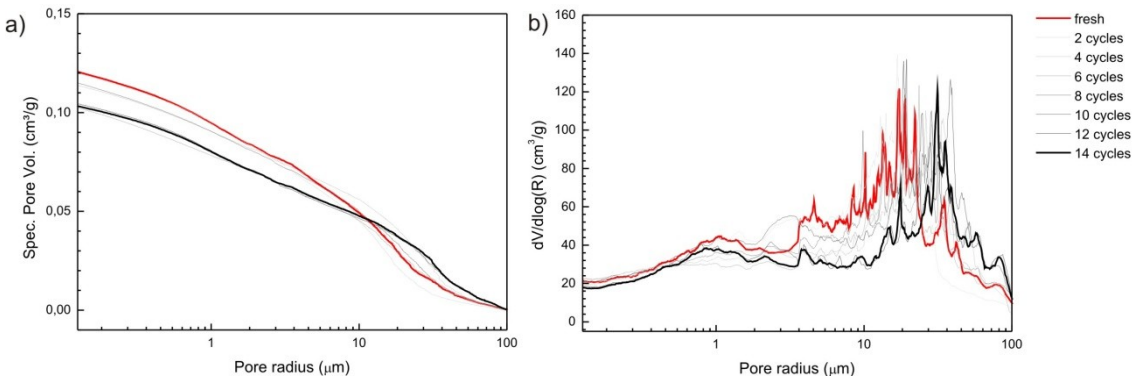

Figure 3.1 - (a) Cumulative pore volume vs. pore size and (b) pore size distribution curves (dV/dlog(R) vs. pore size) collected for fresh (in red) and weathered samples (gray scale)

Table 3.1 - MIP results obtained on fresh and weathered samples

N. cycles (weathered samples)	*Total intruded volume (cm^3/g)*	*Real density (g/cm^3)*	*Apparent density (g/cm^3)*	*Porosity (%)*	*Total surface area (m^2/g)*	*Average pore radius (µm)*	*Modal pore radius (µm)*	*Median pore radius (µm)*
fresh	0.136 (±0.001)	1.98 (±0.05)	2.71 (±0.06)	26.86 (±0.94)	1.89 (±0.20)	0.144 (±0.008)	8.557 (±3.088)	2.249 (±0.119)
2 cycles	0.096 (±0.72)	1.978 (±0.039)	2.698 (±0.047)	26.687 (±0.223)	2.191 (±0.234)	0.124 (±0.011)	7.799 (±1.168)	2.005 (±0.154)
4 cycles	0.126 (±0.014)	2.148 (±0.296)	2.939 (±0.431)	26.860 (±0.609)	1.743 (±0.182)	0.145 (±0.007)	14.693 (±2.81)	3.231 (±0.598)
6 cycles	0.117 (±0.117)	2.056 (±0.036)	2.705 (±0.095)	23.973 (±1.383)	1.739 (±0.210)	0.135 (±0.012)	12.843 (±3.043)	2.653 (±0.256)
8 cycles	0.131 (±0.131)	1.949 (±0.109)	2.614 (±0.163)	25.383 (±3.194)	1.976 (±0.224)	0.132 (±0.010)	11.636 (±2.159)	2.757 (±0.919)
10 cycles	0.150 (±0.008)	1.935 (±0.026)	2.722 (±0.026)	28.933 (±1.230)	2.070 (±0.040)	0.144 (±0.007)	10.395 (±1.614)	2.679 (±0.208)
12 cycles	0.118 (±0.013)	2.045 (±0.067)	2.696 (±0.022)	24.135 (±1.860)	1.299 (±1.102)	0.133 (±0.015)	13.835 (±2.858)	1.978 (±0.041)
14 cycles	0.117 (±0.006)	2.036 (±0.017)	2.671 (±0.030)	23.783 (±1.112)	1.800 (±0.158)	0.130 (±0.005)	12.694 (±3.516)	2.254 (±0.310)

According to Angeli et al., 2007[1] a comparison between fresh and weathered pore size distribution curves (*dV/dlog(R)* vs. pore size) is able to supply information on *weathering mechanism*. In detail, if salt crystals obstruct a pore entry (case 1, Figure 3.2 (a)), the entire volume is seen with a lower diameter (*e.g.*, modal pore radius is low in weathered samples) and the global porosity remains unchanged; otherwise, if salt crystals partially fill a pore(case 2, Figure 3.2(b)), the pore size entry is not modified (*e.g.*, modal pore size is the same for fresh and altered samples) but the global volume will be lower. Finally, if both phenomena arise and salt crystals obstruct a pore entry and partially fill it (case 3, Figure 3.2 (c)), a shift of modal pore size toward lower values and a decrease of global volume can been observed.

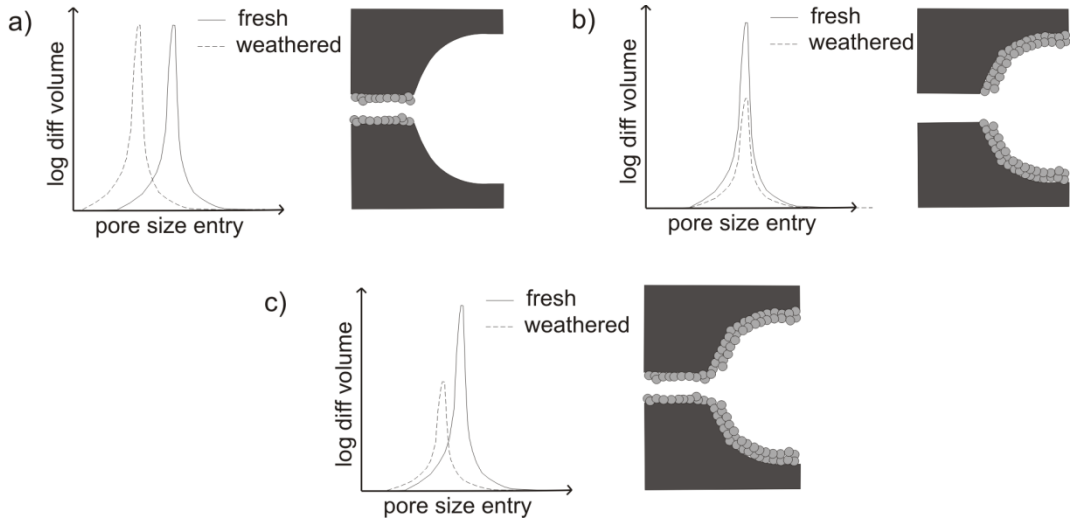

Figure 3.2 - Weathering mechanism due to salts crystallization and porosimetric curves modified from Angeli et al., 2007[1]

For aforementioned, an inspection of pore size distribution curves in weathered samples respect to fresh one (Figure 3.1(b)) allow to understand the pore network modification of stone due to

salts action. In detail, at the second cycle, total pore volume is quite unchanged while modal pore radius is lower than fresh sample; this behavior suggests that, in a first stage, salt crystals obstruct pore entries (case 1). From the fourth weathering cycle, samples show a lower total pore volume values and a shift of modal pore radius towards higher values. These evidences suggest that in weathered samples salts crystals fill pores characterized by larger pore entries than in fresh one, with an enlargement of the throats (case 2 with larger pore entries).

3.2.2 Cleaned samples: location of salts

In Table 3.2 results obtained on cleaned samples are summarized, while in Figure 3.3 cumulative pore volume vs. pore size and pore size distribution curves (*dV/dlog(R)* vs. pore size) collected for fresh (in red) and cleaned samples (gray scale) are shown.

As can be seen in Figure 3.2(a), the total pore volume generally increase from freshly quarried sample to cleaned ones, suggesting in increasing of the global volume accessible to mercury due to the weathering effects and the subsequent removing of salts.

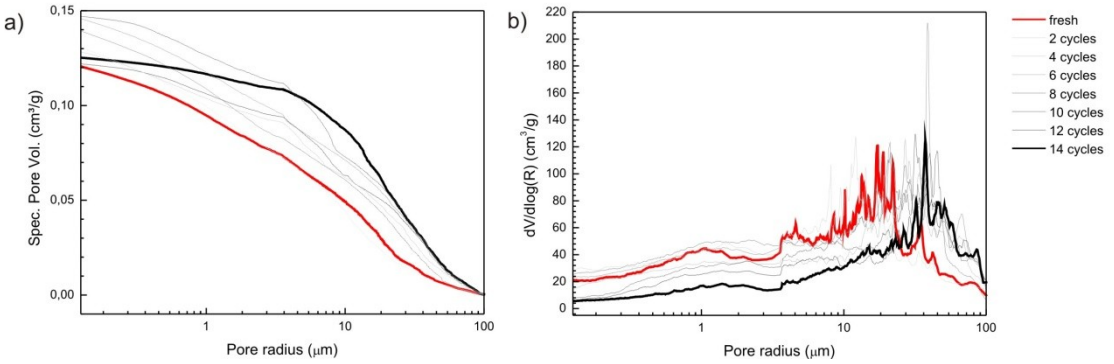

Figure 3.3- (a)Cumulative pore volume vs. pore size and (b) pore size distribution curves (dV/dlog(R) vs. pore size) collected for fresh (in red) and cleaned samples (gray scale)

Table 3.2 - MIP results obtained on fresh and cleaned samples

N. cycles (cleaned samples)	*Total intruded volume (cm^3/g)*	*Real density (g/cm^3)*	*Apparent density (g/cm^3)*	*Porosity (%)*	*Total surface area (m^2/g)*	*Average pore radius (μm)*	*Modal pore radius (μm)*	*Median pore radius (μm)*
fresh	0.136 (±0.001)	1.98 (±0.05)	2.71 (±0.06)	26.86 (±0.94)	1.89 (±0.20)	0.144 (±0.008)	8.557 (±3.088)	2.249 (±0.119)
2 cycles	0.152 (±0.001)	1.888 (±0.039)	2.649 (±0.073)	28.715 (±0.474)	2.783 (±0.195)	0.11 (±0.01)	4.663 (±0.850)	1.553 (±0.271)
4 cycles	0.136 (±0.008)	1.987 (±0.032)	2.720 (±0.014)	26.927 (±1.072)	1.95 (±0.07)	0.139 (±0.011)	12.971 (±1.680)	2.886 (±0.581)
6 cycles	0.161 (±0.013)	1.860 (±0.079)	2.653 (±0.089)	29.913 (±1.411)	2.313 (±0.309)	0.141 (±0.016)	14.957 (±6.231)	3.189 (±0.64)
8 cycles	0.158 (±0.029)	1.9 (±0.1)	2.708 (±0.120)	29.81 (±3.88)	2.413 (±0.580)	0.133 (±0.017)	15.430 (±7.472)	2.157 (±0.165)
10 cycles	0.153 (±0.003)	1.933 (±0.075)	2.743 (±0.131)	29.513 (±0.737)	2.067 (±0.276)	0.149 (±0.017)	16.036 (±2.781)	2.367 (±0.262)
12 cycles	0.127 (±0.01)	2.012 (±0.085)	2.702 (±0.087)	25.567 (±0.961)	1.805 (±0.353)	0.143 (±0.015)	15.926 (±4.155)	2.112 (±0.258)
14 cycles	0.130 (±0.002)	2.020 (±0.076)	2.739 (±0.131)	26.227 (±0.805)	1.695 (±0.066)	0.153 (±0.005)	18.001 (±4.827)	2.264 (±0.596)

The empirical model proposed by Angeli et al., 2007[1]suggests also the possibility to estimate the *location of salts* by comparing weathered and cleaned porosimetric curves and, in detail, identifying the areas where the spectrum of the cleaned stone is over the weathered one.

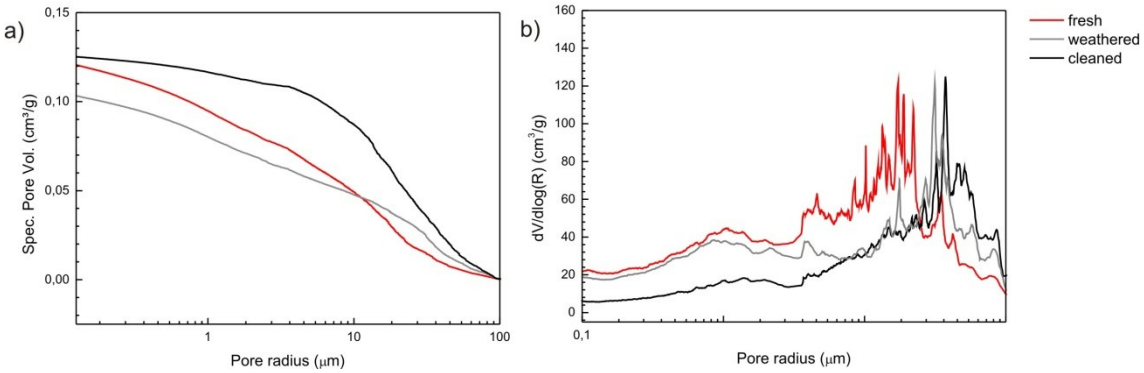

Figure 3.4 - Comparison between fresh (red), weathered (gray) and cleaned (black) samples.

An inspection of pore size distribution curves in weathered (gray) and cleaned stones (black) (Figure 3.4) suggests a location of salts in a range of 50-100 μm. Moreover, a shift of modal pore radius towards higher values is also visible, confirming the decay mechanism hypothesized previously by comparing weathered and fresh stone. In fact, the areas where cleaned spectrum is below weathered one is indicative of obstruction of pore throats by salts, whereas the higher value of total pore volume than fresh stone one highlights a significant enlargement of pores, suggesting a combined weathering mechanism interesting both entry and effective volume of pores.

3.2.3 Final remarks

The investigation of the changes in pore size distribution by using MIP technique allows to highlight interesting features related to salt weathering phenomena. In detail, the obtained results allow us to obtain a good explanation of the degradation style of the stone showed by the mass loss curve (*see Chapter 1, Section 2, Paragraph 2.3.4*); in fact, from the first to the sixth cycles the curve is "salt controlled" (positive mass variation) and the porosimetric curve suggests the crystallization of salts in the entry of pores, while from the seventh cycle the curve is "weathered controlled" (negative mass variation), with an increase of dimension of throats and crystallization of salts inside the enlarged pores.

3.3 Nuclear Magnetic Resonance (NMR) application

In recent years, the use of Nuclear Magnetic Resonance (NMR) as useful tool for studying pore structure in stones has largely increased, also in association with other methodologies[1-6]. In detail, the technique allows to get information about the pore size distribution in a water-

saturated rock by measuring the transverse and longitudinal relaxation times of water hydrogen nuclei in a non-destructive and non-invasive way. Furthermore, the investigation of water diffusion through the porous structure provides information on the restricted geometry of the network as well as on average pore radius and pore interconnection. The main goal of this section is to compare portable NMR and mercury intrusion porosimetry in characterizing pore size distributions of building stones and quantify pore network modification due to salt weathering.

For this study, measurements have been performed at the Laboratory of Nuclear Magnetic Resonance Anna Laura Segre of the Chemical Methodologies Institute of CNR in Rome in the framework of an internship activity. In detail, a single-sided NMR sensor by RWTH Aachen University, Aachen, Germany[7] has been used for the experiments (Figure 3.5). This sensor generates a magnetic field with an extremely uniform gradient (14T/m) to resolve near surface structure of arbitrary large samples. For depth investigation the sample remains on top of the sensor and relaxation time at different depths are acquired by exciting the whole region of interest in a single experiment.

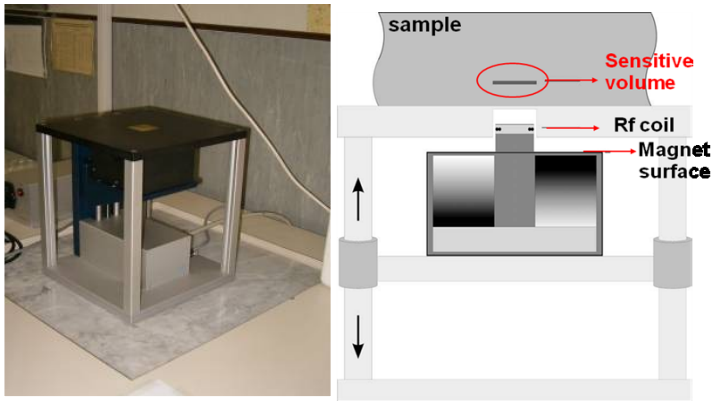

Figure 3.5 - Single-sided NMR sensor by RWTH Aachen University

The sensitive volume is a thin slice above the device, at a distance of 1 cm, parallel to its surface. The sensitive slice is 25x25 mm^2 and the thickness of the sensitive volume can be adjusted from a few to 100 µm and depends on the setting of the measurement parameters.

In the experiment, transverse relaxation times T_2 were measured with the CPMG sequence on 5x5x2 cm fresh and artificially weathered samples (according to UNI EN 12370) at different degradation degree (after eight and fourteen crystallization cycles), with a operating frequency at 13.619 MHz and 90° pulses each 3.5 µs. A total of 4096 echoes were recorded with an echo time of 0.0585 ms.

3.3.1 Transverse relaxation times and distributions

As claimed in the methodological section (*see Chapter 2, section 3*), by using portable NMR it is possible to measure dynamic parameters known as relaxation times which give information closely related to the porosity of the material under study[7,8]. In detail, being $T_2$the time constants of the multi-exponential CPMG decay, transversal relaxation times have a dependence on the degree of confinement of a liquid (water) within a porous structure. Because T_2 depends on the surface-to-volume ratio (see Figure 3.6), water in small pores relaxes rapidly, whereas water in large pores relaxes more slowly.

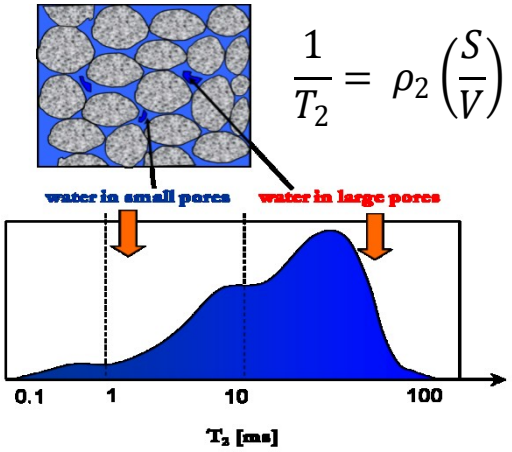

Figure 3.6 - The equation shows the relation between pore distribution and transverse relaxation time, where T2 is the transverse relaxation time resulted from surface interactions, ρ_2 is a constant representing the transverse relaxation strength and S/V refers to the surface to volume ratio of the analyzed solids.

A T_2 distribution corresponds therefore to a pore size distribution with the smallest pores having the shortest relaxation times and the largest pores having the longest relaxation times. The measurement of T_2 of a liquid confined in a porous matrix allows the investigation of the pore size distribution of the studied material, particularly useful in comparing materials showing different degrees of porosity, in investigating the occurrence of degradation processes which may affect the porous structure, and in studying changes of the degree of open porosity which may occur due to treatments.

Referring to the trend of acquired data, the result obtained by applying a CPMG sequence is a mono- or multi-exponential decay of the magnetization vs. the echo time. It is worth noting that in the case of bulk water, a mono-exponential decay is measured, whereas in the case of water confined in a heterogeneous porous structure a multi-exponential decay is measured[9]. The amount of water associated to each T_2 component is defined as the *spin population of that component*. The sum of spin populations is normalized to 100%.

In this experimental session, CPMG decays have been measured on unweatehred and artificially weathered stone samples at eight and fourteen salts crystallization cycles in order to highlight the potential of the method in detecting the modification in pore structure network due to

degradation processes. Measurements have been performed at depths of 400, 700 and 1000 μm from the sample surface.

The experimental data obtained applying the CPMG pulse sequence were fit according to the equation:

$$Y = C_0 + \sum_{i=1}^{n} W_i \cdot e^{\frac{-2\tau}{T_{2i}}} \qquad (42)$$

where *n* is the number of components of the decay of the magnetization, *Wi* is the weight of the *i* component (spin population), C_0 is the offset value which accounts for the noise of the measurement and T_{2i} is the relaxation time of the *i*-component.

A regularized inverse Laplace transformation[11]has been applied to the echo envelopes obtained from the CPMG sequence. After the transformation, data have been represented as a distribution of T_2 relaxation times, where the peaks of the distribution corresponded to the most probable T_2 values and the area of each peak corresponded to the normalized spin population *Wi*.

The results for each sample are reported in Table 3.3, while in Figures 3.7 the T_2 relaxation time distributions obtained at the different depths (400, 700 and 1000 μm) for un-weathered sample are shown.

In fresh sample, beside the presence of a small population (WA, 1% centered at 0.7 ms) in the mesopore range, that could be not related to the effective pore network arrangement of the stone due to set-up reasons, the more populated range is represented by macropores one, in accordance with MIP measurements (see *Chapter 3, Section 2*). The T_2 spectrum distribution of un -weathered sample in macropore range is mainly trimodal, with the presence of three well defined peaks, whose the W_C is the more populated one at almost all investigated depths (*about the 50% of population density is centered at ~10 ms*). Noteworthy is that no significant differences can be observed at the three investigated depths (400, 700 and 1000 μm, respectively), claiming a homogeneity in the pore structure arrangement of the stone in the first mm up to the surface. Finally, a really small population (about 1-4%, W_E) in a greater pore size range has been observed only in spectra acquired closer to the surface.

Table 3.3 - T_2 values and populations density W_i for each relaxation time components for fresh sample at the different depths investigated

Fresh sample	***W_A (%)***	***T_{2A} (ms)***	***W_B (%)***	***T_{2B} (ms)***	***W_C (%)***	***T_{2C} (ms)***	***W_D (%)***	***T_{2D} (ms)***	***W_E (%)***	***T_{2E} (ms)***
400 μm	1	0.7	17	2.05	**46**	**10.33**	32	35.11	1	126.15
700 μm	17	0.15	15	2.37	**40**	**9.5**	34	29.17	4	119.33
1000 μm	17	0.07	24	2.12	**52**	**12.9**	20	43.86		

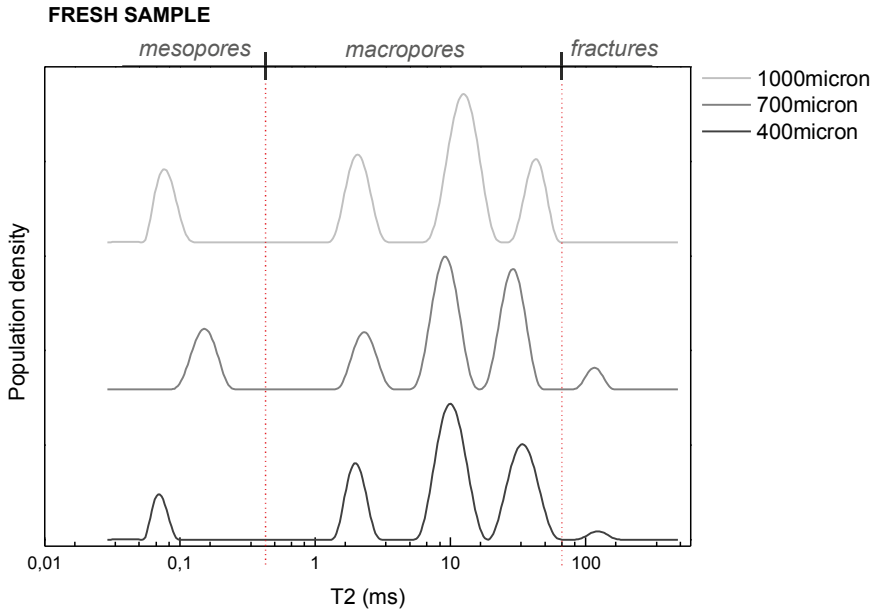

Figure 3.7 - T_2 relaxation time distributions obtained at the different depths (400, 700 and 1000 µm) for unweathered sample

Referring to sample subjected to VIII crystallization cycles, the T_2 distributions (see Table 3.4 and Figure 3.8) highlight the presence of almost three peaks in the macropores range, with the presence of an additionally one in spectra acquired at 400 and 1000 µm depths; moreover, the more populated components are represented by W_C% and W_D%, *covering a range of 10-50 ms*. By comparing the behavior of this sample with the unweathered one, a modification of the pore structure of the stone due to weathering action can be assessed, resulting in higher population densities in correspondence of largest pores having longer relaxation times. Finally, the higher population density detected at 400 µm in the range of longer relaxation times highlights how the surface is greater affected by the weathering process respect to the inner structure.

Table 3.4 - T_2 values and populations density W_i for each relaxation time components for sample subject to VIII salt crystallization cycles at the different depths investigated

VIII cycles	***W_A (%)***	***T_{2A} (ms)***	***W_B (%)***	***T_{2B} (ms)***	***W_C (%)***	***T_{2C} (ms)***	***W_D (%)***	***T_{2D} (ms)***	***W_E (%)***	***T_{2E} (ms)***
400 µm	19	0.1	5	1.65	**29**	**7.4**	**20**	**24.45**	42	62.95
700 µm			18	2.23	**43**	**10.62**	**40**	**50.39**		
1000 µm	8	0.07	20	2.11	**25**	**8.27**	**35**	**22.51**	15	61.23

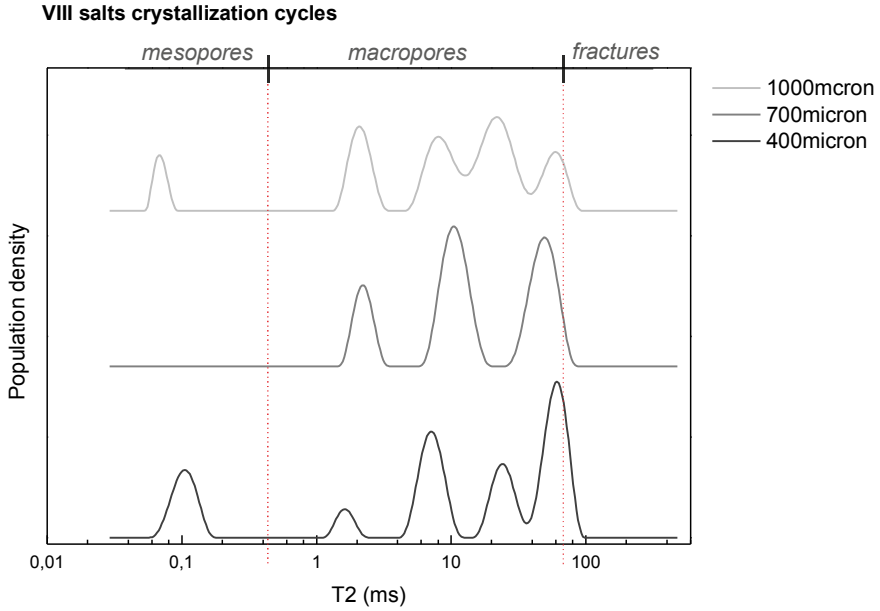

Figure 3.8 - T_2 relaxation time distributions obtained at the different depths (400, 700 and 1000 µm) for sample subjected to VIII crystallization cycles.

In the case of sample subjected to XIV salt crystallization cycles (see Table 3.45 and Figure 3.9), the behavior of the stone is quite similar to sample subjected to VIII crystallization cycles, as the greater population densities are centered at *longer relaxation times, namely 60 ms*. However, in this case, an homogeneity through the investigated depths can be observed, suggesting that, at this step of degradation degree, both surface and sub-surface pore structure is equally affected by the weathering process.

Table 3.5 - T_2 values and populations density W_i for each relaxation time components for subject to XIV salt crystallization cycles at the different depths investigated

XIV cycles	***W_A (%)***	***T_{2A} (ms)***	***W_B (%)***	***T_{2B} (ms)***	***W_C (%)***	***T_{2C} (ms)***	***W_D (%)***	***T_{2D} (ms)***	***W_E (%)***	***T_{2E} (ms)***
400 µm	7	0.07	4	1.18	25	6.99	**70**	**66.55**		
700 µm	13	0.07	19	3.03	31	14.82	**48**	**61.22**		
1000 µm	27	0.07	26	4.46	34	19.04	**33**	**61.22**		

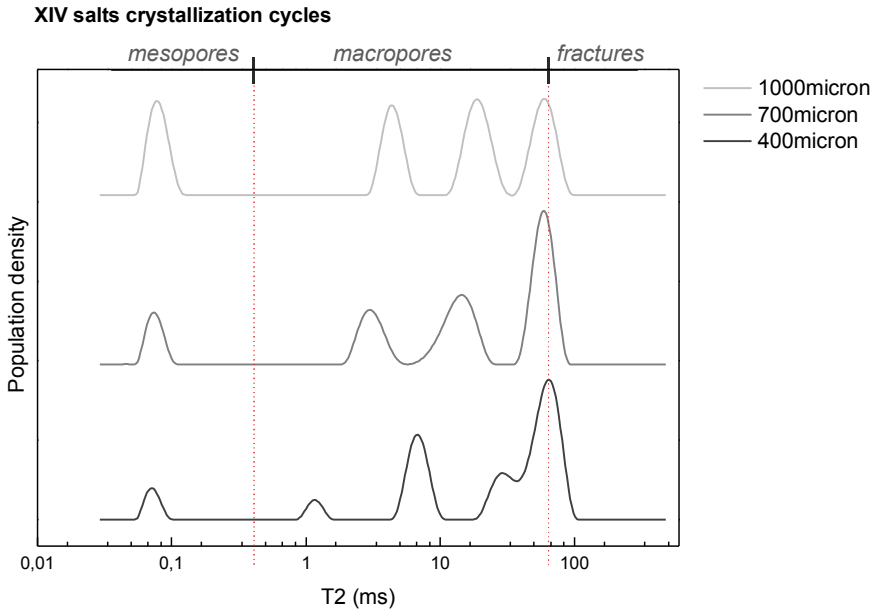

Figure 3.9 - T_2 relaxation time distributions obtained at the different depths (400, 700 and 1000 µm) for sample subjected to XIV crystallization cycles.

In conclusion, by comparing the average depths values of T_2 and populations' density W_i for each relaxation time components collected in fresh and weathered samples (Table 3.6; Figure 3.10), the following statements can be assessed:

- ✓ the decay constant T_2 is proportional to the pore size with small pores characterized by relaxation times shorter than those measured in large pores;
- ✓ Sabucina fresh sample shows a whole of five component of T_2 with the more populated W_i centered in the medium pores size (*about the 50% of population density is centered at ~10 ms*);
- ✓ as the number of weathering cycles increase, the longest component of T_2 (at about *60 ms*) reaches the 40% of the total pore size population, indicating an increasing of the largest pores.

Table 3.6 - T_2 values and populations density W for each relaxation time components for fresh and weathered samples. In bold the most significant variation attributable to weathering action.

Sample ID	W_A (%)	T_{2A} (ms)	W_B (%)	T_{2B} (ms)	W_C (%)	T_{2C} (ms)	W_D (%)	T_{2D} (ms)	W_E (%)	T_{2E} (ms)
fresh sample (NT)	17	0.08	16	2.06	**40**	**10.33**	**25**	**35.10**	2	112.88
8 cycles (N3)	10	0.07	14	2.06	30	8.74	25	27.33	**21**	**68.55**
14 cycles (N6)	16	0.07	5	2.30	18	5.92	18	20.70	**40**	**62.95**

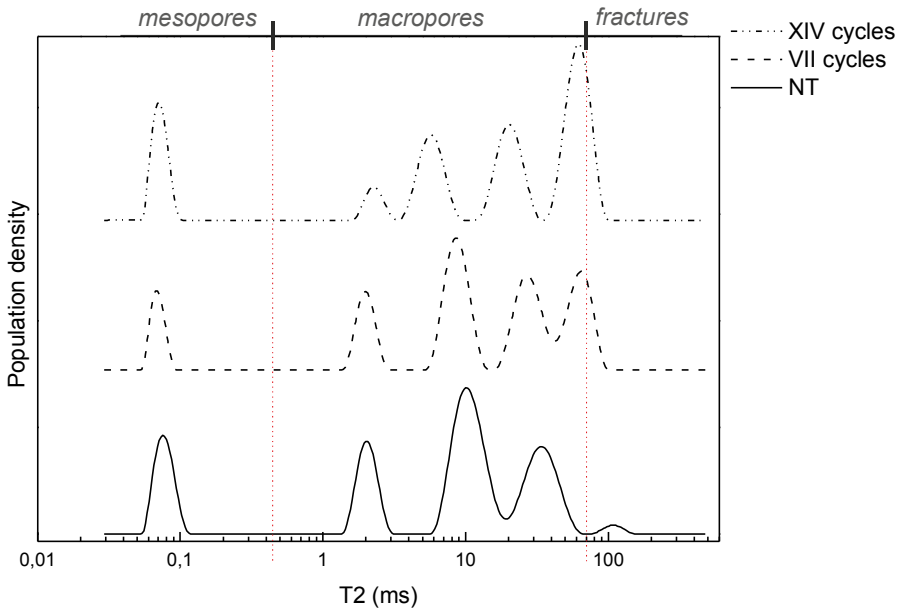

Figure 3.10 - Average T_2 relaxation time distributions for fresh and artificially weathered samples

3.3.2 Final remarks

The obtained data allow to highlight the potential of the applied analytical methods in studying building stone materials. In detail, as shown in Fig. 3.11, the pore size distributions of macropores range analyzed by portable NMR equipment corresponds very well with the result obtained by MIP for both unweathered and weathered samples subjected to eight and fourteen salt crystallization cycles, claiming the highly efficiency of NMR technique in describing in easily-handled, convenient, fast, and, most importantly, non-destructive way changes in pore structure network of building stones due to weathering processes.

This can be considered a really valuable results in the framework of Cultural Heritage studies, as the possibility to obtain suitable information about building stones sub-surface features by using portable equipments whose analytical protocol set in the laboratory can be applied also *in situ*; moreover, as the highly precision of the information obtained by NMR data, the possible inaccurate estimations due to the application of high-pressure intrusion method by mercury (*e.g.* compressibility effects, underestimation effects, uncertainty of results due to mercury entrapment) can be avoided, keeping away also problems related to sampling of specimens and use of not eco-friendly materials for the analysis of stones.

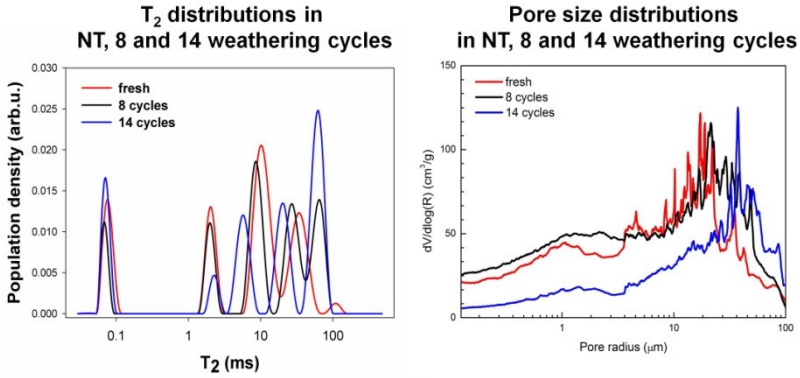

Figure 3.11- Comparison between NMR and MIP data obtained on fresh and artificially weathered samples subjected to eight and fourteen salt crystallization cycles according to UNI EN 12370.

3.4 Changes in physical and mechanical proprieties

Even if a large bibliography exists about durability esteem procedure for building stones[9-15], really a few examples of integrate study on both microtextural, microstructural and physical-mechanical proprieties changes due to salts weathering are available[16,17].

As is well known, physical and mechanical proprieties of rocks represent fundamental knowledge in engineering applications and are strongly influenced by petrographic features such as texture and structure[18-21]. For aforementioned, the knowledge of the relationship among these features allow to better understand the behavior of the stones, especially in the framework of restoration works. In particular, during restoration actions the choice of a replace stone is strictly related to proprieties as availability, aesthetical compatibility, mechanical resistance and durability.

For aforementioned, comparative physical-mechanical tests have been carried after accelerated weathering tests and the obtained results have been compared with the data collected during the preliminary characterization of the stone (see *Chapter 1*), in order to study the eventually changes in physical and mechanical proprieties determined by degradation action by salts.

3.4.1 Physical proprieties changes after salt weathering

Results obtained from hydric tests are able to supply useful information on porous system of stones; in detail, by using data about free (at atmospheric pressure) and forced (under vacuum) water absorption, parameters as interconnection between the pores (A_x[22]) and saturation (S[23]) can be determined. By monitoring changes in these parameters in samples subjected to different degradation degree, the evaluation on the eventually modification of the porous system and about the material capacity to absorb water can be therefore verified[24].

In view of the aforementioned, water absorption tests by total immersion at atmospheric pressure and under vacuum have been performed on samples subjected to salts crystallization

tests (following UNI EN 12370) and previously washed in distilled water in order to remove salts. The A_x and S parameters have been calculated as following:

$$A_x = \frac{A_f - A_b}{A_f} \cdot 100 \quad (43)$$

$$S = \frac{M_{48h} - M_0}{M_S - M_0} \cdot 100 \quad (44)$$

with A_b, free water absorption at atmospheric pressure

$$A_b = \frac{M_L - M_0}{M_0} \cdot 100 \quad (45)$$

A_f, forced water absorption under vacuum

$$A_f = \frac{M_S - M_0}{M_0} \cdot 100 \quad (46)$$

M_L, mass (g) of the sample saturated with water at atmospheric pressure (until constant mass is reached); M_{48h}, mass (g) of the sample after 48 h immersion in water at atmospheric pressure; M_S, mass (g) of the sample saturated under vacuum.

An inspection of the obtained results (see Table 3.7) highlights an increasing of saturation coefficient, with no substantial changes in the interconnection among pores. Therefore, even if weathered samples absorb much more water than the unweathered ones, the ability of the stone to vehicle moisture is maintained quite unaltered by salts crystallization process.

Table 3.7 - Free water absorption at atmospheric pressure and under vacuum, interconnection between the pores and saturation parameters obtained for fresh and weathered samples

	Fresh	***Weathered***			
Parameters		***4 cycles***	***8 cycles***	***12 cycles***	***15 cycles***
A_b	12,95	12,63	12,74	13,10	12,86
A_f	16,68	16,16	16,24	16,84	16,36
A_x	22,44	21,92	21,66	22,14	21,39
S	71,80	72,75	73,62	73,21	77,47

3.4.2 Mechanical proprieties changes after salt weathering

The mechanical properties of weathered stone samples, and in particular the Uniaxial Compressive Strength (UCS), density and ultrasonic velocity have been estimated through laboratory tests according to standard recommendations on artificially weathered samples on Sabucina Stone (according to UNI EN 12370) in order to highlight the eventually changes in mechanical proprieties due to salt crystallization in the studied material.

UCS, which is considered one of the basic geomechanical parameters for the characterization of a rock, has been measured on 13 specimens subjected to different salts weathering cycles according to UNI EN 1926[25]. The propagation speed of longitudinal ultrasonic waves has been measured for each specimen according to the European recommendation NORMAL 22/86[26]along three directions (x, y and z), arbitrarily chosen since neither preferential orientation in the quarry, nor sedimentary planes in the stone were observed. The test has been performed by a pulser/receiver device (M.A.E. A5000U) and a couple of transducers operating at 200 kHz, allowing the input of the sound energy in the specimen and the measurement of its travel time. Finally, information on real and apparent density and porosity has been obtained following UNI EN 1936 standard[27].

The obtained results (Table 3.8, Fig. 3.12) suggest that the variation on structural arrangement after salt crystallization in pores greatly influences the physical proprieties and the mechanical behavior of the stone.

In fact, a decrease of real density determined by pycnometer method (Fig. 3.12 (a)) and total porosity (Fig. 3.12(b)) can be observed; in detail, the decrease of total porosity is due to the presence of salts filling the pores, while referring to real density, such behavior has to be correlated to the dissolution of salts during the water pycnometer measurements and the consequently increasing of porosity in the range below 30 μm inside the powered material used for the test. In addition, a decrement of ultrasound velocity (Fig. 3.12 (c)) has been observed, especially up to the 6thsalt crystallization cycle, due to the occurring of macro- and micro-fractures generated by the growth of salts within the pore network. Finally, a slight and irregular increasing of compressive strength can be observed (Fig. 3.12 (d)).

About to the latter one aspect, a correlation between the change in mechanical behavior of the stone and the modification of the degradation mechanism determined by porosimetric analyses has been observed (*see Chapter 3, Section 1*). In fact, up to the 2ndto the 4th crystallization cycles, salts fill the pore throats, determining a slight and progressive increment of compressive strength resistance. Otherwise, when the enlargement of the throats and the filling of the pores have occurred (*i.e.* up to 6thcrystallizationcycle) a decrease of UCS values has been observed, claiming a strictly relation between the location of salts and the mechanical resistance of the stone.

The presence of salts in the pore network modifies also the mechanical behavior of the stone, from quasi-brittle to quasi-plastic. On the contrary, the removal of salts from the samples(residuals in Fig. 3.12) determine a significant worsening of physical and mechanical proprieties, due to an intense degradation action, as testified by accelerated aging tests previously performed.

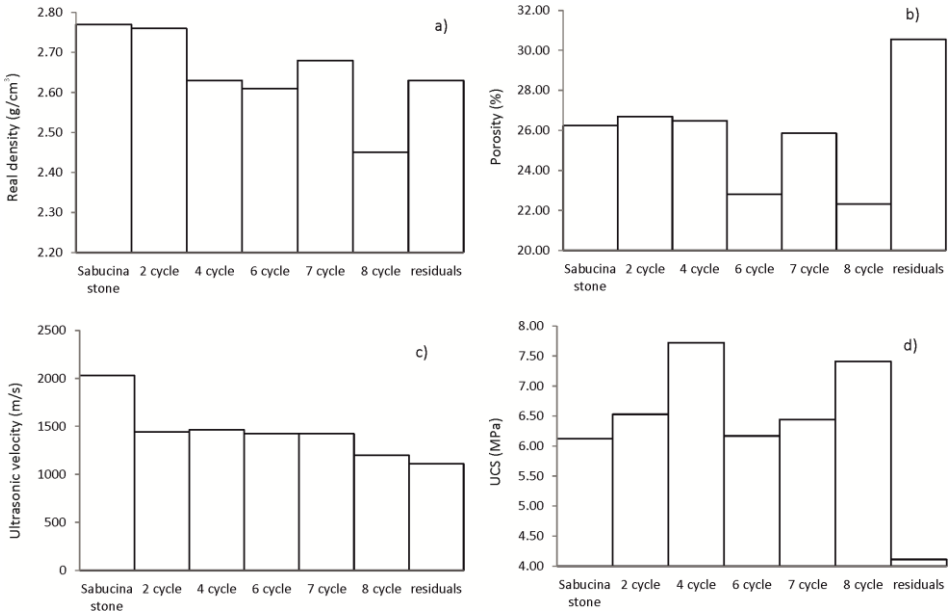

Figure 3.12 - Variation of average values of (a) real density (g/cm3); (b) porosity (%); (c) ultrasonic velocity (m/s) and (d) UCS (MPa) parameters in function of weathering cycles.

Table 3.8 - Average values of the main physical-mechanical parameters of Sabucina Stone at different salt weathering cycles.

Samples	***Apparent density (g/cm^3)***	***Real density (g/cm^3)***	***Ultrasonic velocity (m/s)***	***Porosity (%)***	***UCS (MPa)***
Fresh	2.04	2.77	2028.01	26.24	6.12
2 cycles	2.02	2.76	1443.50	26.70	6.53
4 cycles	1.94	2.63	1463.00	26.47	7.72
6 cycles	2.01	2.61	1423.67	22.81	6.17
7 cycles	1.97	2.68	1423.67	25.85	6.44
8 cycles	1.90	2.45	1200.00	22.32	7.41
Residuals	1.83	2.63	1110.88	30.55	4.11

3.4.3 Final remarks

The measurements performed on samples after weathering degradation process and the comparison of the obtained data with fresh samples ones allow to highlight how the porosimetric changes observed through MIP analysis affect also the physical-mechanical properties of the studied rock.

In fact, the obtained values of interconnection and saturation parameters suggest that salts crystallization process influences the hydric proprieties of stone in term of amount of water absorbed, as testified by the increasing of saturation coefficient with the advancement of degradation degree, even if no substantial changes in ability to vehicle moisture have been observed (the interconnection among pores is quite constant for all samples).

Referring to physical parameters, a globally decrease of density and ultrasound velocity can be observed, especially from the 6th salt crystallization cycle, even if a non homogeneous trend may be delineated. Finally, about compressive strength, the irregular increasing of UCS values in samples with salts and the subsequently decrease of them can be explained only thanks to a deepened knowledge of the weathering mechanism occurred into the pore network of the stone. In addition, the significant decrease of UCS values after cleaning the stone strongly suggests the necessity to remove salts from weathered samples in order to have a correct esteem of mechanical proprieties in degraded stones.

3.5 Pore structure changes quantified by using X-ray computed μ-CT[28]

The durability of natural building stones is a current issue in geological, engineering and conservation fields from the perspective of preserving Cultural Heritage. Estimation of durability is strongly related to several features of rocks, namely mineralogical, petrographic, chemical, textural and mechanical characteristics, and especially to their physical proprieties, including pore structure[29].

Usually, in order to evaluate the durability of natural stones, accelerated aging tests, such as frost resistance (UNI EN 12371), resistance to ageing by SO_2 action in the presence of humidity (UNI EN 13919), resistance to ageing by thermal shock (UNI EN 14066), and resistance to ageing by salt mist (UNI EN 14147) and by sodium sulphate solutions (UNI EN 12370) are carried out on fresh samples. Sodium sulphate is one of the most deleterious salts in regard to damage to porous materials[30]. Moreover, numerous durability estimates are described in the recent literature based on physical, mechanical and porosimetric parameters[31]. Finally, investigations on the pore structure are essential for the correct use of protective products, especially those based on nanomaterials[32].

During accelerated aging tests, however, evaluation of the weathering behavior of stones is mainly based on visual inspection, and only a few non-destructive, quantitative analyses of inner micro-structural modification are available (*e.g.*, sound propagation tests[33]). Furthermore, although the origin of the extensive damage caused by sodium sulphate in durability testing is well known (i.e., hydration and crystallization stress[34]), the comprehension of how salt crystallization modifies the complex porous network of a stone is incomplete[35].

In recent years, many researchers have focused on non-invasive and non-destructive imaging techniques as powerful tools to investigate the internal structure of geomaterials[36,37]. In particular, the use of X-ray micro-tomography (X-ray μCT) has been successfully applied in studying natural building stones[38-50].

In this experimental study, X-ray μCT has been used to visualize and quantify the structural changes in the pore network, by comparing fresh quarried and artificially salt-weathered samples at different degrees of degradation.

In detail, cylindrical samples with a diameter of 7 mm drilled from the 4 cm wide samples subjected to UNI EN 12370 as described above have been scanned at the Centre for X-ray Tomography (UGCT; Ghent University, Belgium)[51]. The analyses have been carried out on two fresh and four degraded cubes 4 cm wide, the latter ones subjected to four, eight, twelve and fifteen salts crystallization cycles, respectively. All the cubes have been sampled from the same fresh quarried block.

For both fresh and weathered samples a total of 1201 projections were acquired over an angle of 360° with a source-detector distance of 1165 mm and a source-object distance of 22 mm, resulting in a voxel size of 7.5 μm. The acquisition time was 999 ms per frame. A voltage of 120 kV was imposed with a power of 10 W and 83 μA tube current. A thin Al-filter (1 mm) was used to block the low-energetic X-rays to prevent beam hardening. The total period of time for one scan was around 30 minutes.

The obtained raw CT data have been reconstructed with the UGCT Octopus software[52]. For the reconstruction the same parameters, like beam hardening correction, normalization, ring and spot filter, exposure time and amount of frames were used.

For 2D analysis ImageJ[53] software has been used. In particular, the 2D reconstructed slices of the fresh sample and the weathered ones have been analyzed by using the plug-in NeuronJ in the ImageJ software that allows drawing fractures and analyzing their features.

Finally, for 3D visualizations and for 3D quantification of pore network features VGStudio MAX (Volume Graphics) and the UGCT software tool Morpho+[54] have been used, respectively. It is worth of noting that to evaluate ED and MO, only objects with a minimum of 3 voxels were retained for analysis.

3.5.1 2D image analysis

Salt crystallization is often responsible for the development of a system of fractures, micrometric in dimension, which cause loss of material during the accelerated aging tests. In order to study the fracture systems and highlight the possible variation of their features with increasing number of weathering cycles, a 2D-image analysis of tomographic slices has been carried out. For each sample, a total of ten slices selected in the central part of the specimens has been analyzed; after drawing the fractures, the number, length and orientation have been calculated. The fractures are represented on 2D reconstructed slices in (Figure 3.13(a)). Moreover, the obtained results have been processed with the software Open Rose with the aim of obtaining the frequency of fractures in a given orientation. The overall data suggest that the salt-crystallization process causes the development of two main fracture systems, which exhibit an angle of ~110° with each other (Figure3.13 (b)). However, during the fifteenth salt crystallization cycle, additional fractures with no preferred orientation have developed. It is worth noting that fractures decrease in number and increase in length from four to eight

crystallization cycles, after which they increase in number and decrease in length until the fifteenth cycle (Table 3.9).

This behavior suggests that in the early stage of the weathering process salts are responsible for the formation of a great number of fractures of a short length. With increasing weathering cycles the fractures propagate and coalesce, resulting in an increased fracture length. At the end of the accelerated aging test, samples show a greater number of fractures than in previous cycles, with an average length of 1100 µm.

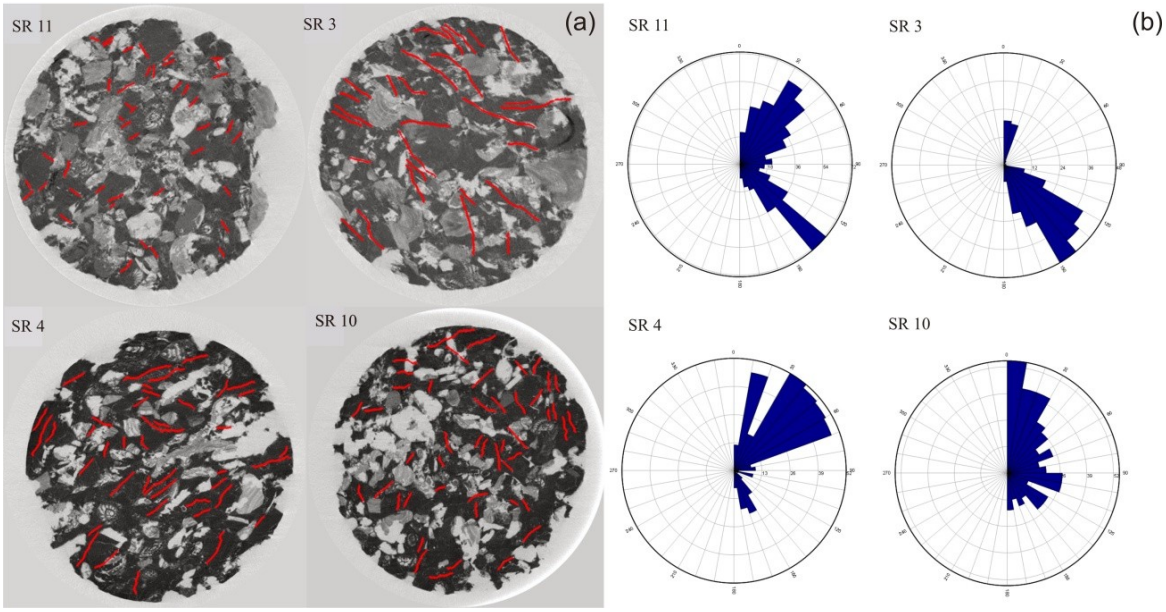

Figure 3.13 - (a)Drawing of fractures on 2D-reconstructed slices by using NeuronJ; cracks have been indicated with red lines (b) Rose diagram for analyzed samples, representing the frequency of fractures in a given orientation.

Table 3.9 - Features of fractures in analyzed samples.

Samples ID	***Salt crystallization cycles***	***Number of fractures average on 10 slices***	***Average number of fractures for each slice***	***Length of fractures (µm) average on 10 slices***	***Systems and orientation***
SR1a	fresh	N=102	9	1002	poorly oriented
SR11	4	N=566	51	606	two main systems of fractures; angle of 100° with each other
SR3	8	N=255	23	2697	two main systems of fractures; angle of 140° with each other
SR4	12	N=371	33	1460	two main systems of fractures; angle of 110° with each other
SR10	15	N=444	40	1121	only one preferential orientation

3.5.2 Open, closed and total porosity

Open (interconnected pore space), closed (isolated pores) and total porosity (sum of the two before) have been calculated for fresh and weathered cleaned samples by using Morpho+

software with the aim of quantifying the changes in pore network structure after the salt crystallization degradation process. The obtained results are valid in the pore size range > 7.5 μm. Pores which are interconnected by throats below this value will be recognized as closed porosity.

Figure 3.14 displays the changes in open, closed and total porosity for fresh and degraded samples. On the whole, the total porosity increases with the degree of weathering (i.e., from 11.30% in a fresh sample to 15.19% after 15 weathering cycles), with the creation of cracks and enlargement of pores. In detail, the open porosity increases from 9.78% to 14.44% over the crystallization cycles, whereas the closed porosity decreases with the induced degradation (i.e., from 1.50% in a fresh sample to 0.75% after 15 crystallization cycles). This behavior is visualized in the 3D-image reconstructions (Fig. 3.15) in which the bulk is shown in grey and the pore structure in red and blue; in detail, the blue structures represent closed porosity, whereas the red colors show the open porosity.

The open porosity obtained by using image analysis is smaller than the effective porosity measured by EN 1936 (28.67 vol %). In fact, pore sizes smaller than three times voxel resolution and larger than the sample size are both excluded from the measurements. However, micro-CT analysis allows quantifying changes at the pore scale of the analyzed size range.

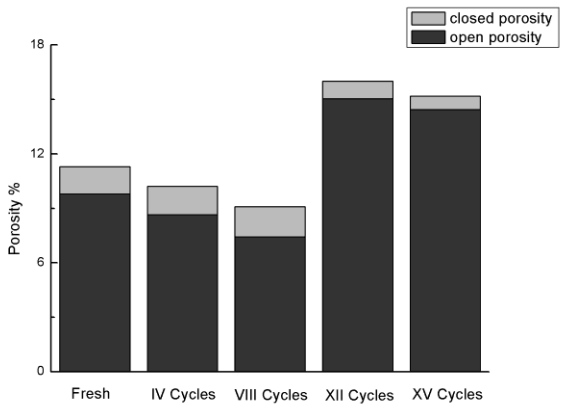

Figure 3.14 - Changes in open, closed and total porosity for fresh and weathered samples.

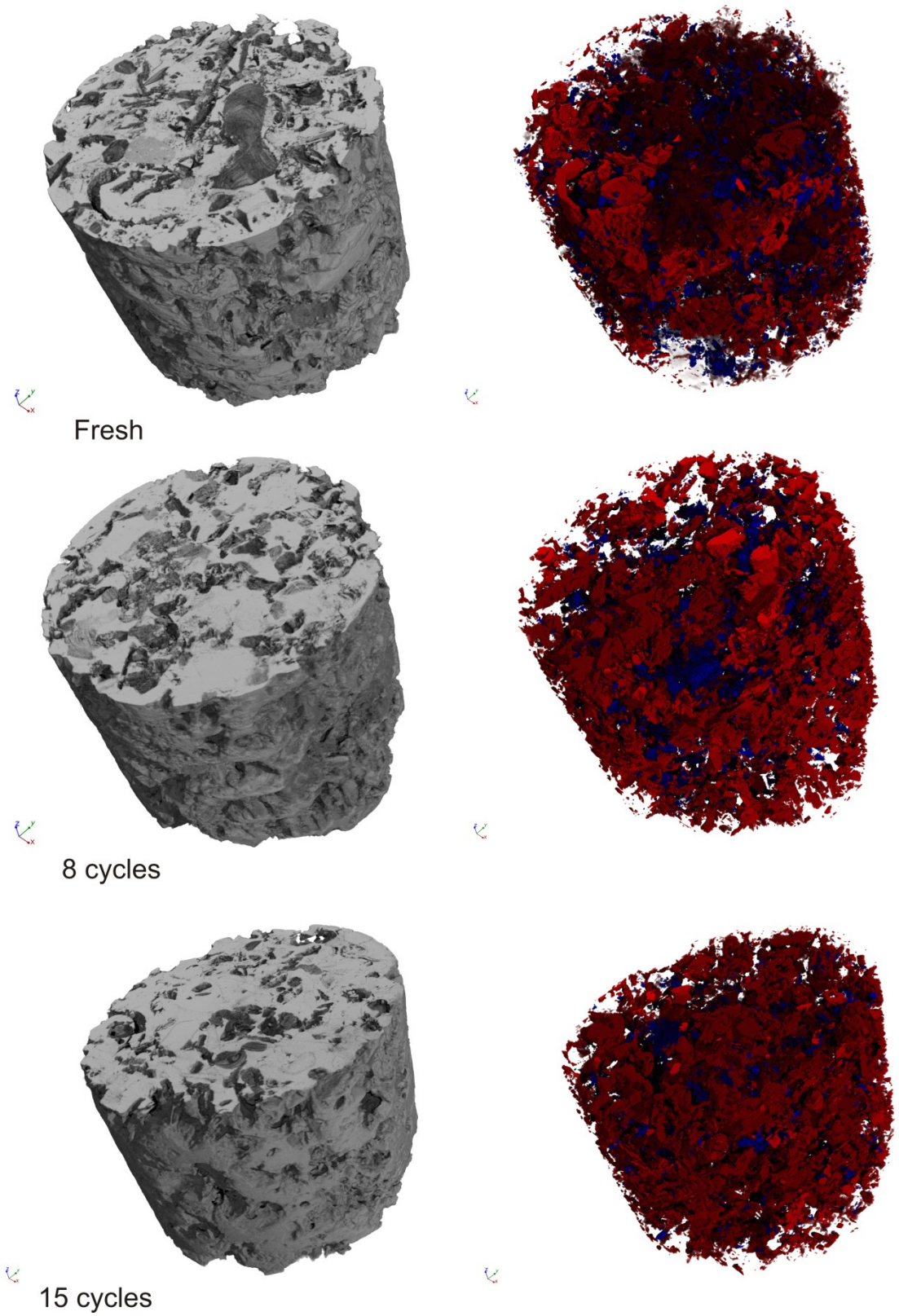

Figure 3.15 - 3D reconstruction images of the bulk (left) and pore structure (right). Closed porosity (blue) and open porosity (red) network are shown. Diameter sample size is about 7 mm.

3.5.3 Equivalent diameter and maximum opening

The ED (*i.e.* equivalent diameter) is defined as the diameter of a sphere with the same volume as the selected pore, whereas MO (*i.e.* maximum opening) is the diameter of the maximum inscribed sphere of a selected pore. The variation in terms of volume and size of these parameters has been used with the aim of quantifying the dimensional change in the pore structure of the Sabucina Stone caused by salt crystallization. The ED and MO values for fresh and weathered samples have been calculated using Morpho+ software.

Figure 3.16 shows the volume (μm^3) vs. size (µm) curves of ED and MO for fresh and weathered samples. Inspection of the curves suggests that the degradation process is responsible for a shift of this parameter towards larger size and for a decrease of the amount of small EDs and MOs.

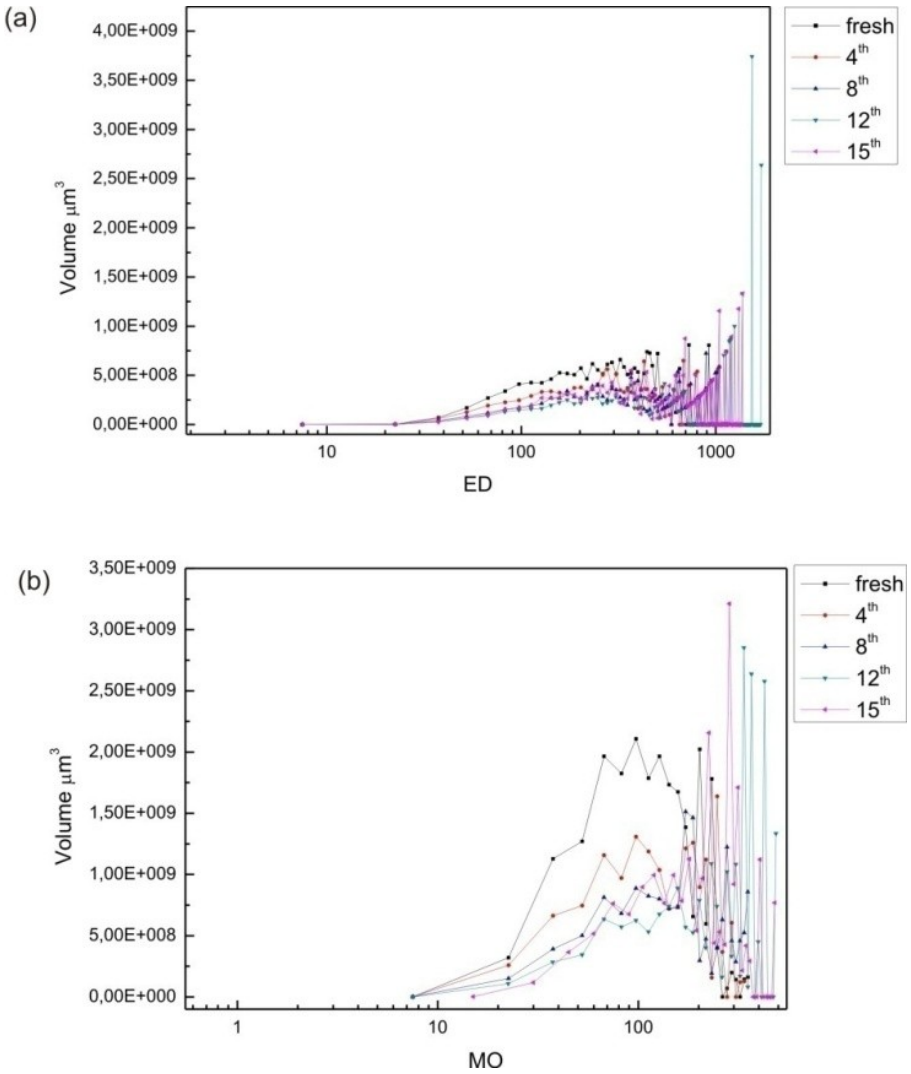

Figure 3.16 - Pore volume vs. equivalent diameter ED (a) and maximum opening OM (b) curves as a function of the number of salt weathering cycles. Step intervals 2 voxels (i.e. 15 µm).

The points at high ED and MO are the result of the analysis being performed in discrete classes. The step interval is the same for all studied classes (2 voxels, i.e. ~15 µm). At high ED and MO,

there is only one (or maximum a few) object. They have a large volume, representing the peak, but there are no objects present in the neighboring classes, causing the zero values in between.
A similar trend can be observed in the volume fraction of ranges in ED (Fig. 3.17(a)) and in MO (Fig. 3.17(b)) with respect to the total open porosity. In fact, in the fresh quarried sample, 87% of the porosity is attributed to pores with ED between 100 µm and 1000 µm; the pores with ED <100 µm represent about 8% of the total porosity, whereas the pores with ED >1000 µm cover only 5% of the total porosity. After salt-crystallization weathering (12 weathering cycles), the main dimensional changes cover the range of pores with ED > 1000 µm, with an increase to 50% of the total porosity and consequently a decrease in porosity with ED between 100 and 1000 µm. Slight variations in this trend can be observed in samples subjected to 15 crystallization cycles, in which the interval > 1000 µm decreases again. This behavior could be related to the development of a random fracture pattern (see 2D-analysis) or to a local heterogeneity in the texture of the studied sample. Finally, the porosity attributed to pores with ED < 100 µm drastically decreases in the weathered samples. In regard to MO, in the freshly quarried sample, 60% of the porosity is attributed to pores with MO values < 150 µm and 40% between 150 and 350 µm. After salt-crystallization weathering, the pore structure changes significantly. In fact, the percentage of pores with an MO value < 150 µm decreases to 49%, 38% and 30-20% from 4 to 15 cycles, respectively, whereas an increase of the range between 150 and 350 µm is observed (from ~50% to 63% from 4 to 15 cycles). Noteworthy is that the range >350 µm is present only in the samples submitted to 12 and 15 crystallization cycles, contributing to ~30% of the total porosity.

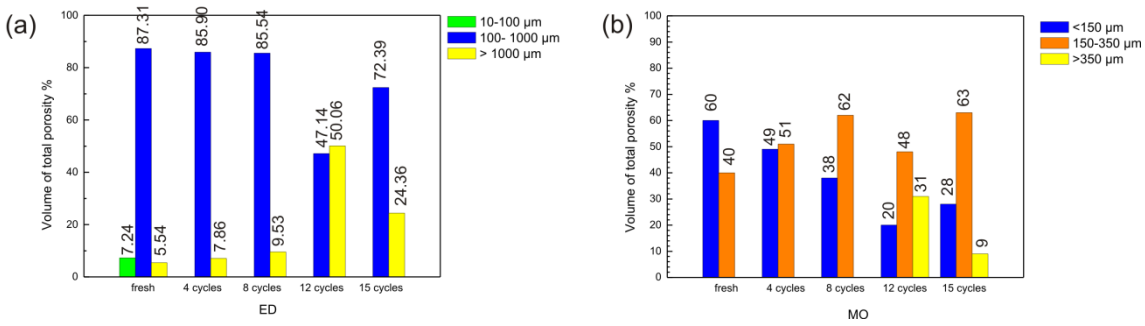

Figure 3.17 - Volume fraction (%) of ranges in equivalent diameter (a) and in maximum opening (b) with respect to the total open porosity.

In Figure 3.18 the dimensional changes of the pore network in the Sabucina Stone are shown by using a 3D-renderedvolume of the bulk and the pore structure before and after12 weathering cycles. In the pictures, the 3D rendered volume of the bulk is shown in grey, and the pore structure is color-coded according to its equivalent diameter and maximum opening. The visualizations illustrate that the weathering cycles cause a shift in the ED and MO towards larger sizes.

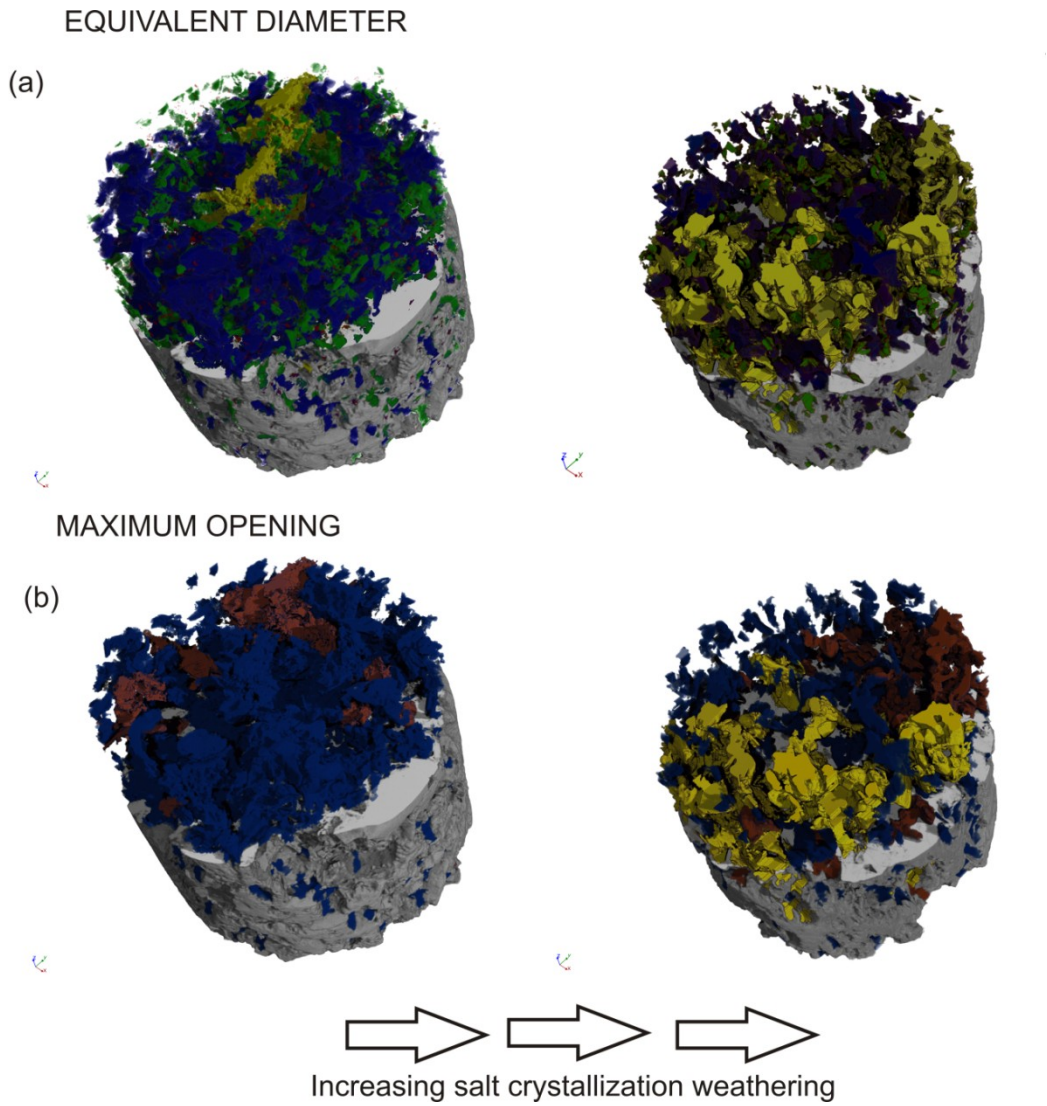

Figure 3.18 - 3D volume reconstruction of Sabucina Stone. Equivalent diameter and maximum diameter are visualized in function of porosity ranges and crystallization cycles. (a) Green, blue and yellow colors represent pores with ED values of 10–100 µm, 100–1000 µm, and 1000 µm, respectively. (b) Blue, orange and yellow colors represents pores with MO <150 µm, 150–350 µm, and > 350 µm, respectively.

3.5.4 Micro-cracks estimation by using sphericity

The micro-crack porosity was estimated by using sphericity data calculated in Morpho+. Micro-cracks are characterized by a sphericity <<1; in contrast, the original pores are more spherical (sphericity ≤1). According to the graph shown in Figure 3.19, it is possible to assume that sphericity shifts slightly towards lower numbers with increasing cycles in the interval between 0.2 and 0.4, suggesting that micro-cracks develop as of the 12th weathering cycle. However, assessment of sphericity has to be considered with caution, as some pores will have a low sphericity, related to their origin, e.g., shelter pores or moldic shells. Depending on the sample, more or less of these kinds of pores could be present, thereby influencing the sphericity distribution given in Figure 3.19.

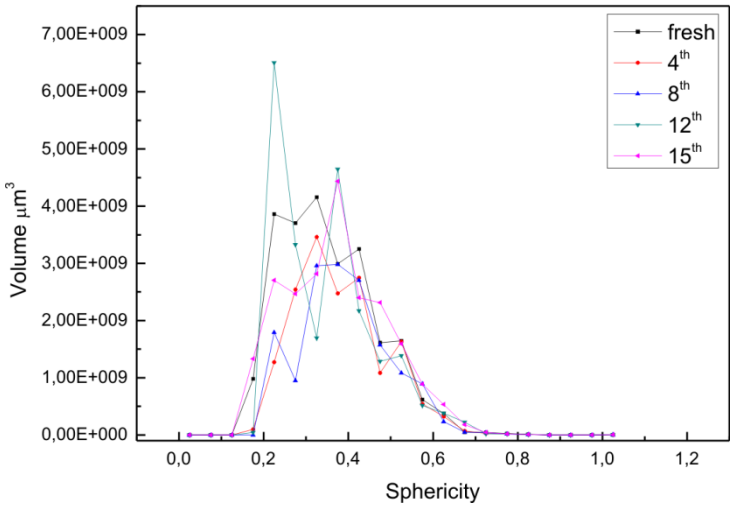

Figure 3.19 - Variation of sphericity as a function of the number of salt-weathering cycles.

3.5.5 Final remarks

The obtained data allowed us to quantify and visualize the pore network modification to weathering by using parameters, such as equivalent diameter ED and maximum opening MO. In general, salt crystallization acts to increase the total porosity with an increase of open porosity and a concomitant decrease of the closed porosity. Overall, the enlarged pores in weathered samples exhibit higher MO and ED values than the freshly quarried sample.

The experimental section of this research has been supported by the Italian Association of Archeaometry (AIAr) through a grant to Simona Raneri during her Ph.D. studies.

3.6 Visualization and quantification of weathering effects and water uptake process by using neutron imaging

In the previous section has been demonstrated that X-ray computed tomography represents a powerful method for the qualitative and quantitative evaluation of the pore modification in building stones due to weathering. In fact, the obtained results have highlighted a strong modification of the pore network due to salts crystallization into the inner structure of the stone. Such a behavior has a great influence in the mechanical proprieties of the stone, as well as in the general decay mechanism and the durability of the materials. In addition, as the water and moisture transport through pore network has a key role in the weathering processes, changes in pore size distribution, open and closed porosity and interconnectivity determine relevant modifications in fluid-flow patterns inside stone. Therefore, the quantification of water movement in degraded stones and the visualization of fluid transport into the pore network represent additional useful tools in understanding the weathering evolutions and the transport processes into the porous media.

Classical approaches, including gravimetric methods for the determination of the amount of water uptake in function of time, are usually performed in order to esteem the capillarity

coefficient in porous media (*e.g.* by applying laboratory test routines following standard recommendations). However, even if these methods are able to supply useful information on the behavior of stones against water, they cannot give back a description of the local distribution of water inside the stone; moreover, especially for capillary uptake tests, several factors should be considered in the modeling of complex geometry of pores. Is therefore quite clear that, beside the determination of absorption coefficients, the visualization of the internal processes occurring inside the materials during a water uptake process represents a relevant source of extra information for the comprehension of degrade phenomena, especially in building stones.

The visualization of water movements inside porous materials can be achieved by using imaging techniques. The recent developments in this field have provided innovative and non-invasive methods for the visualization of phase-structure and flow of hydrogen-rich fluids in porous media. In this framework, the use of neutron imaging has been demonstrated as powerful technique for the visualization and quantification of water distribution in partially saturated porous media; in fact, the significant difference in the total neutron cross section of water, bulk and air allows to obtain a weighty contrast in a neutron transmission images, so that a detailed information on arrangement and distribution of particles and voids (saturated by water) can be achieved. In addition, the possibility to perform dynamic measurements in function of time allows to monitor the water uptake movements in order to explore the complex processes involved in fluids transport.

In geomaterials studies, the distribution of water in both static and dynamic conditions has been largely investigated by using neutrons[55].For example, Pleinert and Degueldre[56] used NTR to determine the total porosity of crystalline rock samples saturated with water; de Beer et al.[57] and de Beer andMiddleton[58] determined the porosity of water-saturated sandstones using NTR.

Neutron imaging in dynamic condition has been largely applied both in preservation of natural building stone materials and reservoir characterization in petroleum engineering fields. Referring to the first one, Pleinert et al.[59] studied the moisture distribution in mortar under drying condition by means of neutron radiography with high resolution; Hassan in et al.[60,61] also presented the possibility and successfully studied the water imbibitions into different building stones using neutron radiography; Masschaele et al.[62] studied fluid motion into porous sand and limestone in three dimensions visibly; Ridgway et al.[63] established the network absorption model based on the experimental water absorption data of red clay brick and white siliceous brick by neutron radiography. Pugliesi[64] has utilized neutron radiography to observe cracks in concrete; Zhang and Zhao[65] also started applying neutron radiography to study water uptake into porous cement-based materials. Cnudde et al.[66] further explored the usefulness of high-speed NTR for quantifying water uptake in porous rocks by capillarity. Kang et al.[67] estimated the sorptivity and unsaturated diffusivity of Berea sandstone from neutron radiographs acquired continuously during spontaneous imbibitions. Masschaele et al.[68] and Diericket al.[69] presented

tomography for water and other fluids moving into limestone and sandstone rock samples, some of which have been treated with a water repellent. Hameed et al.[70] and Zawisky et al.[71] conducted neutron imaging experiments (both NTR and NCT) to compare the uptake of two different consolidants by porous building stone used in historic buildings.

On the basis of the above mentioned, it is quite clear that neutron radiography represent the most suitable method for water movement studies in porous media, especially in building stone materials applications.

In this work, neutron radiography and tomography have been used with the aim to a) visualize water movement inside porous structure of Sabucina Stone in order to study the effects of weathering on the behavior of the stone against water; b) monitor and visualize the fluid-flow patterns inside the degraded stone and quantify the water content distribution in function of time.

In detail, samples of un-weathered and weathered Sabucina stone have been scanned with neutron imaging technique, at the IMAGINE beam line situated at the Laboratoire Léon Brillouin (CEA/CNRS) in Saclay (France), in the framework of an experimental session approved in 2015. IMAGINE is located in the neutron guide hall on a cold neutron guide with 3Å $<\lambda<$20 Å. The detector was placed at L = 4 m from the aperture and the aperture diameter was D = 10 mm, giving L/D = 400. The neutron flux was $2x10^7$ neutrons/s/cm². A sCMOS camera (Andor) coupled with a lithium scintillator of 100 µm thick was used for the data acquisition. In this configuration, the spatial resolution was 250 µm. Neutron radiography was used to monitor the wetting front over time, while the neutron tomography was used to produce 3-D images of the water distribution within the samples. During radiographies, the exposure time was 40 s. For tomographies, the sample was set on a rotating table and a projection was acquired every 2° over 180°, with an exposure time of 30 s (Table 3.10).

Images were first filtered to remove hot spots, the camera offset was corrected with the dark field, and the images were normalized with the open beam and then corrected for the beam intensity variation with time. For tomographies, the reconstruction was done with the Octopus (Inside Matters) software.

Table 3.10 - Neutron imaging experimental parameters

L	4 m
D	10 mm
L/D	400
Fluency rate	$2x10^7$ neutrons/s/cm²
Neutron energy range	3-20 Å
Spatial resolution	250 µm
Number of projections	91
Exposure time	Radiography: 40 s Tomography: 30 s

For the experiment, three reference of un-weathered samples and twelve weathered samples have been scanned; the artificial weathering has been obtained by applying the UNI EN 12370 standard test. In detail, samples subjected to four, eight, twelve and fifteen salts crystallization cycles have been scanned in order to obtain information on changes in water uptake process in function of time and degradation degree. Samples have been taped in aluminum boxes (which is transparent for neutrons) placed in-between source and detector. A reference radiograph of the initial dry sample has been taken for the subsequent quantitative evaluation of the results. Then, the water container has been filled with water, manually; immediately after the water was in contact with the surface of the samples, neutron images have been acquired at regular intervals (40 seconds). In this way the process of water absorption has been followed in function of time.
Neutron radiography images have been processed by using ImageJ software[53]. First of all, a dark-field and flat-field image correction was performed on radiographs. Moreover, a spot filter has been applied in order to clean images and remove pixels due to noise. Additionally, in order to obtain two-dimensional images representing the water distribution inside the stone, the initial dry scan and four samples scans with different gravimetric water contents are used for analysis. The dry image is formed from the attenuation of neutrons through the stone sample. The wet images are the result of the sum of attenuations associated with water, bulk rock and air. The intensity of pixels corresponding to wet stone sample (I_{Wet}) and dry stone samples (I_{stone}) can be represented using Eqs. 47 and 48, respectively.

$$I_{wet}(x,y) = I_0(x,y) \cdot e^{-(\Sigma_w t_w + \Sigma_s t_s)} \quad (47)$$

$$I_{stone}(x,y) = I_0(x,y) \cdot e^{-\Sigma_s t_s} \quad (48)$$

The macroscopic cross sections of water and dry stone are denoted as Σ_w and Σ_s, respectively. The thicknesses of water and stone layers in the neutron ray path are denoted as t_w and t_s.
The wet images is divided by the dry ones, in order to isolate the contribute of water (see Figure 3.20).

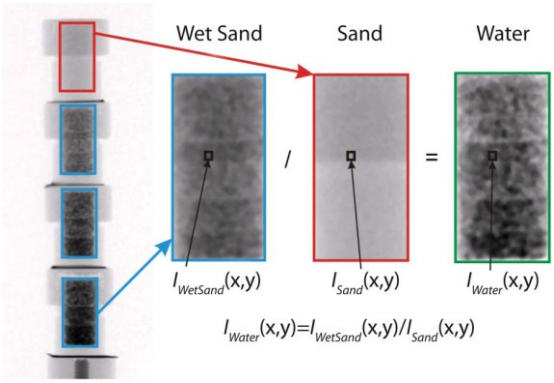

Figure 3.20 - From Kim et al., 2012[72], as example of image processing

A radiography image of water distribution is typically used to measure the 2D water distribution in flow experiments.

In this work, the water content for Sabucina stone samples has been obtained according to the method proposed by Kim et al.[72]. In detail, by normalizing a wet image with a dry reference image, the 2D distribution of the water thickness (t_w) can be directly obtained from the Eq. 49:

$$t_w(x,y) = -\frac{\ln\left[\frac{I_{wet}(x,y)}{I_{dry}(x,y)}\right]}{\Sigma_w} \qquad (49)$$

with $\Sigma_w = macroscopic\ cross\ section\ of\ water = 0.978\ mm^{-1}$

By dividing the total water thickness (t_w) by the total thickness of the sample (t_c) at each pixel, the water content (WC) at each pixel can be simply calculated from Eq. 50:

$$WC(x,y) = \frac{t_w(x,y)}{t_c(x,y)} \cdot 100\% \qquad (50)$$

with $t_w = 200\ mm$

3.6.1 Neutron images of water capillary absorption: the effects of weathering on the behavior of the stone against water

Water kinetics in porous natural building stones represents a key tool in engineering and conservative fields for the understanding of the degradation processes due to both chemical and physical interactions. Capillary absorption is one of the main mechanisms for water transport in porous materials. It is described by the water absorption coefficient determined following the UNI 10859 standard recommendation[73] and expressed as the amount of water uptake per square meter as a function of the square root of time. Although this parameter provides useful information on the properties of the studied materials when liquids spontaneously spread over solid surfaces, it is not suitable to describe the internal processes that occur when aqueous solutions move through the porous structure of stone, causing degradation effects due to two freeze/thaw cycles, solvent action of water and/or salt crystallization. Consequently, a quantitative analysis of these processes is important. Therefore, in order to study the capillary absorption behavior in degraded stones and the influence of degradation effects due to salt crystallization in fluid motions, the water flow inside Sabucina stone samples have been monitored by using neutron imaging, enabling the direct determination of the location of the wetting front inside the stone as a function of time.

During this experiment, a sequence of radiographs of weathered Sabucina stone samples (representative of different degradation degree induced by salt crystallization) have been scanned in both dry and wet conditions. In particular, in consideration of the slightly

heterogeneity of the stone, three samples for each crystallization cycle (*i.e.* four, eight, twelve and fifteen) have been scanned in order to obtain representative results.

Firstly, a reference dry image has been acquired before the contact with water. After taking radiographs of each dry sample, imaging has been interrupted for the filling of the containers with water. Water was added to the set-up and a sequence of several radiographs at different time-intervals was taken until diffusion started; in detail, for each stone sample, a series of radiographs every 40 s has been acquired until saturation.

Water movement monitored in weathered samples through neutron radiography is shown in Figure 3.21. As example, a sequence of five radiographs taken after about 5, 10, 15 and 20 minutes until the diffusion starts are shown.

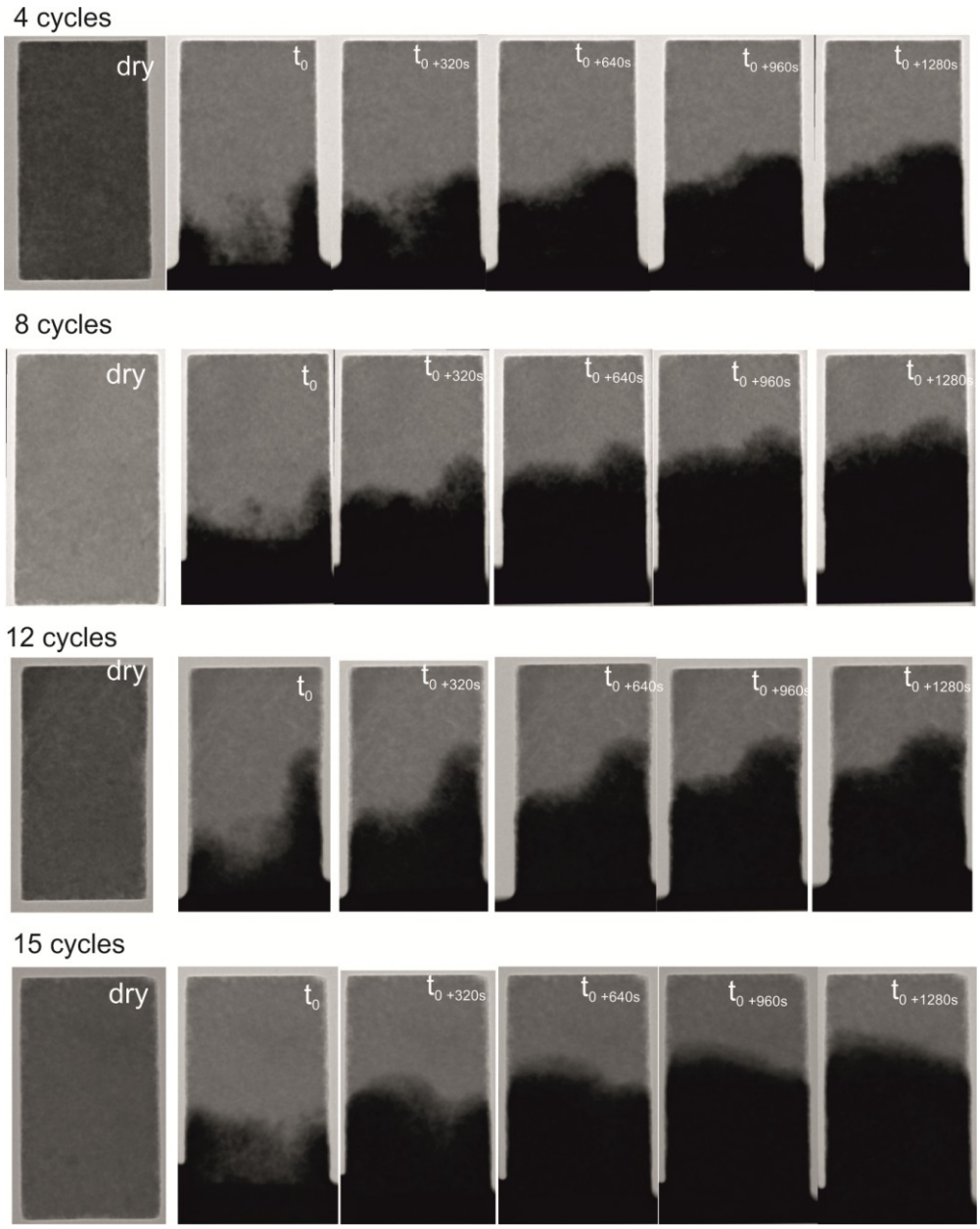

Figure 3.21 - Water movement inside samples as examples of un-weathered and weathered Sabucina stone.

Since the capillary uptake process can be considered in one-dimensional direction, a length-related water-penetration coefficient can be determined experimentally from the radiographs looking at the wetting front position; the coefficient B can be expressed as:

$$B = \frac{h}{\sqrt{t}} \qquad (51)$$

where h (m) is the position of the wet front over the time (t expressed in second).

Fig. 3.22 shows the position of the wetting front as a function of the square root of time for representative samples subjected to different weathering degree, while in Table 3.11 the penetration coefficients of the same samples, obtained from the transmission images and determined as the slope of the curves$h(t) vs. \sqrt{t}$are reported.

Table 3.11 - Penetration coefficients calculated for representative samples subjected to different weathering degree

Sample ID	***Weathering cycle***	***Penetration coefficient (m/√s)***
Sab5	4 cycles	$3*10^{-4}$
Sab9	8 cycles	$3.1*10^{-4}$
Sab10	12 cycles	$3.7*10^{-4}$
Sab14	15 cycles	$3.7*10^{-4}$

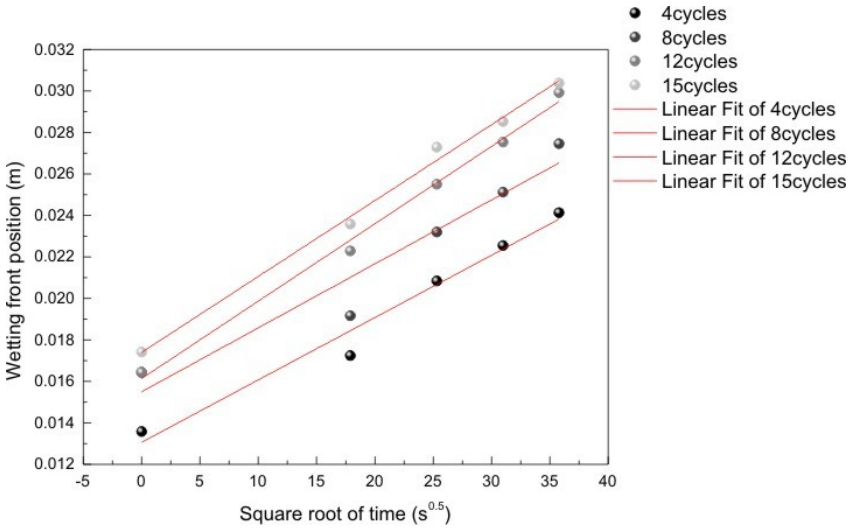

Figure 3.22 - Position of the wetting front as a function of the square root of time for representative samples subjected to different weathering degree

As expected, a link between speed of the wetting front and degradation degree of the samples can be found; in fact, more degraded is the sample, more is the advancement of the wetting front at the same time. Such a behavior is confirmed also by the values obtained for penetration coefficient, as it is higher in samples subjected to 12 and 15 crystallization cycles than the other ones (four and eight, respectively).

Even if a correlation between degradation process and water absorption behavior has been established, the inspection of the raw neutron radiographs suggests that complex processes are involved during the water uptake, as claimed by the presence of multiple waterfronts in degraded samples. This evidence could be explained only considering the modification of the

pore network induced by salts crystallization inside the stone volume. In fact, the presence of salts, as well as the new pore structure arrangement due to the weathering action, can be responsible of the establishing of sub-volumes characterized by different capillarity proprieties; in these conditions, irregular water spreading inside the pores occurs, resulting in the appearance of two or more waterfronts in neutron images. For aforementioned, the assumption of capillarity absorption as a one-dimensional process should be reconsidered in view of the really multifarious effects related to water spread in porous media characterized by complex geometry.

3.6.2 Quantification of water content: the fluid-flow patterns inside the degraded stone

In order to quantify the water distribution in stone samples and better understand the water uptake process in degraded samples, reference dry and wet images are evaluated for the mass thickness of water as described previously and according to Kim et al.[72]. In detail, the image processing method allow to quantify the water content percentage inside the stone volume, highlighting therefore the spread mechanism and the eventually multiple penetration patterned determined by sub-volumes with different capillarity proprieties.

In Figure 3.23 the contour plots of water content distribution (WC%) obtained from neutron radiography images are shown; in particular, a sequence of five plots obtained from radiographs taken after about 5, 10, 15 and 20 minutes until the diffusion start are shown. It is worth of note that the contact time labeled as t_0 has to be considered a reference start value for the evaluation of the whole sequence, as it effectively represents the first wet acquisition available after the manually adding of water and the opening of the neutron beam in safety conditions.

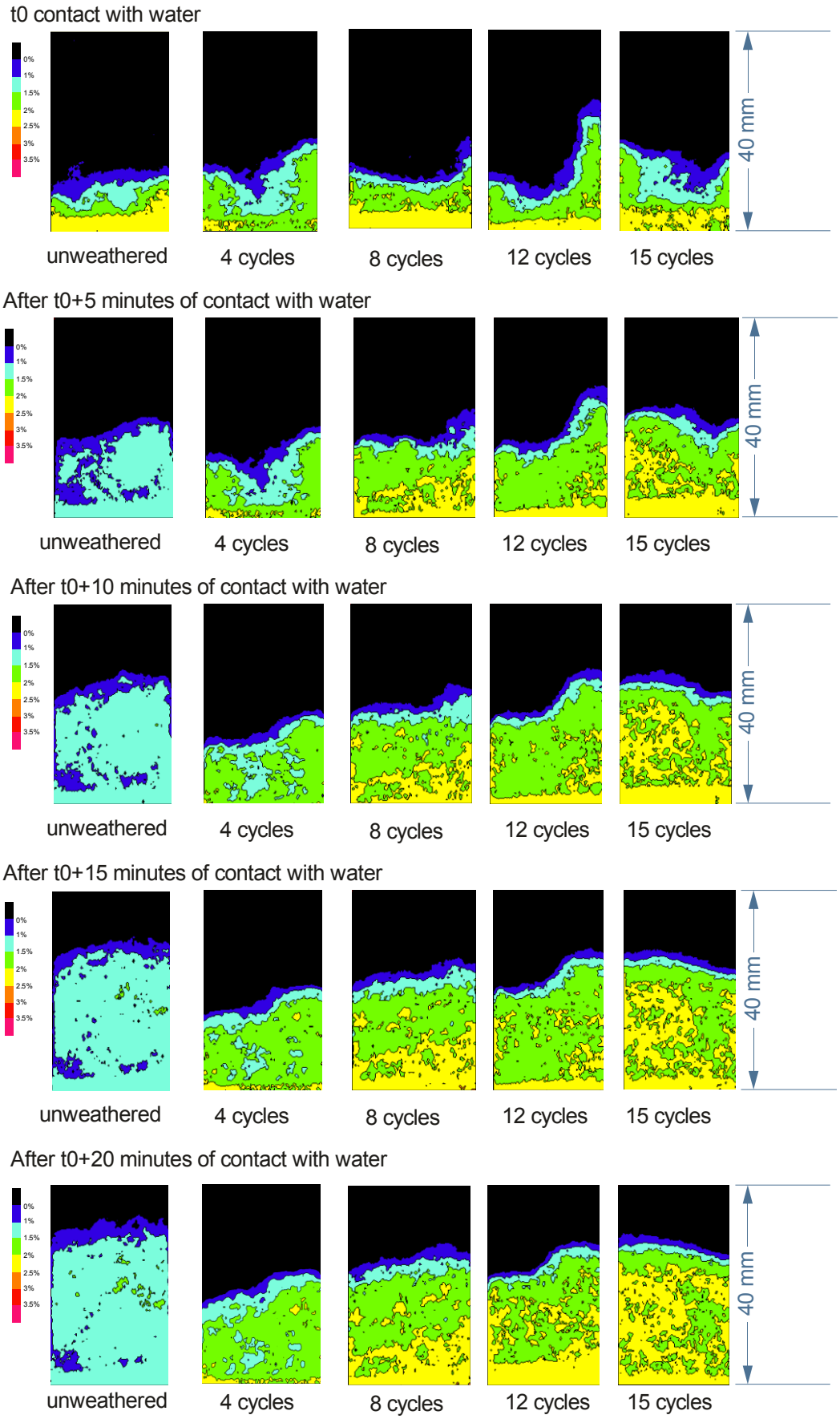

Figure 3.23 - Water content distribution (WC%) obtained from neutron radiography images in function of time and degradation degree.

The inspection of the processed images allows to better understand the evidence about the multiple waterfronts observed in the raw radiographs. In fact, contours describing the quantitative distribution of water inside the stone volumes clearly show the presence of different flow paths over the time, both in un-weathered and weathered samples.

Referring to sample representative of un-weathered stone, the contours show that during the first minutes of contact with water, the absorption front spreads quite homogeneously through the stone volume; however, two main paths irregularly distributed inside the stone can be distinguished, corresponding to water contents from 0.5 to 1 WC% and from 1 to 1.5WC%, respectively. As the uptake process proceeds, noteworthy is the presence of sub-volumes interested by a greater WC% (about 2 %) respect to the neighbor areas, suggesting the existence of pore structures that allow the absorption of greater water contents. These areas tend to enlarge themselves over the time, while the distribution of the lower WC% (<1.5 WC %) areas decrease. Overall, the waterfront can be considered due to two different WC% contributes, at 1.5 WC% and <1 WC%, respectively.

In samples subjected to salts weathering, the capillary uptake process and the distribution of water inside the stone volume is greatly affected by the degradation process. In fact, in all artificially degraded samples, the WC% contours highlight areas characterized by water content > 1.5 WC% up to the first minutes of contact with water.

Different observations can be inferred for degraded samples. For example, in the case of samples subjected to 4 crystallization cycles, the waterfront seems to proceed through irregular flow paths, highlighting *side effects* probably due to the more intense action of the degradation process in the areas closer the sample surface. Since these effects continues, the water uptake proceeds in irregular way, determining different capillarity absorption proprieties for inner and surface sides, respectively.

The contour images of the samples subjected to 8, 12 and 15 crystallization cycles highlight a similar behavior, now showing the presence of almost three different waterfronts at increasing WC% values. Also in these cases, the WC% is overall greater than in un-weathered stone, reaching during the first stage of absorption water content values >2%. It is really interesting that as the water uptake process proceeds, some areas at higher water content percentages are surrounded by lower ones, claiming the presence of several sub-volumes able to vehicle more water than other ones. This evidence suggests a really complex pore structure and the WC% variations from the first to the ultimate degradation state claim the strongly pore network modification of the stone due to salts crystallization action. In all cases, side effects can be asses, maybe related to the more intense effects of the degradation process close the surface of the sample than the inner part of it.

In order to compare the results obtained by using non-destructive imaging techniques and classical gravimetric methods, the same capillarity experiment has been performed in the

laboratory; in detail, water absorption tests by capillarity following the standard recommendations have been carried out.

In Table 3.12 the results obtained by water capillarity test according to the UNI recommendation are reported[73], while in Figure 3.24 the amount of water absorbed per area in function of time during the first 30 minutes of water absorption by capillarity is shown.

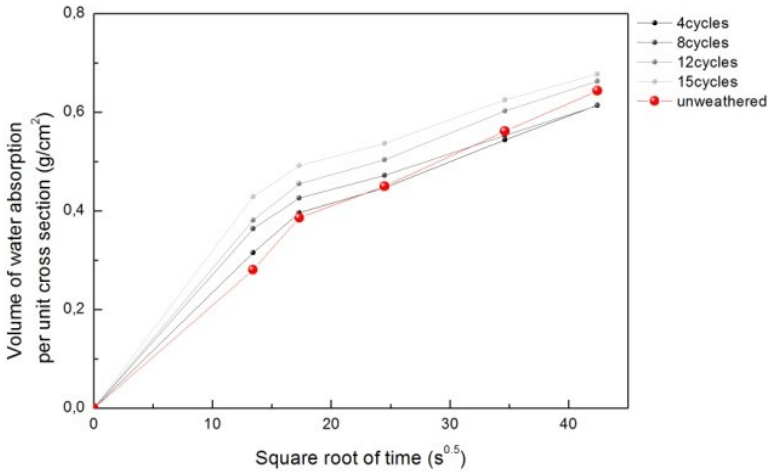

Figure 3.24 - Amount of water absorbed per area in function of time during the first 30 minutes of water absorption by capillarity for unweathered and weathered samples at different degradation degree

Table 3.12 - Report of NORMAL 11/88 recommendation test

t (√s)	***Volume of water absorption per area (g/cm²)***					***Water % absorbed per area***				
	NT	***4cycles***	***8cycles***	***12 cycles***	***15 cycles***	***NT***	***4cycles***	***8cycles***	***12 cycles***	***15 cycles***
0	0	0	0	0	0	0	0	0	0	0
13	0.280	0.315	0.364	0.381	0.429	30.907	36.602	42.347	44.393	52.414
17	0.386	0.397	0.426	0.455	0.492	42.561	46.092	49.563	52.980	60.102
24	0.450	0.446	0.472	0.504	0.537	49.562	51.845	54.859	58.648	65.619
35	0.562	0.544	0.553	0.602	0.625	61.884	63.204	64.334	70.105	76.424
42	0.644	0.615	0.614	0.663	0.678	70.958	71.383	71.356	77.183	82.835
60	0.766	0.719	0.708	0.736	0.726	84.431	83.544	82.362	85.624	88.761
85	0.800	0.768	0.765	0.761	0.728	88.208	89.175	88.946	88.519	89.017
147	0.802	0.778	0.778	0.764	0.730	88.415	90.388	90.452	88.932	89.170
170	0.808	0.784	0.791	0.774	0.742	89.083	91.092	91.958	90.075	90.702
294	0.832	0.804	0.807	0.797	0.760	91.732	93.325	93.853	92.727	92.925
416	0.852	0.818	0.821	0.811	0.773	93.874	95.000	95.432	94.357	94.432
509	0.867	0.825	0.828	0.820	0.783	95.532	95.874	96.234	95.403	95.709
588	0.877	0.834	0.835	0.828	0.790	96.684	96.917	97.109	96.400	96.526
778	0.894	0.848	0.847	0.842	0.803	98.572	98.447	98.494	98.030	98.135
831	0.900	0.853	0.853	0.849	0.809	99.217	99.078	99.125	98.857	98.927
882	0.907	0.859	0.856	0.855	0.811	99.954	99.709	99.514	99.562	99.183
930	0.907	0.860	0.860	0.858	0.814	100.000	99.879	99.976	99.854	99.438
975		0.861	0.860	0.859	0.818		100	100	100	100
slope	***0.012***	***0.016***	***0.016***	***0.018***	***0.019***					
CA g/cm²	***0.03***	***0.04***	***0.04***	***0.05***	***0.05***					

The obtained results, both in term of percentage of water absorbed and capillary coefficient, highlight a correlation between the percentage of water per unit cross section and the degradation degree of samples, claiming a change in the physical proprieties of the stone due to salt crystallization effects. In fact, in the first 30 minutes of absorption, the absorbed water percentage increase from 70% in unweathered samples to 82% in samples subjected to 15 crystallization salt cycles.

A comparison between the quantitative data obtained from neutron radiographs analysis and the water absorption trend and percentages obtained by using classical gravimetric method highlights the same behavior for samples subjected to the different artificially degradation cycles, suggesting therefore the occurring of a relevant modification in pore network of the stone through which fluids can flow.

Overall, the behavior of the stone against water capillary uptake is clearly affected by the degradation process and higher water contents are absorbed by weathered stone samples during the same time interval of monitoring.

3.6.3 3D visualization of water movement by neutron tomography

Neutron tomography instead of radiography can add important information of the water migration inside natural building stones; in fact, a multi-dimensional investigation of water uptake process can be achieved only by a 3D visualization.

In this framework, additionally dynamic experiments by using neutron tomography have been carried out on cylinders of about 20 mm in diameter in order to obtain 3D images of samples, useful to better understand the water absorption process in Sabucina Stone in function of salt weathering. In detail, seven samples previously subjected to artificially weathering by salt crystallization (following UNI EN 12370 standard recommendation) have been scanned at the IMAGINE beam line situated at the Laboratoire Léon Brillouin (CEA/CNRS) in Saclay (France) (see Table 3.10). For tomographies, the samples were set on a rotating table and a projection was acquired every 2° over 180°, with an exposure time of 30 s. During the measurements, samples were in contact with a water reservoir, allowing the acquisition of the tomographic images during the capillary uptake process. The image resolution was about 1 mm/voxel.

The reconstruction of the tomographies has been obtained by using Octopus Software (InsideMatter), while for the 3D visualization MyVGStudio software has been used.

In Figure 3.25 two examples of 3D reconstructed images of samples subjected to eight and twelve weathering cycles are shown, as examples. Beside some uncertainty in the image rendering, due to the occurrence of several artefacts related to the experimental set-up, the 3D visualization of samples allow to better understand the occurrence of non-linear and multiple waterfronts observed in the framework of the radiographs analysis. In this sense, the presence of

well defined penetration patterns highlight how the advancement of the degradation process is responsible of the occurrence of differential flows inside the whole investigated volume, with an increasing of both water penetration depth and contents in samples subjected to more weathering cycles.

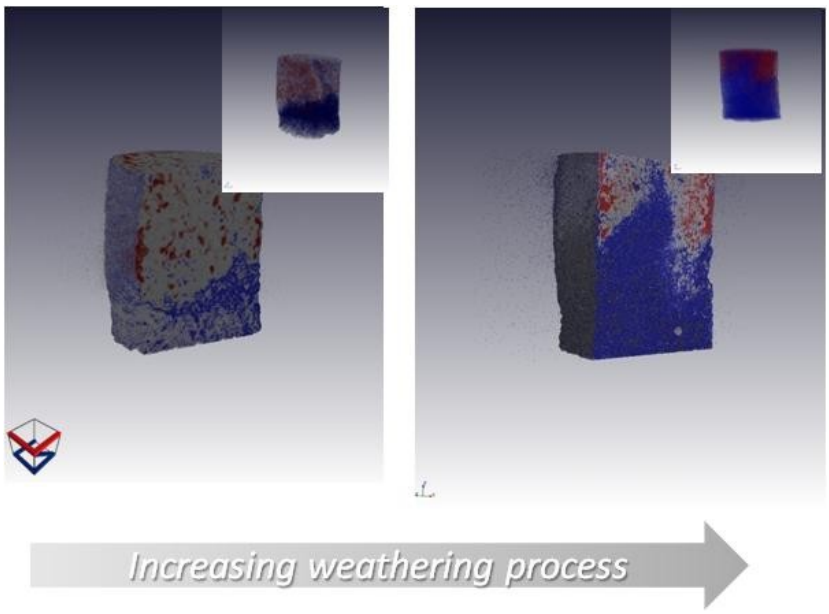

Figure 3.25 - 3D reconstruction images of the bulk (gray), pore structure (red) and water flow (blue).Diameter sample size about 2 cm.

3.6.4 Final remarks

The experiments on the interaction of the natural building stones with water demonstrate how sensitively the capillary uptake process can be studied with neutron radiography. The method appears in fact to be really powerfully in observing water flow in porous building materials.

Beside the qualitative data acquired from the observation of the raw neutron images, also quantitative results have been obtained thanks to the image processing of the radiographs. First of all, the evolution of the wetting front position over the time has been observed and the penetration coefficient has been determined. The obtained results demonstrate that a change in the physic proprieties of the stone occurs with the intensification of the degradation process, determining faster water absorption in samples subjected to several artificially salts weathering cycles. Values for water penetration depth obtained from neutron images and from capillary absorption are in good agreement; however, the non-perfect linearity of capillary uptake process has to be considered due to the evidence of multiple waterfronts related to sub-volumes with different capillary absorption proprieties. This behavior has been strongly observed in degraded samples, suggesting a correlation with the modification of the pore network due to the salts crystallization action.

The neutron images have been therefore further evaluated in order to obtain quantitative water distributions in stone as function of time with high precision and high spatial resolution. The contour of water content percentage (WC %) highlight that degraded samples absorb much more water than the un-weathered stone. Water also penetrates more quickly and deeper into weathered samples and such a behavior has to be related to the modification of pore structure that determine an higher ability to absorb greater volume of water, especially in enlarged pores created by the intense degradation action. In the weathered stone samples, the ability to speedy vehicle the water in vertically orientation is associated with a relevant horizontally spread of the water in coarser pores, in which more water is absorbed; this process determines the presence of isolated and irregularly distributed areas that exhibit higher WC% values than the surrounding. In addition, an evidence of side effects due to more intense action of the degradation process close the surface is claimed by the speedy advancement of the waterfront and the high WC% content in the edges of the weathered stone samples respect to the inner part.

On the basis of the obtained results, it is possible asses that water penetrates by capillarity in not homogenous way, due to slight heterogeneity in capillarity absorption proprieties of sub-volumes inside the samples. These evidences are particularly emphasized in weathered stone samples, in which the vertical spreading of the water is associated to an intense horizontal migration through an enlarged pore network determined by the degradation action; therefore, until the water vertically flows up to saturate the entire volume sample, a lower WC% waterfront proceed upwards, while the coarser pore structures allow the absorption of higher water content, determining subsequent waterfronts at different WC% values and the highlighting of the distribution of the pore structure inside the stone.

Finally, beside limits due to relevant artefacts effects, the reconstruction of tomographies have permitted to solve interpretative problems related to non-linear waterfront evidences on neutron radiographies, highlighting a 3D visualization of dynamic processes related to capillary absorption in both unweathered and weathered samples.

In conclusion, neutron imaging techniques have allowed to better understand how deterioration mechanisms affect physical proprieties of building stone that represent really relevant aspect in planning powerful action finalized to improve their durability.

3.7 Surface modifications due to salt weathering

As surface represents the direct interface of building stones with atmosphere, the quantification of weathering effects on exposed rocks is an additional parameter useful in studying the impact of degradation processes in conservation science. In view of the aforementioned, the application of surface metrology in the field of conservation and restoration of building stone materials has recently increased, thanks also to the advancement in imaging techniques that allow to monitor the surface features of stones in non-destructive and non-invasive way.

For example, Fitzner[74] used the image analysis for the quantification of the rock porosity by direct observation and quantification of shape, size and sections of pores by optical and electron microscope images; Zezza[75] applied digital image processing in the diagnosis of the state of monument alteration, along with the ultrasounds; Aires-Barros et al.[76]showed the alteration in surface of the stone by application of profilometry lines; Kapsalas et al.[77] used digital imaging and surface parameters as decay indicators on black crusts; Vázquez et al.[78] used digital image processing of weathered stone caused by efflorescence as a tool for mapping and evaluation of stone decay; Stephenson and Finlayson[79] and others[80,81], deployed microerosion meters in measurements of building stone weathering rates; Kamh and Hanna[82] used an MEM to establish a surface roughness index; López-Arce et al.[83] have quantified weathering by examining the surface roughness of building stone, such as of Spanish granites; Jaynes and Cooke[84]attributed changes in surface roughness of building stones to both the action of salts as well as air pollution. Therefore, as surface metrology can be considered as useful tool for monitoring and study weathering process in building stone, in this section, the results of a surface morphometrical analysis performed on unweathered and weathered samples of Sabucina Stone by using a 3D digital microscope are reported.

3.7.1 Roughness and waviness analysis

The surfaces of a fresh reference sample and four degraded cubes 4 cm wide, the latter ones subjected to four, eight, twelve and fifteen salts crystallization cycles, respectively, have been analyzed. Images have been acquired by using Hirox KH-7700 digital microscope with an MXG-10C body, an OL-140II lens and an AD-10S Directional Lighting Adapter. The Auto Multi Focus tool enabled the creation of a 3D image obtained by the composition of one hundred planes taken at different focus levels.

On the samples surface, a rectangular area of about *1 x 0.5 cm* has been selected for the acquisition of the images.

In order to obtain the surface texture parameters (both in term of roughness and waviness), the 2D gray scale projection of the 3D images have been processes by using the ImageJ plug-in*SurfCharJ*[85]. The plug-in is based on several developed routines for surface assessment[86], and provides global and local roughness analysis, gradient analysis, domain segmentation, surface leveling and directional analysis. Having suitable surface representations, both roughness/waviness surface map and several surface roughness/waviness parameters can be derived from the analysis, according to the ISO 4287/2000 standard.

In order to discriminate waviness (*i.e.* undulations that are several times longer than deep) and roughness (*i.e.* ondulations that are just a few times longer than deep) a limit defined by the cut-off wavelength λc[87] has to be established. The length of λc is not predetermined but influences the value of roughness parameters. Usually, the length of the measured profile is six or seven

times the length of λc[87]. Therefore, the unfiltered primary surface map has been filtered by using Gaussian filters having a radius corresponding to the lower structure size limit input, represented by the wavelength λc; in this way, roughness and waviness images can be been obtained, representing components having shorter-length and longer-length structures than the applied wavelength λc, respectively.

According to the previously, the wavelength (λc) has been established, each time, as about the sixth part of the length of the measured profiles. The obtained roughness and waviness images have been, finally, processed by using the ImageJ plug-in *Interactive 3D surface plot*, in order to extract 3D topographically information and better visualize the peak and valley events related to the 2D analyzed images.

In Figure 3.26 the roughness maps and surface plots of unweathered and weathered stone surfaces are shown, while in Table 3.13 the obtained parameters from the roughness analysis are reported.

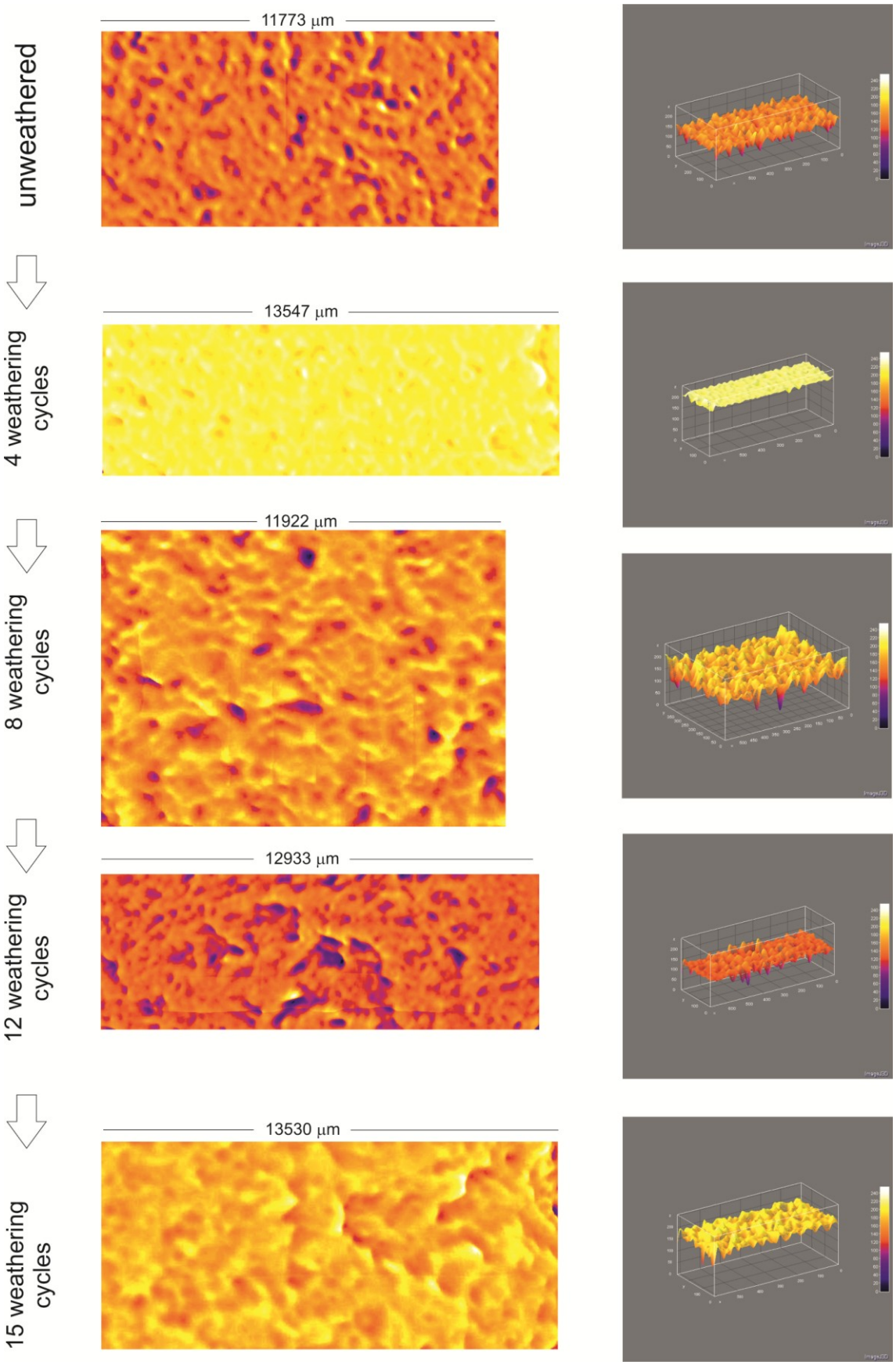

Figure 3.26 - Roughness maps and surface plots of unweathered and weathered stone surfaces

Table 3.13 - Roughness parameters (μm) obtained by applying a Gaussian filter with SurfCharJ plug-in in ImageJ

Sample ID	***Rq***	***Ra***	***Rsk***	***Rku***	***Rv***	***Rp***	***Rt***	***Rc***
NT	7.3258	5.648	-0.5491	0.856	-29.6927	21.0776	50.7703	0.0111
4cycles	5.7352	4.4256	-0.5935	4.4727	-35.217	18.2312	53.4481	0.1152
8cycles	5.6189	4.416	-0.6025	0.6934	-20.8765	13.6637	34.5402	0.0262
12cycles	8.2656	6.2838	-0.5765	1.2358	-35.0023	25.3116	60.3139	-0.0139
15cycles	4.7365	3.658	-0.4986	0.7964	-18.8667	13.7798	32.6465	0.025

Among the reported values, the more relevant ones are represented by R_a, R_q and R_t, being the a*rithmetical mean deviation of the assessed profile*, r*oot mean square deviation from the assessed profile and total height of the profile*, respectively. An inspection of them highlights a correlation between the surface texture features and the degree of weathering (Figure 3.27).

In detail, a negative trend can be observed, as the values of R_a, R_q and R_t decrease significantly with the advancement of the weathering process, due to a smoothing of the exposed surface in term of ondulations that are just a few times longer than deep, as can be also inferred from a visual inspection of the surface plots in Figure 3.27.

Exception is represented by the sample subjected to twelve accelerating aging cycles, maybe due to the presence of a wide valley structure in the selected area.

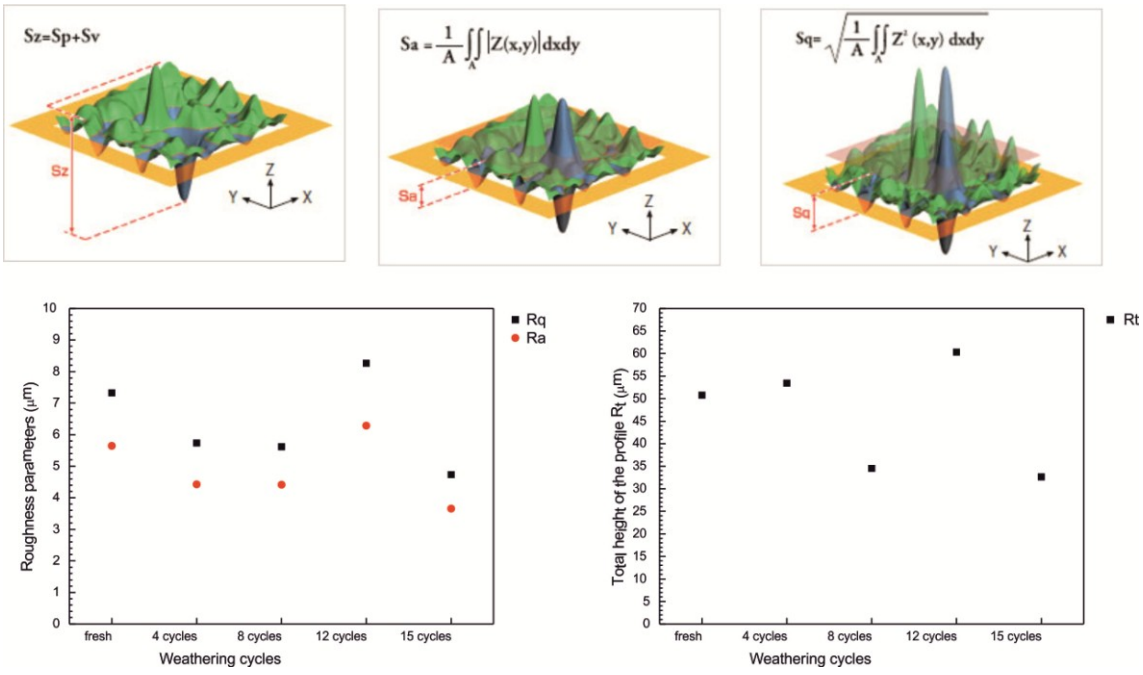

Figure 3.27 - Correlation between roughness parameters and weathering cycles

A different trend can be observed for the waviness analysis data, whose results are reported in Figures 3.28 and 3.29 and Table 3.14.

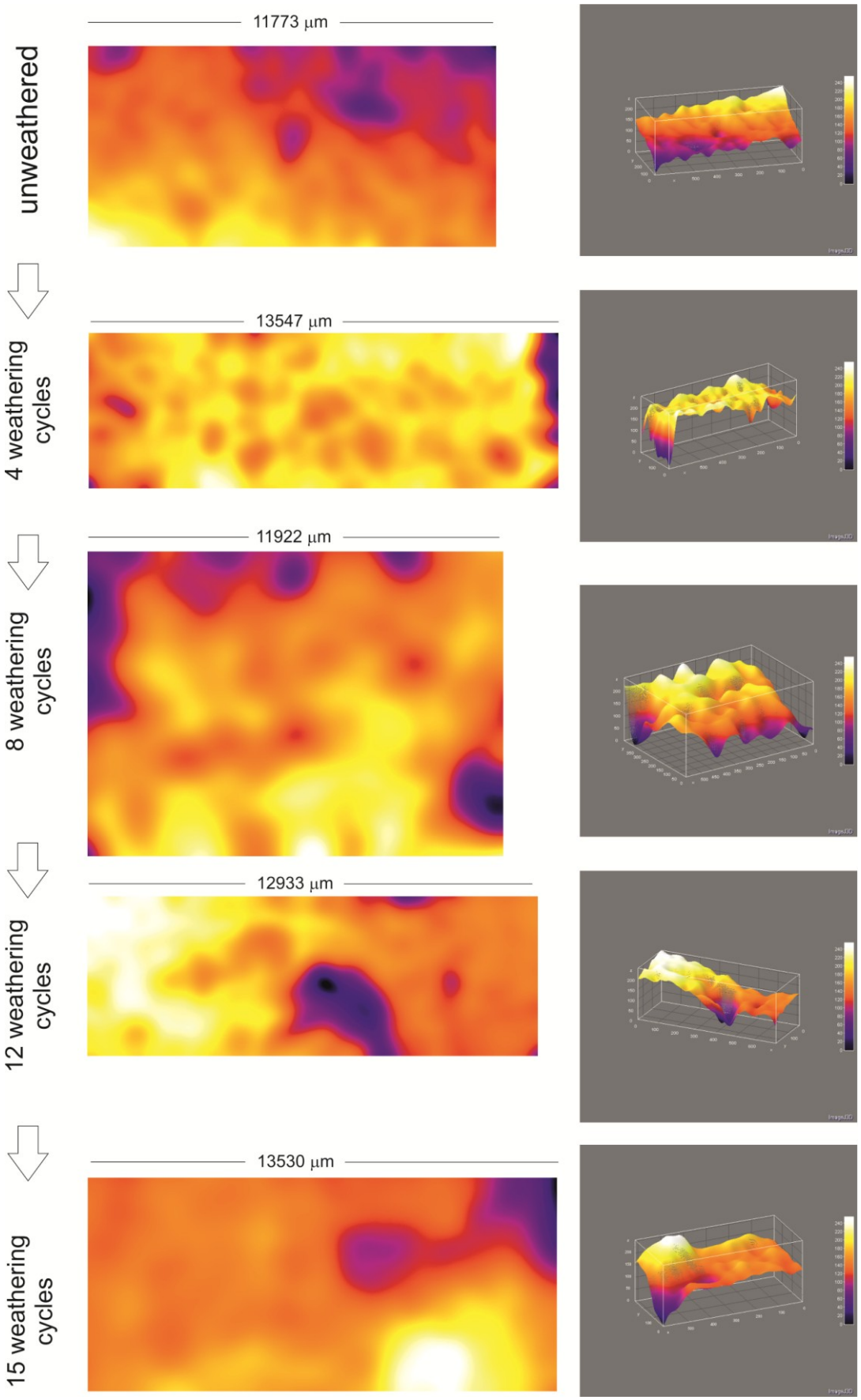

Figure 3.28 - Waviness maps and surface plots of unweathered and weathered stone surfaces

Table 3.14 - Waviness parameters (µm)obtained by applying a Gaussian filter with SurfCharJ plug-in in ImageJ

Sample ID	***Wq***	***Wa***	***Wsk***	***Wku***	***Wv***	***Wp***	***Wt***	***Wc***
NT	5.163	4.2688	-0.4247	-0.2748	184.052	207.4326	23.3806	198.1945
4cycles	5.9865	4.7225	-0.7291	0.4169	189.4461	218.2377	28.7916	208.4893
8cycles	4.3765	3.6387	-0.285	-0.2868	212.2334	230.479	18.2457	222.6724
12cycles	12.4268	10.0627	-0.5708	0.4243	146.838	208.5718	61.7338	187.0715
15cycles	10.9475	9.3109	-0.095	-0.7557	147.0225	193.6263	46.6037	172.0755

In fact, a whole increasing of undulations parameters and profiles evaluated in term of waviness (*i.e.* structures exhibiting wavelength several times longer than deep) can be observed (see Figure 3.29).

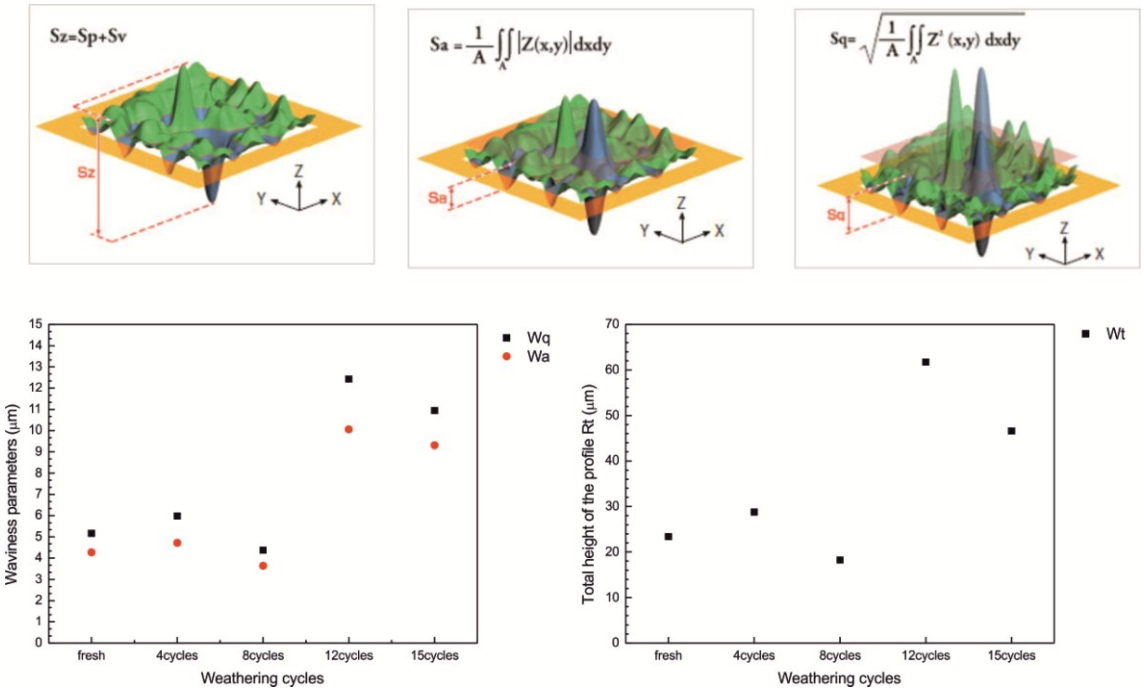

Figure 3.29 - Correlation between waviness parameters and weathering cycles

3.7.2 Final remarks

The digital imaging analysis of unweathered and weathered Sabucina stone samples allows to describe the evolution of surface degradation process due to salts weathering.

In detail, by monitoring the roughness changes over the different artificially weathering cycles, a decrease of parameters and profiles has been observed, claiming a smoothing of the surface evaluated at smaller wavelengths. On the contrary, an increasing of longer-length ondulation structures has been observed, as testified by the inspection of waviness surface plot images and the calculated parameters. In this sense, the image sequence analyzed by this technique and the surface profiles acquired on images (see Figure 3.30) helps to better understand the evolution of stone decay process in term of time and space. In fact, as the weathering process proceeds, the granular disintegration and powdering of the surface, representing the main degradation forms

observed on studied samples, determines a decrease of shorter-length ondulation and, at the same time, an increasing of the longer wavelength component.

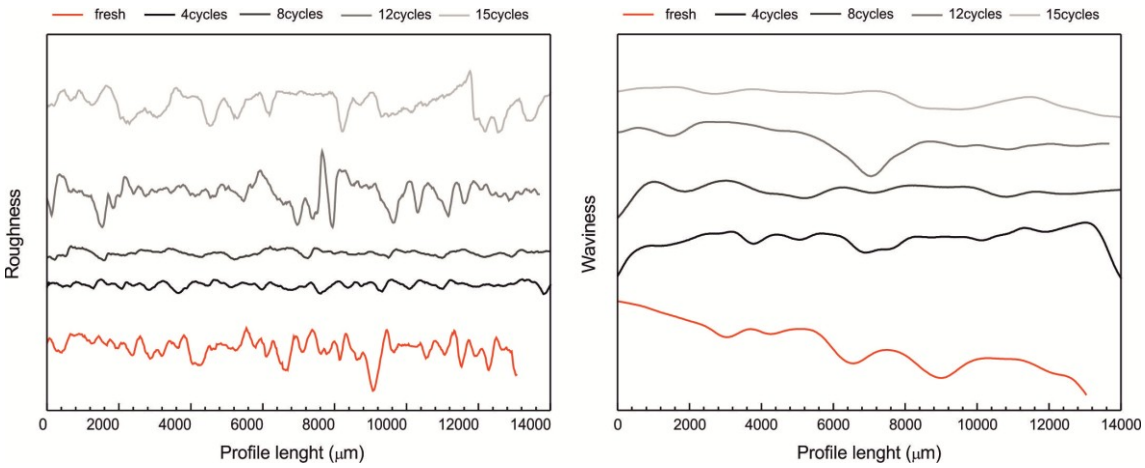

Figure 3.30 - Surface roughness and waviness profiles in function of weathering cycles

In conclusion, we can asses that the digital image processing of the weathered surfaces constitutes a useful tool to create damage maps of building stone affected by weathering, allowing to monitor and quantify the changes in surface texture due to salt crystallization action.

3.8 Discussion and Conclusions

In this section we have demonstrated that the complete quantification and visualization of surface and sub-surface features changes due to salt weathering can be achieved by applying a multi-methodological approach, able to combine classical and innovative analysis techniques.

First of all, the application of classical intrusion method as mercury intrusion porosimetry (MIP) and the subsequent treatment of data according to empirical models have allowed to obtain information on weathering mechanism as well as location of salts in the studied stone. These statements have been therefore used for the interpretation of physical and mechanical parameters esteemed by following standard recommendations on weathered samples; in fact, the data trends obtained in this framework couldn't be completely explained without the supporting case of porosimetric measurements.

Beside the successfully results obtained by applying the aforementioned destructive and micro-destructive methods, the use of innovative methods has allowed to obtain extremely accurate data, improving the quality of previously ones and taking advantage of non-destructive and non-invasive features of the used techniques. In this sense, the application of portable single side NMR technique has evidenced the possibility to obtain pore size distribution data absolutely comparable with MIP results, allowing therefore a complete porosimetric analysis of a porous media in easily-handled, convenient, fast, and, most importantly, non-destructive way. In addition, this technique allows to avoid possible inaccurate estimations due to the application of

high-pressure intrusion method by mercury, keeping away also problems related to the specimens sampling and the use of not eco-friendly materials for the analysis of stones.

However, all the aforementioned methods don't allow the visual inspection of both processes and effects related to weathering action; in this framework, the application of imaging techniques that use X-ray and neutron sources has been demonstrated the most powerful ones in quantifying and visualizing the pore network arrangement and hydric proprieties changes in stone samples subjected to salt weathering. In this sense, the use of X-ray tomography has allowed to obtain better results in term of quantification of pore structure changes due to degradation; otherwise, the visualization and quantification of changes in capillary absorption proprieties of the stone have been reached by using neutrons.

Summarizing, in the case of Sabucina Stone, the comparative measurements performed on unweathered and artificially weathered samples subjected to different degradation degree have allowed to conclude the following:

- weathering process due to sodium sulphate crystallization acts in a first stage by filling the entry of pores, whit a subsequent enlargement of them; then, a filling in pores characterized by larger throats from the 4th crystallization cycles has been observed. In fact, the modal pore radius shifts from a values of about 8 μm in unweathered sample to 12 μm in weathered ones, with a peak of 14 μm corresponding to the change in degradation mechanism; in this framework, salts are located in pores ranging from 50 to 100 μm. Trends obtained by MIP measurements are confirmed by NMR data, that allow to infer the same conclusion in a non-destructive and non-invasive way (shift of T_2 more populated component from ~10 ms to ~60 ms).
- The data about pore changes have been accurately quantified and visualized by using X-ray μ-CT; salt crystallization acts to increase the total porosity with an increase of open porosity and a concomitant decrease of the closed one. Overall, the enlarged pores in weathered samples exhibit higher MO and ED values than the freshly quarried sample.
- All the previously observations have a great influence on the mechanical behavior of the stone, as the UCS values measured exhibit a trend inversion in correspondence with the degradation mechanism change at the 4th crystallization cycle. In fact, up to the 2nd to the 4th crystallization cycles, salts fill the pore throats, determining a slight and progressive increment of compressive strength resistance. Otherwise, when the enlargement of the throats and the filling of larger pores have occurred (i.e. up to 6th crystallization cycle), a decrease of UCS values has been observed, claiming a strictly relation between the location of salts and the mechanical resistance of the stone.
- As far as the pores are enlarged, the stone become able to absorb much more water, as testified by the increasing of saturation coefficient with the advancement of the degradation process. However, the comparison between interconnection parameters in

unweathered and weathered samples highlights that the salt weathering process doesn't alter the ability of the stone to vehicle moisture. These evidences are enforced by the results obtained by both gravimetric tests and neutron imaging. In particular, the neutron images analysis allows to highlight that water penetrates more quickly and deeper into weathered samples and such a behavior has to be related to the modification of pore structure that determine an higher ability to absorb greater volume of water, especially in enlarged pores created by the intense degradation action. In the weathered stone samples, the ability to speedy vehicle the water in vertically orientation is associated with a relevant horizontally spread of the water in coarser pores, in which more water is absorbed; this process determines the presence of isolated and irregularly distributed areas that exhibit higher WC% values than the surrounding. Therefore, until the water vertically flows up to saturate the entire volume sample, a lower WC% waterfront proceeds upwards, while the coarser pore structures allow the absorption of higher water content, determining subsequent waterfronts at different WC% values.

- However, water penetrates by capillarity in not homogenous and non perfect linear way, due to slight heterogeneity in capillarity absorption proprieties of sub-volumes inside the samples. In addition, an evidence of side effects due to more intense action of the degradation process close the surface is claimed by the speedy advancement of the waterfront and the high WC% content at the edges of the weathered stone samples respect to the inner part. These evidences are better visualized in neutron tomographies by the occurrence of differential flow patterns inside the whole investigated volume of weathered samples.
- The more intense action of weathering on surface has been claimed, finally, by a significant change of roughness and waviness parameters measured by 3D digital microscope and a consequently general smoothing of the surface.

On the basis of aforementioned, is possible to assume that the studied system (both in term of sub-surface and surface features) become more complex with the advancement of weathering process; in fact, surface is smoothed, new range of pores appear, part of closed porosity is opened and therefore become accessible to moisture flow, water can spread rapidly both vertically and horizontally thanks also the presence of enlarged pores and, finally, the new arrangement cause the development of preferential water uptake fluid-flow pattern.

As aspects such process operating, weathering mechanism, stone response and quantification of damage are clarified, interesting implication about the complicate relation between rate and scale can be also concluded. On the whole, all methods suggest, in fact, that the most intense effects of the degradation occur up to the 4-6th crystallization cycles (giving therefore information on rate) and that the salts crystallization process in the studied material is

independent from the scale, as comparable results have been obtained on samples exhibiting different dimension and shape used in the different experimental setups.

Therefore, the overall of the obtained data has to be considered a good example of how the applied experimental and empirical approach is able to investigate salt weathering processes, suggesting also the possibility to apply it on a wide class of building stone materials, also exhibiting complex textural and structural features as in the case of Sabucina Stone.

3.9 Bibliography

[1] Angeli M, Bigas JP, Benavente D, Menéndez B, Hébert R, David C. Salt crystallization in pores: quantification and estimation of damage. Environmental Geology, 2007. 52:213-205.

[2] Matthews GP, Canonville CF, Moss AK. Use of a void network model to correlate porosity, mercury porosimetry, thin section, absolute permeability, and NMR relaxation time data for sandstone rocks. Physical Review E, 2006. 73: 031307.

[3] Padhy GS, Lemaire C, Amirtharaj ES, Ioannidis MA. Pore size distribution in multiscale porous media as revealed by DDIF–NMR, mercury porosimetry and statistical image analysis. Colloids and Surfaces A: Physicochem. Eng. Aspects, 2007.300: 222–234.

[4] Jarzyna J, Puskarczyk E. Nuclear magnetic resonance (NMR) and mercury porosimetry measurements for permeability determination. Scientific Annals, School of Geology, Aristotle University of Thessaloniki, 2010. 99: 371-376.

[5] Yao Y, Liu D. Comparison of low-field NMR and mercury intrusion porosimetry in characterizing pore size distributions of coals. Fuel, 2012.95:152–158.

[6] Di Tullio V, Cocca M, Avolio R, Gentile G, Proietti N, Ragni P, Errico ME, Capitani D, Avella M. Unilateral NMR investigation of multifunctional treatments on stones based on colloidal inorganic and organic nanoparticles. Magnetic Resonance in Chemistry, 2015. 53: 64-77

[7] Capitani D, Di Tullio V, Proietti N. Nuclear magnetic resonance to characterize and monitor cultural heritage. Progress in nuclear magnetic resonance spectroscopy, 2012. 64: 29-69

[8] Proietti N, Capitani D, Di Tullio V. Applications of Nuclear Magnetic Resonance Sensors to Cultural Heritage. Sensors, 2014. 14:6977-6997

[9]Richardson BA. The durability of porous stones. Stone Industries, 1991. 26 (10):22–25.

[10] Mod'd BK, Howarth RJ, Bland CH. Rapid prediction of building research establishment limestone durability class from porosity and saturation. Quarterly Journal of Engineering Geology, 1996. 29:285–297.

[11] Matsukura Y, Matsuoka N. The effect of rock properties on rates of tafoni growth in coastal environments. Zeitschrift für Geomorphologie, Supplement Bd., 1996. 106: 57–72.

[12] Ordóñez S, Fort R, García del Cura MA. Pore size distribution and the durability of a porous limestone. Quarterly Journal of Engineering Geology, 1997. 30: 221–230.

[13] Benavente D, García del Cura MA, Fort R, Ordóñez S. Durability estimation of porous building stones from pore structure and strength. Engineering Geology, 2004. 74:113–127.

[14] Angeli M, Bigas JP, Benavente D, Menéndez B, Hébert R, David C. Salt crystallization in pores: quantification and estimation of damage. Environmental Geology, 2007. 52: 205–213.
[15] Yu S, Oguchi CT. Role of pore size distribution in salt uptake, damage, and predicting salt susceptibility of eight types of Japanese building stones. Engineering Geology, 2010. 115:226–236.
[16] Tugrul A. The effect of weathering on pore geometry and compressive strength of selected rock types from Turkey. Engineering Geology, 2004. 75:215–227.
[17] Ludovico-Marques M, Chastre C. Effect of salt crystallization ageing on the compressive behavior of sandstone blocks in historical buildings. Engineering Failure Analysis, 2012. 26:257-247.
[18] Tugrul A, Zarif IH. Correlation of mineralogical and textural characteristics with engineering properties of selected granitic rocks from Turkey. Engineering Geology, 1999. 51:303–317.
[19] Andriani GF, Walsh N. Physical properties and textural parameters of calcarenitic rocks: qualitative and quantitative evaluations. Engineering Geology, 2002. 67: 5 –15.
[20] Tamrakar NK, Yokota S, Shrestha SD. Relationships among mechanical, physical and petrographic properties of Siwalik sandstones, Central Nepal Sub-Himalayas. Engineering Geology, 2007. 90:105-123.
[21] Zorlu K, Gokceoglu C, Ocakoglu F, Nefeslioglu HA, Acikalin S. Prediction of uniaxial compressive strength of sandstones using petrography-based models. Engineering Geology, 2008. 96:158-141.
[22] Cultrone G, de la Torre MJ, Sebastián E, Cazalla O. Evaluación de la durabilidad de ladrillos mediante técnicas destructivas (TD) y no-destructivas (TND). Mater. Constr., 2003. 53: 41–59.
[23] RILEM. Recommended test to measure the deterioration of stone and to assess the differences of treatment methods. Mater. Struct., 1980. 13: 175–253.
[24] Molina E, Benavente D, Sebastian E, Cultrone G. The influence of rock fabric in the durability of two sandstones used in the Andalusian Architectural Heritage (Montoro and Ronda, Spain). Engineering Geology, 2015. 197: 67-81.
[25] UNI EN 1926 Natural stones test methods: Determination of compression strength, UNI ed., Milano, 2000.
[26] NORMAL 22/86 Natural stones test methods: Determination of ultrasonic waves velocity.
[27] UNI EN 1936 Natural stones test methods: Determination of real density and apparent density and of total and open porosity, UNI ed., Milano, 2001.
[28] Raneri S, Cnudde V, De Kock T, Derluyn H, Barone G, Mazzoleni P. X-ray computed micro-tomography to study the porous structure and degradation processes of a building stone from Sabucina (Sicily). European Journal of Mineralogy, 2015. 27: 279–288.
[29] Anania L, Badalà A, Barone G, Belfiore C, Calabrò C, Mazzoleni P, Pezzino A. The stones in monumental masonry buildings of the "Val di Noto" area: New data on the relationships between petrographic characters and physical-mechanical properties. Construction and Building Materials, 2012. 33: 122-132.
[30] Steiger M, Asmussen S. Crystallization of sodium sulfate phases in porous materials: The phase diagram Na2SO4–H2O and the generation of stress. Geochimica et Cosmochimica Acta, 2008. 72: 4291–4306.
[31] Yu S, Oguchi CT. Role of pore size distribution in salt uptake, damage, and predicting salt susceptibility of eight types of Japanese building stones. Engineering Geology, 2010. 115: 226–236.

[32] Bergamonti L, Alfieri I, Lorenzi A, Montenero A, Predieri G, Barone G, Mazzoleni P, Pasquale S, Lottici PP. Nanocrystalline TiO2 by sol–gel: Characterization and photocatalytic activity on Modica and Comiso stones. Applied Surface Science, 2013. 282: 165–173.

[33] Barbera G, Barone G, Mazzoleni P, Scandurra A. Laboratory measurement Ultrasound propagation during salt crystallization test: implication for the determination of limestone durability. Construction and Building Materials, 2012. 36: 977–983.

[34] Scherer GW. Stress from crystallization of salt. Cement and Concrete Research, 2004. 34: 1613–1624.

[35] Barone G, Crupi V, Longo F, Majolino D, Mazzoleni P, Raneri S, Teixeira J, Venuti V. A multi-technique approach for the determination of the porous structure of building stone. European Journal of Mineralogy, 2014. 26: 189 – 198.

[36] Barone G, Crupi V, Longo F, Majolino D, Mazzoleni P, Raneri S, Teixeira J, Venuti V. Neutron radiography for the characterization of porous structure in degraded building stones. Journal Instrumentation, 2014. 9: C05024.

[37] Dewanckele J, De Kock T, Boone MA, Cnudde V, Brabant L, Boone MN, Fronteau G, Van Hoorebeke L, Jacobs P. 4D imaging and quantification of pore structure modifications inside natural building stones by means of high resolution X-ray CT. Science of the Total Environment, 2012. 416: 436–448.

[38] Ruiz de Argandoña VG, Rodríguez Rey A, Celorio C, Suárez del Río LM, Calleja L, Llavona J. Characterization by computed x-ray tomography of the evolution of the pore structure of a dolomite rock during freeze-thaw cyclic tests. Physics and chemistry of the earth part A – solid earth and geodesy, 1999. 24: 633-637

[39] Ketcham RA, Carlson WD. Acquisition, optimization and interpretation of X-ray computed tomographic imagery: applications to the geosciences. Computers & Geosciences, 2001. 24: 381-400.

[40] Cnudde V. Jacobs PJS. Monitoring of weathering and conservation of building materials through non-destructive X-ray computed microtomography. Environmental Geology, 2004. 46: 477-485.

[41] De Graef B, Cnudde V, Dick J, De Belie N, Jacobs P, Verstraete W. A sensitivity study for the visualization of bacterial weathering of concrete and stone with computerized X-ray microtomography. Science Of The Total Environment, 2005. 341: 173-183.

[42] Cnudde V, Cwirzen A, Masschaele B, Jacobs PJS. Porosity and microstructure characterization of building stones and concretes. Engineering Geology, 2009. 103: 76-83.

[43] Cnudde V, Silversmit G, Boone M, Dewanckele J, De Samber B, Schoonjans T, Van Loo D, De Witte Yonib Y, Elburg M, Vincze L, Van Hoorebeke L, Jacobs P. Multi-disciplinary characterisation of a sandstone surface crust. Science of the Total Environment, 2009. 407: 5417-5427.

[44] Noriel C, Renard F, Doan ML, Gratier JP. Intense fracturing and fracture sealing induced by mineral growth in porous rocks. Chemical Geology, 2010. 269: 197-209.

[45] Cnudde V, Dewanckele J, Boone M, de Kock T, Boone M, Brabant L, Dusar M, de Ceukelaire M, de Clercq H, Hayen R, Jacobs P. High-Resolution X-Ray CT for 3D Petrography of Ferruginous Sandstone for an Investigation of Building Stone Decay. Microscopy Research and Technique, 2011. 74: 1006-1017.

[46] De Muynck W, Leuridan S, Van Loo D, Verbeken K, Cnudde V, De Belie N, Verstraete W. Influence of pore structure on the effectiveness of a biogenic carbonate surface treatment for limestone conservation. Applied and Environmental Microbiology, 2001. 77: 6808-6820.

[47] Cnudde V, Boone MN. High-resolution X-ray computed tomography in geosciences: a review of the current technology and applications. Earth-Science Reviews, 2013. 123: 1–17.

[48] Derluyn H, Griffa M, Mannes D, Jerjen I, Dewanckele J, Vontobel P, Sheppard A, Derome D, Cnudde V, Lehmann E, Carmeliet J. Characterizing saline uptake and salt distributions in porous limestone with neutron radiography and X-ray micro-tomography. Journal of Building Physics, 2013. 36: 353-374.

[49] Wildenschild D, Sheppard A P. X-ray imaging and analysis techniques for quantifying pore-scale structure and processes in subsurface porous medium systems. Advances in Water Resources, 2013. 51: 217-246.

[50] Derluyn H, Dewanckele J, Boone MN, Cnudde V, Derome D, Carmeliet J. Crystallization of hydrated and anhydrous salts in porous limestone resolved by synchrotron X-ray microtomography. Nuclear Instruments and Methods in Physics Research B, 2014. 324: 102-112.

[51] Masschaele BC, Cnudde V, Dierick M, Jacobs P, Van Hoorebek L, Vlassenbroeck J. UGCT: New x-ray radiography and tomography facility. Nuclear Instruments & Methods In Physics Research Section A-Accelerators Spectrometers Detectors And Associated Equipment, 2007. 580: 266-269.

[52] Vlassenbroeck J, Dierick M, Masschaele B, Cnudde V, Van Hoorebeke L, Jacobs P. Software tools for quantification of X-ray microtomography at the UGCT. Nucl Instrum Meth A, 2007. 580: 442–445.

[53] Abramoff MD, Magalhães Paulo J, Ram Sunanda J. Image Processing with ImageJ. Biophotonics International, 2004. 11:36-42.

[54] Brabant L, Vlassenbroeck J, De Witte Y, Cnudde V, Boone MN, Dewanckele J, Van Hoorebeke L. Three-Dimensional Analysis of High-Resolution X-Ray Computed Tomography Data with Morpho+. Microscopy And Microanalysis, 2011. 17: 252-263.

[55] Perfect E, Cheng CL, Kanga M, Bilheux MZ, Lamanna JM, Gragg MJ, Wright DM. Neutron imaging of hydrogen-rich fluids in geomaterials and engineered porous media: A review. Earth-Science Reviews, 2014. 129:120-135.

[56] Pleinert H, Degueldre C. Neutron radiographic measurement of porosity of crystalline rock samples, a feasibility study. J. Contam. Hydrol.,1995. 19: 29–46.

[57] de Beer FC, Middleton MF, Hilson J. Neutron radiography of porous rocks and iron ore. Appl. Radiat. Isot.,2004. 61: 487–495.

[58] de Beer, F.C., Middleton, M.F. Neutron radiography imaging, porosity and permeability in porous rocks. S. Afr. J. Geol., 2006. 109, 541–550.

[59] Pleinert H, Sadouki H, Wittmann F H. Determination of moisture distributions in porous building materials by neutron transmission analysis. Mater Struct., 1998. 31(4): 218−224

[60] Hassanein R, Lehmann E, Vontobel P. Methods of scattering corrections for quantitative neutron radiography. Nucl Instrum Meth A, 2005. 542(1-3): 353−360

[61] Hassanein R, Meyer HO, Carminati A, Estermann M, Lehmann E, Vontobel P. Investigation of water imbibition in porous stone by thermal neutron radiography. J Phys D: Appl Phys, 2006. 39(19): 4284−4291

[62] Masschaele B, Dierick M, Cnudde V. High-speed thermal neutron tomography for the visualization of water repellents, consolidants and water uptake in sand and lime stones. Radiat Phys Chem, 2004. 71(3-4): 807−808

[63] Ridgway C J, Gane P A C, Ei-Abd AEG, Czachor A. Water absorption into construction materials: comparison of neutron radiography data with network absorption models. Transp Porous Media, 2006. 63(3):503−525

[64] Pugliesi R, Andrade MLG. Study of cracking in concrete by neutron radiography. Appl Radiat Isot, 1997. 48(3): 339−344

[65] Zhang P, Wittmann FH, Zhao TJ. Observation of water penetration into water repellent and cracked cement-based materials by means of neutron radiography. Int J Restor Build Monum, 2009. 15(2): 91−100

[66] Cnudde V, Dierick M, Vlassenbroeck J, Masschaele B, Lehmann E, Jacob P, Van Hoorebeke L. High-speed neutron radiography for monitoring the water absorption by capillarity in porous materials. Nucl. Instrum. Methods Phys. Res. B.,2008.266: 155–163.

[67] Kang M, Perfect E, Cheng CL, Bilheux HZ, Gragg M, Wright DM, Lamanna JM, Horita J, Warren JM. Diffusivity and sorptivity of Berea sandstone determined using neutron radiography. Vadose Zone J.,2013. http://dx.doi.org/10.2136/vzj2012.0135.

[68] Masschaele B, Dierick M, van Hoorebeke L, Cnudde V, Jacobs P. The use of neutrons and monochromatic X-rays for non-destructive testing in geological materials. Environ. Geol., 2004. 46: 486–492.

[69] Dierick M, Vlassenbroeck J, Masschaele B, Cnudde V, van Hoorebeke L, Hillenbach A. High-speed neutron tomography of dynamic processes. Nucl. Instrum. Methods Phys. Res. A, 2005. 542: 296–301.

[70] Hameed F, Schillinger B, Rohatsch A, Zawisky M, Rauch H. Investigations of stone consolidants by neutron imaging. Nucl. Instrum. Methods Phys. Res. A, 2009. 605: 150–153.

[71] Zawisky M, Hameed F, Dyrnjaja E, Springer J, Rohatsch A. Digitized neutron imaging with high spatial resolution at a low power research reactor: applications to steel and rock samples. Nucl. Instrum. Methods Phys. Res. Sect. B, 2010. 268: 2446–2450.

[72] Kim FH, Penumadu D, Hussey DS. Water Distribution Variation in Partially Saturated Granular Materials Using Neutron Imaging, J. Geotech. Geoenviron. Eng., 2012.138:147-154.

[73] NORMAL 11/88 Natural stones test methods: Determination of water absorption coefficient by capillarity.

[74]Fitzner B. Porosity properties and weathering behavior of natural stones. Methodology and examples. Stone material in monuments: diagnosis and conservation. 2nd Course of CUM. Heraklion; 1993. 43–54.

[75] Zezza F. Digital image processing of weathered stone in polluted atmosphere. Weathering and air pollution. 1st Course of CUM. Lago di Garda (Portese); 1991. 217–28.

[76] Aires-Barros L, Mauricio A, Figueiredo C. Profilometry and image analysis applications to ‘‘in situ’’ study of monuments stone decay phenomenon. In: Proceeding of the III international symposium on the conservation of monuments in the Mediterranean Basin, Venezia, 1994. 19–24.

[77] Kapsalas P, Maravelaki-Kalaitzaki P, Zervakis M, Delegou ET, Moropoulou A. A morphological fusion algorithm for optical detection and quantification of decay patterns on stone surfaces. Construct Build Mater, 2006. 22:228–38.

[78] Vázquez MA, Galán E, Guerrero MA, Ortiz P. Digital image processing of weathered stone caused by efflorescences: A tool for mapping and evaluation of stone decay. Construction and Building Materials, 2011. 25: 1603–1611

[79] Stephenson WJ, Finlayson BL. Measuring Erosion with the Micro-Erosion Meter—Contributions to Understanding Landform Evolution. Earth-Science Reviews, 2009. 95, 53-62.

[80] Sharp D, Trudgill ST, Crooke RU, Price CA, Crabtree RW, Pickles AM, Smith D. Weathering of the Balustrade on St Paul's Cathedral, London. Earth Surface Processes and Landforms, 1982. 7, 387-390.

[81] Trudgill ST, Gosling W, Yates T, Collier P, Smith DI, Cooke RU, Viles HA, Inkpen R, Moses C. Twenty-Year Weathering Remeasurements at St Paul's Cathedral, London. Earth Surface Processes and Landforms, 2001. 26, 1129-1142.

[82] Kamh GME, Hanna H. Measuring Rock Surface Roughness by Micro-Erosion Meter as Indication of Weathering Intensity of St. John Medieval Church, Chester City, UK. Egyptian Journal of Geology, 2002. 46, 461-469.

[83] López-Arce P, Varas-Muriel MJ, Fernández-Revuelta B, Álvarez de Buergo M, Fort R, Pérez-SobaC. Artificial Weathering of Spanish Granites Subjected to Salt Crystallization Tests: Surface Roughness Quantification. Catena, 2010. 83: 170-185.

[84] Jaynes SM, Cooke RU. Stone Weathering in Southeast England. Atmospheric Environment, 1987. 21, 1601-1622.

[85] Chinga G, Johnsen PO, Dougherty R, Lunden Berli E, Walter J. Quantification of the 3D microstructure of SC surfaces. Journal of Microscopy, 2007. 227: 254–265.

[86] Chinga G, Gregersen Ø, Dougherty R. Paper surface characterisation by laser profilometry and image analysis. J. Microsc. Anal., 2003. 84: 5–7.

[87] Volk R. Rauheitsmessungen, Theorie und Praxis, eds. DIN Deutsches Institut fürNormung, 2005, Berlin, Wien, Zürich: Beuth Verlag.

Chapter 4. Use of fractal models to describe pore structure of building stones

4.1 Fractal geometry of stone pore surface

In recent years fractal geometry has been successfully used to describe a great variety of porous solid materials, as it represents a suitable geometric model to study and model pore networks, especially in the case of materials in which pores cover wide ranges of dimension.

In this framework, interesting studies have been proposed in the recent literature; among them, the fractal dimensions has been determined in coal particles using mercury porosimetry and a model based on the Menger sponge has been developed[1]. Fractal geometry has been also used in studies about soils[2], also evidencing the suitability of the method in describing their evolution during different processes[3,4] and predicting their hydraulic proprieties[5]. Referring to natural stones, the fractal dimension of several natural stone used as building materials has been calculated by using different mathematical models[6], demonstrating as this parameter can be used to describe the microtextural features of studied materials[7]; moreover, the fractal behavior of the pore space of sandstone has been studied to predict several stone prorpieties[8-10];the micropore surface fractal dimension has been calculated in marble, studying the evolution of this parameter with mechanical pressure[11]. Moreover, fractal dimension has been used to predict the permeability in sedimentary rocks[12]. Interesting application is represented by the correlation between fractal dimension and degradation in natural building stones[13], highlighting the potential of this parameter as weathering descriptor.

This latter approach has been used in the present work with the aim to highlight the potential of fractal dimension in describing the pore network changes that occur in natural building stones when they are subjected to salt weathering degradation processes. Fractal dimension has been calculated by using mercury porosimetry; the obtained results allow us to determine a positive trend between the obtained D values and degradation degree, demonstrating the suitability of the method in describe pore structure modification in building stones.

Finally, the calculated fractal dimension has been also used to predict permeability and tortuosity in the studied stone and evaluate the changes of these parameters in relation to salt weathering process.

4.2 Fractal dimension as weathering descriptor of stone pore surface

Starting from porosimetric analyses performed on fresh, weathered and cleaned samples of Sabucina Stone (*see Chapter 3, Section 2*), the fractal dimension of pore surface has been extracted following the surface fractal model by Friesen and Mikula[1].According to it, the

cumulative intrusion volume derivative with respect to pressure and the surface fractal dimension D are related by the relation:

$$\log\frac{dV}{dP} \propto (D-4)\log(P) \qquad (52)$$

being V the cumulative intrusion volume at a given pressure P.

Using those relations the surface fractal dimension can be easily calculated; in fact, plotting the logarithm of derivative cumulative intrusion volume vs. pressure logarithm, if pore surface is fractal between ranges of pore diameters, a linear tendency should be observed and D is obtained from the slope of that line.

As far as the aforementioned, the fractal dimension for fresh, weathered and cleaned samples has been calculated (average data on almost three MIP measurements); the obtained results are summarized in Table 4.1 and in Figure 4.1 the linear fit plots of logarithmic derivative intrusion volume vs. logarithmic pressure for fresh, weathered (14 cycles) and cleaned (14 cycles) samples are reported, as examples.

Table 4.1 - Slopes and fractal dimension calculated for fresh, weathered and cleaned samples

Sample ID	***Salt weathered***			***Cleaned***		
	Slope	***R^2***	***Fractal dimension D***	***Slope***	***R^2***	***Fractal dimension D***
fresh	1.23	0.98299	2.77	1.23	0.98299	2.77
4 cycles	1.18046	0.98334	2.81954	1.10894	0.97876	2.89106
6 cycles	1.19412	0.97855	2.80588	1.17861	0.98917	2.82139
8 cycles	1.19978	0.98651	2.80022	1.15809	0.98721	2.84191
10 cycles	1.1604	0.98513	2.8396	1.1295	0.98295	2.8705
12 cycles	1.09306	0.96723	2.90694	1.08853	0.97604	2.91147
14 cycles	1.10181	0.9766	2.89819	1.08737	0.97873	2.91263

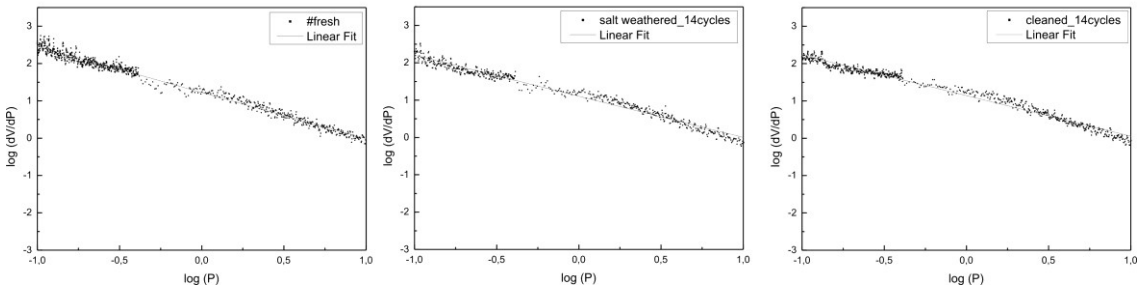

Figure 4.1 - Logarithmic derivative intrusion volume vs. logarithmic pressure plot for fresh weathered and cleaned samples.

In detail, according to Perez Bernal & Bello Lopez, 2000[13] the weathering process determine a progressive increase of pore surface fractal dimension, *i.e.* from 2.77 in fresh samples to 2.90 in weathered samples and to 2.92 for cleaned ones (at the end of the 14 cycles), as testified by the linear positive trend of fractal dimensions vs. degradation degree described both for weathered and cleaned samples (Figure 4.2). Considering that the fractal dimension describe the *complexity* of the pore surface, the obtained behavior suggests a progressive increase of pore complexity, maybe due to the presence of salts, in the case of weathered samples, and the

appearance of new pores, especially in the case of cleaned samples, according to the porosimetric curves shown in *Chapter 3, Section 2*. Noteworthy is that in the cleaned samples the fractal dimension D is greater than in the weathered ones subjected at the same degradation degree.

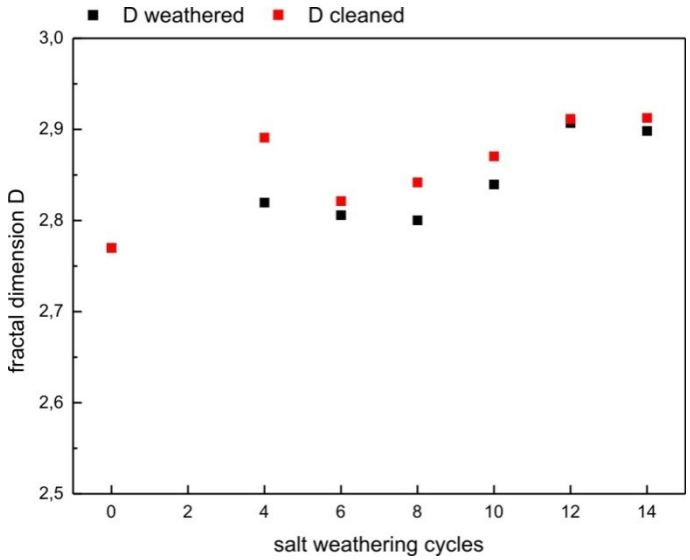

Figure 4.2 - Correlation between fractal dimension as obtained by mercury intrusion porosimetry and weathering cycles.

4.3 Bibliography

[1] Friesen WI, Mikula R J. Fractal dimension of coal particles. Colloid Interface Sci., 1987.120, 263-271.

[2] Perfect E, Kay B D. Applications of fractals in soil and tillage research: a review. Soil and Tillage Res., 1995. 36, 1–20.

[3] Comegna V, Damiani P, Sommella A. Use of a fractal model for determing soil water retention curves Geoderma, 1998.85, 307-323.

[4] Rappoldt C, Crawdord JW. The distribution of anoxic volume in a fractal model of soil. Geoderma, 1999.88, 329-347.

[5] Giménez D, Perfect E, Rawls WJ, Pachepsky Y, Fractal models for predicting soil hydraulic properties: a review. Engineering Geology, 1997.48, 161–183.

[6] Perez Bernal JL, Bello Lopez MA. Fractal geometry and mercury porosimetry. Comparison and application of proposed models on building stones. Appl. Surf. Sci., 2001. 185, 99-107.

[7] Pape H, Clauser C, Iffland J. Variation of permeability with porosity in sandstone diagenesis interpreted with a fractal pore space model. Pure applied Geophysics, 2000.157, 603-619.

[8] Pape H, Clauser C, Iffland, J. Permeability prediction based on fractal pore-space geometry. Geophysics, 1999. 64, 1447-1460.

[9] Barone G, Crupi V, Longo F, Majolino D, Mazzoleni P, Raneri S, Teixeira J, Venuti V. A multi-technique approach for the determination of the porous structure of building stone. European Journal of Mineralogy, 2014. 26, 189-198.

[10] Katz A J, Thompson AH. Fractal Sandstone Pores: Implications for Conductivity and Pore Formation. Phys. Rev. Lett. 1985.54, 1325–1328.
[11] Xie H, Wang J, Qan P. Fractal characters of micropore evolution in marbles. Phys. Lett. A, 1996. 218, 275–280.
[12] Schlueter EM, Zimmermana RW, Witherspoon PA, Cook NGW. The fractal dimension of pores in sedimentary rocks and its influence on permeability. Eng. Geol. 1997. 48, 199-215.
[13] Perez Bernal JL, Bello Lopez MA. The fractal dimension of stone pore surface as weathering descriptor. Appl. Surf. Sci., 2000. 161, 47-53.

Chapter 5. Innovative consolidant and protective treatments for calcarenite substrate: efficiency tests

5.1 Protective and consolidant treatment for protection and conservation of natural building stones

Stone consolidation and coating with protective treatments are current issues in conservation and restoration of Cultural Heritages. Consolidant and water repellent protective products should exhibit stability, compatibility and suitable penetration depth, allowing also improvement of mechanical proprieties and decrease of water absorption, respectively.

In recent years, the introduction of *nanostructured materials* developed by using *sol-gel processes* has largely increased in the framework of preservation and conservation of stone and ligneous-cellulosic materials, as the process allows to produce various materials with novel, predefined properties in a simple way and at relatively low cost.

In this section, an experimental study finalized to test the efficiency of innovative consolidant and protective synthesized at Department of Chemistry in University of Parma has been proposed.

In detail, a routine based on standard tests[1-6] has been applied in order to verify the compatibility of the product and the suitability of them on calcarenite substrate.

Moreover, in order to visualize the penetration depth and the distribution of the investigated products inside the studied stone (*Sabucina Stone)*, neutron imaging have been collected at X-ray micro-tomography facility UGCT, Ghent, Belgium and at the LLB Laboratories (Saclay, France)[7].

5.1.1 Sol-gel process

The sol-gel process is a well-established colloidal chemistry technology which offers the possibility to obtain various materials with new proprieties by simple process and at relatively low cost. It consists in the chemical transformation of a liquid (the *sol*) into a *gel* state, with subsequent transition into solid material and represents the unique method in material science for producing solid materials from very small particles[8]. This experimental approach, known as *bottom to up process*, is able to build up nanostructures starting from atoms or molecules.

In detail, the sol-gel process usually consists in the following stages:

a) *hydrolysis* of the precursors (usually alkoxides) with the formation of hydroxide species;
b) *condensation*, with the formation of oxide species;
c) *gelation,* with the formation of a network which entraps the remaining solution;
d) *ageing*, with the formation of further cross-links and development of porosity;

e) *drying*, with the loss of solvent and the associated development of capillary stress;
f) *densification*, with the collapse of the open structure and formation of a dense and solid material.

The reactions of hydrolysis and condensations occur simultaneously and can be catalyzed by acids or bases. The hydrolysis consists in the formation of reactive hydroxyl groups from the hydrolysis reaction of metal alkoxides M $(OR)_m$ (where M represents Si or a metal like Al or Ti); subsequently, the hydroxyl group on the metal condenses to form M-O-M bonds, as following:

$$M(OR)_m + xH_2O \rightarrow M(OH)_x(OR)_{(m-x)} + xR(OH)(\boldsymbol{hydrolysis})$$

$$\equiv M - OH + \equiv M - OH \rightarrow \equiv M - O - M \equiv + H_2O\ (\boldsymbol{condensation})$$

After the condensation stage, when the repulsive charges located on the surface of M-O-M aggregates are low enough, progressively an aggregation into three- dimensional networks growths from the solution (*gelation phase*). Before the gelation point and under acidic conditions, the precursor of the gel consists of linear or randomly branched polymers, while, under basic conditions this is made up of individual highly branched clusters. At the gelation point, the viscosity increases and a transparent gel is formed. This latter one system, depending on temperature, solvent and pH conditions, is subjected to a process known as *ageing,* consisting in shrinkage and stiffening of the material, with evaporation of the residual liquid phase. During the ageing stage, the differential evaporation rate of the solvent inside and on the surface of the system can cause the formation of cracks; to avoid this phenomenon, a slow evaporation rate of the solvent is required.
The last stage of the process consists in the *densification* of the dry gel structure to form a solid material. This stage requires both time and temperature in such a way that the thermal treatment can influence the characteristics of the resulting solid material.
By using sol-gel process it is possible to fabricate *nanocomposites* (*i.e.*, materials consisting of various phases with different compositions and at least one constituent phase has one dimension less than 100 nm) and *hybrid organic-inorganic materials*, both exhibiting features useful for stone protection and consolidation.

5.1.2 Titanium nanoparticles based products

In recent years, the use of self-cleaning photocatalytic coatings for building stones has largely increased, due to their less expensive production processes, high efficiency and eco-friendly features[9]. Among them, titanium dioxide (TiO_2) is considered the most promising material for

the photocatalytic degradation of environmental pollutants, being highly efficient, non-toxic and stable under irradiation. In detail, beside several applications in environmental fields, TiO_2nanoparticle sols have been successfully tested on calcarenite substrates in order to preserve ancient masonry in Cultural Heritage sciences[10-12].

TiO_2 is present in nature as rutile, anatase, and brookite[13]; among them, the anatase phase is the most active[14,15], even if important results were also obtained withTiO_2 in brookite and rutile pure or mixed forms[16-18]; TiO_2 is nontoxic, highly efficient, economic, easily available, and stable under ultraviolet (UV) light.

There are lots of ways to prepare TiO_2-based photocatalysts (for example, chemical vapor deposition, co-precipitation, hydrolysis and impregnation), but, among these, the sol–gel method is the most advantageous because it allows to obtain a nanocrystalline material with high purity at a relatively low temperature, with controlled particle morphology.

The photocatalytic activity of TiO_2 is based on the ability of titanium dioxide to catalyze reaction under UV light. In detail, when TiO_2 is irradiated by UV, it adsorbs photon producing electron–hole pairs (an electron (e^-) promoted from the valence band to the conduction band with simultaneous generation of a positive hole (h+) in the valence band) as following:

$$TiO_2 + UV = TiO_2(e^- + h^+) \qquad (53)$$

The electrons can either recombine with the holes or the electron-hole pairs can participate in red-ox reactions, leading to the formation of reactive oxygen species. Electrons may reduce organic compounds or reacts with electron acceptors such as O_2 adsorbed on the Ti-surface or dissolved in water, reducing it into superoxide radical anion$O_2^{\cdot}$.

$$O_2 + TiO_2(e^-) = TiO_2 + O_2^{\cdot} \qquad (54)$$

The photo-generated holes can oxidize organic molecules to form R+, or react with surface hydroxyls or H_2O, oxidizing them into $OH^{\cdot}$ radicals.

$$H_2O + TiO_2(h^+) = TiO_2 + OH^{\cdot} + H^+) \qquad (55)$$

Decomposition of most organic compounds occurs as the result hydroxylation of the primary reduction products. Also the reactions of organic compounds with $O_2^{\cdot}$ and with radicals formed upon the photoprotonation of $O_2^{\cdot}$ may lead to the decomposition of organic compounds. Both $OH^{\cdot}$ and $O_2^{\cdot}$ radicals are then effective to drive organic compounds degradation. The electron transfer between organic compounds and nanosized semiconductor particles can degrade them

to smaller organic substances and ultimately mineralized completely to water, carbon dioxide, and other inorganic ions.

5.1.3 Hybrids organic-inorganic products

The term *hybrids*[19] is usually referred to a product characterized by both the robustness of an inorganic skeleton and the functional proprieties of organic material; it can be obtained by the sol-gel process. In this latter case, both the organic and the inorganic phases are formed together through the simultaneous polymerization of an organic monomer and of a sol-gel precursor of the inorganic domains. There are several methods to synthesize organic-inorganic hybrids but the sol-gel process is the most common as it guarantees mild processing characteristics and easy control over the preparation.

Among hybrids, the silicon based products obtained by sol–gel process are becoming widely diffused in the field of inorganic–organic hybrid materials, due to the good processability and the stability of the Si—C bond during the formation of a silica network which allowed the production of organic-modified inorganic networks in one step.

On the basis of the level of interaction between the organic and inorganic phase, two type of hybrid materials cab be distinguished; the first one, named *class I*, are characterized by weak interactions between the two phases (*i.e.* van deer Waals or hydrogen bonds),whereas the *class II* exhibits strong chemical interactions (*i.e.* covalent bonds) between the components.

5.2 Protective treatments

5.2.1 Self-cleaning photocatalytic products based on TiO_2 nanoparticles

5.2.1.1 Synthesis via sol-gel and application of TiO_2 nanoparticles

TiO_2 nanoparticles obtained by sol-gel techniques at two different pH (1.3-10.6)[20] have been tested on carbonate substrate, namely Sabucina Stone.

Referring to the synthesis of the TiO_2 (0.1 M) sols, they have been obtained by mixing, under dry conditions, titanium isopropoxide $Ti\{OCH(CH_3)_2\}_4$ with glacial acetic acid or malonic acid in 1/1 molar ratio; after 30 min of stirring distilled water was added. At this stage two synthetic routes were followed which differ for the choice of the peptizing medium, acid in the first case (i), basic in the second one (ii).

(i) The sol called TiAcN has been obtained by adding HNO_3 as peptizer to the TiO_2 starting sol, till to pH≈1 and refluxed at 100 °C for 3 hours. The refluxing is necessary to promote the transformation from amorphous to nanocrystalline titania. The resulting sol is completely transparent.

(ii) The sol named TiMaA has been synthesized from the starting sol containing malonic acid as complexing agent by refluxing in a basic environment after addition of triethylamine till to the complete peptization. TiMaA is found to be transparent and stable.

The two TiO_2 sols have been applied with a bristle brush directly on the stone samples.

After each treatment the samples have been kept at 60 °C for 24 hours and then dried in a dessiccator and weighted, repeating the cycle up to weight stabilization. It was assumed that the dry weight is reached when the difference between two consecutive weight measurements is less than 0.1% of the initial weight of the sample. The stone samples were then stored in a dessiccator at a temperature of (25± 1) °C.

As the use of coatings with a self-cleaning activity on architectural elements requires that they do not alter the original aspect of stone substrates and do not produce physical and chemical changes causing harmful effects[21], efficiency test have been carried out according to UNIEN standards[1-6].

5.2.1.2 Efficiency test

5.2.1.2.1 Colorimetric tests

To evaluate the changes of the stone surface appearance due to the TiO_2 based coatings, colorimetric analysis has been performed by a Techkon Spectrodens colorimeter. At least ten spot of about 1 mm^2in area have been examined and averaged on each stone sample, using one sample for each case and performing almost nine analysis points on the surface before and after the treatment.

According to UNI EN 15886[4] the color difference (ΔE) due to TiO_2 applications with respect to the uncoated stone was measured in the CieLab space:

$$\Delta E = \sqrt{\Delta L^{*2} + \Delta a^{*2} + \Delta b^{*2}} \qquad (56)$$

where ΔL* is the change in lightness, Δa*and Δb* the change in hue (a* is the red (>0)/green (<0) coordinate and b* the yellow (>0)/blue (<0) coordinate, in the CIELAB notation).

In Table 5.1 the chromatic coordinates a*, b* and L* collected on untreated and treated samples are summarized, while in Table 5.2 the ΔE values calculated are reported.

Table 5.1 - Chromatic coordinates a, b* and L* collected on untreated and treated samples*

Points	***Untreated***			***TiAcN***			***Untreated***			***TiMaA***		
	L*	***a****	***b****	***L****	***a****	***b****	***L****	***a****	***b****	***L****	***a****	***b****
1	62.83	10.35	30.11	66.13	8.68	22.99	67.57	9.41	29.04	63.25	9.7	22.84
2	67.06	8.02	26.1	65.81	8.18	25.2	64.83	7.51	20.18	65.85	8.95	28.61
3	65.01	10.07	28.81	63.35	7.69	23.09	62.27	8.59	23.19	64.48	8.8	25.33
4	67.96	9.62	28.33	65.94	7.36	20.86	69.22	9.03	24.67	66.42	9.62	26.27
5	65.95	10.78	33.14	64.18	9.24	25.78	64.44	8.96	25.48	62.02	9.13	26.09
6	64.35	7.07	20.07	62.02	7.76	21.59	67.96	9.88	31.81	65.56	9.81	27.16
7	63.6	9.52	28.77	59.82	10.51	27.74	66.86	7.9	23.84	63.08	7.6	20.96
8	64.2	8.6	25.2	68.82	6.53	17.54	63.23	10.01	27.34	61.61	8.41	25.75
9	69.38	7.2	22.06	64.27	11.19	28.92	60.38	10.18	28.8	63.2	9.3	23.99
Average	***65.59***	***9.03***	***26.95***	***64.48***	***8.57***	***23.75***	***65.20***	***9.05***	***26.04***	***63.94***	***9.04***	***25.22***

Table 5.2 - Color difference ΔE values for each treatment

Samples	***L****	***a****	***b****	***ΔE***
untreated	65,59	9,03	26,95	**3,43**
TiAcN	64,48	8,57	23,75	
untreated	65,20	9,05	26,04	**1,50**
TiMaA	63,94	9,04	25,22	

According to Italian guidelines for the restoration of stone buildings[22], *ΔE* after an intervention must be less than 5. Therefore, the values of overall color difference *ΔE**can be considered acceptable after the application of the TiO_2 treatments.

5.2.1.2.2 Photocatalytic test

The self-cleaning properties of the TiO_2 coatings under UV (Helios-Italquartz medium pressure mercury-vapor lamp; 125W; λ_{max}= 365 nm) and Daylight (OSRAM Ultra Vitalux; 300W) lamps has been checked as a function of time. Untreated and treated samples of stones were stained with methyl orange dye (MeO; C = 0.01 M; 400 µg) and methylene blue dye (MB; C = 0.01 M; 500 µg) and placed at 10 cm from the lamps. To evaluate the photocatalytic discoloration of MeO and MB stains during time, colorimetric measurements have been performed by a Techkon Spectrodens colorimeter. The normalized chrome change ΔC was obtained by the chromatic coordinates a* and b* measured by the colorimeter, at different exposure time t:

$$\Delta C = \sqrt{\frac{(a^*(t) - a^*(0)^2 + b^*(t) - b^*(0)^2)}{(a_C^* - a^*(0))^2 + (b_C^* - b^*(0))^2}} \qquad (57)$$

where a*(t) and b*(t) are the colorimetric coordinates at time t, whereas a_C* and b_C*are measured on clean stones before the staining with dyes.

At least ten spot of about 1 mm^2 area have been collected and averaged on each stone sample, using one sample for each case.

In Figure 5.1 the variation of normalized chrome change ΔC in function of time is reported for samples stained with MeO and MB dyes under UV and daylight lamps.

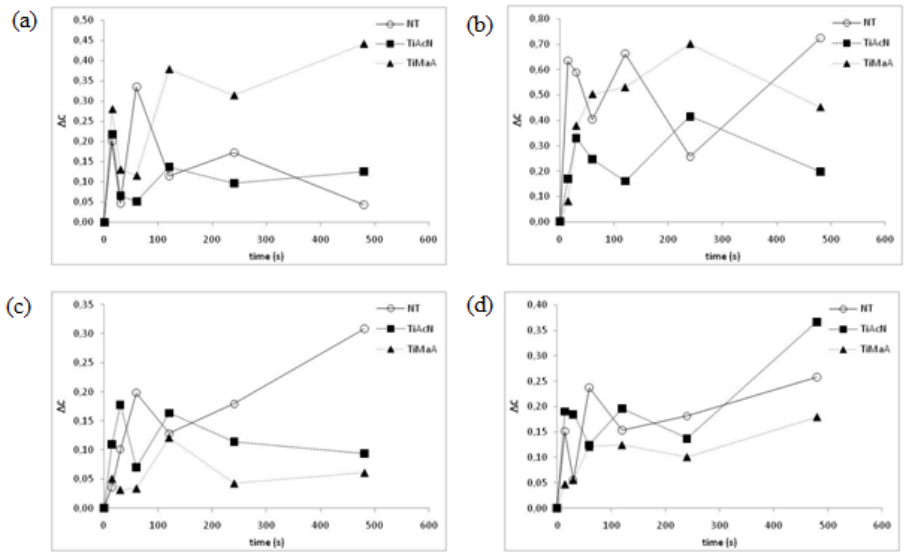

Figure 5.1 - Normalized chromatic changes ΔC (chrome) of the stained at 0.01 M as a function of the irradiation time on Sabucina stone samples of (a) MeO with the UV source, (b) MeO with Daylight source, (c) MB with the UV source and (d) MB with Daylight source

The obtained results show, in general, non-homogenous trends, mainly due to the heterogeneous color of the stone and the high porosity of the surface. Overall, it is possible state that the presence of TiO_2 coating catalyzes the photodegradation of both dyes; in particular, a high efficiency can be observed for the basic preparation (TiMaA) under UV lamp and the acid preparation (TiAcN) under daylight one.

5.2.1.2.3 Comparative water absorption test and accelerated aging test

In order to evaluate the effects of the coating on the behavior of the stones against water, comparative measurements of water absorption by capillarity[1] and total immersion[2] have been carried out on untreated samples and TiO_2 coated samples, by using both the preparation, namely the acid and the basic one.

Referring to capillarity absorption, the average of measurements on three samples for each case is reported in Figure 5.2. The absorption coefficients AC, evaluated as the slope of the fitted line to the Q_i curve vs. square root of time in the first 30 minutes interval, are reported in Table 5.3.

As shown by the absorption curves, the treated samples show capillarity absorption curves nearly indistinguishable with respect to the untreated stones. In any case the difference is barely larger than the expected error.

Samples	*AC (g/cm²)*
NT	0.02
TiAcN	0.03
TiMaA	0.02

Table 5.3 - Water absorption coefficient (AC) by capillarity estimated for untreated and treated samples

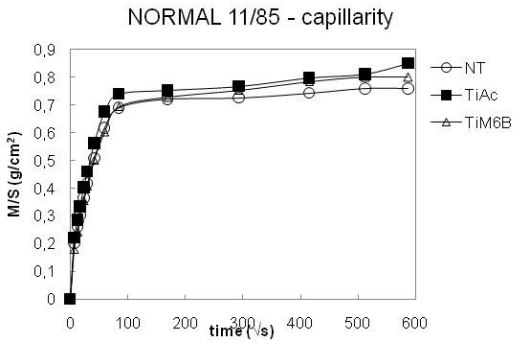

Figure 5.2 - Capillarity water absorption curves (in g/cm² units) of Sabucina stone samples before and after the application of TiO_2 coatings.

A similar behavior can be observed in the case of total immersion (average values for fifteen samples for each set), as shown in Figure 5.3. The CI parameters obtained for treated and untreated samples (Table 5.4) highlight a slight increment of water absorption in the case of basic treatment (TiMaA).

Samples	*CI%*
NT	11.62 ± 1.34
TiAcN	11.89 ± 1.16
TiMaA	13.29 ± 1.21

Table 5.4 - Water absorption coefficient (CI%) by total immersion estimated for untreated and treated samples

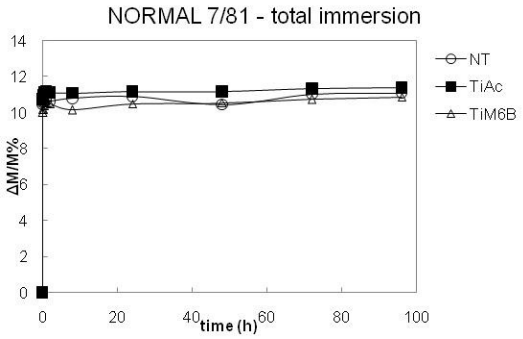

Figure 5.3 - Water absorption curves by total immersion of Sabucina stone samples before and after the application of TiO_2 coatings.

Finally, comparative accelerated aging tests have been performed in order to evaluate the effects of the TiO_2coatings against salts crystallization. According to UNI EN 12370 standard[3], data are reported as total mass loss percentage versus the number of crystallization cycles.

Figure 5.4 and Table 5.5 display the average mass loss for each salt crystallization cycle for untreated and treated stone samples (eight samples for each set). The results show a similar trend for coated and uncoated stones. The mass loss curves are, in both cases, roughly "salt-controlled" up to the fourth cycle (*i.e.*, a slight increase of the total mass) and "weathering-controlled" from the fifth cycle, as suggested by a decrease of total mass. In particular, a similar behavior can be observed in the "salt-controlled" part of the curves, while the presence of the coatings causes a slightly increase of the total loss mass in the "weathering-controlled" curves. Considering the error calculated, a similar stone durability against salts can be assessed for untreated and treated samples.

Samples	*ΔM % (15 cycles)*	*ΔM % (after cleaning)*
NT	-11.09 ± 1.25	-12.72 ± 1.13
TiAcN	-13.43 ± 2.43	-15.43 ± 2.55
TiMaA	-13.24 ± 3.47	-15.22 ± 3.63

Table 5.5 - Percentage mass difference during the 15 crystallization cycles of coated and uncoated Sabucina stone samples. Average values on fifteen samples are reported.

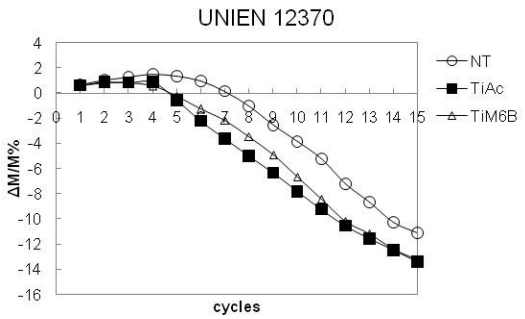

Figure 5.4 - Percentage mass difference curves during the 15 crystallization cycles of coated and uncoated Sabucina stone samples. Average curves on fifteen samples are reported.

5.2.1.2.4 Scanning-electron microscope (SEM) observations

The surface distribution of the coatings of TiO_2has been evaluated through SEM and EDS analyses by a Tescan Vega LMU scanning electron microscope, equipped with an EDAX NeptuneXM4-60 micro-analyzer, characterized by an ultra-thin Be window. Measurements were carried out by using spot mode analysis on coated surfaces, with 20 kV accelerating voltage and0.2 nA beam current.

The stone surface treated with the nanosol coating TiAcN (Fig. 5.5(a)) has a more grainy look with holes between the TiO_2 plates. This should be due to the acid nature of the applied nanosol, which causes micro-erosions on the stone surface. When drying, both coatings may suffer shrinkage, but in the acid case the cracking looks greater. In the samples treated with TiMaA (Fig. 5.5(b)), the TiO_2 plates are larger and the surface coverage is more homogeneous than samples treated with the acid nanosol.

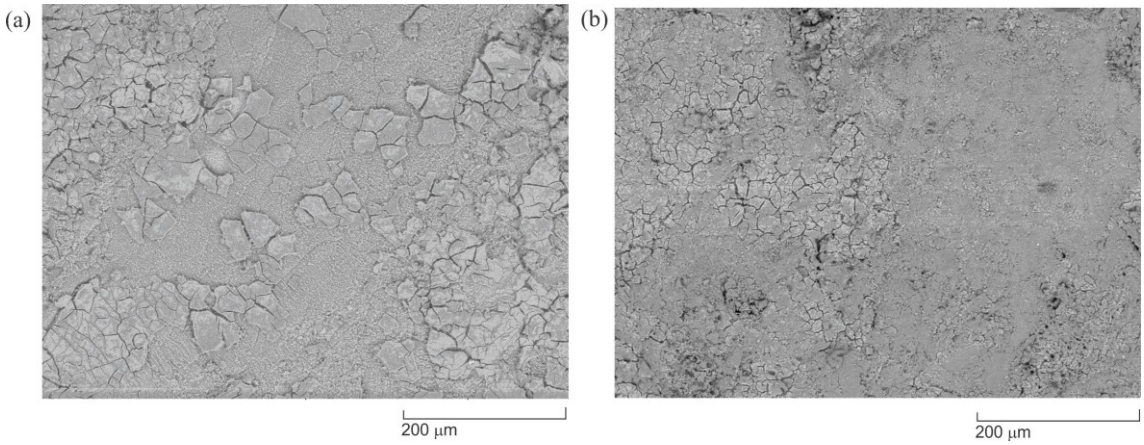

Figure 5.5 - SEM images taken on (a) TiAcN and (b) TiMaA coated Sabucina Stone sample surfaces

5.2.2 Colloidal silicon-based hydrophobic treatment (WS3)

A colloidal silica and silicone with fluorurate groups named WS3 has been tested on Sabucina Stone with the aim at verify the hydrophobic efficiency of the treatment and the suitability of the product on calcarenite substrate.

5.2.2.1 Synthesis via sol-gel and application of WS3

The coating is composed by a water solvent combined with a commercial product, added in appropriate concentration. The product is, therefore, constituted by chains of -O-Si-O-Si(R_f)-O-, with R_f = fluorurate groups. The hydrophobic action of the coating is determined by the presence fluorurate groups that are linked to an inorganic system of silica nanoparticles aggregates.

The application of the coating has been performed by brushing on stone sample, consequently dried at 105 °C to constant mass before the efficiency tests.

5.2.2.2 Efficiency tests

5.2.2.2.1 Contact angle

According to UNI 11207[6], contact angle measurements have been performed on samples after the application of the hydrophobic treatment.

In detail, the obtained results highlight a *hydrophobic* behavior of the product (Figure 5.6), being the contact angle measured about 130° ±6.4°.

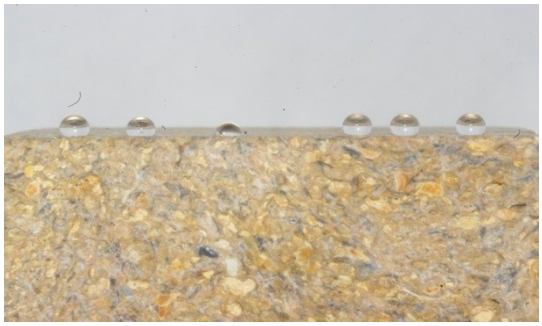

Figure 5.6 - Picture of water drops on WS3 coated Sabucina stone sample

Further tests finalized to investigate the performance of the hydrophobic product WS3 have been carried out on samples preliminary treated with hybrid organic-inorganic consolidants (*see next paragraph*), in order to verify the efficiency of both protective and consolidant products.

5.3 Hybrid organic-inorganic consolidant treatments

5.3.1 Polyammidoammine with silicon alkoxide functions (PAASi)

The hybrid product PAASi is a patented wood protective material (*Bergamonti L., Chappini E., Maistrello L., Palanti S., Predieri G., Wood preservative compositions, WO 2015004590 A1*)

modified for its application on stone substrate. In detail, it has been obtained by using a minopropyltriethoxisilane (with a functional silicon-alkoxide group) for the reaction with the bisacrylamide producing the polymer PAASi. In Figure 5.7 a schematic chemical structure of the product is shown.

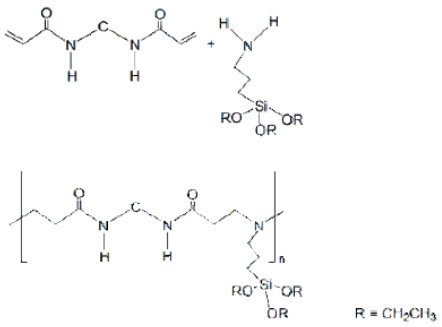

Figure 5.7 - Functionalized polyammidoammine

5.3.1.1 Synthesis and application of PAASi

In a flask placed in a thermostatic bath at room temperature, $5 \cdot 10^{-2}$ moles of N,N'-Methylenebisacrylamide (MBA) have been added to 190 ml of deionised water and the solution has been stirred for 20 minutes; after a complete dissolution of MBA in water, 10 ml of Ethanol (EtOH) and$5 \cdot 10^{-2}$ moles of 3-Aminopropyltriethoxysilane (APTES) have been added. The obtained solution has been stirred in the thermostatic bath for 2 h.

Referring to application of the product to the stone, cubic samples (4x4x4 cm) have been plunged into PAASi sol in a sealed container for 1h and dried at 60°C to constant mass. A selection of treated samples has been also coated by brushing with the hydrophobic product WS3 in order to evaluate the combined use of consolidant and protective products.

5.3.1.2 Efficiency test

5.3.1.2.1 Colorimetric tests

To evaluate the changes of the stone surface appearance due to the treatment and coating, colorimetric analysis has been performed by a Techkon Spectrodens colorimeter. In Table 5.6 the color difference ΔE calculated on the basis of the colorimetric parameters measured a*, b* and L* are reported.

Table 5.6 - Color difference ΔE values for each treatment (PAASi and PAASi+WS3)

Samples	***L****	***a****	***b****	***ΔE***
Untreated	66.02	4.94	21.32	
PAASi	62.83	6.98	24.89	**5.20**
PAASi + WS3	63,20	5,67	24,41	**4.25**

According to Italian guidelines for the restoration of stone buildings[22], ΔE after an intervention must be less than 5. The values of overall color difference ΔE* can be considered acceptable after the application of the both consolidant and hydrophobic treatments even if the ΔE measured after PAASi treatment is slightly higher of the limit.

5.3.1.2.2 Comparative water absorption and accelerated aging test

In order to evaluate the effects of the treatments on the behavior of the stones against water, comparative measurements of water absorption by capillarity[1] and total immersion[2] have been carried out on untreated samples and PAASi and PAASi + WS3 coated samples.

Referring to capillarity, the average of measurements on three samples for each case is reported in Figure 5.8. The absorption coefficients AC, evaluated as the slope of the fitted line to the Q_i curve vs. t½ in the first 30 minutes interval, as well as the data collected during the test are reported in Table 5.7.

Table 5.7 - Data report of the water absorption by capillarity test carried out on PAASi treated and untreated Sabucina Stone samples

t (√s)	***Volume of water absorption per area (g/cm²)***			***Water % absorbed per area***		
	NT	***PAASi***	***PAASi+WS3***	***NT***	***PAASi***	***PAASi+WS3***
0	0	0	0	0	0	0
24	0.271	0.291	0.092	29.9	34.7	11.0
35	0.362	0.392	0.127	40.0	46.8	15.1
42	0.427	0.473	0.180	47.1	56.4	21.4
60	0.567	0.644	0.276	62.6	76.8	32.8
120	0.822	0.769	0.547	90.7	91.8	65.0
147	0.828	0.783	0.641	91.5	93.5	76.2
294	0.839	0.789	0.791	92.6	94.2	94.0
416	0.876	0.822	0.844	96.8	98.1	100
509	0.894	0.833		98.7	99.4	
588	0.906	0.838		100	100	
Slope	**0.009**	**0.010**	**0.005**			
AC (g/cm²)	**0.023**	**0.003**	**0.018**			

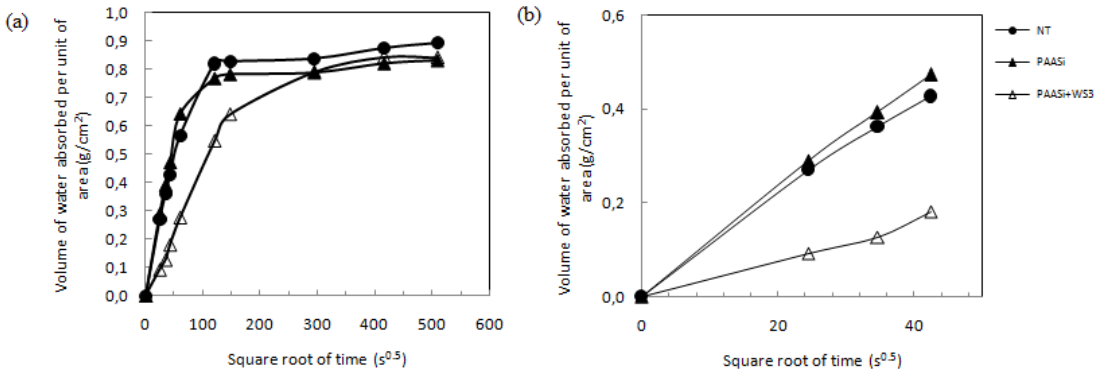

Figure 5.8 - Water absorption by capillarity average curves (a) referred to the whole duration of test and (b) in the first 30 minutes for untreated and treated Sabucina stone samples with PAASi and PAASi+WS3

As shown by the capillarity absorption curves (see Figure 5.8), the treated samples show capillarity absorption curves slight lower than to the untreated stones, even if in the first 30 minutes of the test a low increase of absorption can be observed, as testified by the AC calculated.

Such a behavior has been also observed by associating the hydrophobic coating to the consolidant treatment (PAASi+WS3). The results obtained from total immersion test (average curves for fifteen samples, for each set) are reported in Figure 5.9, while the CI% parameters at 72h are shown in Table 5.8.

Samples	***CI%***
NT	11.52 ± 1.23
PAASi	10.75± 0.82
PAASi + WS3	11.07 ± 2.02

Table 5.8 - Water absorption coefficient (CI%) estimated for untreated and treated samples (PAASi and PAASi+WS3) after 72h of total immersion

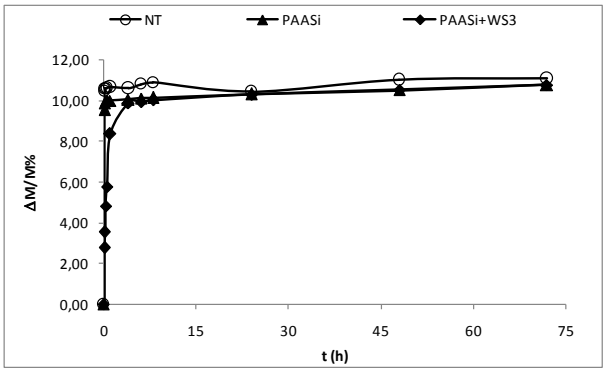

Figure 5.9 - Water absorption curves by total immersion of Sabucina stone samples before and after the application of PAASi and PAASi+WS3 treatments

The obtained data highlight a slight decrease of C.I.% parameters for samples treated with the consolidant PAASi; this behavior is also observed for samples treated with the hydrophobic coating (WS3), with a decrease of the imbibitions coefficient evaluated in the same time interval (72h).

Finally, referring to dry index measurements, both treated and coated samples exhibits a rapidly drying respect to untreated stone in the monitored time interval, as suggested by the inspection of curves in Figure 5.10 and values reported in Table 5.9.

Table 5.9 - Data report of dry index measurement test on untreated and PAASi treated Sabucina samples

t (h)	*NT*	*PAASi*	*PAASi+WS3*
0.0	7.37	11.29	10.61
0.1	6.82	11.07	10.42
0.2	6.75	10.95	10.29
0.3	6.68	10.87	10.17
0.5	6.30	10.80	10.12
1	6.61	10.75	10.06
4	6.48	10.71	9.98
6	6.40	10.68	9.94
8	6.35	10.64	9.90
24	6.12	10.32	9.59
96	4.82	8.91	7.65
120	4.51	8.08	6.94
144	4.27	7.25	6.08
168	3.56	6.52	5.34
192	3.61	5.76	4.65
264	2.80	3.14	2.49
288	2.61	2.26	1.50
Qi loss (%)	**8.84**	**8.84**	**9.15**
Qmax	**13.46**	**12.13**	**11.93**
IA	**1522.53**	**2580.99**	**2343.21**

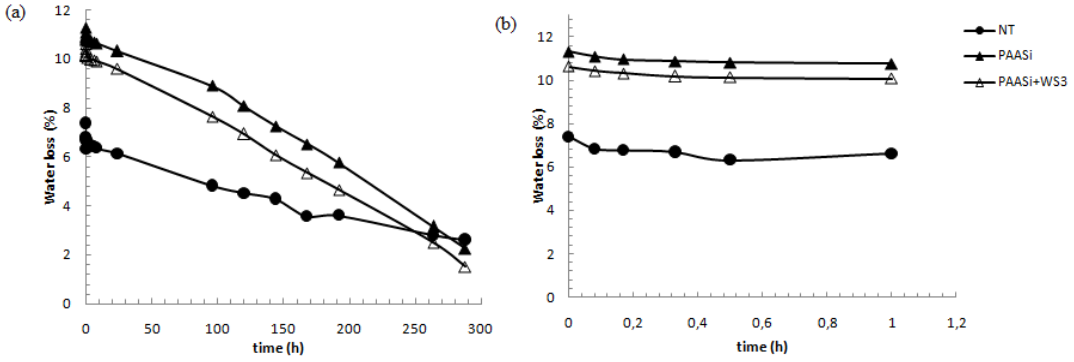

Figure 5.10 - Curves of the amount of water loss Qi plotted as a function of time (in hours) for untreated and PAASi treated samples of Sabucina stone

An enhancement on the behavior of the stone due to the presence of the consolidant PAASi has been detected in term of resistance to salt crystallization; in fact, a significant decrease of loss mass at the end of 15 cycles (see Table 5.10 and Figure 5.11), namely from -11.09% (untreated samples) to -6.60% (PAASi treated samples) has been observed. Noteworthy is that the presence of hydrophobic coating accelerates the degradation process, with a low increase of the mass loss percentage, namely from -11.09% to -12.67%.

Samples	*ΔM %* *(15 cycles)*
NT	-11.09 ± 1.25
PAASi	-6.6 ± 1.52
PAASi+WS3	-12.67 ± 0.85

Table 5.10 - Percentage mass difference during the 15 crystallization cycles of PAASi treated and untreated Sabucina stone samples. Average values on fifteen samples are reported.

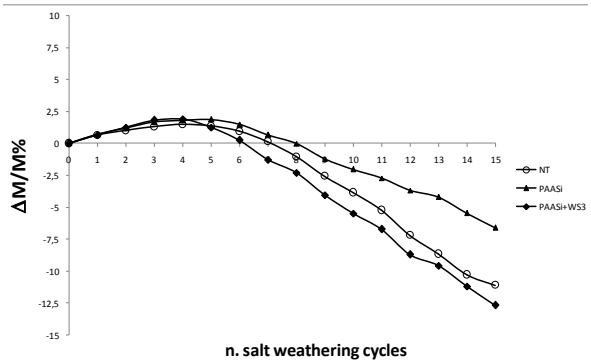

Figure 5.11 - Percentage mass difference curves during the 15 crystallization cycles of PAASi treated and untreated Sabucina stone samples. Average curves on fifteen samples are reported.

5.3.2 Silicon alkoxide with epoxidic functional group and aluminium oxide (AlSiX)

The product named AlSiX is a hybrid sol developed at the Department of Chemistry of Parma University (Italy) based on an Al-Si network functionalized with organic chains, having the latter ones the role of assuring a better compatibility between product and stone substrate.

5.3.2.1 Synthesis and application

The sol has been synthesized by sol-gel process by using water and isopropyl alcohol in volumetric proportion 1:2. The acid pH allows the stability of the sol.

In Figure 5.12 a pictorial sketch is reported showing the main reactions involved in the sol formation.

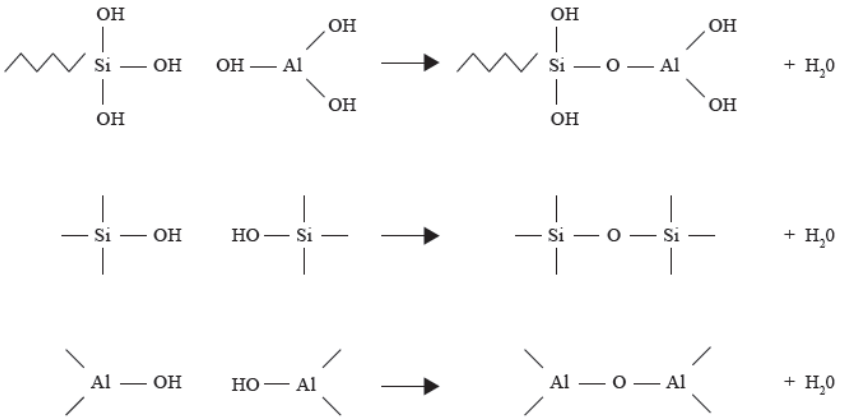

Figure 5.12 - Pictorial sketch is reported showing the main reactions involved in the sol formation.

For the treatment of the studied substrate, cubic samples of Sabucina stone (4x4x4 cm) have been plunged into AlSiX sol, in a sealed container for 1h and dried at 60°C to constant mass. A

selection of treated samples has been also coated by brushing with the hydrophobic product WS3 in order to evaluate the combined use of consolidant and protective products.

5.3.2.2 Efficiency test

5.3.2.2.1 Colorimetric tests

To evaluate the changes of the stone surface appearance due to the treatments, colorimetric analysis has been performed by a Techkon Spectrodens colorimeter. In Table 5.11 the color difference ΔE calculated on the basis of the colorimetric parameters measured a*, b* and L* are reported. In the case of AlSiX treatment the color difference ΔE* is more high than 5, limit considered acceptable for restoration and conservation action in Cultural Heritage science[22].

Table 5.11 - Color difference ΔE values for each treatment (AlSiX and AlSiX+WS3)

Samples	***L****	***a****	***b****	***ΔE***
untreated	66.02	4.94	21.32	
AlSiX	55,85	8,33	28,84	**13.09**
AlSiX + WS3	51,97	12,22	30,13	**18.11**

5.3.2.2.2 Comparative water absorption and accelerated aging test

In order to evaluate the effects of the treatments on the behavior of the stones against water, comparative measurements of water absorption by capillarity[1] and total immersion[2] have been carried out on untreated samples and AlSiX and AlSiX + WS3 coated samples.

Referring to capillarity, the average of measurements on three samples for each case is reported in Figure 5.13. The absorption coefficients AC, evaluated as the slope of the fitted line to the Q_i curve vs. t½ in the first 30 minutes interval, as well as the data collected during the test are reported in Table 5.12.

Table 5.12 - Data report of the water absorption by capillarity test carried out on AlSiX treated and untreated Sabucina Stone samples

t (√s)	***Volume of water absorption per area (g/cm²)***			***Water % absorbed per area***		
	NT	**AlSiX**	**AlSiX+WS3**	**NT**	**AlSiX**	**AlSiX+WS3**
0	0	0	0	0.0	0.0	0.0
24	0.271	0.195	0.126	29.9	23.2	16.1
35	0.362	0.241	0.201	40.0	28.6	25.7
42	0.427	0.277	0.233	47.1	32.9	29.8
60	0.567	0.339	0.296	62.6	40.3	37.9
120	0.822	0.552	0.527	90.7	65.6	67.4
147	0.828	0.629	0.635	91.5	74.7	81.2
294	0.839	0.733	0.733	92.6	87.1	93.8
416	0.876	0.756	0.792	96.8	89.7	100
509	0.894	0.785		98.7	93.2	
588	0.906	0.842		100	100	
slope	**0.009**	**0.005**	**0.004**			
AC (g/cm²)	**0.023**	**0.013**	**0.015**			

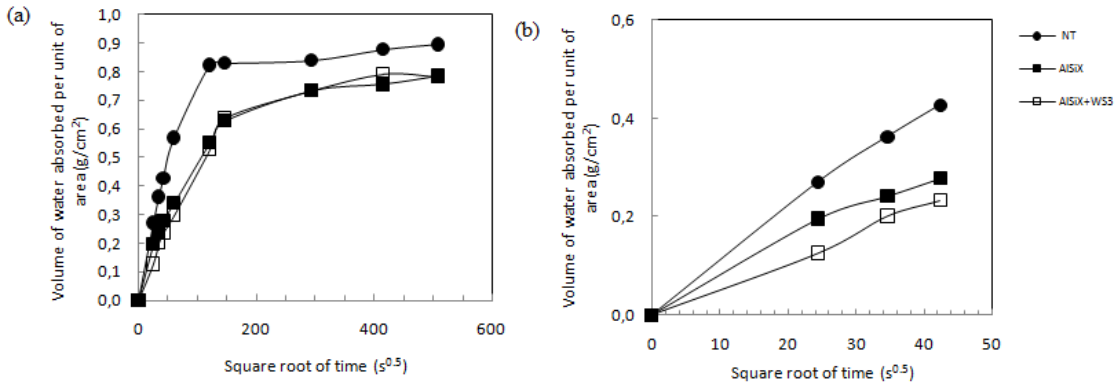

Figure 5.13 - Water absorption by capillarity average curves (a) referred to the whole duration of test and (b) in the first 30 minutes for untreated and treated Sabucina stone samples with AlSiX and AlSiX+WS3

As shown by the capillarity absorption curves, the treated samples show capillarity absorption trends lower than to the untreated stones, even if the first 30 minutes of absorption samples treated with AlSiX exhibit a slight increase of water absorption, as testified also by the AC calculated. Such a behavior has been also observed by associating the hydrophobic coating to the consolidant treatment (AlSiX+WS3).

The results obtained from total immersion test (average curves for fifteen samples for each set) are reported in Figure 5.14, while the CI% parameters at 72h in Table 5.13.

The obtained data highlight a decrease of C.I.% parameters for samples treated with both the consolidant AlSiX, also in association with the hydrophobic coating (WS3), with a decrease of the imbibitions coefficient evaluated in the same time interval (72h).

Samples	***CI%***
NT	11.52 ± 1.23
AlSiX	10.44± 0.41
AlSiX + WS3	10.77 ± 0.53

Table 5.13 - Water absorption coefficient (CI%) estimated for untreated and treated samples after 72 h of total immersion

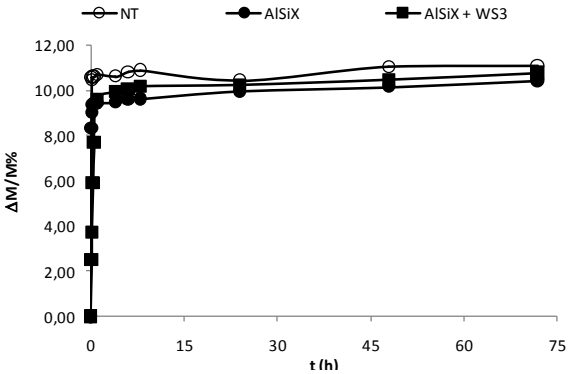

Figure 5.14 - Water absorption curves by total immersion of Sabucina stone samples before and after the application of AlSiX and AlSiX +WS3 treatments

Finally, referring to dry index measurements, both treated and coated samples exhibits a rapidly drying respect to untreated stone in the monitored time interval, as suggested by the inspection of curves in Figure 5.15 and Table 5.14.

Table 5.14 - Data report of dry index measurement test on untreated and AlSiX treated Sabucina samples

t (h)	*NT*	*AlSiX*	*AlSiX+WS3*
0.0	7.37	10.92	9.84
0.1	6.82	10.62	9.45
0.2	6.75	10.51	9.40
0.3	6.68	10.48	9.29
0.5	6.30	10.41	9.28
1	6.61	10.37	9.22
4	6.48	10.29	9.12
6	6.40	10.22	9.08
8	6.35	10.17	9.00
24	6.12	9.72	8.25
96	4.82	8.09	4.78
120	4.51	6.70	3.90
144	4.27	5.41	3.05
168	3.56	4.01	2.59
192	3.61	2.86	2.05
264	2.80	0.54	0.15
288	2.61	0.00	-0.79
Qi loss (%)	**8.84**	**10.92**	**9.61**
Qmax	**13.46**	**11.86**	**12.16**
IA	**1522.53**	**2268.27**	**1874.78**

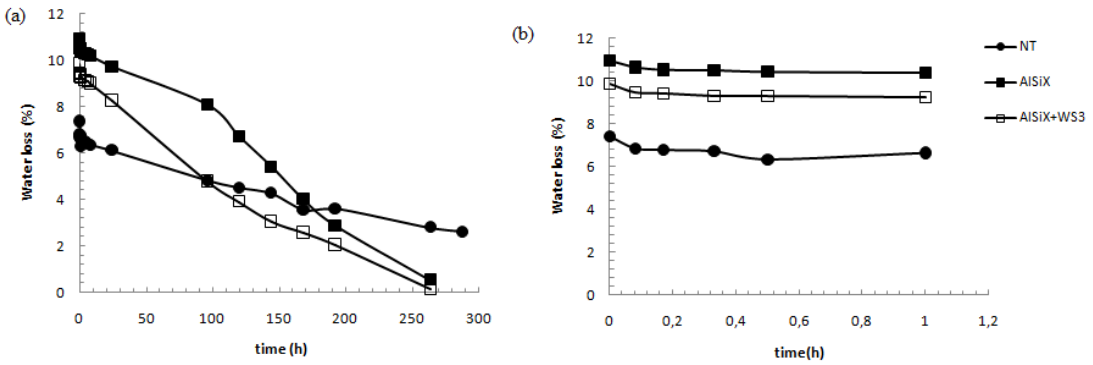

Figure 5.15 Curves of the amount of water loss Qi plotted as a function of time (in hours) for untreated and AlSiX treated samples of Sabucina stone

Even if the treatments enhance the generally behavior of the stone against water, they determine a slight decrease of the durability of the studied material.

In fact, an increase of the mass loss percentage at the end of 15 cycles (see Table 5.15) is observed in both cases, namely treatment with AlSiX and AlSiX+WS3. In detail, from -11.09% for untreated stone, the value pass to -21.81% and -19.55% for the two treatments, respectively (Figure 5.16).

Samples	*ΔM % (15 cycles)*
NT	-11.09 ± 1.25
AlSiX	-21.81 ± 0.92
AlSiX+WS3	-19.55 ± 0.89

Table 5.15 - Percentage mass difference during the 15 crystallization cycles of AlSiX treated and untreated Sabucina stone samples. Average values on fifteen samples are reported.

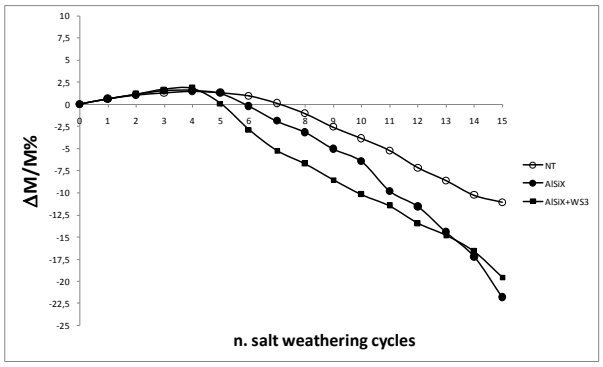

Figure 5.16 - Percentage mass difference curves during the 15 crystallization cycles of AlSiX treated and untreated Sabucina stone samples. Average curves on fifteen samples are reported.

5.4 Discussion and Conclusions

Water based sols containing titanium dioxide have been deposited on calcarenite substrates (Sabucina stone) to obtain self-cleaning coatings taking advantage of the well known TiO_2 photocatalytic properties.

Basic and acid sols were synthesized by sol-gel method, working at low temperatures and in different environments, with the aim to evaluate the effects of sols at different pH on calcarenite substrate. The TiO_2 obtained were principally made of anatase with a few percent of brookite. Both acid and basic titanium nanosols exhibit good properties, in terms of preserving the characteristics of the stone; in fact, the treatments do not significantly alter the color and water absorption proprieties of the studied material. Referring to durability of the stone, the resistance to salt crystallization is generally improved, as showed by accelerated degradation test. As concern the self-cleaning properties, both TiO_2 coatings exhibit a good photodegradation activity on methylene blue and methyl orange dyes, being harmless against the stone. Moreover, beside the general non-homogenous trends observed in photocatalisis curves, mainly due to the heterogeneous color of the stone and the high porosity of the surface, the presence of TiO_2 coatings catalyse the photodegradation of both dyes with a better efficiency of the basic preparation (TiMaA) under UV lamp and the acid preparation (TiAcN) under daylight one.

One of the most important requirement in the usage of a protective coating is the ability of minimizing the capillarity absorption and improving the durability, without modifying the chromatic appearance distinctive of the monuments; therefore, considering the high solubility of calcite-based materials in acid environment, the basic coating should be preferred, the latter one determining a lower chromatic changes in stone (ΔE 1.5) and exhibiting better filmogenic proprieties (as inferred by SEM analysis).

Referring to consolidant treatments and hydrophobic coating (Figure 5.17), the obtained results show good performance of the products in term of global enhancement of the stone proprieties, even if some disadvantages have to be highlighted.

In fact, the silicon alkoxide product (AlSiX) determines strong chromatic changes, especially used in association with the hydrophobic coating, as well as a slightly decrease of resistance of stone against salts crystallization. Otherwise, the use of polyammidoammine-based product (PAASi) seems to be less invasive in term of chromatic changes, assuring at the same time lower absorption of water by capillarity and total immersion as well as a significant enhancement of durability of the stone against salt crystallization weathering. Finally, the overall of the obtained data on treated samples coated also with the hydrophobic product (WS3) claims an improvement of the performances of both consolidants respect to usage by themselves, even if a slight decrease of the salt crystallization resistance has to be claimed.

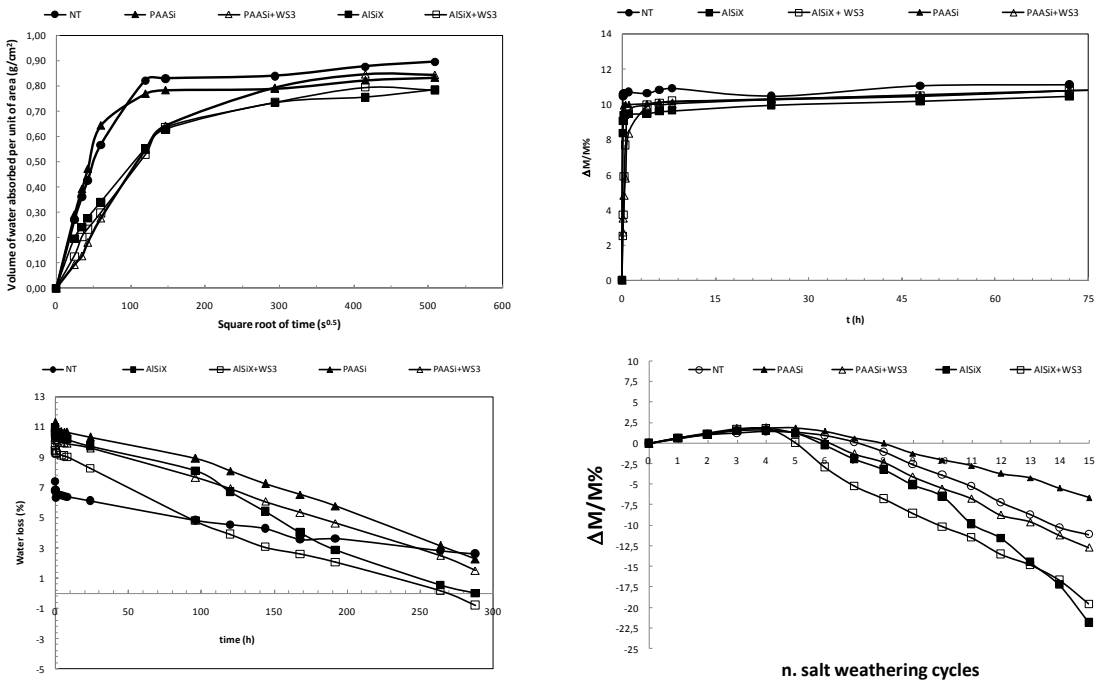

Figure 5.17 - Final report of the comparative water absorption by capillarity and total immersion, drying and durability tests performed on untreated and treated samples with both consolidants and hydrophobic.

In conclusion, in consideration of the obtained results, the application of TiO_2 nanosols, as well as hybrid organic-inorganic consolidants in association with hydrophobic coating on Sabucina stone can be considered as case in point for the other Sicilian calcarenites that exhibits similar compositional, textural, structural and porosimetric features.

5.5 Bibliography

[1] NORMAL 11/88 Natural stones test methods: Determination of water absorption by capillarity immersion.

[2] NORMAL 7/81 Natural stones test methods: Determination of water absorption by total immersion.

[3] UNI EN 12370, Natural stones test methods: Determination of resistance to salt crystallization, UNI ed., Milano, 2001.

[4]UNI EN 15886, Conservation of cultural property - Test methods - Colour measurement of surfaces UNI ed., Milano, 2010.

[5] UNI EN 1926 Natural stones test methods: Determination of compression strength, UNI ed., Milano, 2000.

[6] UNI 11207Cultural heritage - natural and artificial stones - Determination of static contact angle on laboratory specimens, UNI ed., Milano, 2007.

[7] Barone G, Mazzoleni P, Predieri G, Rabot E, Raneri S, Teixeira J. Investigation on suitability of consolidant and protective products on Sicilian calcarenite by using neutron imaging. Laboratoire Leon Brillouin LLB, Saclay, France, 2005. N. experiment 12115.

[8] Brinker J, Scherrer GW. Sol-gel Science. The Physics and Chemistry of Sol-Gel Processing, Academic Press, San Diego, CA. 1990.

[9] Panniello A, Curri ML, Diso D, Licciulli L, Locaputo V, Agostiano A, Comparelli R, Mascolo G. Nanocrystalline TiO2 based films onto fibers for photocatalytic degradation of organic dye in aqueous solution, Appl. Catal. B Environ., 2012. 121–122:190–197.

[10] Bergamonti L, Alfieri I, Lorenzi L, Montenero A, Predieri G, Barone G, Mazzoleni P, Pasquale S, Lottici PP. Nanocrystalline TiO_2 by sol-gel: characterization and photocatalytic activity on Modica and Comiso stones. Appl. Surf. Sci.,2013. 282:165-173.

[11] Bergamonti L, Alfieri I, Franzò M, Lorenzi L, Montenero A, Predieri G, Raganato M, Calia A, Lazzarini L, Bersani D, Lottici PP. Synthesis and characterization of nanocrystalline TiO2 with application as photoactive coating on stones. Environ. Sci. Pollut. R., 2014. 21:13264-13277.

[12] Bergamonti L, Alfieri I, Lorenzi A, Predieri G, Barone G, Gemelli G, Mazzoleni P, Raneri S, Bersani D, Lottici PP. Nanocrystalline TiO2 coatings by sol–gel: photocatalytic activity on Pietra di Noto biocalcarenite. Journal of Sol-Gel Science and Technology, 2015. Doi: 10.1007/s10971-015-3684-6

[13] Djaoued Y, Brüning R, Bersani D, Lottici PP, Badilescu S. Sol–gel nanocrystalline brookite-rich titania films. Mater. Lett., 2004. 58: 2618– 2622.

[14] Kawahara T, Konishi Y, Tada H, Tohge N, Nishi J, Ito S. A patterned TiO2 (Anatase)/TiO2 (Rutile) bilayer-type photocatalyst: Effect of the anatase/rutile junction on the photocatalytic activity. Angew. Chem. Int. Edit., 2002. 41:2811-2813.

[15] Alapi A, Sipas P, Ilisz I, Wittmann G, Ambrus Z, Kiricsi I, Mogyoròsi K, Dombi A. Synthesis and characterization of titania photocatalysts: the influence of pretreatment on the activity. Appl. Catal. A-Gen., 2006. 303:1-8.

[16] Zhang HZ, Banfield JF. Understanding Polymorphic Phase transformation behavior during growth of nanocrystalline aggregates: insights from TiO2. J. Phys. Chem. B, 2000. 104: 3481-3487.

[17] Ardizzone S, Bianchi CL, Cappelletti G, Gialanella S, Pirola C, Ragaini V. Tailored Anatase/Brookite Nanocrystalline TiO2. The optimal particle features for liquid- and gas-phase photocatalytic reactions. J. Phys. Chem. C , 2007. 111: 13222–13231.

[18] Kandiel TA, Robben L, Alkaim A, Bahnemann D. Brookite versus anatase TiO2 photocatalysts: phase transformations and photocatalytic activities. Photochem. Photobiol. Sci., 2013. 12: 602-609.

[19] Kickelbick G. Hybrid Materials. Synthesis, Characterization, and Applications.Wiley-VCH: Weinheim, Germany, 2007.

[20] Bergamonti L, Alfieri I, Lorenzi A, Montenero A, Predieri G, Di Maggio R, Girardi F, Lazzarini L, Lottici PP. Characterization and photocatalytic activity of TiO_2 by sol-gel in acid and basic environments. Journal of Sol-Gel Science and Technology, 2014. 73: 91-102.

[21] Quagliarini E, Bondioli F, Goffredo G, Licciulli A, Munafò P. Self-cleaning materials on Architectural Heritage: Compatibility of photo-induced hydrophilicity of TiO_2 coatings on stone surfaces, J. Cult. Herit., 2013. 14: 1-7.

[22] Vigliano G. Graffiti and antigraffiti project; http://www.icr.beniculturali.it, 16 Oct 2002.

Chapter 6. Quantification of pore structure and surface texture modifications due to protective and consolidant treatments

6.1 Introduction

Natural building stones used in the historical masonry are subjected to different typology of decay due to environmental conditions and several risk factors. The main problem in conservation field is the use of suitable consolidant and protective treatments able to preserve the masonry, being compatible with the stone substrate and not affecting its aesthetical proprieties.

There are numerous tests able to verify the efficiency of consolidant or protective products, mainly devoted to verify their ability to not modify the appearance of stone and its physical proprieties, especially against water; however, particularly in the case of consolidant, one of the most important feature is related to its penetration depth, often difficult to evaluate by using the standard test routine. In addition, the ability of a product to penetrate in the inner structure of the stone, by assuring high efficiency performances is strictly dependent not only by the features of the product itself but also from the porosimetric proprieties of the substrate material.

In this section, the changes in porosimetric and physical proprieties of Sabucina Stone due to the application of the protective and consolidant treatments, namely TiO_2 nanosols, AlSiX and PAASi, previously tested by standard test routine (*see Chapter 5*), have been evaluated by using different methodological approaches in order to highlight the potential and the complementary tools of the used methods.

In particular, in order to inspect and evaluate the penetration depth of consolidant treatments, a classical micro-destructive method, *i.e.* MIP, has been integrated and compared with non-destructive and non-invasive imaging techniques (*i.e.*, micro-computed X-ray tomography and neutron radiography) largely applied in the recent literature to investigate and study the performances of protective and consolidant products[1-6].

Although X-ray imaging has been proven to be successful tool for the inspection of geological samples, the visualization of water inside the samples is not easy, despite the weak contrast. Among the imaging techniques able to give back these information, neutron imaging has been demonstrated a really powerful method for monitoring water in porous media as well as visualize the distribution of consolidant and repellent products[7-8], also in dynamic monitoring condition[9-11]. In consideration of aforementioned, neutron radiography has been also used in order to visualize and quantify the modification in capillary absorption proprieties of Sabucina stone treated with the studied consolidant (*i.e.*, AlSiX and PAASi) and hydrophobic (WS3) products.

Finally, referring to protective products based on TiO_2 nanoparticles, surface modifications have been evaluated by performing 3D surface digital microscope measurements.

6.2 Pore structure modifications due to consolidant treatments

6.2.1 Porosimetric test by Mercury Intrusion porosimetry (MIP)

Mercury intrusion porosimetric measurements have been performed by using a Thermoquest Pascal 240 macropore unit in order to explore a porosity range ~0.0074 μm < r <~15 μm (r being the radius of the pores) and a Thermoquest Pascal 140 porosimeter instrument in order to investigate a porosity range from ~ 3.8 μm< r <~ 116 μm. In detail, the distribution of pore size and porosimetric parameters has been determined on small specimens similar in dimension and shape sampled from cubic samples coated by total immersion. Samples have been plunged in the products in a sealed container for 1 h and dried at 60 °C to constant mass.

Data have been processed by using Thermo Scientific SOL.I.D (Solver of Intrusion Data) Software. Measurements have been performed on almost three samples in order to verify the reproducibility of the test; the results have been then interpolated and average pore distributions and cumulative volume curves have been obtained for each treatment. With the aim to de-noise the original data to produce high-resolution distribution curve, two models have been applied: the *moving average method*, able to rebuilds the experimental data curve considering the average value calculated on a chosen number of points (N can be chosen between 1 and 100 points; in this case 19 value has been used) and the *exponential smoothing*, a mathematical operation that reduces the discrepancy between one point and the next one; a Smooth Factor F = 0.8 has been applied.

6.2.1.1 Results

In Tables 6.1 and 6.2 the porosimetric data obtained on untreated and treated samples with AlSiX and PAASi products have been reported, respectively.

As can be observed by the comparison among the measured parameters in untreated and treated samples reported in Figure 6.1, the presence of products determines variations in term of porosity and pore size distribution.

Table 6.1 - Porosimetric parameters obtained on untreated (NT) and treated samples with AlSiX product

	NT1	***NT2***	***NT3***	***Av.NT***	***St. Dev.***	***AlSiX_1***	***AlSiX_2***	***AlSiX_3***	***Av._AlSiX***	***St. Dev.***
Total intruded volume (cm^3/g)	0.128	0.143	0.136	0.136	0.007	0.122	0.122	0.143	0.129	0.012
Bulk density (g/cm^3)	2.045	1.955	1.947	1.983	0.054	2.015	1.996	1.915	1.975	0.053
Apparent density (g/cm^3)	2.773	2.713	2.646	2.711	0.063	2.670	2.637	2.640	2.649	0.019
Porosity %	26.240	27.940	26.410	26.863	0.936	24.560	24.310	27.460	25.443	1.751
Total surface area (m^2/g)	1.680	2.072	1.911	1.888	0.197	1.108	0.992	1.410	1.170	0.216

Average pore radius (µm)	0.153	0.138	0.142	0.144	0.008	0.220	0.246	0.204	0.223	0.021
Modal pore radius (µm)	5.110	9.488	11.072	8.557	3.088	10.000	12.651	14.990	12.547	2.497
Median pore radius (µm)	2.112	2.310	2.325	2.249	0.119	3.838	4.709	4.087	4.211	0.448

Table 6.2 - Porosimetric parameters obtained on untreated (NT) and treated samples with PAASi product

	NT1	***NT2***	***NT3***	***Av.NT***	***St. Dev.***	***PAASi_1***	***PAASi_2***	***PAASi_3***	***Av. PAASi***	***St. Dev.***
Total intruded volume (cm^3/g)	0.128	0.143	0.136	0.136	0.007	0.149	0.114	0.156	0.140	0.022
Bulk density (g/cm^3)	2.045	1.955	1.947	1.983	0.054	1.878	2.068	1.903	1.950	0.103
Apparent density (g/cm^3)	2.773	2.713	2.646	2.711	0.063	2.605	2.708	2.705	2.673	0.058
Porosity %	26.240	27.940	26.410	26.863	0.936	27.910	23.640	29.650	27.067	3.092
Total surface area (m^2/g)	1.680	2.072	1.911	1.888	0.197	1.933	1.823	1.505	1.754	0.222
Average pore radius (µm)	0.153	0.138	0.142	0.144	0.008	0.154	0.125	0.207	0.162	0.041
Modal pore radius (µm)	5.110	9.488	11.072	8.557	3.088	19.082	8.965	14.626	14.224	5.070
Median pore radius (µm)	2.112	2.310	2.325	2.249	0.119	2.545	1.822	4.345	2.904	1.299

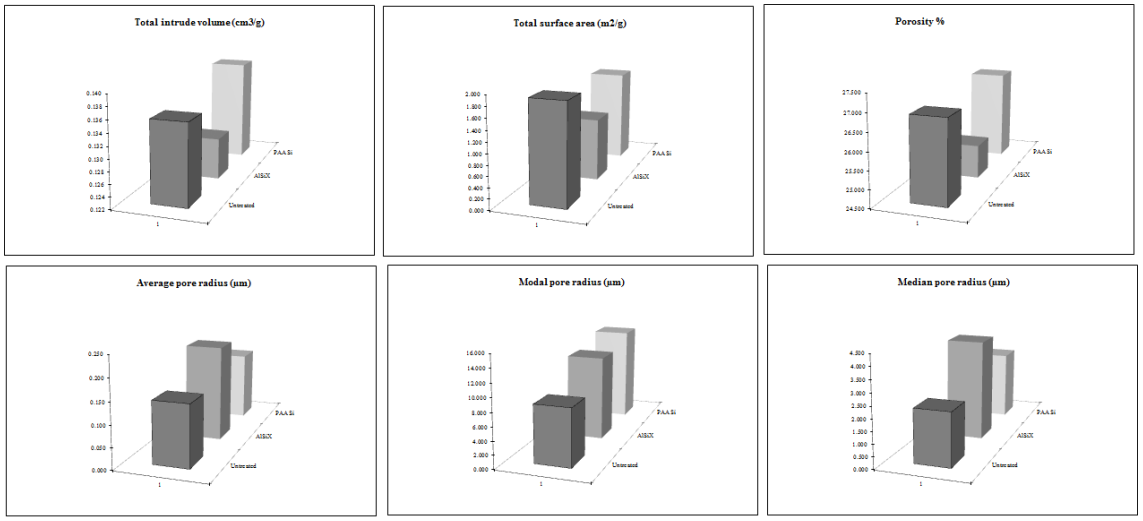

Figure 6.1 - Variation of porosimetric parameters in function of treatment applied

In particular, referring to AlSiX, the presence of the products determine a decrease the accessible porosity % of the stone, namely from 26.9% to 25.4 %, with consequently decrement of total intruded volume and total surface area.

The evidence of an increasing of the average pore radius and the statistical pore size parameters (mode and median) can be explained with the partial filling of pores in the range between 1-10 µm and up to 100 µm, interval not investigable by using MIP method, with consequent appearance of new pores in the range 10-100 µm maybe representing part of larger pores not

completely filled by the product. The ranges of these variations are expressed by the cumulative volume intrusion and pore size distribution curves (Figure 6.2).

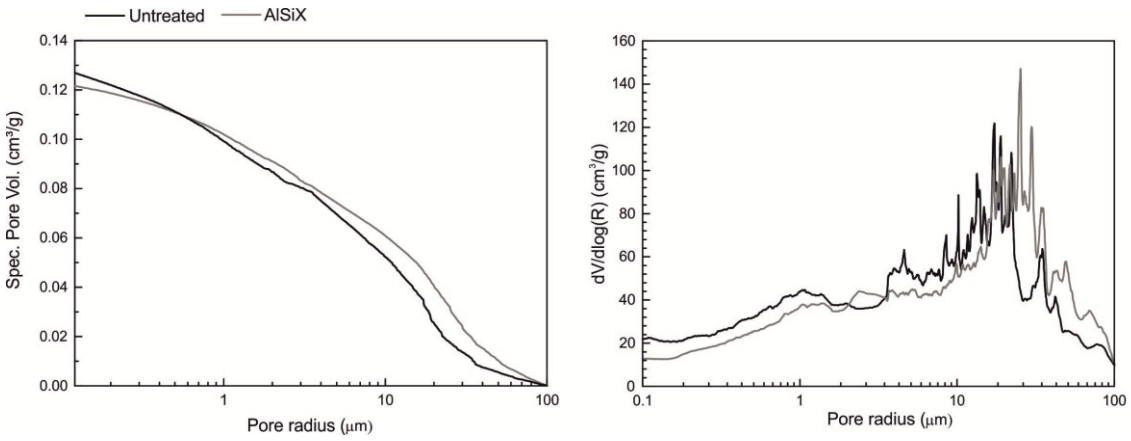

Figure 6.2 - (a)Cumulative pore volume vs. pore size and (b) pore size distribution curves (dV/dlog(R) vs. pore size) collected for untreated (in black) and treated AlSiX (gray) samples.

Referring to the changes in pore network of the stone determined by the PAASi treatment (Figure 6.3), the obtained results by using MIP are not really convincing and the slightly modification of porosimetric parameters could be related to the already attested variability of the stone.

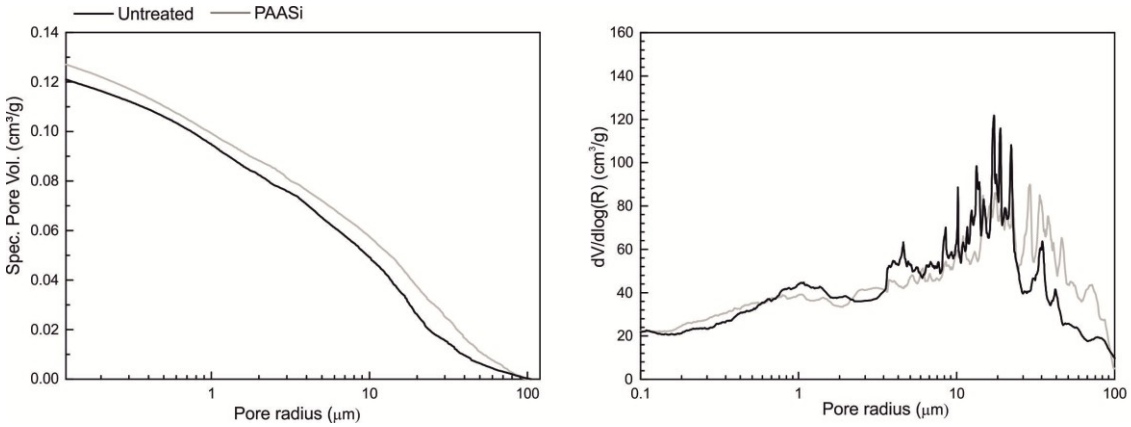

Figure 6.3 - (a)Cumulative pore volume vs. pore size and (b) pore size distribution curves (dV/dlog(R) vs. pore size) collected for untreated (in black) and treated PAASi (gray) samples.

6.2.1.2 Final remarks

The investigation of pore structure changes due to consolidant treatments performed by MIP allows to compare the pore size parameters and distributions of a porous material before and after a treatment, evidencing therefore the ability of the product to penetrate into pore network. However, the obtained results on Sabucina stone samples treated with the organic-inorganic sols highlight some limits of the method in powerfully showing the penetration depth of the consolidants. In fact, even if in the case of AlSiX consolidant some changes have been detected,

especially in accessible porosity and total pore volume parameters, evidencing a partial filling of pore network due to the presence of the product, the questionable data about PAASi treatment suggest some limit of the technique, may be related to the pore range limit of the instrument. In fact, it is plausible that, considering the coarse grain size of the studied stone and the features of the applied products, consolidants are able to penetrate only into the larger and surface-exposed pores, not detectable by MIP, being larger than 100 μm.
In this latter case, X-ray micro-computed tomography represents a suitable tool for visualizing these larger pores and verifying this hypothesis.

6.2.2 Determination of the impregnation depth of consolidants by X-ray μ-CT

Because the consolidation products tend to have a similar attenuation for X-rays as some of the minerals inside the stone samples, the studied products have been doped with Ag before the application on Sabucina Stone. Noteworthy is that the doping process doesn't alter the physical proprieties of applied products.
In order to better visualize the distribution of consolidants inside the pore space network of the stone, scans have been performed on small cylindrical samples before and after the application of the products. Therefore, the CT scans describing the distribution of products inside the stone have been obtained through a differentiate images between treated and untreated samples.
Micro-CT scans have been performed on cylindrical samples with a diameter of 7 mm at the Centre for X-ray Tomography (UGCT; Ghent University, Belgium)[12]. For both untreated and treated samples a total of 1201 projections were acquired over an angle of 360° with a source-detector distance of 1165 mm and a source-object distance of 22 mm, resulting in a voxel size of 7.5 μm. The acquisition time was 999 ms per frame. A voltage of 120 kV was imposed with a power of 10 W and 83 μA tube current. A thin Al-filter (1 mm) was used to block the low-energetic X-rays to prevent beam hardening. The total period of time for one scan was around 30 minutes. The same acquisition parameters were used for each scan. The obtained raw CT data have been reconstructed with the UGCT Octopus software[13]. Also for the reconstruction the same parameters, like beam hardening correction, normalization, ring and spot filter, exposure time and amount of frames were used. Finally, for 3D visualizations and for 3D quantification of pore network features VGStudio MAX (Volume Graphics) and the UGCT software tool Morpho+[14] have been used, respectively. It is worth of noting that to evaluate ED and MO, only objects with a minimum of 3 voxels were retained for analysis.

6.2.2.1 AlSiX product

The original stone had a total porosity of about 11.72% (10.06% and 1.65%, open and close porosity respectively) and pore distribution described by equivalent diameter (ED) and

maximum opening (OM) ranging from 7.5 µm and 967.5 µm and 7.5 µm and 372.5 µm, respectively, with a volumetric distribution show in Figure 6.4.

After the scan of the untreated sample, the cylinder was impregnated with the doped product and scanned again. By subtracting scans referred to treated samples from the reference sample one acquired before the treatment, the distribution of the product and the pore network impregnated by it has been visualized.

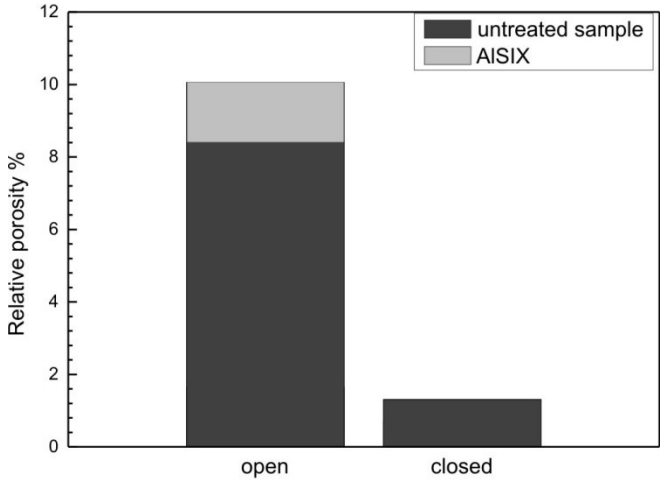

Figure 6.4 - Changes in open, closed and total porosity for fresh and treated samples (with AlSiX consolidant).

Firstly, a reduction of 2.02% of total porosity has been calculated, interesting almost the open and accessible one. As can be assessed from an inspection of ED and OM distributions (Figure 6.5), the product AlSiX impregnates pores exhibiting ED values spanning from 10 to 500 µm and pores with MO values between 10 and145 µm; the interval of pores having ED higher than 500 µm and MO higher than 150µm are not interested by the coating process.

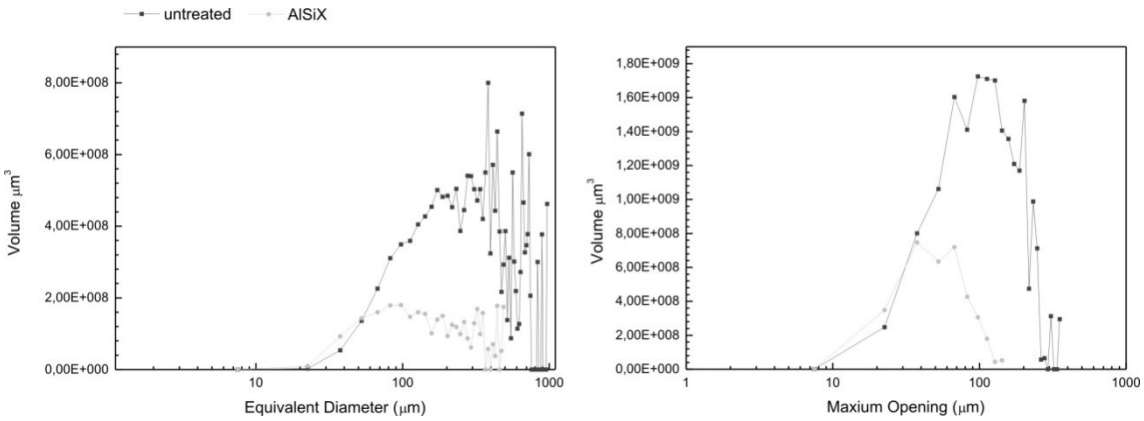

Figure 6.5 - Pore volume vs. equivalent diameter ED (a) and maximum opening OM (b) curves as a function of the AlSiX treatment. Step intervals 2 voxels (i.e. 15 µm).

This behavior is visualized in the 3D-image reconstructions (Fig. 6.6) in which the bulk is shown in grey and the distribution of AlSiX in red.

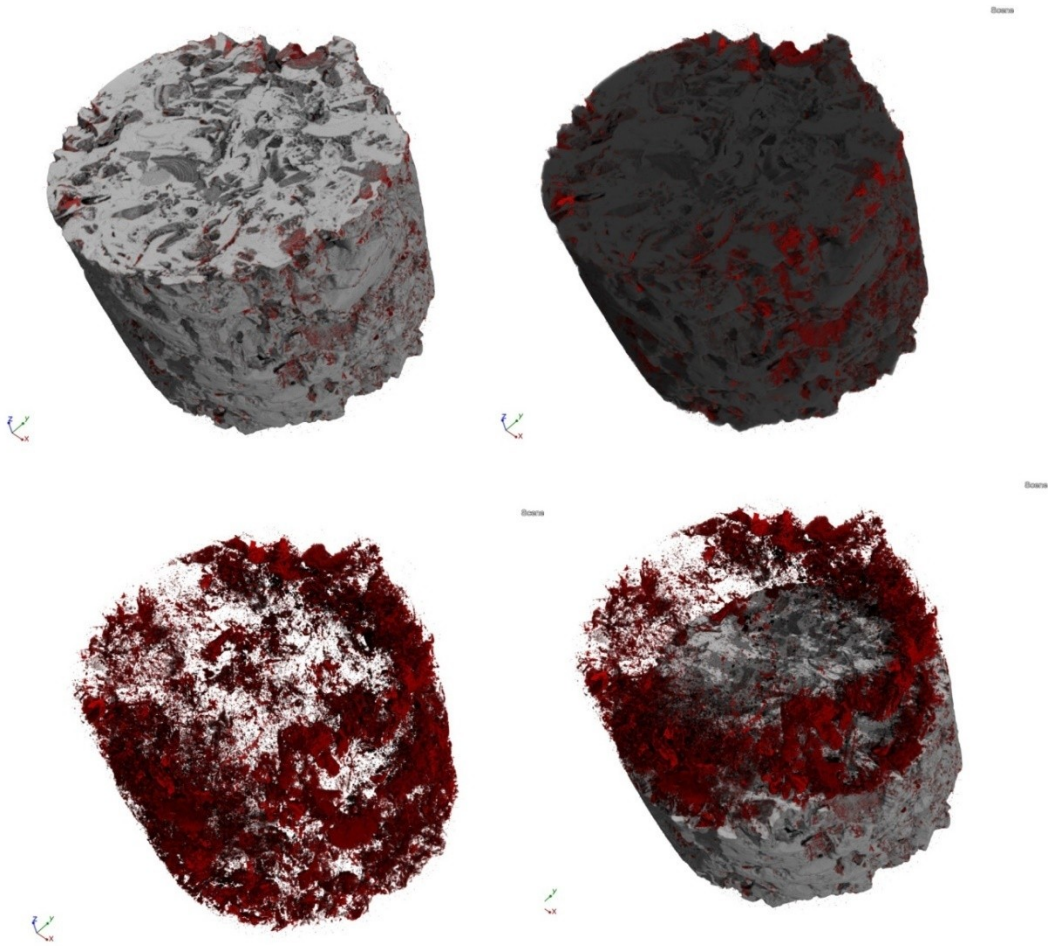

Figure 6.6 - 3D reconstruction images of the bulk (in gray) and AlSiX product distribution (red). Diameter sample size about 7 mm.

6.2.2.2 PAASi product

Referring to PAASi, the scans of the sample before and after the treatment with the doped consolidant allow also in this case the visualization of product distribution in the pore network of the stone.

The reference value of porosity for the untreated samples is of about 12.32% (with open and closed porosity values of 10.82% and 1.50 %, respectively). The pore size distribution of the material is described by equivalent diameter (ED) and maximum opening (OM) size vs. volume curves, in which the porosimetric features of the stone are shown in Figure 6.7; in detail, the pore network is characterized by pores ranging from 7.5 µm and 1220 µm in ED and 7.5 µm and 400 µm in MO. Noteworthy is that the obtained results on this cylinder sample are quite similar to the previously scanned one, highlighting a good representativeness of the small cylinder respect to the general proprieties of the studied stone.

Also in this case, by subtracting scans referred to treated samples from the reference sample ones acquired before the coating, the distribution of the product and the pore network impregnated by it has been visualized.

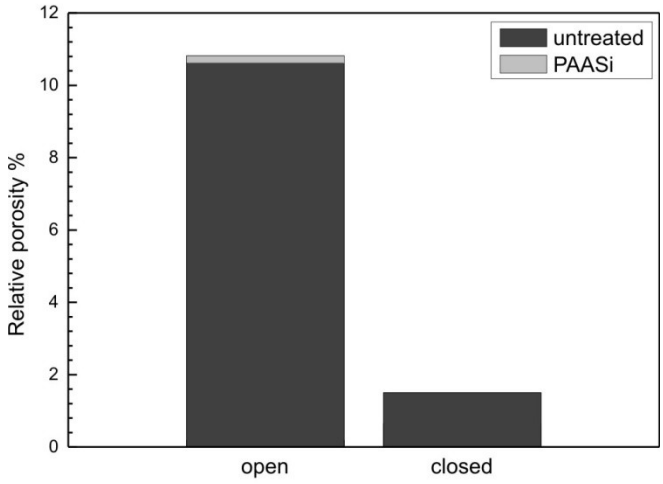

Figure 6.7 - Changes in open, closed and total porosity for fresh and treated samples (with PAASi consolidant).

About total porosity, a reduction of 0.84% affecting open porosity has been calculated, suggesting a really poor impregnation ability of the PAASi product. This behavior is confirmed by an inspection of ED and OM distributions relative to pores filled by the consolidant (Figure 6.8), interesting only a really limited range of pores, in ED ranges between ~40 - 300 µm and with MO < ~70 µm, non-involving the large part of the pore network of the stone .

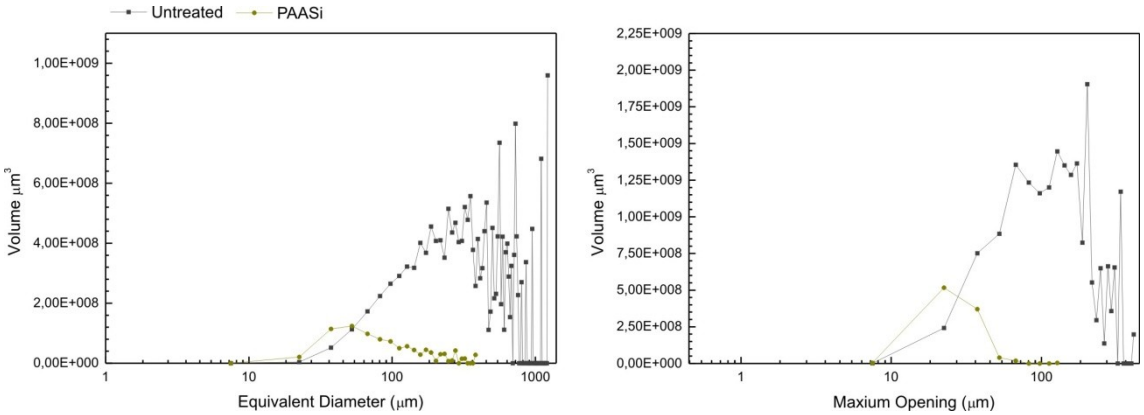

Figure 6.8 - Pore volume vs. equivalent diameter ED (a) and maximum opening OM (b) curves as a function of the PAASi treatment. Step intervals 2 voxels (i.e. 15 µm).

All the collected data allow to asses, therefore, the scarce penetration depth and impregnation ability of the product, as visualized in the 3D-image reconstructions (Fig. 6.9) in which the bulk, in grey, and the distribution of PAASi, in green, are reported.

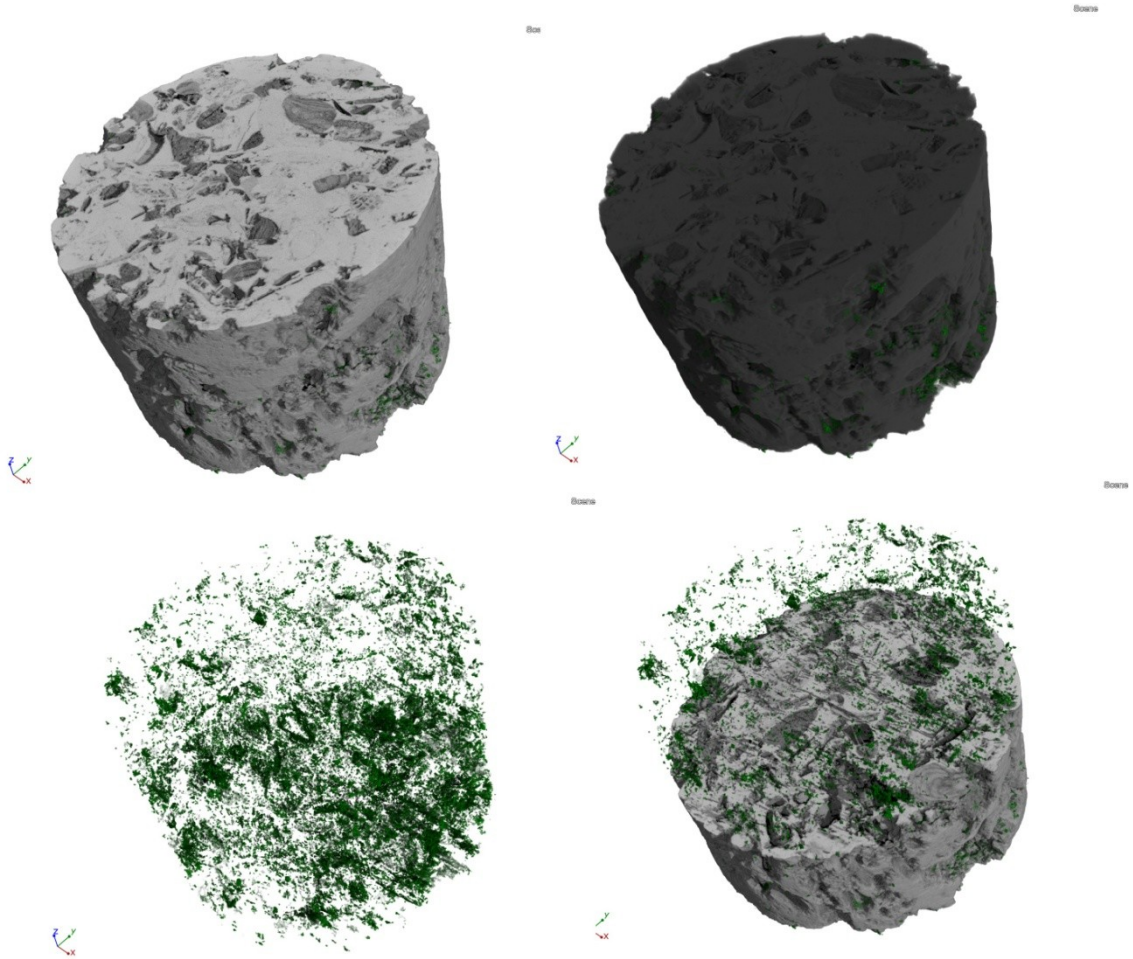

Figure 6.9 - 3D reconstruction images of the bulk (in gray) and PAASi product distribution (green). Diameter sample size about 7 mm.

6.2.2.3 Final remarks

As demonstrated in *Chapter 3*, X-ray μ-CT represents a really useful tool for visualizing the structure of natural building stones and quantifying changes in pore network due to extern processes. In the case of the application of protective products, the knowledge of these aspects is of a great interest, as the necessity to understand how the products interact with the structure of stones in order to evaluate their efficiency. On the basis of the potential of μ-CT, the method allows therefore the visualization of products inside natural building stones, as well as the quantification of pore changes due to the presence of them. However, as the low contrast attenuation of organic products, the application of μ-CT needs the use of doping materials in order to obtain a good contrast between stone and product.

In this study, by doping the investigated products (namely AlSiX and PAASi) with Ag, more contrast has been obtained between bulk material and consolidants; therefore the visualization and quantification of porosity parameters have been gained. The obtained results permit to observe a general decrease of open porosity as well as changes in equivalent diameter and

maximum opening distribution, allowing also the quantification of these changes and the visualization of the distribution of products inside the stone matrix.

Beside the satisfactory results obtained on Sabucina stone samples treated with AlSiX and PAASi consolidants, that add significant information to data obtained by classical intrusion methods allowing to inspect pore range up to 100 µm, some uncertainty have to be highlighted. In fact, in both cases and especially for samples treated with PAASi product, scarce penetration depth and distribution of consolidant inside the pore structure of the stone have been observed, mainly due to the poor impregnation of the samples during the coating procedure. However, as the powerfully of the technique in giving back 3D images and quantitative data on pore network arrangement and changes due to treatments, several interesting consideration can be supplied, especially by comparing the behavior of the two different studied products (Figure 6.10).

In fact, in the case of PAASi, the product impregnates mainly pore in a range of 10 µm< ED<100µm and MO<50µm, while in the case of AlSiX the product distribution affects larger pore range (ED between 100 and 500 µm; MO between 50 and 150 µm), claiming a different interaction of the products with the pore network structure of the stone.

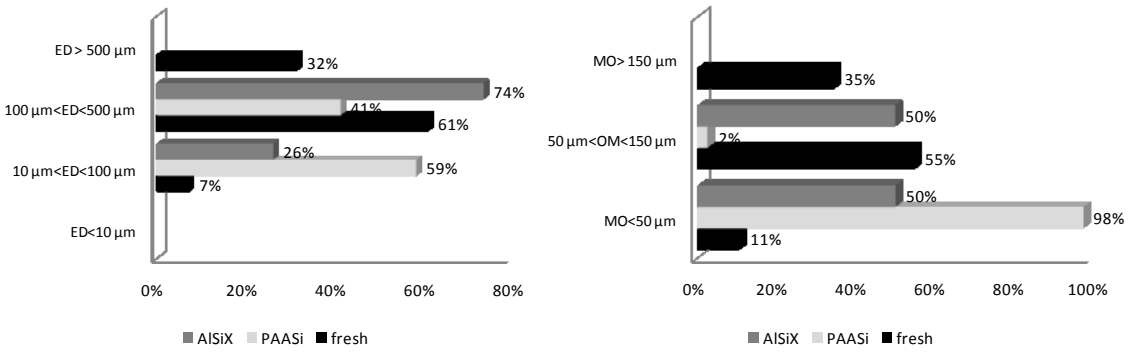

Figure 6.10 - Comparison between ED and MO parameter ranges in treated and untreated samples.

In conclusion, the use of X-ray micro-CT for investigating pore network changes due to consolidant treatments can be considered a suitable method in building stone materials researches, highlighting the whole range of possible results achievable in the framework of Cultural Heritage protection and conservation studies.

6.2.3 Visualization of water repellents and consolidants in building stones and monitor water uptake by neutron radiography

A really key factor for the assessment of conservation and protection treatments is represented by the interaction between the product and the substrate, including features as penetration depth and its distribution in the stone matrix, strictly related to the stone material proprieties as pore structure and surface texture. For this reason, the understanding of the interaction between stone pore network and consolidant and repellent represents a relevant question in the evaluation of

the performance and the efficiency of the products. Therefore, techniques able to investigate these issues are really highly in demand. In this prospective, neutron imaging represents a really sensitive method, as the capability of neutron to detect hydrogen-based materials; in consideration of the hydrogenous nature of the most diffused consolidants and repellents used in conservation of building stones, by using neutrons the distribution of products and their behavior can be easily visualized inside stone materials.

In consideration of the aforementioned, the mean purpose of this section consists in the evaluation of the potential of the non-destructive neutron radiography technique for the visualization of the impregnation depth of hybrid organic-inorganic consolidant and hydrophobic products after polymerization previously tested by standard laboratory test routine and X-ray tomography. Additionally, in a subsequent phase of the experiment, a dynamic set-up has been established in order to monitor water absorption process by capillarity inside the samples and investigate the eventually modification of the physical proprieties of the stone against water due to the treatments.

6.2.3.1 Visualization of treatments and water capillary uptake monitoring

In this experiment, a total of fifteen parallelepiped samples (2x2x4 cm) of Sabucina stone selected for treatment with either consolidant products and water repellent have been scanned at the IMAGINE beam line of the LLB Facility (Laboratoire Léon Brillouin CEA/CNRS) in Saclay (France).

Referring to consolidants (AlSiX and PAASi products), the treatment has been performed in laboratory by plunging the samples in the sols in a sealed container for 1h and drying them at 60°C to constant mass. In the case of protective treatment, the hydrophobic silicon based coating (WS3) has been applied by brushing on the specimens surface and dried at 105°C to constant mass.

Radiographs were taken at the IMAGINE beam line situated at the Laboratoire Léon Brillouin (CEA/CNRS) in Saclay (France) (cold neutron guide with 3Å $<\lambda<$20 Å; L = 4 m; D = 10 mm; giving L/D = 400; neutron flux: $2x10^7$ neutrons/s/cm²; detector: sCMOS camera (Andor) coupled with a lithium scintillator of 100 μm; spatial resolution: 250 μm).

Among the selected specimens, three sets of three samples were treated with AlSiX, PAASi, WS3, respectively. In addition two set of three samples were treated with AlSiX+WS3 and PAASi + WS3, respectively, in order to explore also the combined effect of both consolidant and water repellent. In Figure 6.11 the radiographs of samples representative of the treatments are shown; they allow to illustrate the distribution of the products inside the stone matrix.

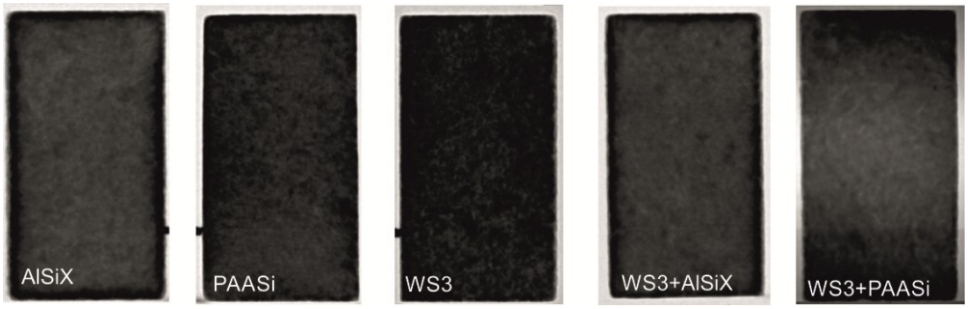

Figure 6.11 - Radiographs of samples representative of each treatment applied

In sample treated with AlSiX consolidant, the radiographs clearly show the presence of the product inside sample, resulting in an increased attenuation of the neutron beam underneath the sample edges; in detail, the product penetrates in the sample for about 2-3 mm and it is homogeneously distributes close the sample surface. Such a behavior can be observed also in the case of the combined used of the consolidant and the water repellent WS3, the latter one really difficult to detect.

In the case of sample treated with PAASi, the presence of consolidant is scarcely detectable by observing the radiographs, being non-homogenously distributed both inside the stone matrix and close to the surface; in fact, really few mm of penetration are visible from the images inspection. Similar observation can be asses for the sample treated with both consolidant and hydrophobic products. As can be inferred for the previously, even if both consolidants are more or less detected by neutron radiography, the presence of the water repellent inside sample is impossible to visualize, maybe due to the quantity which is apparently insufficiently large to obtain a good contrast between the untreated and the treated areas in the sample.

Beside the visualization and the penetration depth of the products, the visualization of water absorption by capillarity inside the stone is of great interest in the framework of the understanding the eventually changes in the hydric proprieties of the stone due to the treatments. Therefore, a sequence of radiographs of treated Sabucina stone samples have been scanned in both dry and wet conditions.

In detail, a reference dry image has been acquired before the contact with water; after taking radiographs of each dry sample, imaging has been interrupted for the filling of the containers with water. Water was added to the set-up manually and a sequence of radiographs at constant time-intervals (every 40s) was taken until diffusion started.

Water movement monitored in samples through neutron radiography is shown in Figure 6.12.

In detail, the image provides a sequence of radiographs for each treatment applied (one sample representative for each set) in dry and in wet condition, together with the images resulting of subtraction of radiographs taken in wet and dry state in order to visualize the only water contribute. The water absorption by capillarity has been monitored in function of time and the sequences shown the process in the first 5, 10, 15 and 20 minutes until the diffusion starts.

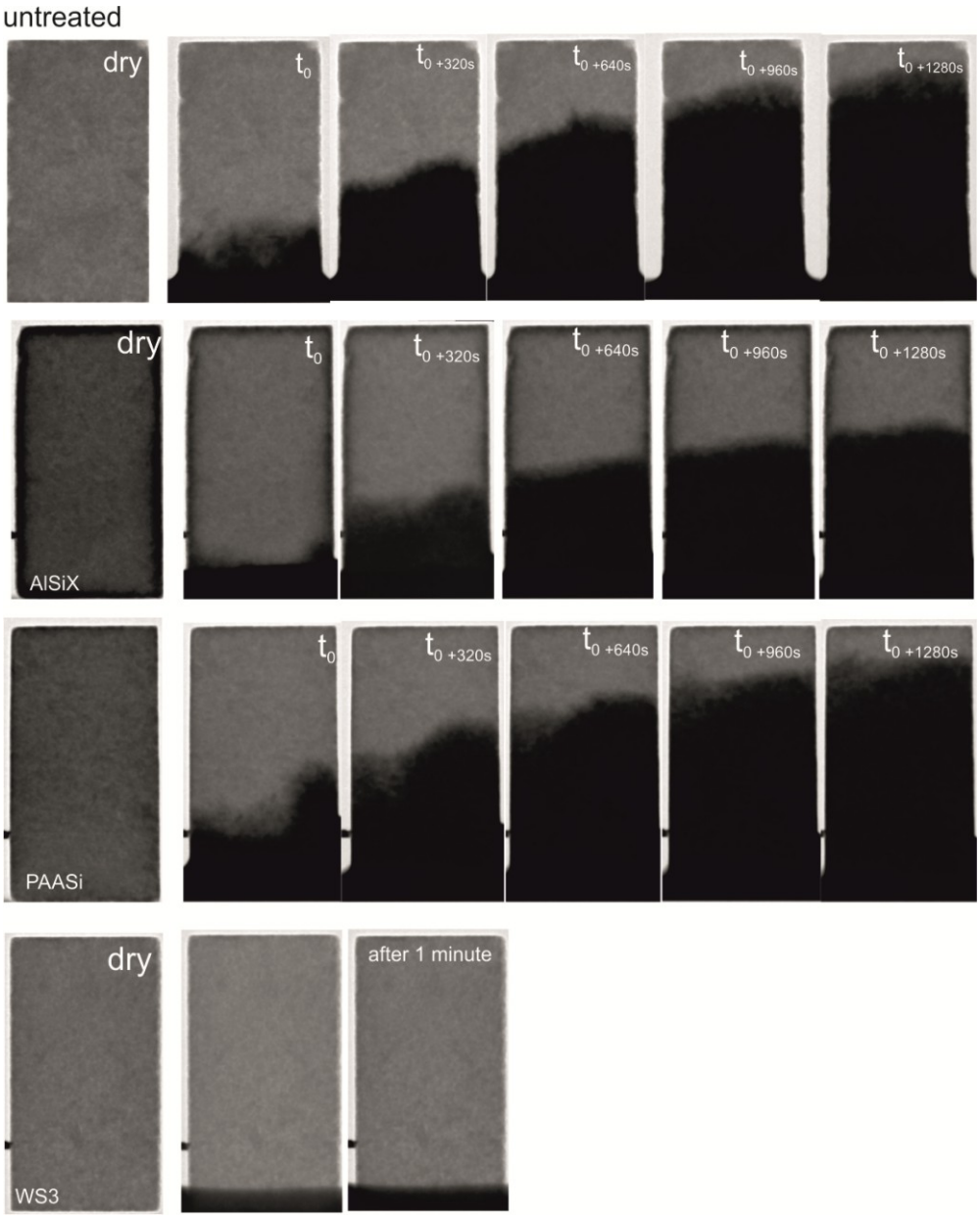

Figure 6.12 - Sequence of radiographs taken at different time intervals for samples treated with consolidant and protective products

The inspection of the radiographs, as well as the possibility to determine the length-related water-penetration coefficient *B* from the wetting front position, allow to visualize the migration of the waterfront inside the samples and quantify the influence of the products in the capillary uptake process occurring in the stone.

Figure 6.13 shows the position of the wetting front as a function of the square root of time for representative samples treated with consolidant and protective products, while in Table 6.3 the penetration coefficients of the same samples, obtained from the transmission images and determined as the slope of the curves$h(t) vs. \sqrt{t}$are reported.

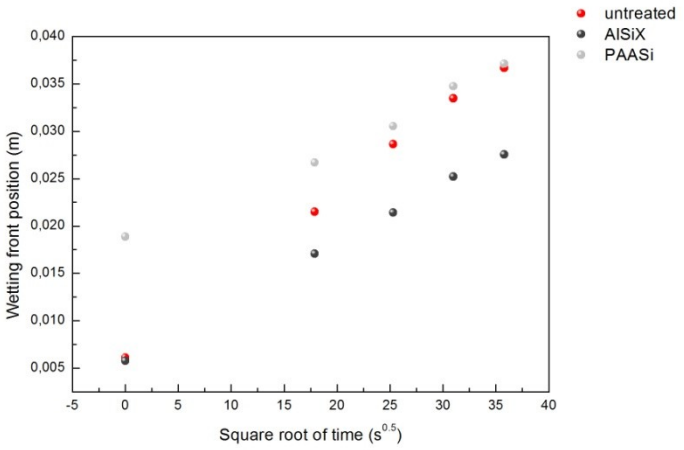

Figure 6.13 - Position of the wetting front as a function of the square root of time for representative samples treated with consolidant and protective products

Table 6.3 - Penetration coefficients calculated for untreated and treated samples

Sample ID	***Penetration coefficient (m/√s)***
Untreated	$8.6*10^{-4}$
AlSiX	$6.1*10^{-4}$
PAASi	$5.1*10^{-4}$

The calculated penetration coefficients clearly demonstrate that the migrating waterfront inside the sample treated with AlSiX is slightly inhibited by the presence of the product; otherwise, the PAASi treatment determines no significantly changes respect to the untreated stone, even if during the first minutes of contact with water a greater advancement of the wetting front position can be observed respect to the untreated sample.

In the case of hydrophobic product, the radiographs images convincingly illustrate that no water invades the stone samples, also when it is used in association with the consolidants.

6.2.3.2 Quantification of changes in capillary absorption proprieties

In order to quantify the water distribution in stone samples and better understand the water uptake process in treated samples, reference dry and wet images are evaluated for the mass thickness of water as described previously and according to Kim et al., 2012[15]. In detail, the image processing method allows to quantify the water content percentage inside the stone

volume, highlighting therefore the spread mechanism and the effects of treatments in the capillarity absorption proprieties of the stone.

In Figure 6.14 the contour plots of water content distribution (WC%) obtained from neutron radiography images are shown; in particular, a sequence of plots obtained from radiographs taken after about 5, 10, 15 and 20 minutes until the diffusion start are shown for one sample representative of each set. For specimens treated with the hydrophobic product, only few minutes of contact have been monitoring, due to the evidence that no water invades the sample during the test.

It is worth of note that the contact time labeled as t_0 has to be considered a reference value for the evaluation of the whole sequence, as it effectively represents the first wet acquisition available after the manually adding of water and the opening of the neutron beam in safety conditions.

The inspection of the processed images allows to better understand the effects of the consolidant and protective hydrophobic products in the behavior of the stone against water by capillarity.

Contours describing the quantitative distribution of water inside the stone volumes clearly show that in the case of AlSiX treatment lower content of WC % than the untreated samples can be observed (always, the WC values are lower than 2%). In addition, really interesting side effects are visible; in fact, water clearly penetrates from bottom to up not involving the areas in which consolidant have penetrated, flowing underneath the thickness of the product whose depth has been previously detected by the inspection of dry images.

Referring to samples treated with PAASi, the quantification of water content percentages confirms the results suggested by the inspection of raw images, *i.e.* the presence of the treatment don't prevent the water absorption in the stone; moreover, the obtained results highlight a worsening of the stone resistance to water capillary uptake, as values up to 2.5-3 WC% has been obtained, the latter ones higher than in the untreated stone.

Finally, the high performances of hydrophobic treatment used both alone and in combination with consolidants, are clearly evidenced by the quantification of water contents. In fact, the contouring plots show that no water invades the samples over the monitoring time. In this framework, the water visualized in the radiographs has to be related only to the set-up reservoir.

In order to compare the results obtained by using non-destructive imaging techniques and classical gravimetric methods, the same capillarity experiment has been performed in the laboratory; in detail, water absorption tests by capillarity following the standard recommendations have been carried out.

In Table 6.4 the results obtained by water capillarity test according to the standard recommendation are reported, while in Figure 6.15 the amount of water absorbed per area in function of time during the first 30 minutes of water absorption by capillarity is shown.

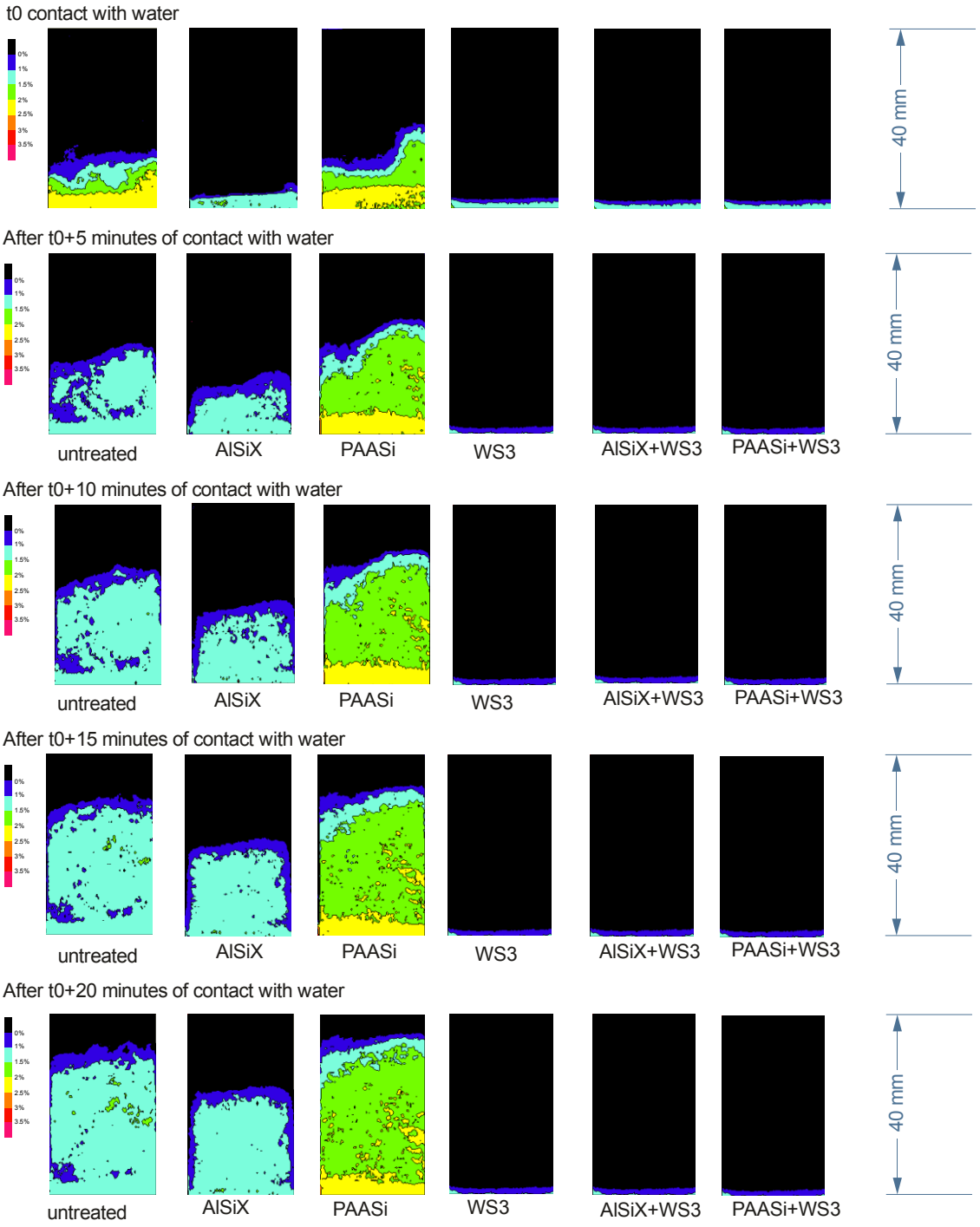

Figure 6.14 - Water content percentage (WC%) contour plots for untreated and treated samples over the monitoring time

Table 6.4 - Report of NORMAL 11/88 recommendation test						
t (√s)	***Volume of water absorption per area (g/cm²)***			***Water % absorbed per area***		
	NT	***PAASi***	***AlSiX***	***NT***	***PAASi***	***AlSiX***
0	0.000	0.000	0.000	0.00	0.00	0.00
24	0.271	0.291	0.195	29.89	34.72	23.17
35	0.362	0.392	0.241	39.98	46.82	28.59
42	0.427	0.473	0.277	47.11	56.39	32.90
60	0.567	0.644	0.339	62.62	76.81	40.30
120	0.822	0.769	0.552	90.74	91.79	65.57
147	0.828	0.783	0.629	91.49	93.47	74.66
294	0.839	0.789	0.733	92.61	94.17	87.07
416	0.876	0.822	0.756	96.76	98.12	89.74
509	0.894	0.833	0.785	98.74	99.37	93.25
588	0.906	0.838	0.842	100	100	100
slope	**0.009**	**0.01**	**0.005**			
AC (g/cm²)	**0.023**	**0.003**	**0.013**			

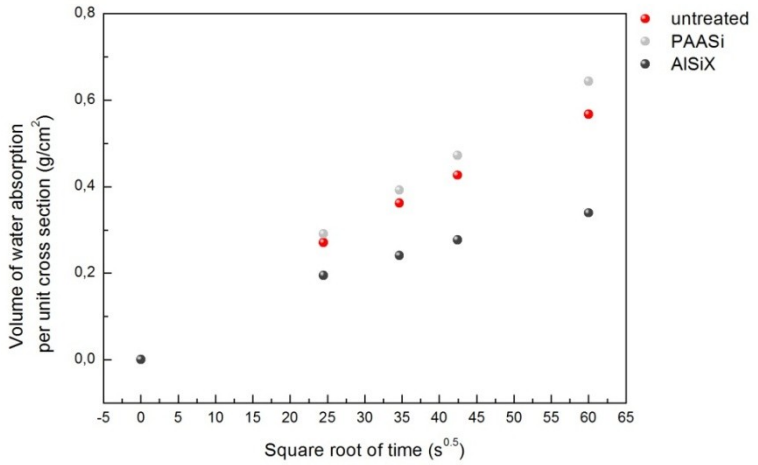

Figure 6.15 - Amount of water absorbed per area in function of time during the first 30 minutes of water absorption by capillarity for untreated and treated samples with consolidant AlSiX and PAASi.

The obtained results highlight a good correspondence between percentage of water calculated by using radiographic images and capillary coefficient determined by gravimetric test, claiming a change in the physical proprieties of the stone due to the presence of products. In fact, in the first 30 minutes of absorption, the absorbed water percentage decrease from 62% in untreated samples to 40% in samples treated with AlSiX product, whereas an increasing of water percentage to 76% can be observed in samples treated with PAASi consolidant.

Referring to hydrophobic treatment, the comparison between data obtained from radiographs and results of gravimetric tests (see Figure 6.16 and Table 6.5), highlight a large decrease of water percentage absorbed by samples, as the percentage of water absorbed in the first 30 minutes of contact with water drastically drop to 30%.

Table 6.5 - Report of NORMAL 11/88 recommendation test						
t (√s)	Volume per unit of area (g/cm²)			Water % absorbed per area		
	NT	PAASi+WS3	AlSiX+WS3	NT	PAASi+WS3	AlSiX+WS3
0	0.000	0.000	0.000	0.00	0	0
24	0.271	0.092	0.126	29.89	11.0	16.1
35	0.362	0.127	0.201	39.98	15.1	25.7
42	0.427	0.180	0.233	47.11	21.4	29.8
60	0.567	0.276	0.296	62.62	32.8	37.9
120	0.822	0.547	0.527	90.74	65.0	67.4
147	0.828	0.641	0.635	91.49	76.2	81.2
294	0.839	0.791	0.733	92.61	94.0	93.8
416	0.876	0.844	0.792	96.76	100	101
509	0.894	0.842	0.782	98.74		
588	0.906			100		
slope	**0.009**	**0.005**	**0.004**			
CA (g/cm2)	**0.033**	**0.018**	**0.015**			

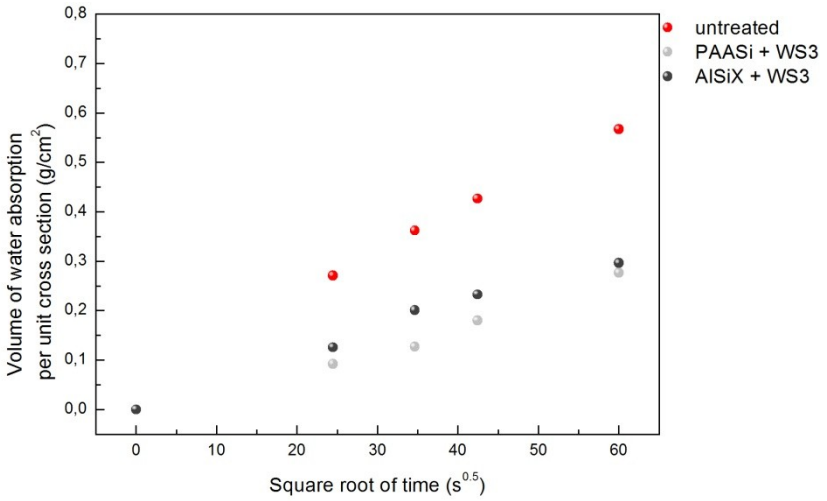

Figure 6.16 - Amount of water absorbed per area in function of time during the first 30 minutes of water absorption by capillarity for untreated and treated samples with the hydrophobic product WS3

6.2.4 Final remarks

The investigation of features as penetration depth of consolidant and repellent products used in preserving natural building stones represents one of the main factor for the evaluation of their efficiency. With this study has been proved that neutron radiography represents a very useful for these purposes, as the strong attenuation of neutrons by hydrogen atoms, the latter ones being the main compositional element of a large number of consolidant and repellent treatments. Therefore, it can be successfully applied for the visualization of impregnation depth of polymerized products; additionally, on the basis of the previously mentioned features, the technique can also be employed for the monitoring of water migration inside porous materials.

The obtained results on treated Sabucina stone samples have allowed to highlight interesting features both in term of penetration depth and changes in the absorption proprieties of the stone

after the application of two consolidants namely AlSiX and PAASi, and a water repellent, namely WS3, the latter one also in combination with the previously.

The inspection of the raw radiographic images allows to detect the distribution of the products inside the stone matrix, permitting to assess the different behavior of the stone coated with several treatments. However, some limitations have been observed, maybe due to the scarce quantity of products used in the coating. In fact, in the case of AlSiX consolidant, a homogenous penetration underneath the stone surface has been observed, while the presence of PAASi consolidant and the hydrophobic treatment has been difficulty detected by using neutrons. Nerveless, the quantification of water distribution inside the stone sample by monitoring the capillary uptake process has been demonstrate really useful in order to evaluate the effects of the treatments in the hydric proprieties of the stone. The WC% contour plots highlight, in fact, a significant reduction of water absorption by capillarity in the stone samples treated with AlSiX consolidant, while in the case of PAASi a slight worsening of the water resistance to absorption by capillarity has been observed. Additionally, even if the inspection of the raw radiographs don't allow the visualization of the hydrophobic coating, its effects on the stone has been certainly detected by the dynamic monitoring of water absorption, highlighting the high performance of the product as no water invading the pore network has been detected. Finally, a good agreement between data obtained from image processing and classical gravimetric test has been observed, having the former method the great advantage to visualize the process occurring inside the samples.

In conclusion, the research demonstrates the powerfully of neutron radiography for qualitative and quantitative studies in the field of conservative treatments and it can be considered a basic step for additional knowledge on the suitability of the investigated products for the treatment of calcarenite type building stones.

6.3 Surface modification due to protective treatments

In this section, the surface of a reference sample and treated surfaces with basic and acid TiO_2 nanosols (TiMaA and TiAcN, respectively) has been analyzed in order to visualize and quantify the eventually modification of surface texture due to the application of coatings.

Images have been acquired by using Hirox KH-7700 digital microscope with an MXG-10C body, an OL-140II lens and an AD-10S Directional Lighting Adapter. The Auto Multi Focus tool enabled the creation of a 3D image obtained by the composition of one hundred planes taken at different focus levels.

On the samples surface, a rectangular area of about 1 x 0.5 cm has been selected for the acquisition of the images.

In order to obtain the surface texture parameters (both in term of roughness and waviness), the 2D gray scale projection of the 3D images have been processes by using the ImageJ plug-

inSurfCharJ[16]. The plug-in is based on several developed routines for surface assessment[17], and provides global and local roughness analysis, gradient analysis, domain segmentation, surface leveling and directional analysis. Having suitable surface representations, both roughness/waviness surface maps and several surface roughness/waviness parameters can be derived from the analysis, according to the ISO 4287/2000 standard.

In order to discriminate waviness (*i.e.* undulations that are several times longer than deep) and roughness (*i.e.* ondulations that are just a few times longer than deep) a limit defined by the cut-off wavelength λc[18] has to be established. The length of λc is not predetermined but influences the value of roughness parameters. Usually, the length of the measured profile is six or seven times the length of λc[18]. Therefore, the unfiltered primary surface map has been filtered by using Gaussian filters having a radius corresponding to the lower structure size limit input, represented by the wavelength λc; in this way, roughness and waviness images can be been obtained, representing components having smaller and greater structures than the applied wavelength λc, respectively.

According to the previously, the wavelength (λc) has been established, each time, as about the sixth part of the length of the measured profiles. The obtained roughness and waviness images have been, finally, processed by using the ImageJ plug-in *Interactive 3D surface plot*, in order to extract 3D topographically information and better visualize the peak and valley events related to the 2D analyzed images.

In Figure 6.17 and 6.18 the roughness and waviness maps with the relative 3D surface plots of reference untreated and coated stone sample surfaces are shown, while in Tables 6.6 and 6.7 the obtained parameters from the roughness and waviness analysis are reported, respectively.

Table 6.6 - Roughness parameters (μm)obtained by applying a Gaussian filter with SurfCharJ plug-in in ImageJ

Sample ID	***Rq***	***Ra***	***Rsk***	***Rku***	***Rv***	***Rp***	***Rt***	***Rc***
reference sample	6.2432	4.9274	-0.5722	0.2712	-20.9165	14.7228	35.6392	0.043
TiMaA	4.9626	3.8386	-1.1617	13.1889	-24.9195	10.9909	35.9104	-0.0651
TiAcN	4.3566	3.3886	-0.889	1.2318	-17.5671	9.4231	26.9901	-0.0392

Table 6.7 - Waviness parameters (μm) obtained by applying a Gaussian filter with SurfCharJ plug-in in ImageJ

Sample ID	***Wq***	***Wa***	***Wsk***	***Wku***	***Wv***	***Wp***	***Wt***	***Wc***
reference surface	6.7604	5.4892	-0.4848	-0.1276	189.085	218.4196	29.3347	207.1659
TiMaA	4.9231	4.1163	-0.3542	-0.5065	203.8603	223.9173	20.057	214.9963
TiAcN	3.0601	2.5175	-0.3637	-0.269	219.4158	233.0525	13.6367	227.036

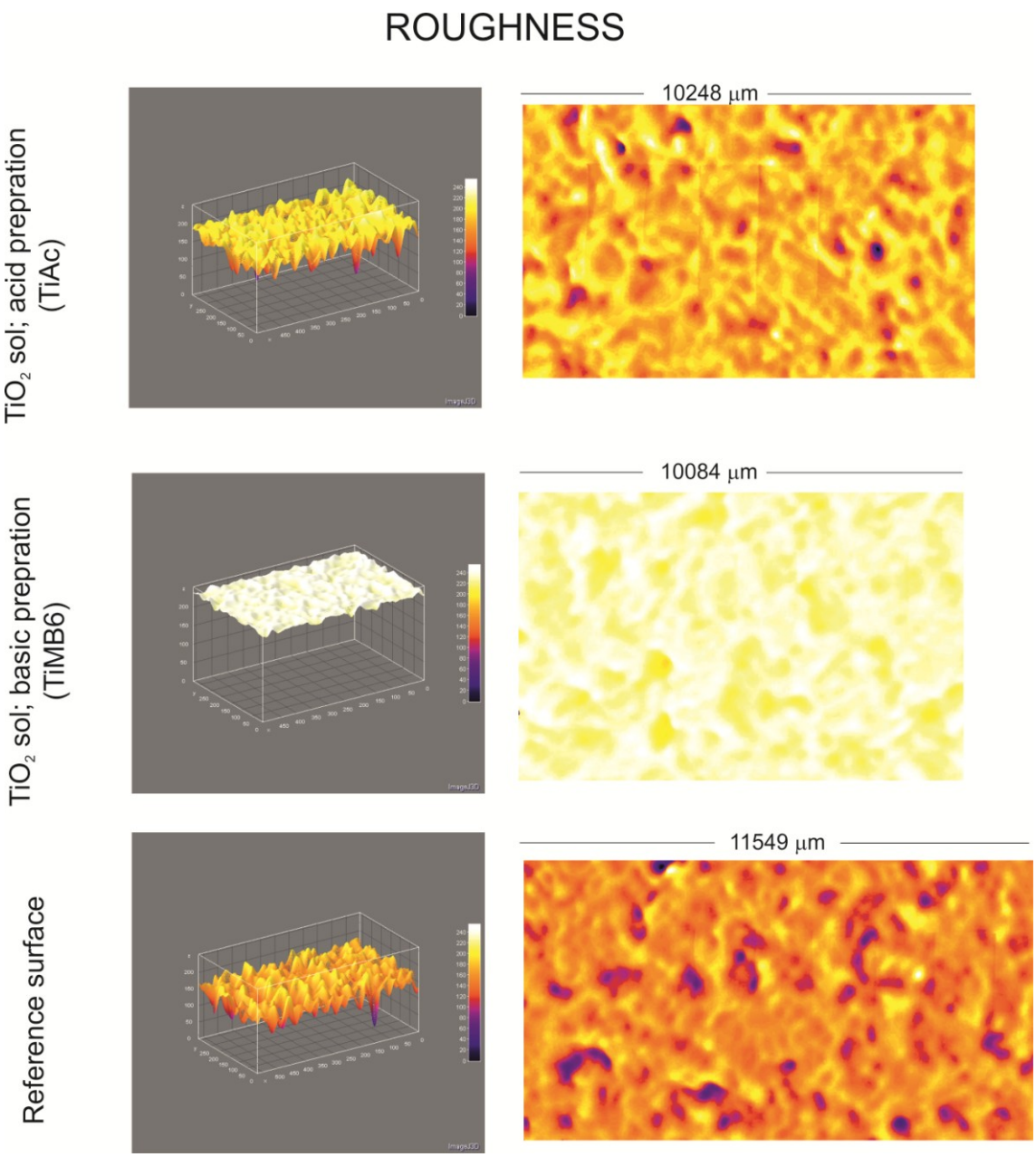

Figure 6.17 - Roughness maps and surface plots of untreated and treated stone surfaces

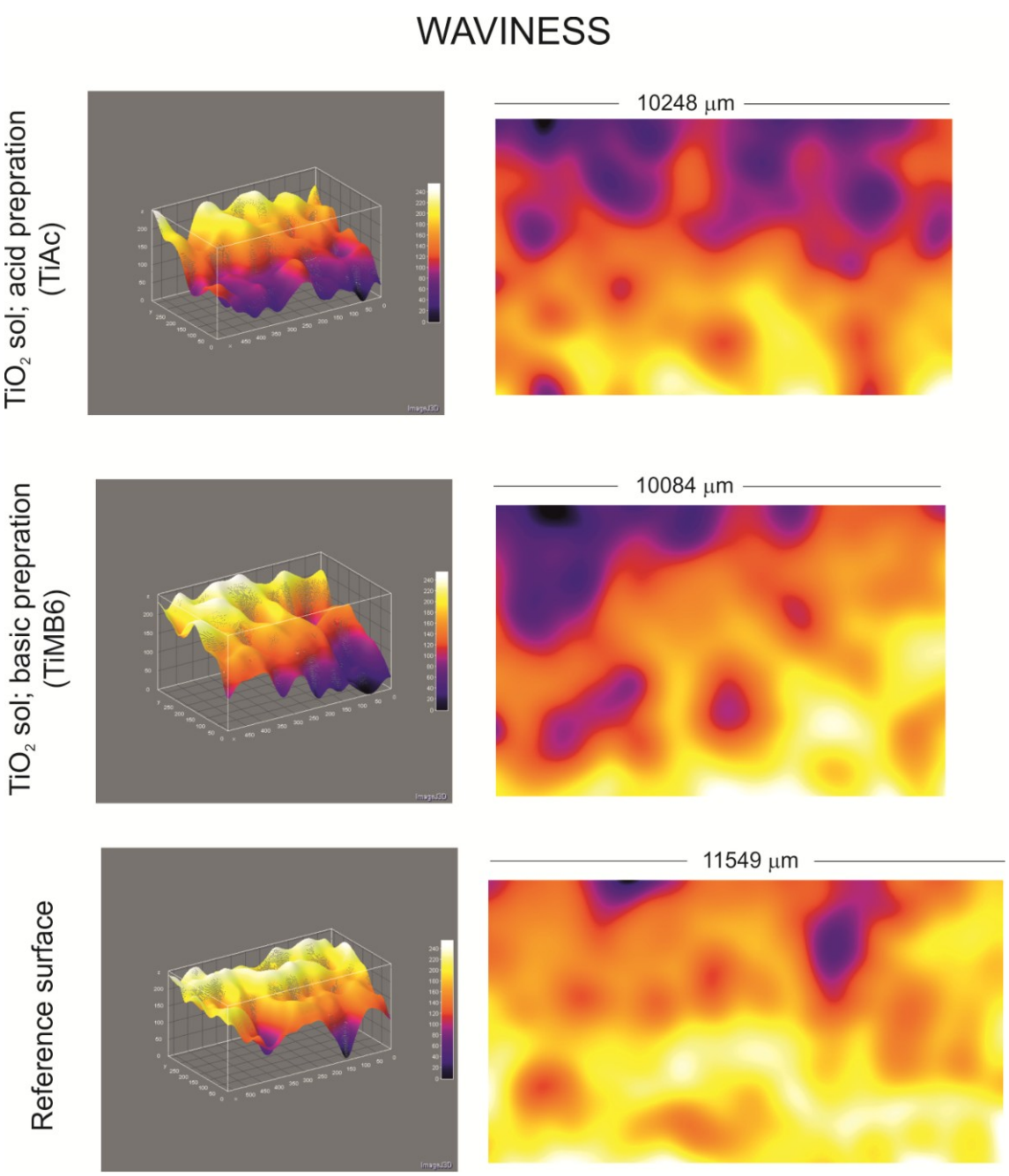

Figure 6.18 - Waviness maps and surface plots of untreated and treated stone surfaces

By comparing parameters obtained from 3D digital analysis of studied surfaces, an overall decrease of surface roughness and waviness due to the coating has been observed; in addition, the variation in term of R_a/W_a, R_q/W_q and R_t/W_t parameters allows to assess that the acid TiO_2preparation determines lower roughness/waviness values than the basic one (Figure 6.19). This statement support and confirm the results obtained by efficiency tests and SEM observations, that had suggested a better performance and compatibility of the TiMaA coating with the calcarenite substrate.

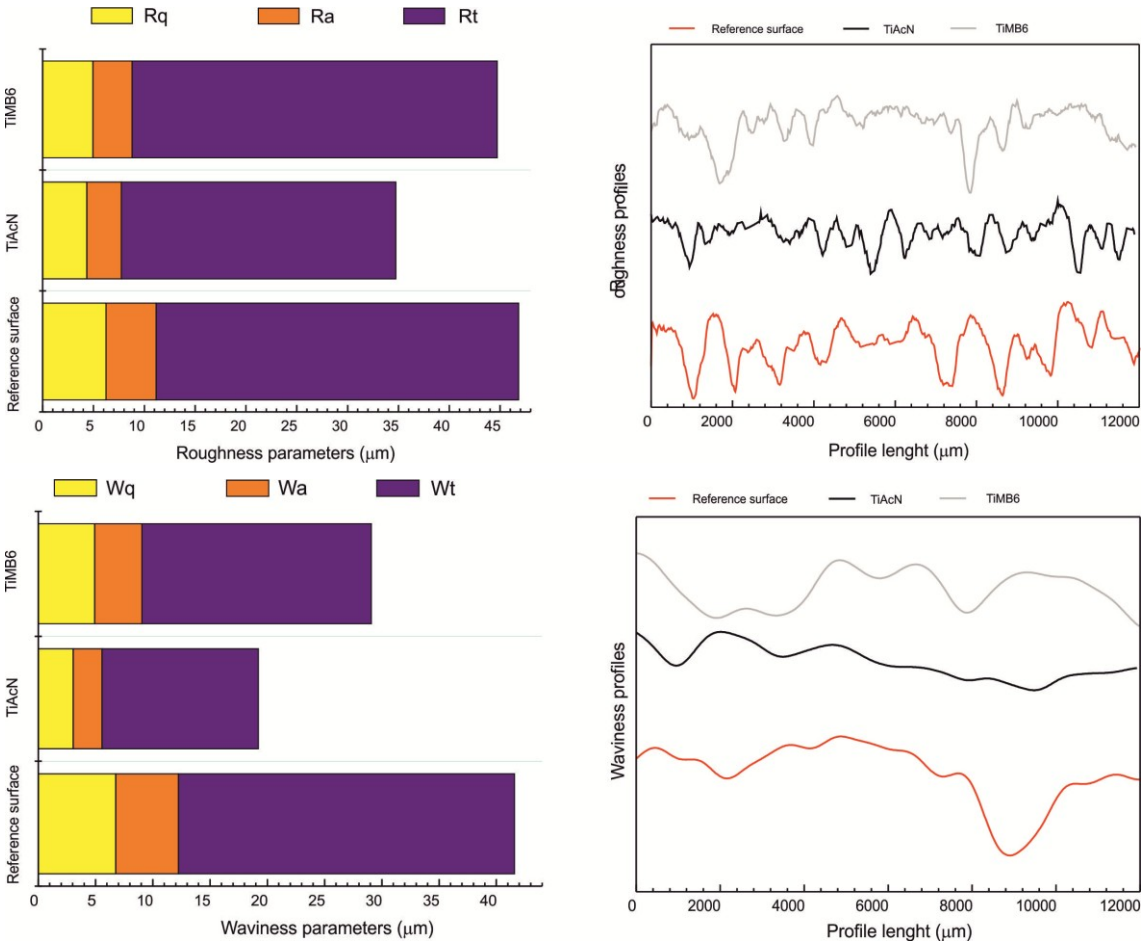

Figure 6.19 - Comparison between R_a/W_a, R_q/W_q and R_t/W_t values for uncoated and coated surfaces and profiles of studied samples in function of treatments

6.4 Discussion and conclusions

Beside successfully results in evaluating performances of consolidant and protective treatments can be obtained by applying efficiency test routines based on standard recommendation, the investigation of additional aspects as penetration depth and interaction with substrate are fundamental for a complete valuation of the suitability of products. In order to achieve these aims, the application of a multi-scalar and multi-methodological approach is required, as it is

needed to inspect different dimensional range and solve problems related to the visualization of organic materials inside the porous structure of stones. Moreover, in the case of nanoparticles coatings is of a great interest the understanding of the eventually modification of stone surface texture after the application of the products.

In view of the aforementioned, in this section several methods, mainly non-invasive and non-destructive, have been applied in order to: evaluate the penetration depth of AlSiX and PAASi consolidant (used also in combination with WS3 hydrophobic treatment), quantify and visualize the eventually modification of the stone in term of behavior against water and, finally, esteem the surface texture changes in samples coated with TiO_2 nano-sols.

Referring to consolidants, the application of intrusion mercury method has given back not really convincing results, maybe due to limits of resolution in term of pore size investigable. Otherwise, better results have been obtained by using X-ray μ-CT; the method is, in fact, able to inspect pores greater than 100 μm, allowing to describe also greater structures; however, also in this case some problems related to impregnation ability of products have been detected. A deepened description of the interaction between products and substrate has been obtained by using neutron radiography, as its high sensitivity to hydrogen-based materials; by using this method it has been possible to estimate and visualize the distribution of products inside the stone matrix and the changes in the stone behavior against water. Finally, the inspection of TiO_2-sols coated surfaces has allowed to highlight the ability of 3D digital microscope in evaluating changes in texture features determined by protective treatments.

Summarizing, in the case of Sabucina Stone, the comparative measurements performed on untreated and treated samples with two consolidant, namely AlSiX and PAASi, and protective products, namely a silicon-based hydrophobic treatment and photocatalytic TiO_2-sols, have allowed to conclude the following:

- referring to the consolidant treatments, in both cases, and especially for samples treated with PAASi product, scarce penetration depth and distribution of consolidant inside the pore structure of the stone have been observed. However, quantitative information on pore ranges interested by the impregnation of the product have been obtained by X-ray μ-CT method. In fact, the analysis of X-ray tomographies has allowed to quantify the impregnation of PAASi in a range of 10 μm< ED<100μm and MO<50μm, while in the case of AlSiX the product distribution affects larger pore ranges (ED between 100 and 500 μm; MO between 50 and 150 μm), claiming a different interaction of the products with the pore network structure of the stone.
- The non-homogeneous penetration of consolidants has been also highlighted by the inspection of neutron radiography; in fact, only for AlSiX a penetration depth of about 2-3 mm has been esteemed, while PAASi and hydrophobic product were impossible to visualize.

- In spite of the scarce penetration depth, the products affect the hydric proprieties of stone; in fact, the monitoring of capillary uptake over the time and the determination of the relative linear penetration coefficients highlight that in samples treated with AlSiX the penetration of water is slightly inhibited by the presence of the product; otherwise, the PAASi treatment determines no significantly changes respect to the untreated stone. Finally, in the case of hydrophobic product, the radiographs images convincingly illustrate that no water invades the stone samples, also when it is used in association with the consolidants.
- The previous qualitative information are confirmed by the quantification of water percentage distribution inside the treated samples; in fact, the WC% contour plots show a significant reduction of water absorption by capillarity in the stone samples treated with AlSiX consolidant (always, the WC values are lower than 2%), while in the case of PAASi a slight worsening of the water resistance to absorption by capillarity has been observed (values up to 2.5-3 WC% has been obtained, higher than in the untreated stone); in the case of hydrophobic treatment, used both alone and in combination with consolidants, the contour plots show that no water invade the samples over the monitoring time.
- Good agreement between data obtained from neutron radiography images and classical gravimetric tests has been observed, having the former method the great advantage to visualize the process occurring inside the samples.
- Finally, referring to TiO_2 nano-sol coatings, an overall decrease of surface roughness due to the treatments has been observed, with a greater variation in term of R_a/W_a, R_q/W_q and R_t/W_t parameters for the TiO_2 acid preparation, maybe more invasive in calcarenite substrates.

Therefore, the overall of the obtained data has to be considered a good example of the potential of the applied experimental and theoretical approach in investigating, visualizing and quantifying pore structure and surface texture modifications due to protective and consolidant treatments in natural building stones, especially in the case of coarse-grained calcite-based materials.

6.5 Bibliography

[1] Cnudde V, Cnudde JP, Dupuis C, Jacobs PJS. X-ray micro-CT used for the localization of water repellents and consolidants inside natural building stones. Materials Characterization, 2004. 53:259-271.

[2] Cnudde V, Dubruel P, De Winne K, De Witte I, Masschaele B, Jacobs P, Schacht E. The use of X-ray tomography in the study of water repellents and consolidants. Engineering Geology, 2009. 103: 84-92.

[3] Ruiz de ArgandoñaVG, Calleja L, Rodríguez-Rey A, Suárez del Río LM, Celorio C. X-ray Computed Tomography study of the influence of consolidants on the hydric properties of sandstones for stone conservation studies. Engineering Geology, 2009. 103: 69-75.

[4] Brunetti A, Princi E, Vicini S, Pincin S, Bidali S, Mariani A. Visualization of monomer and polymer inside porous stones by using X-ray tomography. Nucl. Instr. Meth. Phys. Res. B, 2004. 222: 235–241.

[5] Ruiz de Argandona V, Calleja L, Rodríguez-Rey A, Suárez del Río LM, Celorio C.X-ray computed tomography study of the influence of consolidants on the hydric properties of sandstones for stone conservation studies. Eng. Geol., 2009. 103: 69–75.

[6] Slavíková M, Krejci F, Zemlicka J,Pech M, Kotlík P, Jakubek J. X-ray radiography and tomography for monitoring the penetration depth of consolidants in Opuka – the building stone of Prague monuments. J. Cult.Herit., 2012. 13:357-364.

[7] Cnudde V, Dierick M, Vlassenbroeck J, Masschaele B, Lehmann E, Jacobs P, Van Hoorebeke L. Determination of the impregnation depth of siloxanes and ethylsilicates in porous material by neutron radiography. Journal of Cultural Heritage, 2007. 8: 331-338

[8] Hameed F, Schillinger B, Rohatsch A, Zawisky M, Rauch H. Investigations of stone consolidants by neutron imaging. Nuclear Instruments and Methods in Physics Research Section A: Accelerators, Spectrometers, Detectors and Associated Equipment, Volume 605, Issues 1–2, 21 June 2009, Pages 150-153

[9] Dierick M, Vlassenbroeck J, Masschaele B, Cnudde V, Van Hoorebeke L, Hillenbach A. High-speed neutron tomography of dynamic processes. Nucl.Instr. Meth. Phys. Res. A, 2005. 542: 296–301.

[10]Milczarek JJ, Czachor A, El Abd AE, Wiśniewski Z. Dynamic neutron radiography observation of water migration in porous media. Nucl. Instr. Meth. Phys. Res. A, 2005. 542: 232–236.

[11] Masschaele B, Dierick M, Cnudde V, Van Hoorebeke L, Delputte S, Gildemeister A, Gaehler R, Hillenbach A. High-speed thermal neutron tomography for the visualization of water repellents, consolidants and water uptake in sand and lime stones. Radiat. Phys. Chem., 2004. 71: 807–808.

[12] Masschaele BC, Cnudde V, Dierick M, Jacobs P, Van Hoorebek L, Vlassenbroeck J. UGCT: New x-ray radiography and tomography facility. Nuclear Instruments & Methods In Physics Research Section A-Accelerators Spectrometers Detectors And Associated Equipment, 2007. 580: 266-269.

[13] Vlassenbroeck J, Dierick M, Masschaele B, Cnudde V, Van Hoorebeke L, Jacobs P. Software tools for quantification of X-ray micro tomography at the UGCT. Nucl. Instrum Meth A, 2007. 580: 442–445.

[14] Brabant L, Vlassenbroeck J, De Witte Y, Cnudde V, Boone MN, Dewanckele J, Van Hoorebeke L. Three-Dimensional Analysis of High-Resolution X-Ray Computed Tomography Data with Morpho+. Microscopy and Microanalysis, 2011. 17: 252-263.

[15] Kim FH, Penumadu D, Hussey DS. Water Distribution Variation in Partially Saturated Granular Materials Using Neutron Imaging, J. Geotech. Geoenviron. Eng., 2012.138:147-154.

[16] Chinga G, Johnsen PO, Dougherty R, Lunden Berli E, Walter J. Quantification of the 3D microstructure of SC surfaces. Journal of Microscopy, 2007. 227: 254–265.

[17] Chinga G, Gregersen Ø, Dougherty R. Paper surface characterization by laser profilometry and image analysis. J. Microsc. Anal., 2003. 84: 5–7.

[18] Volk R. Rauheitsmessungen, Theorie und Praxis, eds. DIN Deutsches Institut fürNormung, 2005, Berlin, Wien, Zürich: Beuth Verlag.

Chapter 7. Final remarks

In this Thesis work, an experimental and theoretical approach based on the application of both classical and innovative and non invasive techniques has been tested in order to supply a complete model on porosity changes due to degradation process and conservative treatment in natural building stones. The method has been applied on a local coarse grained calcarenite, namely Sabucina Stone (Caltanissetta, Sicily, Italy), widely used as building material in Sicily and particularly suitable for this study as its really complex pore geometry.

Firstly, a complete characterization of the studied stone form the petrographic, mineralogical, geochemical, physical and mechanical point of view has been obtained by applying a classical methodological routine based on standard recommendation (*Chapter 1*). Noteworthy is that all tests have been performed on samples with different dimension in order to evaluate the eventually dimensional effects of weathering on stones. The overall of the acquired data has allowed to describe the studied material and obtain interesting information about stone features, fundamental in order to establish the appropriate research activity and plan the subsequent analyses. In detail, the obtained results highlight the necessity of a multi-methodological approach in investigating the characteristics of this building stone for allowing the correct interpretation of data, in consideration of its microtextural and microstructural proprieties.

Several samples of Sabucina Stone quarried at the Sabucina Mountain have been artificially weathered by applying UNI EN 12370 standard test. Fresh and degraded samples have been therefore analyzed by using classical and innovative methods (*Chapter 2*) in order to quantify, visualize and model the changes in sub-surface and surface features of the stone due to weathering action (*Chapter 3*).

The application of classical intrusion method as mercury intrusion porosimetry (MIP) and the subsequent treatment of data according to Angeli et al. 2007 have allowed to obtain information on weathering mechanism as well as on location of salts in the studied stone, highlighting also the powerfully of this method in describing pore network changes in degraded building stones. In detail, weathering process due to sodium sulphate crystallization acts in a first stage by filling the entry of pores, whit a subsequent enlargement of them; then, the filling of pores characterized by larger throats from the 4^{th} crystallization cycles hs been observed. In fact, the modal pore radius shifts from a values of about 8 μm in unweathered sample to 12 μm in weathered ones, with a peak of 14 μm corresponding to a change in the degradation mechanism; in this framework, salts are located in pores ranging from 50 to 100 μm. These statements have been therefore used for the interpretation of physical and mechanical parameters esteemed by

following standard recommendations on weathered samples; all the obtained data have highlighted that the pore network changes greatly influenced the mechanical behavior of the stone. In detail, the UCS values measured exhibit a trend inversion in correspondence with the degradation mechanism change up to the 4th crystallization cycle and this data trend couldn't be completely explained without the supporting case of porosimetric measurements. In fact, up to the 2nd to the 4thcrystallization cycles, salts fill the pore throats, determining a slight and progressive increment of compressive strength resistance. Otherwise, when the enlargement of the throats and the filling of the pores have occurred (i.e. up to 6th crystallization cycle) a decrease of UCS values has been observed, claiming a strictly relation between the location of salts and the mechanical resistance of the stone.

Beside the successfully results obtained by applying the aforementioned destructive and micro-destructive methods, the use of innovative techniques has been able to give back extremely accurate and deepened data and improve the quality of the information previously acquired, taking advantage from their non-destructive and non-invasive features. In this sense, the application of portable single side nuclear magnetic resonance (NMR) technique has evidenced the possibility to obtain a complete porosimetric analysis of a porous media in easily-handled, convenient, fast, and, most importantly, non-destructive way. In fact, the good accordance between MIP measurements and NMR data has allowed to infer the same conclusion in a non-destructive and non-invasive way (shift of T2 more populated component from ~ 10 ms to ~ 60 ms).

For the visual inspection of the weathering processes, as well as the accurate quantification of pore network and hydric proprieties changes in weathered material, the application of imaging techniques that use X-ray and neutron sources has been demonstrated really adequate. In fact, the application of X-ray μ-CT has allowed to accurately quantify and visualize pore changes in Sabucina Stone; the obtained data highlight how salt crystallization acts to increase the total porosity, with an increment of open porosity and a concomitant decrease of the closed one. Overall, the enlarged pores in weathered samples exhibit higher maximum opening and equivalent diameter parameters than the freshly quarried sample. As far as the pores are enlarged, the stone become able to absorb much more water, as testified by the increasing of saturation coefficient with the advancement of the degradation process; however, the calculated interconnection parameters for unweathered and weathered samples highlight that the salt weathering process doesn't alter the ability of the stone to vehicle moisture. These evidences are enforced by the results obtained by both gravimetric tests and neutron imaging analysis. In particular, the latter one allows to highlight that water penetrates more quickly and deeper into weathered samples. Such a behavior has to be related to the modification of pore structure that determines an higher ability to absorb greater volume of water, especially in enlarged pores created by the intense degradation action. In the weathered stone samples, the ability to speedy

vehicle the water in vertically orientation is associated with a relevant horizontally spread of the water in coarser pores, in which more water is absorbed; this process determines the presence of isolated and irregularly distributed areas that exhibit higher water content percetages than the surrounding. Therefore, until the water vertically flows up to saturate the entire volume sample, the coarser pore structures allow the absorption of higher water content, determining subsequent waterfronts at different water percentages and the highlighting of the distribution of the pore structure inside the stone. However, water penetrates by capillarity in not homogenous and non perfect linear way, due to slight heterogeneity in capillarity absorption proprieties of sub-volumes inside the samples. In addition, an evidence of side effects due to more intense action of the degradation process close the surface is claimed by the speedy advancement of the waterfront and the high water percentages at the edges of the weathered stone samples respect to the inner part. These evidences are better visualized in neutron tomographies by the occurrence of differential flow patterns inside the whole investigated volume of weathered samples. Finally, the intense action of weathering on surface has been testified by a decreasing of roughness and increasing waviness parameters measured by 3D digital microscope, with a consequently general smoothing of the surface.

On the basis of aforementioned, is possible to assume that the studied system (both in term of sub-surface and surface features) become more complex with the advancement of weathering process; in fact, surface is smoothed in term of small scale ondulation structures, new range of pores appear, part of closed porosity is opened and therefore become accessible to moisture flow, water can spread rapidly both vertically and horizontally thanks also the presence of enlarged pores and, finally, the new structural arrangement causes the development of preferential water uptake fluid-flow pattern. Such a behavior has been successfully described by using fractal models (*Chapter 4*). In fact, by applying fractal geometrical model has been possible to asses that weathering process determine a progressive increase of pore surface fractal dimension, *i.e.* from 2.77 in fresh samples to 2.90 in weathered samples and to 2.92 for cleaned ones (at the end of the 14 cycles). The obtained data suggest, therefore, that fractal dimension of pore surface can be used as descriptor of weathering process in natural building stones.

As aspects such process operating, weathering mechanism, stone response and quantification of damage are clarified, interesting implication about the complicate relation between rate and scale can be also concluded. On the whole, all methods suggest, in fact, that in the studied stone the most intense effects of the degradation occur up to the 4^{th}-6^{th} crystallization cycles (giving therefore information on rate) and that the salts crystallization process is independent from the

scale, as comparable results have been obtained on samples exhibiting different dimension and shape used in the different experimental setups.

The obtained results on Sabucina stone have been therefore employed for planning conservative treatments devoted to coarse grained calcarenite substrate. In particular, nanostructured and innovative hybrids product synthesized at the Department of Chemistry of Parma University by sol-gel process have been tested on Sabucina Stone in order to evaluate the efficiency of the treatments by applying standard tests (*Chapter 5*); moreover, the eventually surface and sub-surface changes due to treatments have been evaluated by using the experimental approach successfully applied in the previous sections in order to esteem weathering effects on pore geometry of studied stone.

In detail, water based sols containing titanium dioxide have been deposited on calcarenite substrates (Sabucina stone) to obtain self-cleaning coatings taking advantage of the well known TiO_2 photocatalytic properties. Basic (TiMaA) and acid (TiAcN) sols were synthesized by sol-gel method, working at low temperatures and in different environments, with the aim to evaluate the effects of sols at different pH on calcarenite substrate. The obtained results by applying a routine based on standard recommendations allow to asses that both acid and basic titanium nanosols exhibit good properties, in terms of preserving the characteristics of the stone; in fact, the treatments do not significantly alter the color and water absorption of the stone. Referring to durability, the resistance to salt crystallization is generally improved as showed by accelerated degradation tests. As concern the self-cleaning properties, both TiO_2 coatings exhibit a good photodegradation activity on methylene blue and methyl orange dyes, being harmless against the stone. Moreover, beside the general non-homogenous trends observed in photocatalisis curves, mainly due to the heterogeneous color of the stone and the high porosity of the surface, the presence of TiO_2 coatings catalyses the photodegradation of both dyes with a better efficiency of the basic preparation (TiMaA) under UV lamp and the acid preparation (TiAcN) under the daylight one. One of the most important requirement in the usage of a protective coating is the ability of minimizes the capillarity absorption and improves the durability, without modifying the chromatic appearance distinctive of the monuments; therefore, considering the high solubility of calcite-based materials in acid environment, a basic coating should be preferred, the latter one determining a lower chromatic changes in stone (ΔE 1.5) and exhibiting better filmogenic proprieties (as inferred by SEM analysis).
In addition, a hybrid product constituted by polyammidoammine with silicon-alkoxide functions, namely PAASi, and a hybrid sol based on a Al-Si network functionalized with organic chains, namely AlSiX, have been tested on Sabucina Stone, also associated with the hydrophobic coating WS3 (based on colloidal silica and silicone with fluorurate groups). On the

whole, the results obtained by performing standard tests show good performance of the products in term of global enhancement of the stone proprieties, even if some disadvantages have to be highlighted. In fact, the siloxan alkoxide product (AlSiX) determines strong chromatic changes, especially if it is used in association with the hydrophobic coating, as well as a slightly decrease of resistance of stone against salts crystallization. Otherwise, the use of polyammidoammine product (PAASi) seems to be less invasive in term of chromatic changes, assuring at the same time lower absorption of water by capillarity and total immersion as well as a significant enhancement of durability of the stone against salt crystallization weathering. Finally, the overall data obtained on treated samples coated also with the hydrophobic product claim an improvement of the performances of both consolidants respect to usage by themselves, even if a slight decrease of the salt crystallization resistance has to be claimed.

Referring to consolidant and protective products, the investigation of additional aspects as penetration depth and interaction with substrate are required. Therefore, a multi-scalar and multi-methodological approach has been applied in order to esteem accurately the suitability of products (*Chapter 6*). In detail, both classical and innovative techniques have been employed in order to evaluate the penetration depth of AlSiX and PAASi consolidant (used also in combination with WS3 hydrophobic treatment), quantify and visualize the eventually modification of the stone in term of behavior against water and, finally, esteem the surface texture changes in samples coated with TiO_2 sols.

Referring to consolidants, the application of intrusion mercury method has given back not really convincing results, maybe due to limits of resolution in term of pore size investigable. Otherwise, better results have been obtained by using X-ray μ-CT; the method is, in fact, able to inspect pores greater than 100 μm, allowing to describe also greater structures. Quantitative information on pore ranges interested by the impregnation of the product have been therefore obtained by processing X-ray tomographies; in fact, the technique has allowed to quantify the impregnation of PAASi in a range of 10 μm< ED <100μm and MO <50 μm and the distribution of AlSiX product in a larger pore range (ED between 100 and 500 μm; MO between 50 and 150 μm), claiming a different interaction of the products with the pore network structure of the stone. More complete description of the interaction between products and substrate has been obtained by using neutron radiography, as its high sensitivity to hydrogen-based materials; by using this method it has been possible to estimate and visualize the distribution of products inside the stone matrix and the changes in the stone behavior against water. In particular, for AlSiX a penetration depth of about 2-3 mm has been esteemed, while PAASi and hydrophobic products were impossible to visualize. In spite of the scarce penetration depth, the products affect the hydric proprieties of stone; in fact, the monitoring of capillary uptake over the time and the determination of the relative linear penetration coefficients highlight that in samples

treated with AlSiX the penetration of water is slightly inhibited by the presence of the product; otherwise, the PAASi treatment determines no significantly changes respect to the untreated stone. Finally, in the case of hydrophobic product, the radiographs images convincingly illustrate that no water invades the stone samples, also when it is used in association with the consolidants. The previous qualitative information are confirmed by the quantification of water percentage distribution inside the treated samples; in fact, the WC% contour plots show a significant reduction of water absorption by capillarity in the stone samples treated with AlSiX consolidant (always, the WC values are lower than 2%), while in the case of PAASi a slight worsening of the water resistance to absorption by capillarity has been observed (values up to 2.5-3 WC% has been obtained, higher than in the untreated stone); in the case of the hydrophobic treatment, used both alone and in combination with consolidants, the contour plots show that no water invade the samples over the monitoring time. A good agreement between data obtained from neutron radiography images processing and classical gravimetric tests has been observed, having the former method the great advantage to visualize the process occurring inside the samples.

Finally, the inspection of TiO_2-sols coated surfaces has allowed to highlight the ability of 3D digital microscope in evaluating the changes in texture features determined by protective treatments. In detail, on the basis of the acquired and processed surface maps, an overall decrease of surface roughness and waviness parameters due to the treatments has been observed, with a greater variation in term of Ra/ Wa, Rq/ Wq and Rt/ Wt parameters for the TiO_2 acid preparation, maybe more invasive in calcarenite substrates.

Therefore, the overall of the obtained data has to be considered a good example of the potential of the applied experimental and teorethical approach in investigating how salt weathering process acts and visualizing and quantifying pore structure and surface texture modifications due to protective and consolidant treatments in natural building stones, especially in the case of coarse-grain calcite-based materials. In addition, the used method has highlighted how by applying interdisciplinary, multiscale and multi-methodological approach in complex systems more relationships can be understood, more questions answered and new questions asked. Therefore, answers to questions associated with how building stones change and how decaying masonry may be conserved can practically help the conservation science disciplines in continuing, evolving and maturing the researches in the stone weathering field.

Chapter 8. Biographic notes

Simona Raneri, Conservator Scientist for Cultural Heritages and Geologist, since 2013 is Ph.D. Student at the Department of Biological, Geological and Environmental Sciences at the University of Catania, where she works on a research project devoted to the modeling of inner structure of natural building stones by applying fractal geometry and test nanostructured products for their conservation and protection, under the supervision of Prof. G. Barone and Prof. P. Mazzoleni. In addition to her main research activity, she works also on archaeometric characterization of artificial stone materials by means innovative non-invasive and non-destructive methodologies. Her work produces several communications at International Conferences and papers on National and International Journals. She is co-author of 16 ISI papers in International Scientific Journals, as well as book chapters and extended abstracts. She received the National Prize Angelo Bianchi 2015 bestowed by the Italian Society of Mineralogy and Petrology (SIMP) for her scientific contribute to the Italian Mineralogical and Petrological Sciences.

8.1 Scientific production

8.1.1 Journal

1. Barone G, Mazzoleni P, Pappalardo G, **Raneri S** (2015) Microtextural and microstructural influence on the changes of physical and mechanical proprieties related to salts crystallization weathering in natural building stones. The example of Sabucina stone (Sicily), Construction and Building Materials, 95, 355-365.
2. Aquilia E, Giuffrida A, Ingoglia C, Mazzoleni P, **Raneri S** (2015): Archaeometric investigation on wall paintings from the most ancient Hellenistic hypogeum found in Sicily (C. da Apaforte - Licata (AG). Rendiconti Lincei. DOI: 10.1007/s12210-015-0419-0
3. Bergamonti L, Alfieri I, Lorenzi A, Predieri G, Barone G, Gemelli G, Mazzoleni P, **Raneri S**, Bersani D, Lottici PP (2015): Nanocrystalline TiO2 coatings by sol–gel: photocatalytic activity on Pietra di Noto biocalcarenite. Journal of Sol-Gel Science and Technology. 10.1007/s10971-015-3684-6
4. Aquilia E, Barone G, Mazzoleni P, **Raneri S**, Lamagna G (2015): Petro-archaeometric characterization of potteries from a kiln in Adrano, Sicily. Heritage Science 12. 3:11. DOI: 10.1186/s40494-015-0043-4
5. **Raneri S**, Barone G, Crupi V, Longo F, Majolino D, Mazzoleni P, Tanasi D, Teixeira J, Venuti V (2015): Technological analysis of Sicilian prehistoric pottery production through small angle neutron scattering technique. Periodico di Mineralogia 84, 1, 1-22. DOI: 10.2451/2015PM0001

6. **Raneri S**, Barone G, Mazzoleni P, Tanasi D, Costa E (2015): Mobility of men versus mobility of goods: archaeometric characterization of Middle Bronze Age pottery in Malta and Sicily (15th-13th century BC). Periodico di Mineralogia, 84, 1, 23-44. DOI: 10.2451/2015PM0003.
7. Barone G, Gullì D, Mazzoleni P, **Raneri S**, Tanasi D (2015): Archaeometric identification of Maltese imports in prehistoric Sicily: Żebbuġ phase pottery from Licata-Caduta (Agrigento). Malta Archaeological Review, 2010–2011, Issue 10 23-30
8. **Raneri S**, Cnudde V, De Kock T, Derluyn H, Barone G, Mazzoleni P (2015):X-ray computed micro-tomography to study the porous structure and degradation processes of a building stone from Sabucina (Sicily). European Journal of Mineralogy. doi: 10.1127/ejm/2015/0027-2433
9. Barone G, Bersani D, Jehlička J, Lottici PP, Mazzoleni P, **Raneri S**, Vandenabeele P, Di Giacomo C, Larinà G (2014): Non Destructive Investigation On The 17th/18th Century Sicilian Jeweler Collection At The Messina Regional Museum Using Mobile Raman Equipment. Journal Raman Spectroscopy. DOI: 10.1002/jrs.4649.
10. Bersani B, Azzi G, Lambruschi E, Barone G, Mazzoleni P, **Raneri S**, Longobardo U, Lottici PP (2014): Characterization of emeralds by micro-Raman spectroscopy. Journal of Raman Spectroscopy, 45, 1293–1300. doi: 10.1002/jrs.4524
11. Barone G, Bersani D, Crupi V, Longo F, Longobardo U, Lottici PP, Aliatis I, Majolino D, Mazzoleni P, **Raneri S**, Venuti V (2014): A portable vs. micro-Raman equipment comparison for gemological purposes: the case of sapphires and their imitations. Journal of Raman Spectroscopy, 45, 1309-1317. doi: 10.1002/jrs.4555.
12. Barone G, Crupi V, Longo F, Majolino D, Mazzoleni P, **Raneri S**, Teixeira J, Venuti V (2014): Neutron radiography for the characterization of porous structure in degraded building stones. Journal Instrumentation 9, C05024. doi:10.1088/1748-0221/9/05/C05024
13. Barone G, Crupi V, Longo F, Majolino D, Mazzoleni P, **Raneri S**, Teixeira J, Venuti V(2014): A multi-technique approach for the determination of the porous structure of building stone. European Journal of Mineralogy 26, 189-198.doi: 10.1127/0935-1221/2014/0026-2355
14. Barone G, Crupi V, Longo F, Majolino D, Mazzoleni P, **Raneri S**, Venuti V (2013): A multi-technique approach for the characterization of decorative stones and non-destructive method for the discrimination of similar rocks. X-Ray Spectrometry, 43, 83-91. doi: 10.1002/xrs.2520.
15. Barone G, Bruno N, Giuffrida A, Mazzoleni P, **Raneri S** (2013): Archaeometric investigation of Late Roman marble statue from Kaucana (RG): new perspectives on the diffusion of Thassos marble in Sicily. Periodico di Mineralogia 82, 305-321.

16. Agostino R, Barone G, Mazzoleni P, **Raneri S**, Sabatino G, Sica MM (2013): Mortars and plasters from the Bruttii - Roman city of Tauriana (Palmi - RC) - preliminary data. Periodico di Mineralogia 82, 489-501.

8.1.2 Books

1. Barone G, Mazzoleni P, **Raneri S**, Tanasi D, Giuffrida A: Archaeometric characterization of Middle Bronze Age pottery from Borg in-Nadur village, in D. Tanasi, N. C. Vella (eds.), The late prehistory of Malta: essays on Borg in-Nadur and other sites, Midsea Books, Malta, 2014.
2. Barone G, Chowanieck R, Fibula M, Mazzoleni P, **Raneri S**: Petro-archaeometric characterization of archeological ceramics from Akrai, in Chowanieck R (Eds), unveiling the Past of an Ancient Town. Akrai/Acrea in south-eastern Sicily. *In press.*

8.1.3 Extended abstracts

1. Barone G, Bersani D, Jehlicka J, Lottici PP, Mazzoleni P, **Raneri S**, Vandenabeele P. Fast on-site identification of minerals by using portable Raman equipment in gemological trade contexts and in collectors exhibitions. Periodico di Mineralogia - ECMS 2015, 208, 27-28.
2. Mazzoleni P, Barone G, Aquilia E, Bersani D, Cirrincione R, **Raneri S**. Potentiality of micro-Raman spectroscopy for the identification of unclassified minerals preserved in old museum collections. Periodico di Mineralogia - ECMS 2015, 208, 117-118.
3. Barone G, Bersani D, Lottici PP, Mazzoleni P, **Raneri S**, Longobardo U. Application of micro-Raman spectroscopy for gemstones characterization. The case of rubies, VIII Congresso Nazionale di Archeometria Scienze e Beni Culturali: stato dell'arte e prospettive, Bologna 5 - 7 Febbraio 2014.
   www.associazioneaiar.com/cms/sites/default/files/Extended_abs_2014/CeD_oral/Barone%20et%20al.pdf
4. Aquilia E, Barone G, Mazzoleni P, **Raneri S**, Lamagna G. Petro-archaeometric characterization of kiln pottery wastes from Adrano, Sicily, VIII Congresso Nazionale di Archeometria Scienze e Beni Culturali: stato dell'arte e prospettive, Bologna 5 - 7 Febbraio
   2014.www.associazioneaiar.com/cms/sites/default/files/Extended_abs_2014/PeD_poster/Aquilia%20et%20al%20.pdf
5. Barone G, Ciliberto E, Corsaro RA, Costagliola P, Di Benedetto F, Mazzoleni P, Miraglia L, Gimeno D, **Raneri S**. The effects of volcanic ashes on the environment and health: first data on Mt. Etna case study, Fist Geoitalia 2013, 15-18 September, Pisa (Italy).

6. Aquilia E, Barone G, Bruno N, Mazzoleni P, **Raneri S**, Tusa S. Caratterizzazione di ceramiche archeologiche subacquee dal porto piccolo di Siracusa, VI Congresso Nazionale di Archeometria "Scienza e Beni Culturali". Pavia, 15-18 Febbraio 2010. ISBN 978-88-555-3181-8. Pag. 1-6.
7. **Raneri S**, Greco E. Use of echo sounders in marine archaeology: survey of harbor in Syracuse, International Conference YOCoCu, YOuth in Conservation of Cultural Heritage. Roma, 24-25 Novembre 2008. ISBN: 978-88-86208-59-8. Pag. 282-287

8.1.4 Proposals at International Facility

1. Mariani G, Bassani F, Carducci F, Dall'orso S, Fuenzalida W, Juan P, Groehn F, Kutz A, Perinelli DR, **Raneri S**, Schweins R. (2014). Dendrimer-dye electrostatic self-assembly: a time-resolved SANS study. Institut Laue-Langevin (ILL) doi:10.5291/ILL-DATA.9-10-1366

2. Barone G, Mazzoleni P, Predieri G, Rabot E, **Raneri S**, Teixeira J. (2015). Investigation on suitability of consolidant and protective products on Sicilian calcarenite by using neutron imaging . Laboratoire Leon Brillouin LLB, Saclay, France, n. experiment 12115

3. Barone G, Mazzoleni P, **Raneri S**, Teixeira J. et al.(2012) LLB "2D and 3D textural analysis of the effects of salt crystallization induced degradation on limestone of interest in cultural heritage, Cea-Saclay (France).

Per aspera ad astra

S. Raneri, Complex Pore Geometries in Natural Building Stones: an experimental and theoretical approach for the modeling of porosity changes in natural, degraded and treated calcarenites, Ph.D. thesis, University of Catania, 2015.